Turbulent boundary layers with adverse pressure gradient

Carlos Sanmiguel Vila

in partial fulfillment of the requirements for the degree of Doctor in
Programa Interuniversitario en Mecánica de Fluidos

Universidad Carlos III de Madrid

Advisor 1:
Stefano Discetti

Advisor 2:
Andrea Ianiro

Tutor:
Stefano Discetti

Leganés, April 2019

A mi madre, gracias por estar siempre a mi lado.

Acknowledgements

This work has been partially supported by the Universidad Carlos III de Madrid through a PIF scholarship awarded on a competitive basis, and by the program "Ayudas para la Movilidad del Programa Propio de Investigación", the Grant DPI2016-79401-R, funded by the Spanish State Research Agency (SRA) and by European Regional Development Fund (ERDF) and by the COTURB project (Coherent Structures in Wall-bounded Turbulence), funded by the European Research Council (ERC), under grant agreement ERC-2014.AdG-669505.

Con estas líneas cierro 4 años de mi vida que no hubiera podido ser capaz de llevar a cabo sin el apoyo de toda la gente que he tenido la suerte de tener a mi lado. Por ello me gustaría poder agradecérselo a todos los implicados que han hecho esta tesis posible. Me gustaría empezar por Javier Rodríguez, ya que en gran medida es el responsable de que este aquí acabando esta tesis. Muchas gracias por responderme aquel correo con tanto entusiasmo e introducirme a las personas que me darían después la oportunidad de trabajar en lo que más me apasionaba. También por estar siempre echándonos una mano o estar disponible para unas cervezas. Después me gustaría dar las gracias a mis dos supervisores Stefano y Andrea, por creer en mi sin conocerme previamente y hacer que hoy pueda terminar esta tesis. Que haya podido cerrar esta tesis es indudablemente gracias a ti, Stefano. Gracias por poner orden en el caos, por estar siempre disponible y por tu apoyo total siempre. A pesar de todas las llamadas a horas intempestivas y los innumerables marrones que siempre te acompañan, también te estoy agradecido a ti, Andrea, por tenerte como supervisor. Es bastante probable que esta tesis sin ti se hubiera acabado antes, pero no hubiera tenido el mismo nivel de calidad que ahora mismo tiene. Gracias por exigirme más, por intentar mejorar mi trabajo, por tus ideas geniales (aunque un tanto caóticas) y por haberte preocupado siempre por mí. Por último, aunque no sea director de esta tesis creo que se merece ir aquí por todas las veces que me ha ayudado, aunque estuviera ocupado en mil cosas. Gracias Marco, por haberme acompañado en esta particular odisea, por todos los momentos en el laboratorio y fuera de él. Creo que sin ti a mi lado, mi salud mental hubiera estado bastante más afectada de lo que ya ha acabado. Muchas gracias a los 3 por todos los momentos tanto en Leganés como por Europa, tanto por los divertidos como por los "terrificantes", ha sido una experiencia inolvidable.

A pesar de no estar ya en ese despacho, toda esta aventura hubiera sido mucho más aburrida sin mis compañeros del H03, gracias tanto los que aún siguen allí como a los que ya terminaron. A Toni, gracias por tu "humor" que echamos de menos (aquí sigue tu Hulk), a Manu, *danke* por toda la ayuda que siempre me diste y por hacer un gran update en mis figuras, a Víctor, te recordamos desde el destierro (gracias por esos *die kurve*), a Rocco, gracias por hacer compañía en el despacho hasta última hora, a Luca, a ver si les echas una mano con el español a Rocco y Marco, a Gonzalo, gracias por hacerme de beta tester y por tener siempre a mano una referencia a los Simpson, a Güemes, suerte con la campaña que te espera y como bien dijo Marco, al final todo termina y a Cayetano, por todo el buen humor y para que veas que esta tesis ya está finalmente terminada. Mención aparte, tiene Alex que desde el H03 me acompaño a donde estoy ahora. Gracias por toda la ayuda estos meses, sé que en San Diego te va a ir genial así que disfrútalo y espero seguir viéndote. También gracias a los vecinos del H05, tanto a la Iglesia del Plasma, como a todos los allí presentes. Gracias a Dani y David, por todos los momentos y en especial, a David como mi

pareja de tenis todo este tiempo (gracias a ti también Fer), animo con lo que os queda que ya casi estáis. A Sara y Dani, mucha suerte con la startup, espero que estéis en el futuro correcto.

I would also like to dedicate some words of gratitude to the people from KTH. This thesis would not have been possible without you (this actually is quite true). Thanks Ramis, Ricardo and Philipp for all your help and for hosting me during the months that I spent in Sweden. It is a pleasure to work with you guys. Thanks Ricardo for introducing me to all the people and for all the Champions League's nights. Thanks Ramis for all your inestimable help during all these years and for being patient with me. I hope that we can work together in the future. Thanks also to the people of Bologna and Cottbus for the experimental campaigns that we carried out there, it was intense but we had a lot of fun.

Me gustaría también agradecer a toda la gente del departamento de aeroespacial por todo el buen ambiente que siempre ha habido. Gracias a Javi, José, Soler y Sanjurjo por los partidos de fútbol y las anécdotas, muchas gracias Pablo por contar siempre conmigo ha sido un placer trabajar contigo, gracias a Óscar por aquel mes en la politécnica (ojalá que podamos cerrarlo) y gracias a Eduardo por contar conmigo para este departamento. Gracias también a Manolo, Gonzalo, Angelo, Mario y Rauno por toda la amabilidad en estos años, y en general a toda la gente que compone el departamento. Muchas gracias a Carlos y a Guille por todo el soporte que me han dado durante este tiempo, sin vosotros no hubiera podido realizar mis experimentos. También esto último incluye a los técnicos de oficina técnica y del departamento de Fluidos, que siempre nos han ayudado.

A mis amigos del colegio Javi y Keko, por todas las tardes en el barrio y todos los momentos que hemos pasado juntos, no podría haber encontrado amigos mejores. Gracias Silvia por haberme acogido en Suecia con Jorge, y a Marta, por preocuparse siempre.

A los aeronáuticos, porque a pesar de que estemos un poco dispersos es un placer teneros en mi vida, gracias a Carlos, Dani, Raúl, Mario, Gallego y Rafa porque aunque no nos veamos tanto como antes siento como si no pasara el tiempo cuando nos vemos. A Pablo, para que esta tesis te sirva de ejemplo y acabes pronto, no se te ocurra irte a Brasil sin pasar por aquí. A Limi y a Antonio, porque no sé qué puedo deciros para agradeceros todo, simplemente sois increíbles.

A toda mi familia que siempre ha estado arropándome, gracias a mis tías Concha y Paloma, que han estado siempre ahí. A mis primos, Rubén y Marta, porque sois como los hermanos que nunca tuve y siempre habéis cuidado de mí. También a mi primo Adrián, sin el que probablemente las reuniones familiares serían más aburridas.

A mis padres, porque gracias a ellos he llegado donde estoy ahora, gracias por todo vuestro amor y apoyo incondicional. Gracias por todo Mama, por ser un ejemplo a seguir y por enseñarme a enfrentarme a cualquier cosa. A mi padre por estar conmigo y cuidar de mí en casa.

Por último, me gustaría darte las gracias Carol por ser el pilar mi vida, por quererme y cuidarme siempre, eres la mejor compañera que podría tener para recorrer este camino (y los que vienen). Gracias por siempre motivarme, por no dejar que me venga abajo y por hacerme mejor persona. Eres parte de todos mis éxitos y de todo lo que vendrá después. Muchas gracias a ti también Mari José, por haberme cuidado todos los fines de semana, gracias por hacerme sentir con el Ronnie y el Canito como en casa.

Published and submitted content

The following publications are fully included in the part II of this thesis:

Paper 1

Carlos Sanmiguel Vila, Ricardo Vinuesa, Stefano Discetti, Andrea Ianiro, Philipp Schlatter, Ramis Örlü, 2017. *On the identification of well-behaved turbulent boundary layers*, Journal of Fluid Mechanics, **822**, 109–138. doi:10.1017/jfm.2017.258

Paper 2

Ricardo Vinuesa, Ramis Örlü, Carlos Sanmiguel Vila, Stefano Discetti, Andrea Ianiro, Philipp Schlatter, 2017. *Revisiting history effects in adverse-pressure-gradient turbulent boundary layers*, Flow, Turbulence and Combustion, **99 (3–4)**, 565–587. doi:10.1007/s10494-017-9845-7

Paper 3

Carlos Sanmiguel Vila, Ramis Örlü, Ricardo Vinuesa, Philipp Schlatter, Andrea Ianiro, Stefano Discetti, 2017. *Adverse-pressure-gradient effects on turbulent boundary layers: statistics and flow-field organization*, Flow, Turbulence and Combustion, **99 (3–4)**, 589–612. doi:10.1007/s10494-017-9869-z

Paper 4

Carlos Sanmiguel Vila, Ricardo Vinuesa, Stefano Discetti, Andrea Ianiro, Philipp Schlatter, Ramis Örlü, 2019. *Large-scale motions and amplitude modulation in adverse-pressure-gradient turbulent boundary layers*, Journal of Fluid Mechanics, **Under Revision**.

Whenever material from these sources is included in this thesis, it is singled out with typographic means and an explicit reference.

Division of work between authors

Paper 1

The experimental set-up has been designed by Ramis Örlü (RÖ). The experiments and the data analysis have been performed by Carlos Sanmiguel Vila (CSV), RÖ, and Ricardo Vinuesa (RV). The paper has been written by CSV with feedback from Stefano Discetti (SD), Andrea Ianiro (AI), RÖ, RV and Philipp Schlatter (PS).

Paper 2

RV and RÖ collected the data from various simulations. The paper has been written by RV with feedback from SD, AI, RÖ, CSV and PS.

Paper 3

The experimental set-up has been designed by CSV, RV, SD, AI, PS and RÖ. The experiments and the data analysis have been performed by CSV, RÖ, RV, AI and SD. RV and RÖ collected the data from various simulations. The paper has been written by CSV with feedback from SD, AI, RÖ, RV and PS.

Paper 4

The experimental set-up has been designed by CSV, RV, SD, AI, PS and RÖ. The experiments and the data analysis have been performed by CSV, RÖ, RV, AI and SD. The paper has been written by CSV with feedback from SD, AI, RÖ, RV and PS.

Other research merits

The following publications, although related, are not included in this thesis:

Carlos Sanmiguel Vila, Ricardo Vinuesa, Stefano Discetti, Andrea Ianiro, Philipp Schlatter, & Ramis Örlü, 2019. *Large-scale energy in turbulent boundary layers: Reynolds-number and pressure-gradient effects*, Progress in Turbulence VIII, **Accepted**

Stefano Discetti, Gabriele Bellani, Ramis Örlü, Jacopo Serpieri, Carlos Sanmiguel Vila, Marco Raiola, Xiaobo Zheng, Lucia Mascotelli, Alessandro Talamelli & Andrea Ianiro, 2019. *Characterization of very-large-scale motions in high-Re pipe flows*, Experimental Thermal and Fluid Science, **104**, 1–8. doi:10.1016/j.expthermflusci.2019.02.001

Fermin Mallor, Marco Raiola, Carlos Sanmiguel Vila, Ramis Örlü, Stefano Discetti & Andrea Ianiro, 2019. *Modal decomposition of flow fields and convective heat transfer maps: An application to wall-proximity square ribs*, Experimental Thermal and Fluid Science, **102**, 517–527. doi:10.1016/j.expthermflusci.2018.12.023

Carlos Sanmiguel Vila & Oscar Flores, 2018. *Wall-based identification of coherent structures in wall-bounded turbulence*, Journal of Physics: Conference Series, **1001**, 012007. doi:10.1088/1742-6596/1001/1/012007

Fermin Mallor, Carlos Sanmiguel Vila, Andrea Ianiro & Stefano Discetti, 2018. *Wall-mounted perforated cubes in a boundary layer: Local heat transfer enhancement and control*, International Journal of Heat and Mass Transfer, **117**, 498–507. doi:10.1016/j.ijheatmasstransfer.2017.10.027

Carlos Sanmiguel Vila, Ricardo Vinuesa, Stefano Discetti, Andrea Ianiro, Philipp Schlatter, & Ramis Örlü, 2017. *Identifying Well-Behaved Turbulent Boundary Layers*, Progress in Turbulence VII, **196**, 67–72. doi:10.1007/978-3-319-57934-4_10

Carlos Sanmiguel Vila, Stefano Discetti, Giovanni Maria Carlomagno, Tommaso Astarita & Andrea Ianiro, 2016. *On the onset of horizontal convection*, International Journal of Thermal Sciences, **110**, 96–108. doi:10.1016/j.ijthermalsci.2016.06.019

Conferences

Part of the work in this thesis has been presented at the following international conferences.

Carlos Sanmiguel Vila, Ricardo Vinuesa, Stefano Discetti, Andrea Ianiro, Philipp Schlatter & Ramis Örlü. *Large-scale energy in turbulent boundary layers: Reynolds-number and pressure-gradient effects.* Interdisciplinary Turbulence Initiative 2018 (iTi 2018). Bertinoro, Italy, September 2018.

Carlos Sanmiguel Vila, Ricardo Vinuesa, Stefano Discetti, Andrea Ianiro, Philipp Schlatter & Ramis Örlü. *Scale contribution in adverse pressure-gradient turbulent boundary layers.* 55^{th} Annual Technical Meeting of the Society of Engineering Science (SES 2018). Leganés, Spain, September 2018.

Andrea Ianiro, Carlos Sanmiguel Vila, Emir Öngüner, Carlo Salvatore Greco, El-Sayed Zanoun, Ramis Örlü, Tommaso Astarita, Christoph Egbers & Stefano Discetti. *High–Dynamic–Range PIV Measurements in Pipe Flows at High Reynolds Numbers.* 55$^{\text{th}}$ Annual Technical Meeting of the Society of Engineering Science (SES 2018). Leganés, Spain, September 2018.

Stefano Discetti, Carlos Sanmiguel Vila, Marco Raiola, Jacopo Serpieri, Ramis Örlü, Xiaobo Zheng, Lucia Mascotelli, Gabriele Bellani, Alessandro Talamelli & Andrea Ianiro. *Very–large–scale–motion measurements in pipe flow with extended POD.* 55$^{\text{th}}$ Annual Technical Meeting of the Society of Engineering Science (SES 2018). Leganés, Spain, September 2018.

Fermin Mallor, Marco Raiola, Carlos Sanmiguel Vila, Ramis Örlü, Andrea Ianiro & Stefano Discetti. *Turbulent convective heat-transfer measurements in boundary layers with ribs.* 5$^{\text{th}}$ International Conference on Experimental Fluid Mechanics (ICEFM 2018). Munich, Germany, July 2018.

Ramis Örlü, Carlos Sanmiguel Vila, Ricardo Vinuesa, Andrea Ianiro, Stefano Discetti & Philipp Schlatter. *Scaling of adverse-pressure-gradient turbulent boundary layers.* 5$^{\text{th}}$ International Conference on Experimental Fluid Mechanics (ICEFM 2018). Munich, Germany, July 2018.

Fermin Mallor, Marco Raiola, Carlos Sanmiguel Vila, Ramis Örlü , Stefano Discetti & Andrea Ianiro. *Modal analysis of instantaneous flow fields and convective heat transfer in a boundary layer downstream of square ribs.* 18$^{\text{th}}$ International Symposium on Flow Visualization (ISFV 2018). Zurich, Switzerland, June 2018.

Stefano Discetti, Carlos Sanmiguel Vila, Marco Raiola, Jacopo Serpieri, Ramis Örlü, Lucia Mascotelli, Tomasso Fiorini, Gabriele Bellani, Alessandro Talamelli & Andrea Ianiro. *Very–large–scale motion measurements in pipe flows at high Reynolds numbers.* 16$^{\text{th}}$ EUROMECH European Turbulence Conference (ETC 16). Stockholm, Sweden, August 2017.

Carlos Sanmiguel Vila, Stefano Discetti, Ricardo Vinuesa, Andrea Ianiro, Philipp Schlatter, & Ramis Örlü. *Single pixel PIV study of adverse-pressure-gradient turbulent boundary layers.* 16$^{\text{th}}$ EUROMECH European Turbulence Conference (ETC 16). Stockholm, Sweden, August 2017.

Ramis Örlü, Ricardo Vinuesa, Carlos Sanmiguel Vila, Stefano Discetti, Andrea Ianiro, & Philipp Schlatter. *Towards canonical adverse-pressure-gradient turbulent boundary layers.* 10$^{\text{th}}$ International Symposium on Turbulence and Shear Flow Phenomena (TSFP10). Chicago, USA, July 2017.

Ramis Örlü, Ricardo Vinuesa, Philipp Schlatter, Carlos Sanmiguel Vila, Stefano Discetti & Andrea Ianiro. *Re-assessment of canonical and non-canonical adverse-pressure-gradient turbulent boundary layers.* 9$^{\text{th}}$ World Conference on Experimental Heat Transfer, Fluid Mechanics and Thermodynamics (ExHFT9). Iguazu Falls, Brazil, June 2017.

Fermin Mallor, Carlos Sanmiguel Vila, Andrea Ianiro & Stefano Discetti. *Wall-mounted porous obstacles: Heat transfer enhancement and control opportunities.* 9$^{\text{th}}$ World Conference on Experimental Heat Transfer, Fluid Mechanics and Thermodynamics (ExHFT9). Iguazu Falls, Brazil, June 2017.

Stefano Discetti, Carlos Sanmiguel Vila, Andrea Ianiro, Ricardo Vinuesa, Philipp Schlatter & Ramis Örlü. *Adverse pressure gradient turbulent boundary layers: flow organization and high resolution statistics.* The 12$^{\text{th}}$ International Symposium on Particle Image Velocimetry (ISPIV2017). Busan, Korea, June 2017.

Carlos Sanmiguel Vila, Ricardo Vinuesa, Stefano Discetti, Andrea Ianiro, Philipp Schlatter & Ramis Örlü. *Identifying well-behaved turbulent boundary layers.* Interdisciplinary Turbulence Initiative 2016 (iTi 2016). Bertinoro, Italy, September 2016.

Ramis Örlü, Carlos Sanmiguel Vila, Ricardo Vinuesa, Andrea Ianiro, Stefano Discetti, & Philipp Schlatter. *Revisiting tripping effects in low-Reynolds number turbulent boundary layer.* 11^{th} Engineering Turbulence Modelling and Measurements (ETMM 11). Sicily, Italy, September 2016.

Carlos Sanmiguel Vila, Ramis Örlü, Ricardo Vinuesa, Andrea Ianiro, Stefano Discetti & Philipp Schlatter. *Wind tunnel studies of history effects in turbulent boundary layers.* 11^{th} European Fluid Mechanics Conference (EFMC 11). Seville, Spain, September 2016.

Ramis Örlü, Alexandra Bobke, Carlos Sanmiguel Vila, Ricardo Vinuesa, Stefano Discetti, Andrea Ianiro & Philipp Schlatter. *History effects in adverse pressure gradient turbulent boundary layers - Simulations & Experiments.* 24^{th} International Congress of Theoretical and Applied Mechanics (ICTAM 2016). Montreal, Canada, August 2016.

Carlos Sanmiguel Vila, Tommaso Astarita, Giovanni Maria Carlomagno, Stefano Discetti & Andrea Ianiro . *An experimental study on the onset of the horizontal convection.* 10^{th} Pacific Symposium on Flow Visualization and Image Processing (PSFVIP-10). Naples, Italy, July 2015.

Carlos Sanmiguel Vila. *Measurements of pressure fluctuations in a turbulent boundary layer.* 11^{th} Pegasus-AIAA Student Conference. Salon de Provence, France, April 2015.

Turbulent boundary layers with adverse pressure gradient

Carlos Sanmiguel Vila
Aerospace Engineering Group, Universidad Carlos III de Madrid
Leganés, Spain

Abstract

The focus of this thesis is the assessment of the adverse-pressure-gradient effects on the flow organization and statistics of turbulent boundary layers (TBLs). To this purpose, a unique high-quality experimental database has been acquired and analysed in detail. A preliminary study of the required conditions to obtain well-behaved turbulent-boundary-layer flows both in zero-pressure-gradient (ZPG) and adverse-pressure-gradient (APG) conditions is carried out in order to ensure the outstanding quality of the presented dataset.

The first part of the thesis aims at assessing well-behaved turbulent-boundary-layer flows, i.e., turbulent boundary layers which are independent of the inflow conditions and exempt of any numerical or experimental artefacts. First, history effects of tripping devices for turbulent boundary layers developing in zero-pressure-gradient conditions are explored. An experimental study which comprises six tripping configurations, including optimal setups as well as both under- and over-tripped cases, is performed to assess the convergence of ZPG TBLs towards well-behaved conditions. The explored Reynolds-number range covers that of recent high-fidelity direct-numerical simulation (DNS) data up to a momentum-thickness-based Reynolds number $Re_\theta \approx 4,000$. The results show that weak tripping configurations lead to deviations within the logarithmic region of the mean flow and of the velocity fluctuations with respect to those of optimally-tripped boundary layers. On the other hand, a strong trip leads to a more energized outer region, with the emergence of an outer peak in the velocity-fluctuation profile and of a more prominent wake region. A new method based on the diagnostic plot (Alfredsson *et al.*, Phys. Fluids, **23**:041702, 2011) is introduced to assess the convergence towards a well-behaved ZPG TBL. The most popular and well-understood methods to assess the convergence towards a well-behaved state rely on empirical skin-friction curves (thus requiring accurate skin-friction measurements), shape-factor curves (hence requiring full velocity profile measurements with an accurate wall-position determination) or wake-parameter curves (requiring both of the previous quantities). On the other hand, the proposed diagnostic-plot method only needs measurements of mean and fluctuating velocities in the outer region of the boundary layer at arbitrary wall-normal positions. The new method is tested on a dataset collected in the Minimum Turbulence Level wind tunnel at KTH and with additional recent high-Re datasets available in the literature for further validation. Skin-friction and shape-factor correlations generally yield equivalent results with respect to the diagnostic-plot method in terms of convergence towards a well-behaved state. The proposed method has the advantage of being a less-time-consuming tool when designing the set-up for TBL experiments, since it diagnoses the state of the boundary layer without the need to perform extensive velocity profile measurements and to accurately determine the wall position.

The next step is to establish operative criteria aimed at assessing whether a particular adverse-pressure-gradient (APG) TBL can be considered well-behaved or not. To this end, several high-quality datasets are analysed, including numerical databases of APG TBLs developing over flat plates and over the suction side of a wing section, and five studies available in the literature. The different streamwise pressure-gradient distributions are characterised with the Clauser pressure-gradient parameter, β, which represents the ratio of the forces acting (per unit spanwise length) on a fluid element due to the pressure gradient and to the wall-shear stress. Due to the impact of the flow history on the particular state of the boundary layer, three criteria to assess convergence to well-behaved conditions are developed. In the first criterion, empirical correlations defining the Re_θ–evolution of the skin-friction coefficient and the shape factor in APG TBLs with constant values of $\beta = 1$ and 2 are developed. In the second one, a predictive method

to obtain the skin-friction curve corresponding to an APG TBL subjected to any streamwise evolution of β, based only on data from ZPG TBLs is proposed. The third method relies on the diagnostic-plot concept modified with the shape factor, which scales APG TBLs subjected to a wide range of pressure-gradient conditions. These three criteria allow to ensure the correct flow development of a particular TBL, and thus to separate upstream-history and pressure-gradient effects in the analysis.

The second part of the thesis is composed of two studies which focus on APG TBLs under pressure-gradient conditions at different Reynolds numbers. In the first study, flow-field measurements are carried out, and supplemented with data from numerical simulations. The study covers a range of Reynolds-number $1,300 < Re_\theta < 22,300$ and analyses TBLs with values of the Clauser pressure-gradient parameter β up to 2.4. The spatial-resolution limits of PIV for the estimation of turbulence statistics were overcome via ensemble-based approaches. A comparison between ensemble-correlation methods and ensemble Particle Tracking Velocimetry was carried out to assess the uncertainty of the two methods. The effects of β, Re and of the pressure-gradient history on turbulence statistics were assessed. A modal analysis via Proper Orthogonal Decomposition was carried out on the flow fields and showed that about 20% of the energy contribution corresponds to the first mode, while 40% of the turbulent kinetic energy corresponds to the first four modes with no appreciable dependence on β and Re within the investigated range. The spatial organization of the modes, on the other hand, shows a dependence on the Reynolds number and on the pressure-gradient strength, in line with the results obtained from the analysis of the turbulence statistics. The contribution of the modes to the Reynolds stresses and the turbulence production were assessed using a truncated low-order reconstruction with a progressively-increasing number of modes. It is shown that the outer peaks in the Reynolds-stress profiles are mostly due to large-scale structures in the outer part of the boundary layer, which are included in few most energetic POD modes.

In the second study, APG TBLs are investigated using a new extensive hot-wire database which covers a range of Reynolds number $450 < Re_\theta < 23,450$ and a β range up to 2.4. Increasing and approximately-constant β distributions with the same upstream pressure-gradient history are characterised. The mean and higher-order statistics of the new APG TBL database are planned to be online under the following URL: `https://www.flow.kth.se/flow-database`. Turbulence statistics are compared among the different pressure-gradient distributions and additional numerical and experimental ZPG TBL data at matched friction Reynolds number Re_τ. Cases at approximately-constant β, which can be considered as "canonical" representations of the boundary layer under a certain pressure-gradient magnitude, exhibit skin-friction and shape-factor curves consistent with those proposed by Vinuesa *et al.* (*Flow Turbul. Combust.*, 99, 565–587, 2017) at lower Reynolds number. These curves resemble those proposed by Nagib *et al.* (*Phil. Trans. R Soc. A.*, 365, 755–770, 2007) for ZPG TBLs. The pre-multiplied power-spectral density is employed to address the differences in the large-scale energy content throughout the boundary layer. Two different large-scale excitation mechanisms are identified, the first one due to the pressure gradient and the second one (also present in high-Re ZPG TBLs) due to the Reynolds number. A decomposition of the streamwise velocity fluctuations using a spatial filter shows that the small-scale velocity fluctuations do not scale in APG TBL flows since the effect of the large-scale features extends all the way down to the near-wall region, resulting in a stronger modulation of the fluctuations. The large-scale modulation is further studied using the methodology proposed by Ganapathisubramani *et al.* (*J. Fluid Mech.*, 712, 61–91, 2012). This analysis provides a picture of more intense fluctuations of the large scales and of enhanced influence on the small scales as the pressure-gradient strength increases. Based on the interaction between high- and low-speed events, a method to locate the outer peak due to pressure-gradient effects is assessed. Recently proposed scaling laws by Kitsios *et al.* (*Int. J. Heat Fluid Flow*, 61, 129–136, 2016) and Maciel *et al.* (*J. Fluid Mech.*, 844, 5–35, 2018) are tested over a wider Reynolds-number range and for different β cases. The mean velocity and streamwise-velocity-fluctuation profiles are found to be

dependent on the upstream development. The mean velocity profile is found to be self-similar only in the outer region, in agreement with the classical theory. The evolution of the outer-peak location and its corresponding streamwise variance magnitude is also presented. The outer-peak location, when scaled in outer units, is found to be weakly dependent on the Reynolds number and more influenced by pressure-gradient effects.

Key words: Wall turbulence, turbulent boundary layer, zero-pressure-gradient turbulent boundary layer, wall-bounded flows, adverse-pressure-gradient turbulent boundary layer, PTV, PIV, hot-wire anemometry, POD

Turbulent boundary layers with adverse pressure gradient

Carlos Sanmiguel Vila
Aerospace Engineering Group, Universidad Carlos III de Madrid
Leganés, Spain

Resumen

El objetivo de esta tesis es el estudio de los efectos del gradiente de presión adverso en una capa límite turbulenta (TBL). Se pretende caracterizar como afecta tanto a la estructura del flujo como a las distintas estadísticas. Con este fin, una nueva base de datos de alta calidad y características únicas ha sido adquirida y analizada en detalle. Un estudio preliminar para determinar las condiciones necesarias para tener una capa límite turbulenta con "buen comportamiento" tanto para las condiciones de sin gradiente de presión (ZPG) como para con gradiente de presión adverso (APG) es llevado a cabo para asegurar la calidad de la base de datos que se presenta en esta tesis.

La primera parte de la tesis tiene como objetivo evaluar las condiciones necesarias para obtener capas límite turbulentas con "buen comportamiento", es decir, que son independientes de las condiciones de entrada del flujo y que están exentas de cualquier artefacto numérico o experimental. Con este propósito, se llevaron a cabo dos estudios diferentes, cada uno relacionado con un tipo específico de capa límite. El primer estudio está dedicado a estudiar el efecto que tienen los dispositivos de "tripping" en la historia y en el desarrollo de las capas límite turbulentas sin gradiente de presión. Para ello se realizo un estudio experimental que comprende seis configuraciones de "tripping", que abarcan tanto configuraciones óptimas, así como configuraciones con poca o excesiva estimulación, para cuantificar la convergencia de las ZPG TBL hacia condiciones de buen comportamiento. Estos estudios se realizaron en el rango de números de Reynolds que está cubierto por recientes Simulaciones Directas Numéricas (DNS) de alta fidelidad que llegan hasta un número de Reynolds basado en el espesor de cantidad de movimiento $Re_\theta \approx 4,000$. Los resultados muestran que las configuraciones de "tripping" débiles, comparadas con las capas límite perturbadas de manera óptima, conducen a desviaciones tanto en el perfil medio como en las fluctuaciones de la velocidad en la zona correspondiente a la región logarítmica. Por otro lado, la sobrestimulación de la capa límite conduce a un flujo con una región exterior más energizada, que se manifiesta en la aparición de un pico exterior en el perfil de fluctuaciones de la velocidad y en una región de estela más prominente en el perfil medio. Se propone un nuevo método basado en el "diagnostic plot" (Alfredsson *et al.*, Phys. Fluids, **23**: 041702, 2011) para evaluar la convergencia hacia las condiciones de "buen comportamiento" para capas límites turbulentas sin gradiente de presión. Los métodos más populares y establecidos para evaluar la convergencia hacia un estado de buen comportamiento dependen de las curvas empíricas del coeficiente de fricción (que requieren mediciones precisas de la fricción en la pared), curvas del factor de forma (que requieren mediciones del perfil de velocidad completas con una determinación precisa de la posición de la pared) o curvas del parametro "wake" (que requieren las dos cantidades anteriores). Sin embargo, el método propuesto basado en el "diagnostic plot" solo necesita mediciones de las velocidades medias y sus fluctuaciones en la región exterior de la capa límite en posiciones arbitrarias en la dirección normal a la pared. El nuevo método es validado usando la base de datos presentada previamente y adicionalmente con bases de datos externas que tienen un rango de número Re más alto. Los resultados mostrados por el nuevo método coinciden con aquellos obtenidos con los criterios basados en las curvas del coeficiente de fricción y las correlaciones del factor de forma, con la ventaja añadida de no necesitar medidas exhaustivas de la velocidad. Esta ventaja lo convierte en una herramienta más eficiente a la hora de diseñar la configuración adecuada para realizar experimentos con capas límite, ya que es capaz de diagnosticar el estado de la capa límite sin la necesidad de medir todo el perfil de velocidad.

En el segundo estudio, el objetivo es presentar un primer paso para poder establecer criterios que sean capaces de evaluar si una capa límite turbulenta con gradiente de presión adverso

puede considerarse con "buen comportamiento". Con este fin, se han analizado varias bases de datos consideradas de alta calidad, que incluyen: bases de datos numéricas de APG TBL que se desarrollan sobre placas planas, APG TBL que corresponden al lado de succión de una sección de un ala, y cinco estudios adicionales que están disponibles en la literatura. Debido al efecto de la historia del flujo en el estado particular de la capa límite, se desarrollan tres criterios de convergencia a condiciones de "buen comportamiento", que se utilizarán dependiendo del caso particular a estudiar. En el primer criterio, las correlaciones empíricas que definen la evolución con Re_θ del coeficiente de fricción y el factor de forma en APG TBL para los casos de valores constantes del parámetro de presión-gradiente de Clauser, $\beta = 1$ y 2 son presentadas. En el segundo, se propone un método predictivo para obtener la curva del coeficiente de fricción correspondiente a un APG TBL sometida a una evolución cualquiera del parámetro β, que esta basado solo en datos de ZPG TBL. El tercer método se basa en el concepto del "diagnostic plot" modificado con el factor de forma, que escala los APG TBL sometidas a un amplio rango de condiciones de gradiente de presión. Estos tres criterios permiten garantizar el desarrollo correcto del flujo de un APG TBL particular y, por lo tanto, separar los efectos de la historia y del gradiente de presión en el análisis del flujo.

La segunda parte de la tesis está compuesta por dos estudios que se centran en el estudio de APG TBLs que están bajo diferentes condiciones de número de Reynolds y gradiente de presión. Las diferentes distribuciones de gradiente de presión impuestas son caracterizadas utilizando el parámetro de Clauser de gradiente de presión, β, que representa el ratio de fuerzas que actúan en un elemento fluido debido al gradiente de presión y a la tensión cortante en la pared. En el primer estudio, se analizan mediciones obtenidas con la Velocimetría de Imágenes de Partículas (PIV) que se complementan con simulaciones realizadas con Large Eddy Simulations (LES). Los datos cubren un rango de número de Reynolds de $1,300 < Re_\theta < 22,300$ y de $0 < \beta < 2.4$. Los límites de la resolución espacial de las medidas de PIV para la estimación de estadísticas turbulentas se han resuelto mediante enfoques basados en el ensamblado de partículas. Se ha realizado un estudio entre los métodos basados en la correlación de ensambles de partículas y los métodos basados en ensambles de velocimetría con seguimiento de partículas para poder evaluar la calidad de los dos métodos, a la hora de calcular las estadísticas turbulentas. También, se evaluaron los efectos de β, Re y de la historia del gradiente de presión $\beta(x)$ en las estadísticas turbulentas. Se ha realizado un análisis modal utilizando la Descomposición Modal Ortogonal en los campos de flujo. Los resultados muestran que aproximadamente el 20 % de la contribución de la energía corresponde al primer modo, mientras que el 40 % de la energía cinética turbulenta corresponde a los primeros cuatro modos, sin una dependencia apreciable de β y Re dentro del rango investigado. La topología de los modos espaciales muestra una dependencia del número de Reynolds y de la intensidad del gradiente de presión, en línea con los resultados obtenidos del análisis de las estadísticas turbulentas. La contribución de los modos a los esfuerzos de Reynolds y a la producción de la turbulencia se evaluaron mediante una reconstrucción truncada de orden reducido. Finalmente, se ha mostrado como los picos en la región exterior de los perfiles de los esfuerzos de Reynolds se deben principalmente a estructuras a gran escala que se encuentran en la parte exterior de la capa límite.

En el segundo estudio, los APG TBL se estudian utilizando una nueva base de datos extensa de Anemometría de Hilo Caliente (Hot-Wire) que abarca un rango de número de Reynolds $450 < Re_\theta < 23,450$ y un rango de β que llega hasta valores de $\beta \approx 2.4$. Se han estudiado distintas configuraciones de gradiente de presión adverso con distribuciones crecientes y aproximadamente constantes de β que cuentan con la misma historia previa. Las estadísticas turbulentas se comparan entre las configuraciones de gradiente de presión y adicionalmente, con datos numéricos y experimentales de ZPG TBL con el mismo número de Reynolds basado en la velocidad de fricción Re_τ. Los casos que tienen distribuciones de β aproximadamente constantes se pueden considerar como representaciones "canónicas" de la capa límite bajo una cierta magnitud del gradiente de presión. Estos casos muestran curvas del coeficiente de fricción y factor de forma consistentes con

las propuestas por Vinuesa *et al.* (*Flow Turbul. Combust.*, 99, 565–587, 2017), también muestran una formulación parecida a que tienen las curvas de ZPG TBL que fueron propuestas por Nagib *et al.* (*Phil. Trans. R Soc. A.*, 365, 755–770, 2007). La densidad espectral de la potencia multiplicada por la frecuencia se emplea para estudiar las diferencias en el contenido de la energía de las escalas grandes a través de la capa límite. De está forma, se identifican dos fenómenos diferentes relacionados con las escalas grandes, el primero debido al efecto del gradiente de presión y el segundo (también presente en las ZPG TBL con alto número de Re) debido al efecto del número de Reynolds. Una descomposición en escalas de las fluctuaciones de velocidad en el sentido de la corriente utilizando un filtro espacial, muestra que las fluctuaciones de velocidad relacionadas con las escalas pequeñas no escalan igual que en los flujos ZPG TBL. Esto es debido a que el efecto de las escalas grandes se extiende en las APG TBLs hasta la región viscosa, lo que resulta en una modulación más fuerte de las fluctuaciones. La modulación provocada por las escalas grandes se estudia más a fondo utilizando la metodología propuesta por Ganapathisubramani *et al.* (*J. Fluid Mech.*, 712, 61-91, 2012). Este análisis permite ver como las fluctuaciones de las escalas grandes se hacen más intensas a la vez que influyen más en las escalas pequeñas cuando aumenta la intensidad del gradiente de presión. Utilizando la interacción entre eventos de alta/baja velocidad, se propone un método para localizar el máximo de la región exterior de la capa límite asociado a los efectos del gradiente de presión. Los escalados propuestos recientemente por Kitsios *et al.* (*Int. J. Heat Fluid Flow*, 61, 129–136, 2016) y Maciel *et al.* (*J. Fluid Mech.*, 844, 5–35, 2018) son evaluados en un rango amplio de números de Reynolds y para diferentes casos de β. Los perfiles de velocidad media y de fluctuación de la velocidad se muestran dependientes del desarrollo del flujo. También se muestra que el perfil de velocidad media es solamente autosemejante en la región exterior, tal y como se describe en la teoría clásica. De la misma forma, se presenta la evolución de la ubicación del pico exterior y su correspondiente valor. La ubicación del pico exterior, cuando se escala en unidades externas, esta poco afectada por efectos asociados al número de Reynolds y se muestra más influenciada por efectos asociados al gradiente de presión. Los perfiles medios de velocidad y las estadísticas turbulentas de orden superior de la nueva base de datos de APG TBLs se van a publicar en abierto en la siguiente URL: `https://www.flow.kth.se/flow-database`.

Palabras clave: Turbulencia de pared, capa límite turbulenta, capa límite turbulenta sin gradiente de presión, capa límite turbulenta con gradientes de presión, PTV, PIV, anemometría de hilo caliente, POD

Contents

Part II - Papers

Part I

Overview and summary

Chapter 1

Introduction

Turbulence is one of the greatest unsolved problems of physics which has always attracted the interest of physicists, engineers, and mathematicians. Part of this fascination derives from the ubiquitous presence of the turbulence in nature and industrial flows. Turbulence plays a crucial role in the atmospheric and oceanic dynamics, being one of the main factors that make life on Earth possible. The influence of turbulence on the transport of gases, nutrients and on the uniformity of the temperature in Earth's atmosphere enable to have suitable conditions of oxygen and temperature across the world. Regarding the industrial processes, turbulence has a prominent influence in almost all man-made flows. It has for instance key relevance in the drag performance of all types of vehicles or in chemical reactions, to cite a few examples.

The relevance of turbulent flows fostered their investigation for centuries. The first use of the word "turbulence" to refer to a flow dates back to 1500 when it was used by Leonardo Da Vinci to describe the chaotic motion of water. Nonetheless, it was not until the XIX century when systematic investigation of turbulent flows took place. The works carried out by Boussinesq (1877) and Reynolds (1883, 1895), addressing the turbulence problem with a statistical approach, paved the way to the development of a flourishing scientific research area. In particular, the work conducted by Reynolds (1895) presented the concept of the Reynolds decomposition which consists in decomposing the flow in a mean and a fluctuating part. This decomposition allowed to introduce key concepts such as the "existence" of the Reynolds stresses. In addition, this work also introduced the closure problem, which still persists unsolved until today. The first attempts to tackle this problem were performed at the beginning of the 20th century (Taylor 1915, 1922; Prandtl 1925; von Kármán 1930) with the so-called mixing length models. Concurrently with these works, the building blocks of the turbulent theory were developed in the works by Richardson (1920) and Kolmogorov (1941). In their works, the turbulence is described as a multiscale phenomenon which covers a wide range of length scales. Kolmogorov (1941) presented the theory of the spectral-energy cascade which assumes that the energy introduced in the turbulent flow generates large-scale structures which eventually break down in smaller eddies due to flow instabilities. This process is repeated several times until reaching the so-called Kolmogorov scales, which are small enough for the viscosity to dissipate them. From the second half of the 20th century to the present day, the number of studies about turbulence has continued to grow, as it can be observed in Figure 1.1. The introduction of computational science as a powerful research tool, combined with the emergence of more sophisticated experimental techniques, have helped triggering this growing tendency. This effort led to a more complete understanding of turbulent flows during the last years. A general approach to the existing knowledge of the turbulent problem can be found in the following monographs: Tennekes & Lumley (1972); Hinze (1975); Townsend (1956) and Pope (2000).

Among the wide variety of turbulent flows which can be found in our daily life, a notable class is that of the so-called shear flows, which are inhomogeneous flows with mean-velocity gradients. The shear flows are divided into two groups: free and wall-bounded shear flows, depending on whether they develop in the absence of boundaries or not, respectively. Jets, wakes or mixing layers are examples or free shear flows; pipe, channel and turbulent-boundary-layer (TBL) flows

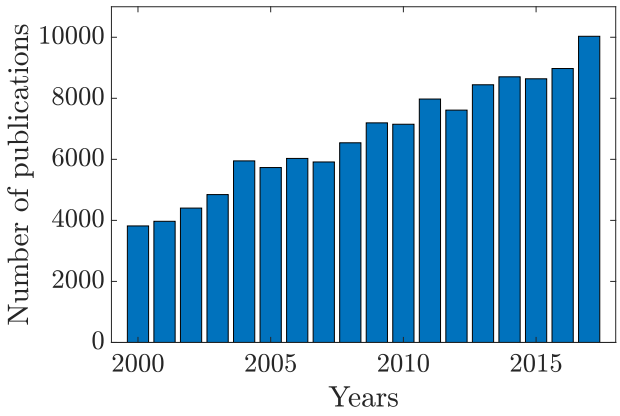

Figure 1.1: Number of scientific publications for the word "Turbulence" in the period 01 January 2000 - 01 January 2018. Source: Scopus.

are examples of wall-bounded flows. This latter type of flow has a paramount relevance since turbulent-boundary-layer flows are crucial for the performances of many engineering processes, such as the drag performance of vehicles through air and water or the heat-transfer efficiency of several industrial processes (Kim 2011). As stated by Jiménez (2012): "Roughly half the energy spent in transporting fluids through pipes and canals, or vehicles through air and water, is dissipated by turbulence in the immediate vicinity of walls." In addition to the economic impact, a better understanding of the turbulent flows could potentially impact the design process of transportation means, paving the way to novel more efficient design concepts. This would have a clear influence on the reduction of greenhouse gases or aircraft noise, which are some of the medium and long term objectives of the European Union's policies. In particular, the goal is to achieve by 2050 a reduction of the greenhouse-gases emission about to 80-95% below the level of 1990 (see `https://ec.europa.eu/clima/citizens/eu_en`).

The rationale behind the inherent complexity of turbulent flows lays within their mathematical framework, the Navier–Stokes equations. Apart from very simple cases, there is no analytical solution for these equations nor it has been shown that a solution exists. The existence of the solution of the Navier–Stokes equations is one of the "Millennium Problems", with a one-million-dollar prize offered (Doering 2009). The advances in the field of turbulence are thus mostly due to the analysis of experimental and numerical data. Each approach offers different advantages and limitations, which explain the current need to combine both. On one hand, the main advantage of the experimental techniques is that they can provide data at high Reynolds numbers. Nonetheless, each technique is inherently limited, either in spatial or temporal resolution, and the results are affected by experimental uncertainty. Furthermore, not all quantities are accessible simultaneously (only a combination of techniques can provide all the required variables of the Navier-Stokes equations, i.e. the velocity vector and two independent thermodynamic quantities, such as pressure and temperature for instance). On the other hand, numerical data fully resolve the flow field with high spatial and temporal resolution in a specific computational domain, but at a moderate Reynolds number or at the prize of introducing turbulence closure models. Depending on the level of accuracy of the results, three different approaches are possible. The most accurate numerical simulation procedure is known as Direct Numerical Simulation (DNS) (Moin & Mahesh 1998). This procedure integrates the Navier–Stokes equations, resolving all the scales down to the dissipative range. This method has also the highest computational cost associated since the number of grid points required scale with $Re^{9/4}$, being Re the Reynolds number, and therefore powerful supercomputers are required for these simulations. To reduce the computational cost, in

Large-Eddy Simulation (LES) (Sagaut 2006) only the largest scales are fully resolved, while the smallest unresolved length and time scales are described by using different sub-grid dissipative scale models. The Reynolds Averaged Navier–Stokes equations (RANS) employing a certain variety of closure models (Kajishima & Taira 2017) represents a computationally–cheap approach based on the Reynolds decomposition (Reynolds 1895) and is the most widely used tool in industrial applications. This last procedure is the preferred method in the industry since it provides an acceptable estimate of the flow field with lower computational times and limited computational power. However, RANS simulations are seldom used in research applications because the required closure models for the Reynolds stresses rely on previous knowledge about the flow case in order to adjust the parameters of the model.

For both numerical and experimental methodologies, the large amount of data and the large dimensionality of the problem obtained from them require different techniques for their complete analysis. On one side, there are the classical statistical tools which allow characterizing the flow from a statistical point of view. These techniques include analysis of the different statistical moments (i.e mean, variance, skewness, kurtosis among others), probability density functions, correlation functions or power density spectra. Their potential applications are described in books such as Tennekes & Lumley (1972); Townsend (1956) and Pope (2000). Modal decomposition tools are also employed with the aim of identifying a more compact description of the most relevant flow features. The final goal would be to obtain reduced-order models describing the essential flow-field features in a compact form (Holmes *et al.* 2012; Rowley & Dawson 2017). Some of the most popular modal decomposition tools are Proper Orthogonal Decomposition (POD) (Berkooz *et al.* 1993) and Dynamic Mode Decomposition (DMD) (Schmid 2010).

Despite the continuous improvements of the experimental and numerical methodologies, real-life cases of wall-bounded turbulent flows are still too complex to be analysed in detail. As a consequence, simplified cases are studied to assess theories and reduced-order models that are extrapolated to more complex cases. The canonical cases for wall-bounded turbulent flows are the pipe, the channel and the zero-pressure-gradient (ZPG) TBL flows. These cases are used as baseline flows which allow studying the effect of different flow disturbances, such as the inclusion of obstacles or flow-control devices, in a much simpler flow configuration. After studying these canonical cases as a first step, more realistic flow conditions are sought out to pave the way towards real-life flow conditions. Among others, the development of a TBL under the effect of a streamwise pressure gradient has recently captured much attention (Bobke *et al.* (2017); Cuvier *et al.* (2017); Kitsios *et al.* (2017); Maciel *et al.* (2018); Yoon *et al.* (2018), **Paper 2, 3, 4**). This type of TBL is a case observed in many practical applications (*i.e* flow around a turbine blade, airfoils, etc.) but its understanding is still quite limited and in large part empirical. Several research questions remain open, such as the changes in the flow organization or of the skin friction curves due to the pressure gradient effect. Addressing these questions could lead to improving our current aerodynamic designs or applying more efficient flow–control techniques.

In this thesis, the effect of a streamwise pressure gradient in a turbulent-boundary-layer flow from both in terms of flow statistics and of flow organization is analysed. The objective is to obtain and analyse a high-quality dataset that allows to characterise these effects and step up the knowledge of these flows. For this purpose, first, the required conditions to achieve a "well-behaved" (i.e not in a post-transitional state or affected by non-equilibrium effects) TBL are examined and discussed. These conditions are needed to obtain a baseline TBL flow that can be used later to include additional effects, such as the streamwise pressure gradient. This is a necessary condition to obtain high-quality experimental/numerical databases, without effects of inflow characteristics, and thus being valid for the comparison with the theory. After this analysis, adverse-pressure-gradient turbulent boundary layers are studied using different experimental and post-processing techniques. As a result, a high-quality database with an unprecedented Reynolds-number range for near-equilibrium and non-equilibrium cases is obtained, providing a

detailed characterisation of APG TBLs. It is planned to make the database available online as a reference case for future studies.

Thesis structure. The thesis is organised as follows: Part I will continue with an introduction to turbulent boundary layers in chapter 2 in which the main concepts for ZPG TBL and APG TBL flows are introduced. Chapter 3 covers a summary of the different experimental techniques and facilities employed in the present thesis. Part I of this thesis ends with a summary of the main results and contributions of the present work. Part II contains four research articles, one on the study of "well-behaved" zero-pressure-gradient turbulent boundary layers and three related to the study of adverse-pressure-gradient turbulent boundary layers.

Paper 1

Carlos Sanmiguel Vila, Ricardo Vinuesa, Stefano Discetti, Andrea Ianiro, Philipp Schlatter, Ramis Örlü, 2017. *On the identification of well-behaved turbulent boundary layers*, Journal of Fluid Mechanics, **822**, 109–138.

Paper 2

Ricardo Vinuesa, Ramis Örlü, Carlos Sanmiguel Vila, Stefano Discetti, Andrea Ianiro, Philipp Schlatter, 2017. *Revisiting history effects in adverse-pressure-gradient turbulent boundary layers*, Flow, Turbulence and Combustion, **99 (3–4)**, 565–587.

Paper 3

Carlos Sanmiguel Vila, Ramis Örlü, Ricardo Vinuesa, Philipp Schlatter, Andrea Ianiro, Stefano Discetti, 2017. *Adverse-pressure-gradient effects on turbulent boundary layers: statistics and flow-field organization*, Flow, Turbulence and Combustion, **99 (3–4)**, 589–612

Paper 4

Carlos Sanmiguel Vila, Ricardo Vinuesa, Stefano Discetti, Andrea Ianiro, Philipp Schlatter, Ramis Örlü, 2019. *Large-scale motions and amplitude modulation in adverse-pressure-gradient turbulent boundary layers*, Journal of Fluid Mechanics, **Under Revision**.

Chapter 2

Turbulent Boundary layer Flows

2.1. Preliminaries

In this chapter, a brief introduction to the problem of wall-bounded turbulent shear flows is presented. The parameters and concepts that are used in the rest of the thesis are introduced and defined. For a more detailed description of the wall-bounded turbulent shear flows the reader is referred to the several monographs available in the literature, such as those by Tennekes & Lumley (1972); Hinze (1975); Townsend (1956) or Pope (2000).

In order to have an overall view of the problem, it is interesting to introduce the definitions of turbulence and boundary layer. The difficulty in identifying a definition which covers the wide variety of turbulent flows generated a large wealth of definitions. One of the first definitions was provided by von Kármán (1937) who gave the following definition: "Turbulence is an irregular motion which in general makes its appearance in fluids, gaseous or liquid, when they flow past solid surfaces or even when neighbouring streams of the same fluid flow past or over one another." Using this definition as a reference, Hinze (1975) reformulated it and proposed a more accurate version as follows: "Turbulent fluid motion is an irregular condition of flow in which the various quantities show a random variation with time and space coordinates, so that statistically distinct average values can be discerned." This definition can be completed with the remarks of Bradshaw (2013) who add that turbulence flows are characterised for having a wide range of wavelengths. In the author's opinions, the combination of these three statement define the turbulence flows adequately. As pointed out in the definition given by von Kármán (1937) the turbulence can be generated and affected by solid walls; these cases are defined as wall-bounded turbulent shear flows. When a fluid stream flows around a solid body, Prandtl (1904) showed that two different regions can be differentiated: an inviscid outer region in which the viscosity effects can be neglected; a region close to the wall in which the viscosity must be taken into account. The latter is the so-called boundary layer. The introduction of this concept allow to apply a certain number of assumptions that simplify the study of the Navier–Stokes equations. In the present chapter, the turbulent-boundary-layer flow for the particular case of steady, two-dimensional and incompressible flow is considered. Herewith, we denote the streamwise, wall-normal and spanwise directions with x, y and z, respectively. In connection with the definition of turbulence introduced previously, the corresponding velocity vectors can be decomposed in a mean part with components, (U, V, W), denoted with capital letters, and a fluctuating part which is indicated with lowercase letters (u, v, w). Additionally, the overbar ($^-$) is used to indicate time averaging of quantities other than the mean ones. The density, the kinematic viscosity and the mean pressure are defined as ρ, ν and P. With this in mind, the momentum equations for a two-dimensional incompressible steady boundary layer flow are introduced as,

$$U\frac{\partial U}{\partial x} + V\frac{\partial U}{\partial y} = -\frac{1}{\rho}\frac{\partial P}{\partial x} + \nu\frac{\partial^2 U}{\partial y^2} - \frac{\partial \overline{uv}}{\partial y} - \frac{\mathrm{d}(\overline{u^2} - \overline{v^2})}{\mathrm{d}x} \tag{2.1}$$

$$\frac{\partial \overline{v^2}}{\partial y} = -\frac{1}{\rho}\frac{\partial P}{\partial y}. \tag{2.2}$$

The mean total shear stress, τ, can be expressed as,

$$\tau = \rho\nu\frac{\partial U}{\partial y} - \rho\overline{uv}. \tag{2.3}$$

The correlation terms $\overline{u^2}$, $\overline{v^2}$ and $\overline{uv}$, multiplied by the density, ρ, are commonly referred as the Reynolds stress in the streamwise, wall-normal and streamwise-wall normal direction, respectively. These terms represent the stresses on the fluid due to the turbulent fluctuations. For the cases of fully–developed channel and pipe flows, the streamwise derivatives of the Reynolds normal stresses are zero, and for the particular case of zero pressure-gradient they are neglected since its contribution is lower compared with respect to the streamwise-wall-normal gradients. Using the definition of τ provided by equation 2.3, the streamwise momentum equation 2.1 can be rewritten as,

$$U\frac{\partial U}{\partial x} + V\frac{\partial U}{\partial y} = -\frac{1}{\rho}\frac{\partial P}{\partial x} + \frac{1}{\rho}\frac{\partial \tau}{\partial y}, \tag{2.4}$$

and the wall-normal momentum equation 2.2 can be integrated as,

$$\overline{v^2} + \frac{1}{\rho}P = \frac{1}{\rho}P_w(x), \tag{2.5}$$

where $P_w(x)$ is the mean pressure at the wall and U_∞ is the free-stream velocity. Following this approach, equation 2.4 can be integrated from the wall to the free stream and therefore the von Kárman integral momentum equation is obtained as,

$$\frac{\tau_w(x)}{\rho} = \frac{\mathrm{d}}{\mathrm{d}x}\left[U_\infty^2(x)\int_0^\infty \frac{U(x,y)}{U_\infty(x)}\left(1-\frac{U(x,y)}{U_\infty(x)}\right)\mathrm{d}y\right] + U_\infty(x)\frac{\mathrm{d}U_\infty}{\mathrm{d}x}\int_0^\infty\left(1-\frac{U(x,y)}{U_\infty(x)}\right)\mathrm{d}y, \tag{2.6}$$

where the wall shear stress is defined as τ_w. This result can be expressed in a more compact form introducing the following definitions,

$$\theta(x) = \int_0^\infty \frac{U(x,y)}{U_\infty(x)}\left(1-\frac{U(x,y)}{U_\infty(x)}\right)\mathrm{d}y \tag{2.7}$$

$$\delta^*(x) = \int_0^\infty \left(1-\frac{U(x,y)}{U_\infty(x)}\right)\mathrm{d}y. \tag{2.8}$$

These integral measures are known as the momentum thickness and the displacement thickness, respectively. With these quantities, the equation 2.6 can be reduced to,

$$\frac{\tau_w(x)}{\rho} = \delta^* U_\infty(x)\frac{\mathrm{d}U_\infty(x)}{\mathrm{d}x} + \frac{\mathrm{d}}{\mathrm{d}x}\left[U_\infty^2(x)\theta\right]. \tag{2.9}$$

This result can be simplified for the particular case of ZPG TBLs. In these flows, there is no pressure gradient along the streamwise direction, ($\partial P/\partial x = 0$), which is analogous to a case with a constant U_∞. This allows to express equation 2.9 using the definition of the skin-friction coefficient, C_f as,

$$C_f = \frac{\tau_w}{\frac{1}{2}\rho U_\infty} = 2\frac{\mathrm{d}\theta}{\mathrm{d}x}. \tag{2.10}$$

For the cases of channel and pipe flows, the wall shear stress is typically expressed as a function of the wall pressure. Simplifying and integrating equation 2.1 for these flow cases, the following relations are obtained for channel and pipe flows, respectively,

$$\tau_w = -\delta \frac{\mathrm{d}P_w}{\mathrm{d}x} \tag{2.11}$$

$$\tau_w = -\frac{\delta}{2} \frac{\mathrm{d}P_w}{\mathrm{d}x}, \tag{2.12}$$

where δ corresponds to the channel half-width, h, for a channel flow or to the pipe radius R for a pipe flow. Consequently, the integration of the equation 2.1 also results in

$$\tau = \tau_w \left(1 - \frac{y}{\delta}\right). \tag{2.13}$$

This result shows that in the region close to the wall ($y/\delta << 1$), the shear stress is constant and equal to the wall shear stress τ_w. This behaviour is also valid for the case of ZPG TBLs, where δ is defined as the boundary layer thickness. Taking this into consideration and with the viscosity acting as the dominant term in this region, the following quantities ρ, ν and τ_w are a natural choice to form reference velocity and length scales in the viscous region. The so-called viscous/inner scales are thus defined as

$$u_\tau = \sqrt{\frac{\tau_w}{\rho}} \tag{2.14}$$

$$\ell_* = \frac{\nu}{u_\tau}, \tag{2.15}$$

where u_τ is defined as the friction velocity and ℓ_* as the viscous length scale. Using these quantities, the friction Reynolds number is expressed as

$$Re_\tau = \frac{u_\tau \delta}{\nu} = \frac{\delta}{\ell_*}. \tag{2.16}$$

The friction Reynolds number is an indicator of the ratio between the outer and inner scales. Normalizing equation 2.13 with the inner scales and assuming a $Re_\tau >> 1$, the mean velocity profile in the inner region acquires the functional form of the so-called law of the wall,

$$U^+ = \frac{U}{u_\tau} = f\left(\frac{y}{\ell_*}\right) = f(y^+), \tag{2.17}$$

where the superscript + indicates normalization with inner scales. This form which was derived by Prandtl (1925) can be expressed for the viscous sublayer region ($y^+ < 5$) as

$$U^+ = y^+. \tag{2.18}$$

In the outer region ($y \sim \delta$), the viscous terms are negligible, and as shown by von Kármán (1930), using dimensional analysis, the mean velocity adopt the following form,

$$U_\infty^+ - U^+ = F\left(\frac{y}{\delta}\right), \tag{2.19}$$

where $U_\infty^+ - U^+$ is known as the velocity defect. In the overlap region ($\ell_* < y < \delta$), both equations 2.18 and 2.19 are valid since $y^+ \to \infty$ and $y/\delta \to 0$. As a consequence, following the procedure known as asymptotic matching described by Millikan (1939), the correspondence between these expressions is only valid if the following relation is fulfilled

$$y^+ \frac{\mathrm{d}f(y^+)}{\mathrm{d}y^+} = \frac{y}{\delta} \frac{\mathrm{d}F(y/\delta)}{\mathrm{d}(y/\delta)} = \frac{1}{\kappa} = const. \tag{2.20}$$

This result is a consequence of the fact that the equations 2.18 and 2.19 do not have any common independent variables, and therefore the only possible outcome is a constant, which is

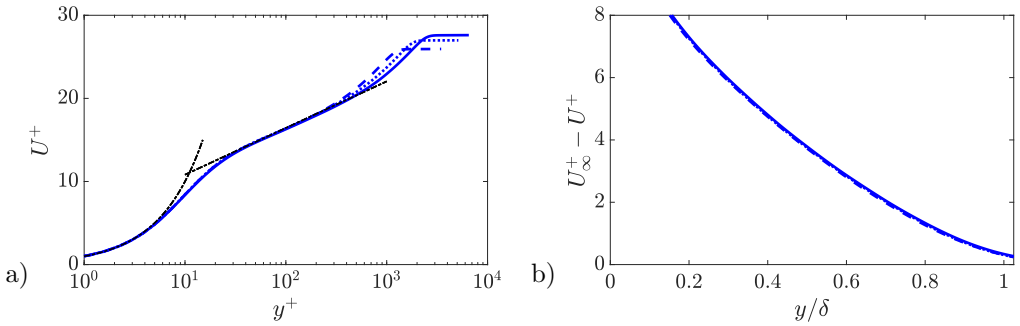

Figure 2.1: Mean streamwise velocity profiles from ZPG TBLs with inner scaling a) and outer scaling b). Blue dashed line correspond to $Re_\theta = 4,000$ from Schlatter & Örlü (2010), blue dotted line correspond to $Re_\theta = 6,000$ from Sillero *et al.* (2013) and blue solid line correspond to $Re_\theta = 8,000$ from Eitel-Amor *et al.* (2014). Black dash dotted auxiliary lines represent the relations $y^+ = U^+$ and $y^+ = \frac{1}{\kappa}\ln y^+ + B$, with $\kappa = 0.41$ and $B = 5.1$.

defined as the inverse of κ, the von Kármán constant. Integrating equation 2.20 the logarithmic velocity profile, known as the "law of the wall" is described as,

$$U^+ = \frac{1}{\kappa}\ln y^+ + B, \tag{2.21}$$

and the defect velocity law is,

$$U^+_\infty - U^+ = -\frac{1}{\kappa}\ln\frac{y}{\delta} + B_0, \tag{2.22}$$

where B and B_0 are the integration constants. The classical theories considered that both κ and B should be universal constants, but different values have been reported for pipe, channel or ZPG TBL flows (George 2007; Marusic *et al.* 2010). Typical values for these constants are close to $\kappa \approx 0.41$ and $B \approx 5.2$. For the case of B_0, there is no agreement in the literature with respect to its behaviour. Despite the universal agreement on the friction velocity as an appropriate scaling length for the inner region of the TBL, there are some doubts about its viability as an outer scaling variable. Indeed, these criticisms are justified for the case of ZPG TBLs where $\tau_w \to 0$ in the outer limit. For this reason, there are authors (George & Castillo 1997) who proposed the use of the free stream velocity as an outer scaling, or a combination of the free stream with the boundary layer thickness (Zagarola & Smits 1998; Wei & Maciel 2018). The use of these scalings instead of the u_τ leads to a power law description for the overlap region.

Figure 2.1 shows the mean streamwise velocity profiles from different numerical databases of ZPG TBLs. The data show a good agreement with the proposed relations from equations 2.18 and 2.21 for the whole range of Reynolds number, with an increased overlap region at higher Reynolds numbers. For the outer region, the collapse of the velocity defect with equation 2.19 is not as good as in the inner region. This is explained by the dependence of the outer region on the Reynolds number since the ZPG TBLs are spatially developing flows. Indeed, equation 2.19 would be strictly valid for the outer region only at large enough Reynolds number (Marusic *et al.* 2010). For the case of spatially developing flows, the Reynolds numbers based on the displacement and momentum thickness,

$$Re_\theta = \frac{U_\infty \theta}{\nu} \tag{2.23}$$

$$Re_{\delta^*} = \frac{U_\infty \delta^*}{\nu}, \tag{2.24}$$

are preferred. In addition, the ratio between δ^* and θ (and consequently of the corresponding Reynolds numbers) is defined as the shape factor,

$$H_{12} = \frac{\delta^*}{\theta}, \tag{2.25}$$

and is used as an indication of the "fullness" of the velocity profile.

In addition to the description of the inner region given by the linear and the logarithmic relations (equations 2.18 and 2.21), there has always been an interest in finding a functional form which represents the entire velocity profile, leading to the definition of composite profiles. These profiles are described as a superposition of the previously defined law of the wall (equation 2.17) and an additive function to describe the outer region. One of the first definitions of composite profiles was given by Coles (1956) which described the mean velocity profile as

$$U^+ = U^+_{inner} + \frac{2\Pi}{\kappa}\mathcal{W}\left(\frac{y^+}{\delta^+}\right), \tag{2.26}$$

where Π and $\mathcal{W}$ are known as the wake parameter and wake function, respectively. After this first attempt, several analytical expressions have been developed; the reader is referred to Örlü *et al.* (2010) where a summary of different composite profiles is reported. Among the existing composite profiles, the one proposed by Chauhan *et al.* (2009) is one of the most noteworthy. This formulation was developed and compared against a large number of databases of mean streamwise velocity profiles. Chauhan *et al.* (2009) provides the following formulation for U^+_{inner},

$$\begin{aligned} U^+_{inner} = \; & \tfrac{1}{\kappa}\ln\left(\tfrac{y^+-a}{-a}\right) + \tfrac{R^2}{a(4\alpha+a)}(4\alpha+a)\left[\ln\left(-\tfrac{a}{R}\tfrac{\sqrt{(y^+-\alpha)^2+\beta^2}}{y^+-a}\right)\right. \\ & \left. + \tfrac{\alpha}{\beta}(4\alpha+5a)\left(\arctan\left(\tfrac{y^+-\alpha}{\beta}\right)+\arctan\left(\tfrac{\alpha}{\beta}\right)\right)\right] + \tfrac{\exp[-\ln^2(y^+/30)]}{2.85}, \end{aligned} \tag{2.27}$$

where $\alpha = (-1/\kappa - a)/2$, $\beta = \sqrt{-2a\alpha - \alpha^2}$, $R = \sqrt{\alpha^2+\beta^2}$, $\kappa = 0.384$ and $a = -10.3061$. The wake function $\mathcal{W}$ is defined as,

$$\mathcal{W}(\eta) = \frac{1 - \exp\left[-(1/4)(5a_2+6a_3+7a_4)\eta^4 + a_2\eta^5 + a_3\eta^6 + a_4\eta^7\right]}{1-\exp[-(a_2+2a_3+3a_4)/4]}\left(1 - \frac{1}{2\Pi}\ln(\eta)\right) \tag{2.28}$$

where $\eta = y^+/\delta^+$, $a_2 = 132.8410$, $a_3 = -166.2041$ and $a_4 = 71.9114$. The composite profile formulation allows to determine the values of δ, Π and u_τ for a mean streamwise velocity ZPG TBL profile by means of a least-square procedure.

2.1.1. *"Well-behaved" ZPG TBLs*

The theory presented in the previous section is valid for an ideal turbulent boundary layer; nonetheless, both numerical and experimental data of turbulent boundary layers might actually have significant discrepancies with respect to this ideal flow if proper caution is not used. Similar issues are encountered in internal flows such as pipes or channels, requiring a distance of hundreds δ to be considered fully developed, *i.e.* not reminescent of their initial state. The main problem is that the natural transition from a laminar to a turbulent boundary layer is a process which requires a considerable development length (Tani 1969). As a consequence, the wind tunnel distances or the computational domains size would need to be quite large to reach a sufficiently high–Reynolds

number, with the following associated costs. For this reason, different types of disturbances are used to trigger the transition in the laminar regime, such as a trip in experimental studies or a proper selection of the inflow conditions in numerical studies. An inadequate choice of the flow perturbation can lead to flows that are no longer representative of a "well-behaved" ZPG TBL, with bizarre values of quantities such as the C_f or even changes in the flow organization. A "well-behaved" TBL is defined as a TBL which is not in a post-transitional state nor affected by non-equilibrium effects, *i.e.* independent of the tripping conditions and flow history (Chauhan *et al.* (2009), **Paper 1**). In particular, the "well-behaved" ZPG TBL is a near-equilibrium boundary layer in which the mean velocity defect is self-similar in the outer region at high Reynolds numbers, as discussed, among others, by Marusic *et al.* (2010).

Following the concerns about the possible impact upon the flow development of the different tripping/inflow conditions, some works started to assess the quality of the existing databases. They also established guidelines and criteria in order to get "well-behaved" TBLs. Classical methods rely on the streamwise evolution of the skin-friction coefficient C_f, the shape factor H_{12} and the wake parameter Π. These parameters are used as diagnostic quantities to assess whether a particular TBL can be considered to be canonical since they have a high sensitivity to different boundary and inflow conditions. These quantities provide, in particular, an estimation of the degree of distortion in the outer part of the TBL, and require a long recovery distance to become independent of upstream disturbances (see Schlatter & Örlü 2012). Based on this approach, it is remarkable the work carried out by Chauhan *et al.* (2009), who built up on the previous works by Coles (1968) and Fernholz & Finley (1996). In their study, they analysed and compared in detail a large number of experimental databases with significant discrepancies among them. They developed a composite profile formulation and obtained equations for the wake parameter Π, the shape factor H_{12} and the skin-friction coefficient C_f. By comparing the streamwise evolution of the measured values of C_f, H_{12} and Π with respect to the ones predicted through numerical integration of the composite profile, Chauhan *et al.* (2009) were able to identify "well-behaved" profiles. In particular, the curves which describe the streamwise evolution of C_f are derived exploiting the logarithmic velocity profile from equations 2.21 and 2.22. Assuming that both B and B_0 are independent of the Reynolds number, these equations can be combined and, using the definition of C_f (equation 2.10), expressed as,

$$C_f = 2\left[\frac{1}{\kappa}\ln\left(Re_\delta^*\right) + C''\right]^{-2}. \tag{2.29}$$

This equation is the so-called Coles–Fernholz relation and can be used to estimate the values of the friction velocity (Marusic *et al.* 2013). This equation can be also expressed in terms of Re_θ as,

$$C_f = 2\left[\frac{1}{\kappa}\ln\left(Re_\theta\right) + C'\right]^{-2}. \tag{2.30}$$

Typical values for this expression are $\kappa = 0.384$ and $C' = 4.127$. This choice of constants is due to Nagib *et al.* (2007), who established them based on a comprehensive analysis of experimental databases. For the shape factor a relation can be found using the following equation,

$$H_{12} = \frac{1}{1 - C^*/U_\infty^+}. \tag{2.31}$$

This equation can be rewritten as a function of Re_θ using asymptotic arguments as shown by Monkewitz *et al.* (2007), based on a vast number of experimental profiles covering a wide range of Reynolds numbers: $450 < Re_\theta < 125,000$. The relation proposed by Monkewitz *et al.* (2007) which relates H_{12} to Re_θ is,

$$H_{12} = 1 + \frac{\kappa I_{WW}}{\ln(Re_\theta)} + \frac{\kappa^2 I_{WW}(I_{WW} - C)}{\ln^2(Re_\theta)} + \frac{\kappa^2 I_{WW}\left(\kappa I_{WW}^2 - I_{WW} - 2\kappa I_{WW} C + \kappa C^2\right)}{\ln^3(Re_\theta)}, \quad (2.32)$$

with $\kappa = 0.384$, $I_{WW} = 7.11$ and $C = 3.3$. The baseline streamwise-evolution of the wake parameter Π is obtained following the integration of the composite profile proposed by Chauhan *et al.* (2009).

All the proposed parameters (C_f, H_{12} and Π) to assess the quality of a ZPG TBL rely on the previous knowledge of the boundary layer parameters (δ, δ^* and θ) or u_τ . These quantities can only be obtained by means of measuring a full velocity profile. As a consequence, their accuracy is conditioned by the uncertainty in the calculation of the boundary layer parameters (Titchener *et al.* 2015). For these reasons, an alternative method is proposed in **Paper 1**. The method is based on the diagnostic-plot concept (Alfredsson *et al.* 2011), which only requires mean and velocity fluctuation intensity measurements in the outer region of the boundary layer. In this scaling, the root mean square of the streamwise velocity fluctuation u' is plotted against the mean velocity U, both normalized by the free-stream velocity U_∞. This plot has been shown to scale "well-behaved" ZPG TBL data over a wide range of Re throughout the logarithmic and outer region of ZPG TBLs (Alfredsson *et al.* 2012; Örlü *et al.* 2016). One of the greatest advantages of this scaling is that, according to Alfredsson *et al.* (2011), the data for a "well-behaved" ZPG TBL collapse in the outer region, especially in the range $0.7 < U/U_\infty < 0.9$, following a linear relation,

$$\frac{u'}{U} = \alpha_d - \beta_d \frac{U}{U_\infty}, \quad (2.33)$$

where α_d and β_d are fitting parameters. This means that the profiles that follow equation (2.33) in the outer region give "a good indication whether the boundary layer is in a natural state" (Alfredsson & Örlü 2010). In the work carried out in **Paper 1**, several numerical and experimental datasets were analysed and the following fitting laws for the diagnostic plot parameters were developed,

$$\alpha_d = 0.280 + \frac{20}{Re_\theta}, \quad (2.34)$$

$$\beta_d = 0.245 + \frac{17.5}{Re_\theta}. \quad (2.35)$$

The main advantage of this method is that allows to discern if a ZPG TBL is "well-behaved" only using velocity measurements from the outer region. Additionally, this method can be applied in the experimental design phase to estimate the proper development distance under a particular tripping configuration.

2.2. Adverse-Pressure-Gradient Turbulent Boundary layers

2.2.1. *Preliminaries*

In real-life applications, turbulent boundary layers develop most often under the effect of pressure gradients. This stimulated the investigation of turbulent boundary layers developing over flat plates under the effect of pressure gradients. In the present thesis, the pressure-gradient distributions which are going to be under study are those that have a $\mathrm{d}P/\mathrm{d}x > 0$. These cases are known as adverse-pressure-gradient since a net force due to the pressure gradient is acting in the adverse direction to that of the development of the boundary layer. High adverse pressure gradients in boundary-layer flows might produce flow separation, with the consequent losses in performances of aerodynamic devices. The applicability of the knowledge from ZPG TBLs to decelerating boundary layers is still rather limited (Clauser 1954; Monty *et al.* 2011; Bobke *et al.* 2017), and, consequently, this flow configuration has recently captured much attention in high-fidelity numerical simulations

and experimental works (Bobke *et al.* (2017); Cuvier *et al.* (2017); Kitsios *et al.* (2017); Maciel *et al.* (2018); Yoon *et al.* (2018); **Paper 2, 3, 4**).

Part of the complexity associated with the study of adverse-pressure-gradient (APG) TBL flows is due to the broader parametric space with respect to the ZPG (Monty *et al.* 2011). This is clearly to be ascribed to the history effects, *i.e.* the local state depends not only on the local pressure gradient but also on the pressure distribution. The pressure-gradient parameter β, proposed by Clauser (1954, 1956), is widely accepted as the most relevant non-dimensional number to assess pressure-gradient effects. This quantity is defined as

$$\beta = \frac{\delta^*}{\tau_w}\frac{\mathrm{d}P}{\mathrm{d}x}, \tag{2.36}$$

and represents the ratio of the forces acting (per unit spanwise length) on a fluid element due to the pressure gradient ($\delta^*\mathrm{d}P$) and to the wall-shear stress ($\tau_w\mathrm{d}x$). As mentioned above, the local state of APG TBLs is strongly affected by their streamwise history as shown by Bobke *et al.* (2017), thus the local value of β does not suffice for a full characterization. Recent investigations aim to include such information in an accumulated β (**Paper 2, 3**). In the work developed in **Paper 2**, Vinuesa *et al.* (2017) report that the accumulated value of β, $\bar{\beta}(Re_\theta)$, can be expressed as

$$\bar{\beta}(Re_\theta) = \frac{1}{Re_\theta - Re_{\theta_0}}\int_{Re_{\theta_0}}^{Re_\theta}\beta(Re_\theta)\mathrm{d}Re_\theta. \tag{2.37}$$

This quantity represents the average value of β (estimated over the momentum-thickness Reynolds-number range $Re_\theta - Re_{\theta_0}$) and provides a good measure to account for the upstream history. It is interesting to note that an integral method for these history effects on the TBL was also proposed in the 1960s by Felsch *et al.* (1968).

Despite the above-mentioned difficulties, some general features of APG flows have already been documented in the past decades. In figure 2.2 the inner-scaled streamwise mean and variance profile of two different APG TBL cases are illustrated; and the same statistics for a ZPG TBL as a reference. For the mean velocity profile in figure 2.2a), the effects of the pressure gradient are more evident in the outer layer, where the velocity profiles show higher inner-scaled velocities with increasing β and a more prominent wake, which is connected to a decreased wall-shear stress. The strengthened wake reflects the local state of the boundary layer as a consequence of the impact of the $\beta(x)$ experienced by the flow. In the streamwise variance profiles, an outer peak is developed. The magnitude of this outer peak increases with β and can be higher than the inner peak located at the near-wall region for sufficiently large β. The appearance of more energetic structures in the outer region (figure 2.2b)) is also accompanied by larger values of the inner peak of the streamwise variance profile. These trends are reported in several studies in the literature (Nagano *et al.* (1993); Lee & Sung (2008); Monty *et al.* (2011); Gungor *et al.* (2016); Vinuesa *et al.* (2018); **Paper 3, 4**).

On the other hand, there is some controversy on whether the logarithmic law of the wall (equation 2.21) still holds in APG TBL flows (Alving & Fernholz 1995; Knopp *et al.* 2015). There are studies where it is claimed that the law of the wall is still valid, but that the region occupied by the logarithmic law is progressively reduced when the pressure gradient is increased. Furthermore, some studies report that the logarithmic region shifts with increasing pressure-gradient strength below the one for canonical ZPG TBLs (Nagano *et al.* 1993; Nagib & Chauhan 2008). The streamwise velocity profile, normalized with respect to the friction velocity, is below the ZPG profile in the buffer region for progressively stronger APGs. Consequently, the U^+ slope is found to increase with increasing APG, leading to lower values of the von Kármán constant κ (Bobke *et al.* 2017; Spalart & Watmuff 1993). Some authors, on the other hand, propose a dependence of the constants in terms of the pressure-gradient parameter in inner units $p_x^+ = (\nu/\rho u_\tau^3)(dP/dx)$ (Nickels 2004).

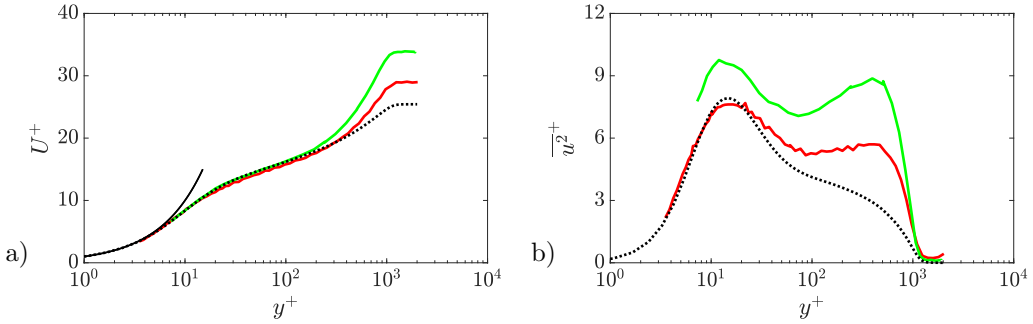

Figure 2.2: Inner-scaled streamwise (a) mean and (b) variance, with approximately matched $Re_\tau \approx 1,200$, where colour (–) (dotted) represents $\beta \approx 0$ (LES Eitel-Amor *et al.* (2014)), (–) $\beta \approx 1.1$, and (–) $\beta \approx 2.2$ (Experimental data from **Paper 4**). Black dashed line indicates the reference Re_τ for every case. Image adapted from **Paper 4**.

2.2.2. *The near-equilibrium state*

In order to isolate pressure-gradient effects on the development of APG TBLs, Clauser (1954) proposed to use constant-β distributions, therefore fixing the ratio of $\delta^* \mathrm{d}P$ and $\tau_w \mathrm{d}x$. According to Rotta (1962) and Mellor & Gibson (1966), this condition is sufficient to reach a near-equilibrium state in which the mean velocity deficit in the outer part is expected to be self-similar at sufficiently high Reynolds numbers (Marusic *et al.* 2010). Several theoretical studies deal with the conditions that are needed to reach the near-equilibrium state. Townsend (1956) and Mellor & Gibson (1966) derived the required streamwise evolution of the free-stream velocity U_∞ for a near-equilibrium state, resulting in a power-law relation,

$$U_\infty = C(x - x_0)^m, \tag{2.38}$$

where x_0 is the power-law virtual origin, and m is a constant which has a value in the range $-1/3 < m < 0$. This condition can be also formulated in a different form as shown in the study by Skote (2001),

$$U_\infty = U_{\infty,0}\left(1 - \frac{x}{x_0}\right)^m, \tag{2.39}$$

where $U_{\infty,0}$ is the power-law virtual origin. A first correlation between the exponent m and the pressure-gradient parameter β was obtained by Tennekes & Lumley (1972) for cases with $\beta \approx const.$ They analysed the integral momentum equation (equation 2.6) assuming that at high Reynolds number the velocity defect law could be linearised, and therefore the following relation can be obtained,

$$m = -\frac{\beta}{1+\beta}. \tag{2.40}$$

This assumption is equivalent to assume $H_{12} = 1$ with $u_\tau/U \to 0$. In order to find a more realistic approximation, Skote *et al.* (1998) made a non-linear analysis with the aim of finding a correlation in the finite Reynolds number regime. Their analysis rely on the fact that the skin friction coefficient (equation 2.29) grows slowly at moderate-to-high Reynolds number. Therefore, the ratio u_τ/U can be considered as approximately constant. Using this assumption, a new relation can be derived as,

$$m = -\frac{\beta}{H_{12}(1+\beta) + 2\beta}. \tag{2.41}$$

Near-equilibrium APG TBLs with constant β are flow cases of paramount importance since these TBLs can be considered as the counterpart of the representative canonical ZPG TBL (Schlatter & Örlü 2012). Indeed, the ZPG TBL can be thought as a special case of the APG TBL, developing under $\beta = 0$. Constant-β APG TBLs allow to characterise Re-effects under a certain pressure-gradient strength. Despite this relevance, the complexity of reaching high-Re constant-β APG TBLs has resulted in only few numerical and experimental studies which deal with this flow condition. On the numerical side, the DNS carried out by Gungor *et al.* (2016), Kitsios *et al.* (2017), Lee & Sung (2008), Lee (2017), the seminal simulation by Skote *et al.* (1998), as well as the well-resolved LES by Bobke *et al.* (2017) are remarkable. These studies are focused on the differences between ZPG and APG TBLs following different approaches. The simulations carried out by Skote *et al.* (1998) and Kitsios *et al.* (2016, 2017) are focused on the analysis of the statistics and on scaling considerations. In these studies, the authors associated the near-equilibrium state with the possibility of finding a self-similar state. While in the work by Skote *et al.* (1998) the low-Reynolds-number range did not allow to obtain self-similarity in the outer region of the Reynolds shear-stress profiles, Kitsios *et al.* (2016, 2017) reported a self-similar region of the mean velocity deficit and Reynolds-stress profiles for Re_θ from 3,500 to 4,800 with $\beta = 1$. These results should be interpreted with some caution, since complete self-similarity can only be achieved for the case of the sink flow (Townsend 1956). On the other hand, the studies by Lee & Sung (2008) and Lee (2017) are focused on the effect of the APG strength on the large-scale features of the flow. These studies identified that the spatial organisation of the u'-structures (u' being the streamwise velocity fluctuations) is affected by the APG strength, as also found in the experimental study by Sanmiguel Vila *et al.* (2017*a*) (**Paper 3**). In both studies, Q4 and Q2 events are observed and connected to high- and low-speed large-scale motions, respectively.

Regarding the well-resolved LES by Bobke *et al.* (2017), this work analysed different near-equilibrium cases for which the pressure-gradient parameter was kept constant for streamwise distances of 37 and 28 boundary-layer thicknesses δ_{99} at values of $\beta = 1$ and 2, respectively. The results, compared to APG TBLs at matched β and Reynolds number values, but with increasing or decreasing $\beta(x)$ curves, highlight the impact of the upstream history on the local turbulence statistics. Moreover, Bobke *et al.* (2017) reported that a streamwise distance of approximately $7\delta_{99}$ with constant β is needed to obtain a "well-behaved" APG TBL with constant-β conditions. This is particularly critical when performing an analysis which compares cases with the same Reynolds number and β, since – as also shown in Sanmiguel Vila *et al.* (2017*a*) (**Paper 3**) and Vinuesa *et al.* (2017) (**Paper 2**)– the cases with a non-constant β distribution need to be analyzed in terms of the accumulated pressure-gradient magnitude (equation 2.37).

Experimental studies of APG TBL flows, on the other side, are rather complex, since the desired pressure-gradient distribution must be imposed by e.g. applying suction or geometrical modifications of the test section. A typical choice for the study of APG TBLs developing on flat plates is to properly shape the wall opposite to the flat plate. The pressure-gradient distribution depends on the TBL development on the plate and roof, thus requiring a trial-and-error process to achieve the desired streamwise (pressure-gradient) history. Additionally, the $\beta(x)$ history depends on the local value of the wall-shear stress and of the displacement thickness, thus requiring extensive measurements for its characterization. This might partly explain the lack of information relative to the $\beta(x)$ distribution in numerous previous studies in the literature, which makes difficult a direct comparison between different databases. A summary of the experimental studies available in the literature is found in Table 2.1. From an experimental point of view, the near-equilibrium state is a challenging condition to be achieved, and there are only very few studies which obtain a relatively-long constant-β region. Some of the most relevant experimental works in these conditions are those by Stratford (1959), in which a TBL with nearly zero skin friction was generated and studied, and by Skåre & Krogstad (1994), where the authors obtained a TBL with a freestream-velocity evolution given by a power-law, with exponent $m = -0.23$, leading to a constant $\beta \approx 20$. In their near-equilibrium region, Skåre & Krogstad (1994) showed self-similarity

Author(s) (year)	Measurement technique	β-history available	Constant-β region	Range of Re_θ	Range of β	Presented quantities
Clauser (1954)	HWA	–	✓	–	1.8–6.13	U
Stratford (1959)	Pitot	–	✓	–	∞	U
Perry (1966)	Pitot	–	–	15900–97200	2.35–71.2	U
Samuel & Joubert (1974)	HWA	–	–	5000–30000	0.07–8	U, $\overline{u^2}$, $\overline{v^2}$, $\overline{w^2}$, $\overline{uv}$
East & Sawyer (1980)	HWA	–	–	18900–34700	0.47–7.27	U, $\overline{u^2}$, $\overline{v^2}$, $\overline{w^2}$, $\overline{uv}$
Cutler & Johnston (1989)	HWA	–	–	12000–25000	2–12	U, V, $\overline{u^2}$, $\overline{v^2}$, $\overline{w^2}$, $\overline{uv}$
Dengel & Fernholz (1990)	HWA	–	–	1260–11200	0–∞	U, $\overline{u^2}$, $\overline{uv}$
Nagano *et al.* (1993)	HWA	–	–	1290–3350	0.76–4.66	U, $\overline{u^2}$, $\overline{v^2}$, $\overline{w^2}$, $\overline{uv}$
Spalart & Watmuff (1993)	HWA	–	–	<1600	0–2	U, $\overline{u^2}$, $\overline{v^2}$, $\overline{w^2}$
Skåre & Krogstad (1994)	HWA	✓	✓	25400–53970	12.2–21.4	U, $\overline{u^2}$, $\overline{v^2}$, $\overline{w^2}$, $\overline{uv}$
Alving & Fernholz (1995)	HWA	✓	–	2849–13305	0.2–324	U
Marušić & Perry (1995)	HWA	✓	–	2206–19133	0.65–7.16	U, $\overline{u^2}$, $\overline{v^2}$, $\overline{w^2}$, $\overline{uv}$
Nagano *et al.* (1998)	HWA	–	–	1070–3350	0.77–5.32	U, $\overline{u^2}$, $\overline{v^2}$, $\overline{w^2}$
Maciel *et al.* (2006)	PIV	–	–	3360–14300	320–∞	U, $\overline{u^2}$, $\overline{v^2}$, $\overline{uv}$
Nagib *et al.* (2004)	HWA	–	–	10000–70000	0—0.3	U
Monty *et al.* (2011)	HWA	–	–	6050–18500	0.822–4.75	U, $\overline{u^2}$
Harun *et al.* (2013)	HWA	–	–	12030	1.74	U, $\overline{u^2}$, $\overline{v^2}$, $\overline{uv}$
Vinuesa *et al.* (2014)	Pitot	–	–	13000–37000	0.2-0.33	U
Sanmiguel Vila *et al.* (2017*a*) (**Paper 3**)	PIV	✓	–	9070–22240	1.3–2.4	U, $\overline{u^2}$, $\overline{v^2}$, $\overline{uv}$
Sanmiguel Vila *et al.* (2019) (**Paper 4**)	HWA	✓	✓	450–23450	0–2.4	U, $\overline{u^2}$

Table 2.1: Previous experimental studies on adverse pressure gradient turbulent boundary layers developing on flat plates. Streamwise mean velocity component is defined as U, wall-normal mean velocity component is defined as V, variance is defined as $\overline{u^2}$, $\overline{v^2}$, $\overline{w^2}$ for the streamwise, wall-normal and spanwise direction, respectively. Reynolds shear stress is indicated as $\overline{uv}$.

for the velocity defect profiles in the outer region (in agreement with classical theory) and reported an increase of the turbulence production in the outer layer.

Classical questions regarding the proper scaling of APG TBLs have recently attracted more attentions thanks to the availability of new high-quality databases. In contrast with the canonical flows presented in §2.1, no agreement exists on the scales and non-dimensional parameters that should be used. In recent studies (Kitsios *et al.* 2017; Wei & Maciel 2018; Maciel *et al.* 2018) different arguments are proposed in order to assess the most appropriate scaling. The outer scaling proposed by Kitsios *et al.* (2017) is based on the freestream velocity U_∞ and the displacement thickness δ^*. Based on these parameters the mean velocity and Reynolds-stresses profiles are expected to collapse under conditions of self-similarity. This scaling was tested by Bobke *et al.* (2017) on the downstream evolution of the mean velocity and Reynolds-stresses profiles. Their results showed no self-similarity nor collapse of the profiles in the constant-β region. In the study by Maciel *et al.* (2018) there is no unique pair of scaling variables, but different scaling variables are proposed according to the pressure-gradient intensity. In that study, it is argued that a good scaling does not need to reveal scale invariance of the mean velocity-defect and Reynolds stresses but should reflect the order of magnitude of the different scaled variables.

2.2.3. *Criteria to Identify "Well-behaved" APG TBLs*

In the §2.1.1 we discussed the importance of developing criteria to ensure that the flow cases under investigation can be considered to be well-behaved, i.e., independent of the inflow conditions and exempt of any numerical or experimental artefacts. The advantage of the ZPG configuration is the fact that the "well-behaved" cases are not affected by (streamwise pressure-gradient) history effects. Therefore, deviations from the proposed empirical correlations can be attributed with little doubt to local non-equilibrium effects or problems with the development of the boundary layer (e.g. due to strong over- or under-tripping). On the other hand, the development of TBLs under PG depends on the PG history, which adds some difficulty when establishing criteria of convergence towards "well-behaved" conditions. There exist as many "well-behaved" evolutions of H_{12}, Π or C_f as possible pressure-gradient histories, in principle. For this reason, classical empirical correlations for boundary layer parameters are typically adapted for the particular case of APG TBLs with constant-β distributions. In order to adapt the C_f and H_{12}, it is assumed that the law of the wall (equation 2.21) is still valid. Therefore, the functional form of the equations that describe the C_f and H_{12} streamwise evolution is the same as the ZPG case. Following these assumptions and the work carried out for ZPG TBL flows by Chauhan *et al.* (2009), **Paper 2** presents the following relations for C_f and H_{12},

$$C_f = 2\left[\frac{1}{\kappa}\ln(Re_\theta) + C + \frac{D_0\ln(Re_\theta)}{Re_\theta} + \frac{D_1}{Re_\theta}\right]^{-2}, \tag{2.42}$$

$$H_{12} = \frac{1}{1-(C^*/U_\infty^+)} + \frac{E_1}{Re_\theta}. \tag{2.43}$$

In these equations, $C^* = \int_0^\infty W^+ \mathrm{d}(y/\Delta)$ with $W+ = U_\infty^+ - U^+$ and $\Delta = U_e^+\delta^*$ which is known as the Rotta-Clauser length scale. The rest of parameters are defined as coefficients that are obtained by means of fitting with the aid of several database. In table 2.2 the values obtained for Vinuesa *et al.* (2017) (**Paper 2**) for different cases are reported.

In addition to these relations, the theoretical work by Mellor & Gibson (1966) also led to expressions for the skin-friction coefficient and the shape factor in PG TBLs subjected to constant values of β. In particular, they proposed a skin-friction relation of the same type as equation 2.29. However, the most relevant difference with respect to the presented in **Paper 2** is the fact that they proposed a constant value of $\kappa = 0.41$ regardless of the pressure-gradient magnitude, and a value of C related to the particular β. Thus, in their analysis they considered the slope of the

Case	κ	C	D_0	D_1	C^*	E_1
ZPG	0.384	4.127	220	-1,945	7.135	-19.12
APG with constant $\beta = 1$	0.361	5.300	250	-2,100	9.932	-2.415
APG with constant $\beta = 2$	0.349	6.886	260	-2,500	12.53	-88.41

Table 2.2: Summary of coefficients used in the C_f and H_{12} correlations equation 2.42 and2.43.

logarithmic region to be independent of the pressure gradient, with different intercepts according to the PG magnitude.

For general PG TBLs flows, Vinuesa *et al.* (2016) showed that the diagnostic-plot scaling proposed in §2.1.1 can be also used to collapse boundary layers subjected to pressure-gradient conditions if properly modified using the shape factor. They reported a scaling of wide range of APG TBLs that showed a linear behaviour in the range $0.8 \leq U/U_\infty \leq 0.9$. This observation was exploited in **Paper 2** to define a criterion of convergence to well-behaved conditions, by inspecting the region of the boundary layer between $U/U_\infty = 0.8$ and 0.9 and fitting it to the relation:

$$\frac{u'}{U\sqrt{H_{12}}} = \alpha_H - \beta_H \frac{U}{U_\infty}, \tag{2.44}$$

where α_H and β_H are different fitting parameters valid for PG TBLs. The idea is to measure profiles of the streamwise mean velocity and streamwise velocity fluctuations, use the diagnostic-plot scaling modified with the shape factor, and assess whether they follow the linear behaviour given by equation 2.44. Note that this criterion is valid for any APG TBL regardless of the flow history. The values of α_H and β_H were obtaining in **Paper 2** by means of fitting data from different databases. In their study, the following empirical correlations which describe the evolution with Re_θ of the coefficients α_H and β_H are reported:

$$\alpha_H = 0.259 + \frac{20}{Re_\theta}, \tag{2.45}$$

$$\beta_H = 0.223 + \frac{17.5}{Re_\theta}. \tag{2.46}$$

The advantage of using this criterion over the ones based on skin-friction curves is the fact that it only relies on velocity profile measurements, without the need of direct measurements of τ_w. Note, however, that these profile measurements require an accurate determination of the wall position, due to the fact that the shape factor H_{12} is necessary to obtain the diagnostic-plot scaling.

2.2.4. *Large/small scale interaction*

The inclusion of the pressure gradient in a TBL flow also affects the scale organization of the boundary layer and the interaction between the different scales. As reported in previous studies (Bobke *et al.* 2017; Harun *et al.* 2013; Lee 2017), the spectral analysis of an APG TBL reveals the appearance of energetic structures in the outer region connected with the pressure-gradient strength. These large-scale structures are different from those reported in high-Re ZPG TBL, since they appear at a different y^+ location and typically exhibit larger wavelengths. Figure 2.3 shows the premultiplied energy spectra ($\kappa_x^+ \Phi_{uu}^+$) plotted against the inner-scaled wall-normal distance y^+ and the streamwise wavelength λ_x^+ from the database of **Paper 4**. The effect of β in the scale organization can be appreciated with the emergence of a peak at a wavelength $\lambda_x \approx 3\delta_{99}$ (Harun *et al.* 2013) that shows an increase in strength with increasing β values. As mentioned above, this peak should not be confused with the outer peak due to the high-Re effect reported

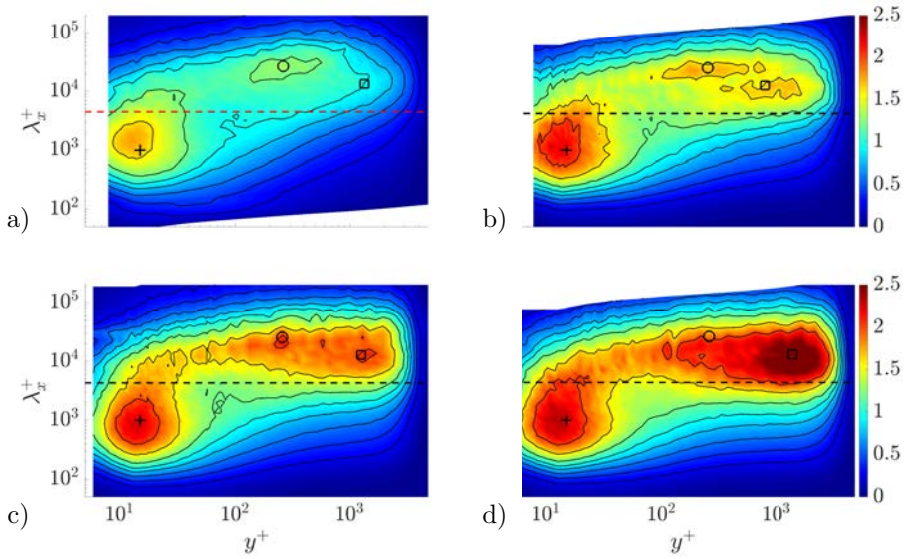

Figure 2.3: Inner-scaled premultiplied energy spectra of the streamwise velocity at $Re_\tau \approx 4,400$ with contour levels at $\kappa_x^+\Phi_{uu}^+ = 0.25, 0.4, 0.575, 0.775, 0.95, 1.2, 1.6, 2.0$, for pressure-gradient strengths a) $\beta \approx 0$ (experimental data from Örlü (2009)), b) $\beta \approx 0.75$, c) $\beta \approx 1.1$, d) $\beta \approx 2.2$. Auxiliary black symbols are located at the following coordinates: (+) $(y^+ = 15, \lambda_x^+ = 1,000)$, (○) $(y^+ = 3.9Re_\tau^{0.5}, \lambda_x/\delta_{99} = 6)$ for all the cases. Additionally black (□) symbols are located at $(y^+ = y^+_{\mathrm{max,outer}}, \lambda_x/\delta_{99} = 3)$ for all the APG cases and $(y/\delta_{99} = 0.3, \lambda_x/\delta_{99} = 3)$ for the ZPG case. An auxiliary horizontal dashed line is placed at $\lambda/\delta_{99} = 1$. Image adapted from **Paper 4**.

for ZPG TBLs (Mathis *et al.* 2009) and also present in the APG TBLs at the same wavelength $\lambda_x \approx 6\delta_{99}$ as observed also for ZPG cases.

These changes in the scale organization have a clear effect on the Reynolds stresses, and are therefore of great interest in the search for understanding of these flows. In order to analyse them, different scale-decomposition approaches that have been applied to ZPG TBLs (Mathis *et al.* 2009; Ganapathisubramani *et al.* 2012; Dogan *et al.* 2018) can also be used in APG TBLs. The scale-interaction techniques are typically based on decomposing the streamwise velocity in large- (u_L) and small-scale fluctuation (u_S) components. The u_L component is computed by applying a low-pass filter to the velocity signal, and the u_S component is obtained by subtracting this large-scale signal component from the raw streamwise velocity fluctuation. In order to choose an appropriate temporal or spatial filter width, the premultiplied energy spectrum map (figure 2.3) is previously analysed to identify a proper cut-off value which effectively separates the inner and outer spectral peaks. This approach requires flow cases at high-enough Reynolds numbers to define a cut-off value allowing sufficient scale separation. For this reason, there are only a few studies which are focused on this aspect in APG TBLs due to the lack of high-Re databases (Monty *et al.* 2011; Harun *et al.* 2013; Lee 2017). In the study carried out by Harun *et al.* (2013), the scale decomposition with a cut-off equivalent to δ was employed to analyse the effect of the scale organization on the outer peak of the streamwise velocity variance. Their results showed that this peak is not only connected with the increasing large-scale activity but also with a small-scale component that becomes more energetic as β increases.

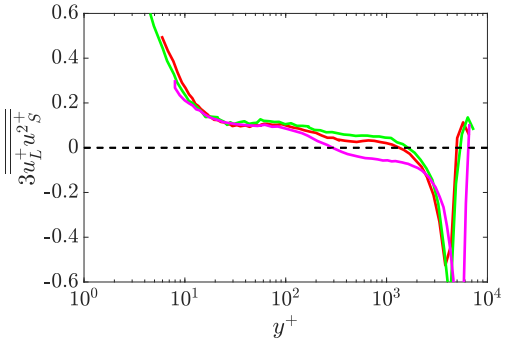

Figure 2.4: Dominant scale-decomposed skewness term, $\overline{\overline{3u_L^+u^{2+}_S}}$ for $Re_\tau \approx 4,400$. Colour (–) represents $\beta \approx 0$, (–) $\beta \approx 1.1$, and (–) $\beta \approx 2.2$. Image adapted from **Paper 4**.

Based on previous works on ZPG TBLs (Mathis *et al.* 2009, 2011), Harun *et al.* (2013) also studied the amplitude modulation with the aim of analysing the large/small scale interaction. The amplitude modulation deals with the influence of the large scales in the outer region on the amplitude of the small-scale fluctuations in the inner region. This effect can be analysed following different strategies that involve u_L and u_S, as reported in the review article by Dogan *et al.* (2018). Following the early investigations of Bandyopadhyay & Hussain (1984), Mathis *et al.* (2009) proposed to analyse the amplitude modulation by computing the envelope of the small-scale component of the signal using the Hilbert transform, and then calculate a correlation coefficient, R, that relates u_L with u_S, as follows,

$$R = \frac{\overline{u_L^+ E_L(u_S^+)}}{\sqrt{\overline{u_L^{+2}}}\sqrt{\overline{E_L(u_S^+)^2}}}, \tag{2.47}$$

where $E_L(u_S^+)$ is the filtered envelope of the small-scale fluctuations. Using this quantity, Harun *et al.* (2013) showed that the small scales in the inner region are strongly amplitude-modulated by the large-scale motions, being this effect higher in the APG cases that in the ZPG cases. These results were later confirmed by Lee (2017) using two-dimensional amplitude-modulation maps.

In **Paper 4**, the amplitude-modulation effects are further investigated using different APG TBL cases and the approaches of Schlatter & Örlü (2010); Mathis *et al.* (2011) and Ganapathisubramani *et al.* (2012). The velocity fluctuation components have obtained using a cut-off equal to $\lambda_x = \delta_{99}$; this choice is motivated by the results shown in figure 2.3. First, the amplitude modulation is quantified in figure 2.4, using the correlation $\overline{\overline{3u_L^+u_S^{2+}}}$ (where $\overline{\overline{X}} = \overline{X}/(\overline{u^{+2}})^{3/2}$ for any variable X). This value is adopted instead of R since, as pointed out in Schlatter & Örlü (2010) and Mathis *et al.* (2011), this quantity is better suited for analysing the amplitude modulation. The results show a highly modulated near-wall region for all the cases, whereas in the log-region an increased modulation is observed for an increasing β. This result is connected with the enhancement of the large-scale organisation in the APG TBLs. In addition to this, the approach presented in Ganapathisubramani *et al.* (2012) is also used to study the amplitude modulation. In this study, the small-scale fluctuation component, u_S^2, obtained using a conditional average for several values of the large-scale fluctuation is analysed. Ganapathisubramani *et al.* (2012) analysed the dependence of the amplitude modulation on the strength of the large-scale fluctuations. They also investigated the effect of u_L on the amplitude of the small-scales fluctuations. In **Paper 4**, this methodology is applied to APG TBLs to explore the changes in the scale organization. Based on the results obtained, a new methodology which connects the emergence of the outer peak in both

premultiplied energy spectra and streamwise variance with the interaction between large and small scales is presented. The reader is referred to the section §5 of **Paper 4** for the full discussion.

Chapter 3

Experimental facilities and techniques

This chapter provides a short overview of the wind-tunnel facility and of the measurement techniques used in this thesis. Detailed descriptions of the measurement configurations and experimental arrangements are presented in the corresponding papers in the part II of this thesis.

3.1. MTL wind tunnel

The experiments reported in the present thesis were performed in the Minimum Turbulence Level (MTL) closed-loop wind tunnel located at KTH Royal Institute of Technology in Stockholm depicted in figure 3.1. The test section is 7 m long with a cross-sectional area of 0.8×1.2 m^2 (height$\times$width). The wind tunnel ceiling, which comprises a total of six panels allowing vertical displacement, can be adjusted in order to control the streamwise pressure-gradient distribution. The MTL is capable of reaching a maximum speed of 70 m/s with a streamwise velocity fluctuation intensity of approximately 0.025% of the free-stream velocity at a nominal speed of 25 m/s.

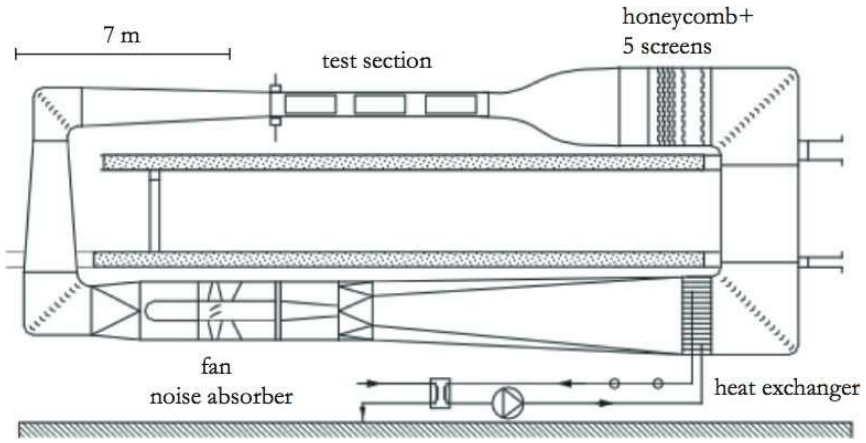

Figure 3.1: Schematic of the Minimum Turbulence Level (MTL) wind tunnel at KTH Mechanics. Image taken from Örlü (2009).

The air temperature can be controlled with an accuracy of ± 0.05 K by means of a heat exchanger. The honeycomb and the screens upstream of the contraction section (which has a ratio of 9:1) along with the specially designed guide vanes in the corners and the noise absorbing material in the inner walls provide an outstanding quality of the air flow enabling the remarkably low level of background turbulence which characterizes this wind tunnel. More details regarding the MTL can be found in the reports by Österlund (1999) and Lindgren & Johansson (2002).

The flat plate used in this thesis is the same that was used in the work by Österlund (1999). The flat plate has a total length of 6 m and a thickness of 26 mm, spanning the entire width of the wind tunnel. The leading edge follow the shape of a modified superellipse. The position of

the stagnation point can be modified by means of a 1.5-m-long trailing-edge flap. The flat plate comprises five 1-m-long pieces of smooth aluminium and one 1-m-long piece of transparent acrylic glass (polymethyl metacrilate) that enables laser illumination for the PIV measurements. For a more detailed description, the reader is referred to Österlund (1999).

The streamwise pressure-gradient distribution for **Paper 1** was obtained by adjusting the wind tunnel ceiling; for **Paper 3** and **4** it was established by means of wall inserts made of foam and hung by threaded rods. A detailed description is available in section §2 of **Paper 1, 3** and **4**, respectively. Figure 3.2 from the experimental campaign shows one roof geometry inside the test section of the MTL.

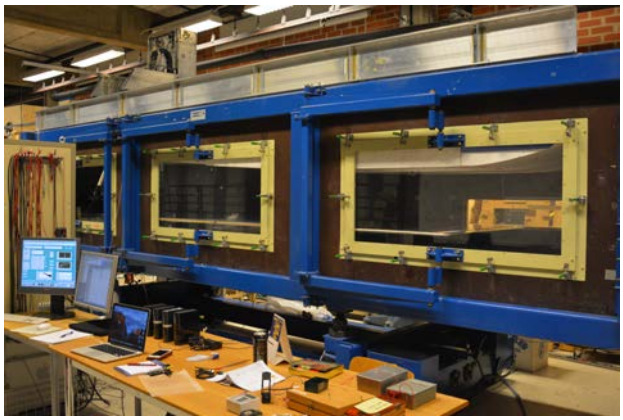

Figure 3.2: Picture from the experimental campaign carried out in the MTL wind tunnel. Panoramic view from the flat plate with a roof geometry.

3.2. Measurement techniques

3.2.1. *Hot-wire anemometry*

A general overview of the hot-wire anemometry settings used in the present thesis is reported herein; for a deeper explanation about the operation and limitations of hot-wire anemometry, the reader is referred to the Bruun (1995), Tropea & Yarin (2007) and Örlü & Vinuesa (2017).

Streamwise velocity measurements were performed by means of home-made single hot-wire probes which resemble a standard *Dantec* boundary-layer probe, *i.e.*, a 55P15. The hot-wire probes were built in-house using a stubless Platinum wire with two lengths of 525 and 275 μm and nominal diameters of 2.5 and 1.25 μm, respectively. The wires were soldered to conical prongs with a diameter of around 30 μm. A picture of one of the hot-wire probes used in the present thesis is shown in Figure 3.3.

Voltage signals from the hot-wire probes were recorded using a *Dantec StreamLine* 90N10 frame in conjunction with a 90C10 constant-temperature anemometer module. An offset and a gain were applied to the top of the bridge voltage in order to match the voltage range of the 16-bit A/D converter used. Additionally, a low-pass filter with cut-off frequency was used prior to the data acquisition in order to avoid aliasing. Calibration of the hot-wire anemometer was performed in situ using as reference a Pitot–static tube located parallel to the incoming freestream. The Pitot-static tube was connected to a micromanometer of type *FC0510 (Furness Control Limited)*, which was also employed to record the ambient temperature and pressure during the calibration and the experiments. The data acquired in the calibration were fitted to a fourth-order polynomial curve, which is a rather common procedure in the wall-turbulence community (Morrison *et al.* 2004; Hultmark *et al.* 2010). Calibration curves were taken at the beginning and end of each set

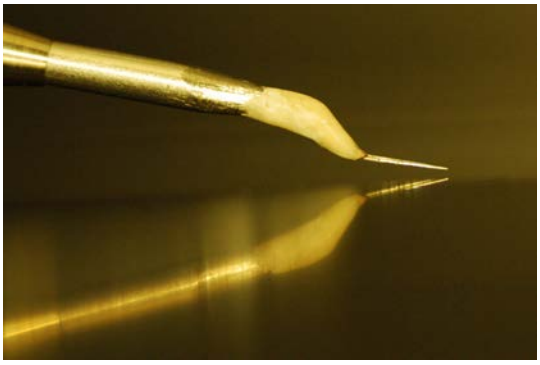

Figure 3.3: Homemade hot-wire probe inside the MTL wind tunnel.

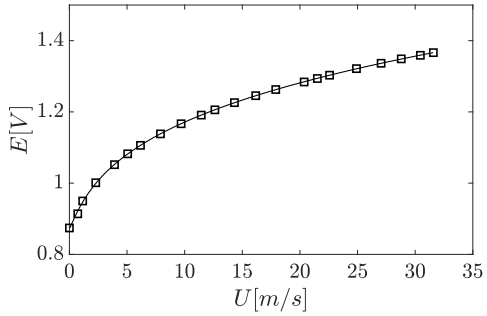

Figure 3.4: Representative calibration curve of hot-wire probe. Square symbols represent calibration points taken before/after a set of measurements. Solid line represents a fourth-order polynomial fitted through the calibration points including the voltage at zero velocity.

of measurements; Figure 3.4 shows an example of calibration fitting. The estimated uncertainty in the velocity measurements is 1%.

3.2.2. *Oil-film interferometry*

Oil-film interferometry (OFI) was used to measure the wall-shear stress at some locations, where optical access was possible. Silicon oil with a nominal viscosity, $\mu_{oil_{nom}}$, of 20, 100 and 200 cSt at 25°C was used. The oil viscosities were calibrated by means of a Ubbelohde capillary-suspended level viscometer immersed in a temperature-controlled heated bath. The resulting points of the calibration were fitted to the relation $\mu_{oil}(T) = A_{cal}e^{B_{cal}(T_{nom}-T)}$, where A_{cal} and B_{cal}, are the calibration constants and T_{nom}, the nominal temperature which corresponds to the nominal viscosity $\mu_{oil}(T_{nom}) = \mu_{oil_{nom}}$. The results of the oil calibration are shown in Figure 3.5. Black Mylar films were attached to the flat plate in order to improve the image contrast. The oil film was illuminated using a low-pressure sodium lamp which had a power of 55 W and a nominal wavelength of 589 nm. The light source was placed on the wind-tunnel roof, aligned with the flow direction. A handheld digital thermocouple *Fluke* was attached to the flat plate close to the recording station to control the oil temperature. The equipment used to obtain the pictures consisted of a digital single-lens reflex camera *Nikon D7100*, and telephoto zoom lens *Nikon Nikkor 200 mm f4*. The camera was placed on the roof of the wind tunnel with an angle of 15° normal to the plate and was controlled remotely via a USB cable. The pictures were acquired at a rate of

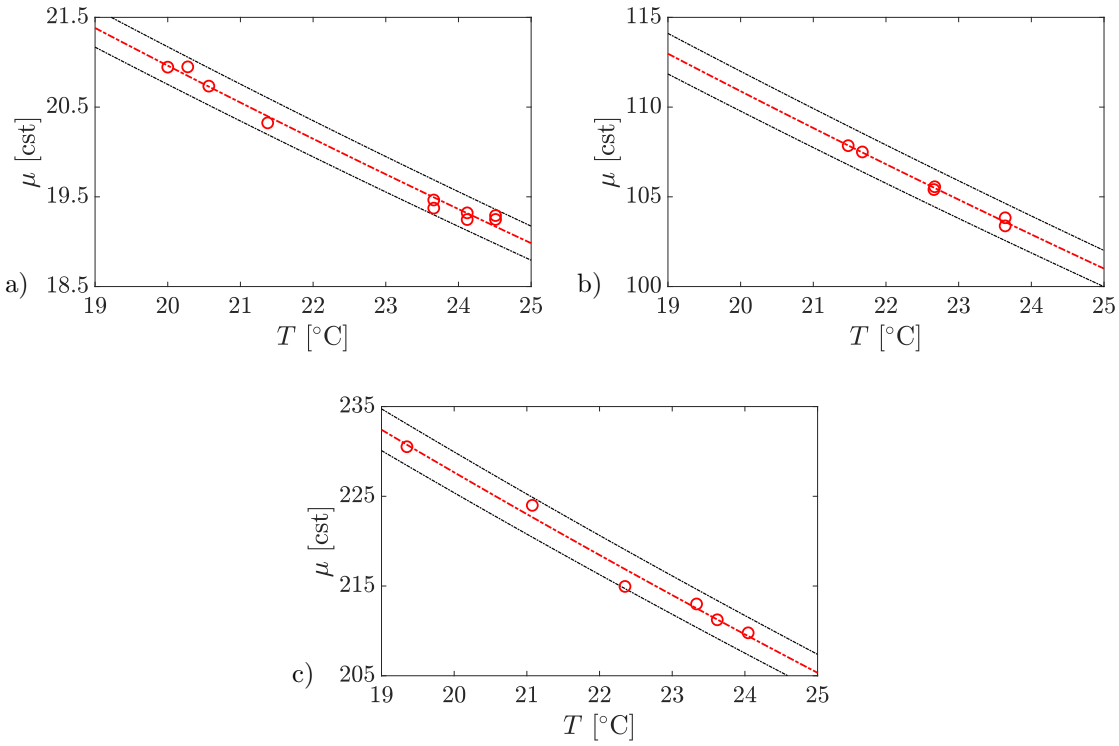

Figure 3.5: Calibration of the oil kinematic viscosity with temperature. Red circles (○) represent the calibration points for a silicon oil with a nominal viscosity at 25°C of a) 20, b) 100 and c) 200 cSt. Red solid line (−) represent the oil calibration. Red dashed lines show ±1% deviation.

0.2 Hz. Before each test, millimetre graph paper was placed on the measurement station and was photographed to calculate the reference length. Figure 3.6 shows a representative image sequence of an oil-film interferometry case. For further details on the post-processing of the data, the reader is referred to Vinuesa & Örlü (2017).

3.2.3. *Flow field measurements*

Particle Image Velocimetry (Raffel *et al.* 2018) was used to perform velocity field measurements in a streamwise/wall-normal planes. The seeding employed for the measurements of this work was Di-Ethyl-Hexyl-Sebacate (DEHS) droplets with 1 μm diameter produced with a smoke generator. Seeding particles were injected into the flow at the end of the test section to minimize flow perturbation and were then recirculated through the wind tunnel. The seeded flow was illuminated by a Quanta Ray double cavity Nd:YAG laser with a pulse energy of 400 mJ at 15 Hz. The acquisition of the PIV images was performed with an ANDOR Zyla sCMOS 5.5MP camera (2560 $\times$ 2160 pixel array, 6.5 μm $\times$ 6.5 μm pixel size). The camera was equipped with a Tokina 100 mm lens. Image quality was improved by removing laser reflections and illumination background using the POD-based approach proposed by Mendez *et al.* (2017). Figure 3.7 shows a picture from the experimental campaign carried out in the MTL wind tunnel.

A custom–made PIV software developed at University of Naples Federico II was used to perform digital cross-correlation analysis of the particle images (Willert & Gharib 1991) to calculate the velocity fields. The interrogation strategy is an iterative multi-grid/multi-pass (Soria

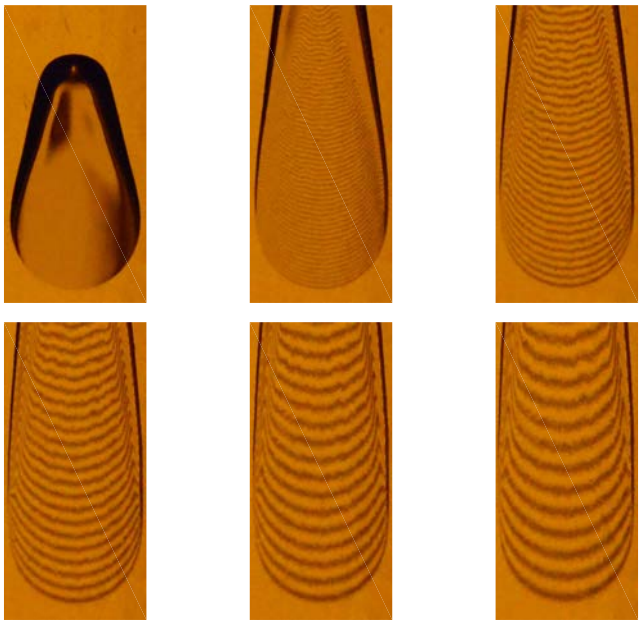

Figure 3.6: Representative oil-film interferometry image sequence for a case with silicon oil with a nominal viscosity of 200 cSt. Flow direction is bottom to top. Time interval between frames is $\Delta t = 3$ s.

1996) image deformation algorithm (Scarano 2001), with final interrogation windows of 40 $\times$ 40 pixels with 75% overlap. B-spline interpolation schemes were used to improve the accuracy of the PIV processing (Astarita & Cardone 2005; Astarita 2007). The vector validation to identify invalid vectors was carried out with a universal median test (Westerweel & Scarano 2005) on a 3 $\times$ 3 vectors kernel and an error threshold equal to 2. Discarded vectors were replaced with a distance-weighted average of neighbouring valid vectors.

Figure 3.7: Picture from the PIV campaign carried out in the MTL wind tunnel.

3.2.4. *High Resolution Turbulence Statistics*

The turbulence statistics evaluated with PIV can be affected by limited spatial resolution issues due to the finite size of the interrogation window. To overcome this issue, different ensemble-based approaches were performed to improve the spatial resolution and accuracy of turbulence statistics. In particular, the following two methods have been used:

- The first method is based on the ensemble-correlation principle (also commonly referred to as *single-pixel* approach (Westerweel *et al.* 2004)). The correlation maps obtained via ensemble-averaging contain information on the probability density function (pdf) of the velocity fluctuations, from which second-order statistics can be extracted (Scharnowski *et al.* 2012). The approach used in this study is to calculate single-pixel correlation maps by correlating individual pixels on the first exposure with a certain interrogation region on the second exposure. A symmetric double-correlation method (Avallone *et al.* 2015) was used to improve convergence. Additionally, the correlation maps were spatially averaged over a certain region (in the streamwise and wall-normal directions).
- The second method is referred to as Ensemble Particle Tracking Velocimetry (Agüera *et al.* 2016; Cowen & Monismith 1997; Kähler *et al.* 2012*a*) and is based on tracking individual particles directly on the images, and then superposing on a common grid the identified vectors of the ensemble. The spatial distribution of vectors is binned to extract statistics. The size of the bin depends on the particle image density and on the number of available samples. In this work a super-resolution technique is used (Keane *et al.* 1995), *i.e.* with predictor for particle matching obtained from planar PIV. The distribution of vectors in each bin is then used to extract the pdf of the velocity fluctuations. Then the computation of turbulence statistics is carried out using two different approaches:
  - A top-hat approach, in which all the locations of the bin have the same weight.
  - A polynomial fit approach, which has demonstrated to reduce systematic errors in the estimation of second-order moments due to unresolved mean velocity gradients (Agüera *et al.* 2016). In order to reduce this issue, within each bin the cloud of vectors is fitted with a second-order polynomial function in x, y. Then the local mean is estimated as the value of the polynomial fit function in the central point of the bin region, while the fluctuations around the mean are evaluated with respect to the local value of the polynomial fit instead of a single mean value assigned to the window.

Chapter 4

Main contribution and Conclusions

In this chapter, the main contributions and conclusions of the papers presented in this thesis are compiled. For the detailed description of the results, the reader is referred to the appended papers which constitute the Part II of the present thesis.

4.1. Paper highlights

Paper 1

Carlos Sanmiguel Vila, Ricardo Vinuesa, Stefano Discetti, Andrea Ianiro, Philipp Schlatter, Ramis Örlü, 2017. *On the identification of well-behaved turbulent boundary layers*, Journal of Fluid Mechanics, **822**, 109–138.

- A novel method to assess "well-behaved" ZPG TBLs is proposed and validated. A new set of experimental data from low-Re zero-pressure-gradient turbulent boundary layers which covers a total of six tripping configurations is provided. The different configurations include a combination of weak, late, optimal and strong tripping conditions.
- Weak tripping cases lead to deviations in the logarithmic region of the inner-scaled streamwise mean velocity profile with respect to the optimum tripping configurations, whereas the overtripping case shows a more prominent wake. The weak tripping cases also lead to small deviations in the streamwise variance when compared with the optimum tripping at approximately $y^+ \approx 100$, where the u' values are lower. The strong tripping case exhibits an enhanced inner peak as well as the development of an outer peak in the variance profile.
- A new methodology based on the diagnostic-plot concept (Alfredsson *et al.* 2011) to evaluate the development of ZPG TBLs towards canonical conditions has been proposed. In contrast with the classical methods, the advantage of this approach is that it only relies on measurements of the streamwise mean velocity and velocity fluctuation intensity at arbitrary wall-normal distances, therefore uncertainties from u_τ or y, among others, are eliminated with its use.
- The results from the analysis of the development of the present ZPG TBL dataset show that well-behaved ZPG TBLs are obtained for $Re_\theta > 2000$, which is in good agreement with the results presented in Schlatter & Örlü (2012).
- The proposed method has also been shown to be able to determine the streamwise location from which on the ZPG TBL is well-behaved using only measurements of the streamwise mean velocity and streamwise Reynolds stress in the outer region of the boundary layer.

Paper 2

Ricardo Vinuesa, Ramis Örlü, Carlos Sanmiguel Vila, Stefano Discetti, Andrea Ianiro, Philipp Schlatter, 2017. *Revisiting history effects in adverse-pressure-gradient turbulent boundary layers*, Flow, Turbulence and Combustion, **99 (3–4)**, 565–587.

- For the first time, an assessment of whether a particular adverse-pressure-gradient turbulent boundary layer can be considered as "well-behaved" is carried out. Different methods for APG TBLs with constant and non-constant-β distributions are proposed.
- For constant-β cases with $\beta = 1$ and 2, relations for the streamwise evolution of the skin-friction coefficient, C_f, and the shape factor, H_{12}, based on those proposed for ZPG TBLs by Chauhan *et al.* (2009), are developed and assessed.
- A relation for the streamwise evolution of the C_f curve of an APG TBL with a particular $\beta(Re_\theta)$ distribution is proposed. The correlation is based on a correction of the ZPG TBL trend by means of an "accumulated" value of β.
- The criterion introduced in **Paper 1** for identifying "well-behaved" ZPG TBLs is extended for APG TBLs with a general $\beta(Re_\theta)$. This new criterion is based on the modified version of the diagnostic-plot scale for APG TBLs flows proposed by Vinuesa *et al.* (2016). In contrast with ZPG TBLs, the APG TBL method requires full profile measurements at several streamwise locations, since the shape factor correction is needed. This requires an accurate determination of the wall position and of the boundary-layer thickness to compute H_{12}.

Paper 3

Carlos Sanmiguel Vila, Ramis Örlü, Ricardo Vinuesa, Philipp Schlatter, Andrea Ianiro, Stefano Discetti, 2017. *Adverse-pressure-gradient effects on turbulent boundary layers: statistics and flow-field organization*, Flow, Turbulence and Combustion, **99 (3–4)**, 589–612

- A new experimental dataset of flow field measurements of adverse-pressure-gradient TBLs with different $\beta(Re_\theta)$ has been acquired and analysed with a complementary LES dataset.
- Different PIV approaches for the measurement of turbulence statistics have been assessed against hot-wire measurements. Ensemble PTV with polynomial fits, as proposed in Agüera *et al.* (2016), is shown to have superior performances, with an excellent agreement also in second-order turbulence statistics from the wake region down to $y^+ \simeq 10$ for TBLs at $Re_\tau \approx 4,100$ and with a small viscous length ($\ell_* \approx 22$ μm).
- Experiments at matched β with different values of the Reynolds number show that the main Re-effect is to displace the outer peak farther away from the wall (when scaled in wall units) without altering significantly the outer-peak intensity. In contrast, changing β at fixed Re_τ has a little influence on the outer-peak location and a strong effect on the peak magnitude.
- Comparison of the experimental data with the LES data with matched β but different flow history shows that the turbulence statistics are significantly affected by the streamwise evolution of the pressure-gradient strength $\beta(Re_\theta)$. As a consequence, it is suggested to analyse the APG TBL features in terms of the accumulated effect of β (as proposed in 4.2, *i.e.* defining an average of the streamwise β evolution as $\overline{\beta}$), rather than in terms of the local value of β.
- Terms associated with streamwise derivatives in the turbulence production have been shown to be non-negligible for the cases with the lowest Reynolds number and the greatest β.
- Proper Orthogonal Decomposition has been used to show the effect of the adverse pressure gradient on the flow features. The Reynolds number and β have little if no effect on the energy eigenspectrum in the range under study. The most energetic modes reflect the interaction between the outer and near-wall regions. In particular, the first POD mode represents a sweep or an ejection depending on the sign of its corresponding time coefficient.

The effect of the pressure gradient and of the Reynolds number is to displace farther from the wall the sweeps/ejections.
- The first POD mode is able identify the location of the outer peak, while the following modes slightly adjust its position and mainly contribute to build the inner peak.

Paper 4

Carlos Sanmiguel Vila, Ricardo Vinuesa, Stefano Discetti, Andrea Ianiro, Philipp Schlatter, Ramis Örlü, 2019. *Large-scale motions and amplitude modulation in adverse-pressure-gradient turbulent boundary layers*, Journal of Fluid Mechanics, **Under Revision**.

- A new extensive high-quality hot-wire database from adverse-pressure-gradient TBLs which cover the Reynolds-number range $450 < Re_\theta < 23,450$ and a Clauser pressure-gradient-parameter range up to $\beta \approx 2.4$ has been provided and will be released publicly. Increasing and approximately–constant β distributions with the same upstream history are characterised.
- The inner-scaled wall-normal locations of the outer peak of the variance, of the zero-crossing of the skewness and of the minimum of the flatness have been found to coincide in APG and ZPG flows.
- Configurations with approximately–constant β distributions are found to converge towards a canonical state after a sufficiently long downstream length ($\sim 10\delta_{99}$). This convergence can be assessed using the defect shape factor G. These cases present skin-friction coefficient and shape factor distributions which appear to follow the empirical laws proposed by Vinuesa *et al.* (2017) for constant-β TBLs, which are similar to those previously proposed for ZPG TBLs (Nagib *et al.* 2007).
- The pre-multiplied power-spectral density of the streamwise velocity $f^+\Phi^+_{uu}$ highlights the presence of large energetic structures in the outer region, whose relevance increases with increasing pressure gradient at all Reynolds number. Additionally, at higher Reynolds numbers, the large structures due to β become more energetic, and also additional large energetic structures resembling the ones observed in high-Reynolds-number ZPG TBLs appear in the middle of the logarithmic region.
- Scale-decomposition analysis shows that the small-scale component of the streamwise velocity does not scale logarithmically with the wall-normal distance as in ZPG cases. Consequently, some caution is advised when using the ZPG corrections based on the inner-scaled hot-wire length L^+ for attenuation effects in APG TBLs.
- The analysis of the amplitude modulation shows that with increasing β the modulation effect of the large scales over the small scales is higher, and furthermore, is extended farther from the wall.
- The intensity and population density of the large-scale fluctuations over the whole boundary-layer thickness are increased with β. The intensity of the small-scales fluctuations is not only enhanced by the large-scale activity but also by the pressure-gradient strength.
- Based on the interactions between high- and low-speed events in APG flows, a novel method to locate the outer peak due to the pressure-gradient effects is presented. The outer-peak location is connected with the interaction of these events.
- The scalings proposed by Kitsios *et al.* (2017) and Maciel *et al.* (2018) are tested with the present database. The results show that no complete self-similarity can be observed in the profiles within our approximately constant-β region. This confirms the previous results from Townsend (1956), who showed that the sink flow is the only turbulent boundary layer exhibiting self-similarity.

Chapter 5

Príncipales contribuciones y conclusiones

En este capítulo, se recopilan las principales contribuciones y conclusiones de los trabajos presentados en esta tesis. Para una descripción detallada de los resultados, se remite al lector a los documentos adjuntos que constituyen la Parte II de la presente tesis.

5.1. Contribuciones de los artículos

Paper 1

Carlos Sanmiguel Vila, Ricardo Vinuesa, Stefano Discetti, Andrea Ianiro, Philipp Schlatter, Ramis Örlü, 2017. *On the identification of well-behaved turbulent boundary layers*, Journal of Fluid Mechanics, **822**, 109–138.

- Un nuevo método para determinar ZPG TBLs con "buen comportamiento" es propuesto y validado. Una nueva base de datos experimental de capas límite turbulentas sin gradiente de presión en el régimen de bajo Re es presentada. La base de datos consta de un total de seis casos con condiciones de "tripping" diferentes. Estas configuraciones abarcan casos con condiciones de "tripping" débiles, tardías, óptimas y fuertes.
- Los casos de "tripping" débiles conducen a desviaciones en la región logarítmica del flujo medio escalado con unidades viscosas cuando se compara con las configuraciones de "tripping" óptimas, mientras que el caso de "tripping" excesivo muestra una estela más prominente. Los casos de "tripping" débiles también conducen a pequeñas desviaciones en la varianza de la velocidad cuando se comparan con el "tripping" óptimo a aproximadamente $y^+ \approx 100$, donde los valores de u' son más bajos. El caso de "tripping" fuerte exhibe un pico interno más fuerte, así como el desarrollo de un pico externo en el perfil de varianza de la componente de la velocidad en la dirección del flujo.
- Se ha propuesto una nueva metodología basada en el concepto "diagnostic plot" (Alfredsson *et al.* 2011) para evaluar el desarrollo de ZPG TBL hacia condiciones de "buen comportamiento". En contraste con los métodos clásicos, la ventaja de este método es que solo se basa en las mediciones de la velocidad media en el sentido de la corriente y la intensidad de la turbulencia en distancias arbitrarias en la dirección normal a la pared y, por lo tanto, no necesita la información de u_τ o de la posición de la pared.
- Los resultados del análisis de los diferentes perfiles de velocidad de ZPG TBL muestran que $Re_\theta > 2000$ es un umbral más allá del cual los perfiles ZPG TBL presentan características canónicas, lo que concuerda con los resultados presentados en Schlatter & Örlü (2012).
- También se ha demostrado que el método propuesto puede determinar la posición en la dirección de la corriente desde donde un ZPG TBL se considera con "buen comportamiento" usando solo mediciones del perfil medio de la velocidad y de la intensidad turbulenta en la región exterior de la capa límite.

Paper 2

Ricardo Vinuesa, Ramis Örlü, Carlos Sanmiguel Vila, Stefano Discetti, Andrea Ianiro, Philipp Schlatter, 2017. *Revisiting history effects in adverse-pressure-gradient turbulent boundary layers*, Flow, Turbulence and Combustion, **99 (3–4)**, 565–587.

- Por primera vez, se estudia como evaluar si una capa límite turbulenta bajo gradientes de presión adversos se puede considerar como un flujo con "buen comportamiento". Se proponen diferentes métodos para APG TBL con distribuciones constantes y no constantes de β.
- Para los casos con distribución de β constante con valores $\beta = 1$ y 2, se proponen correlaciones para la evolución del coeficiente de fricción, C_f, y el factor de forma, H_{12}. Estas correlaciones están basadas en aquellas propuestas para ZPG TBL por Chauhan *et al.* (2009).
- Para los casos con una distribución particular de β en función de Re_θ, $\beta(Re_\theta)$ se propone una correlación para la evolución del coeficiente de fricción C_f. Esta correlación se basa en aplicar una corrección a la curva del caso ZPG TBL utilizando el valor promediado de β, $\overline{\beta}$.
- El criterio propuesto en **Paper 1** para identificar ZPG TBL con "buen comportamiento" es extendido para el caso de APG TBLs con una distribución cualquiera de $\beta(Re_\theta)$. Este nuevo criterio esta basado en la versión modificada del "diagnostic plot" para APG TBLs que fue propuesta por Vinuesa *et al.* (2016).
- En contraste con el caso de ZPG TBLs, el método modificado para APG TBL requiere la medida completa del perfil de velocidad en diferentes posiciones en la dirección de la corriente. Adicionalmente, se necesita una determinación precisa de la posición de la pared y un cálculo preciso de H_{12}.

Paper 3

Carlos Sanmiguel Vila, Ramis Örlü, Ricardo Vinuesa, Philipp Schlatter, Andrea Ianiro, Stefano Discetti, 2017. *Adverse-pressure-gradient effects on turbulent boundary layers: statistics and flow-field organization*, Flow, Turbulence and Combustion, **99 (3–4)**, 589–612

- Una nueva base de datos experimental de APG TBLs con diferentes $\beta(Re_\theta)$ basada en mediciones de PIV es presentada y analizada junto a una base de datos complementario de LES.
- Diferentes metodologías de PIV para el cálculo de estadísticas turbulentas han sido probadas y validadas con medidas de anemometría de hilo caliente. Se ha demostrado como el método de "Ensemble PTV" con ajuste polinomial de Agüera *et al.* (2016) es superior a los demás, con resultados precisos en el perfil medio de la velocidad y también en las estadísticas turbulentas de segundo orden desde la región de estela hasta $y^+ \simeq 10$ para el caso de TBL con un número alto de Reynolds ($Re_\tau \approx 4,100$) y un tamaño de escala viscosa pequeño ($\ell_* \approx 22$ μm).
- Experimentos con el mismo valor de β y diferentes valores del número de Reynolds muestran que el principal efecto de Re es desplazar el pico externo de la varianza de la velocidad lejos de la pared (cuando la velocidad se escala con variables viscosas) sin alterar de manera significativa su intensidad. Por otro lado, cambiar β dejando fijo Re_τ tiene poca influencia en la posición del pico pero un gran efecto en el valor del pico.
- La comparación de los datos experimentales con datos de LES con el mismo β pero con diferente historia muestra como la estadísticas turbulentas se ven afectadas de manera significativa por la evolución en la dirección del flujo del gradiente de presión $\beta(Re_\theta)$. Por esta razón, se propone no utilizar el valor local de β para caracterizar las APG TBLs y utilizar en su lugar un valor promedio (como el valor medio en la dirección del flujo $\overline{\beta}$) que tenga en cuenta el efecto acumulado de β.
- Se ha visto que los términos asociados con las derivadas en la dirección del flujo en la producción turbulenta no son despreciables para casos con número de Re bajo y alto β.

- La Descomposición Modal Ortogonal se ha empleado para mostrar el efecto de las escalas grandes en el campo fluido. El autoespectro de la energía de los modos POD aparentemente no está afectado por el número de Reynolds ó β en el rango estudiado. Los modos más energéticos muestran la interacción entre la región exterior y la zona de cerca de la pared. Concretamente, el primer modo POD representa una eyección o ingestión de flujo dependiendo del signo del coeficiente temporal. La organización modal si que se ve afectada tanto por β como por Re, moviéndose los eventos de eyección/ingestion lejos de la pared cuando estos aumentan.
- El primer modo POD es capaz de reconstruir el pico externo de la varianza de la velocidad y reproduce su localización, los siguientes modos ajustan ligeramente su posición y principalmente contribuyen a construir el pico interno.

Paper 4

Carlos Sanmiguel Vila, Ricardo Vinuesa, Stefano Discetti, Andrea Ianiro, Philipp Schlatter, Ramis Örlü, 2019. *Large-scale motions and amplitude modulation in adverse-pressure-gradient turbulent boundary layers*, Journal of Fluid Mechanics, **Under Revision**.

- Una nueva base de datos de alta calidad de capas límite turbulentas con gradientes de presión que abarca el rango de número de Reynolds correspondiente a $450 < Re_\theta < 23,450$ y del parámetro de Clauser de gradiente de presión $\beta \approx 2.4$ es presentado y sera publicado de manera abierta. Casos con distribuciones de β crecientes y aproximadamente constantes con la misma historia previa son caracterizados.
- La posición en la dirección normal de la pared para: el pico exterior de la varianza de la velocidad normalizado con unidades viscosas, el punto que cruza el cero de la asimetría y del mínimo de la curtosis coinciden. Esto ocurre tanto en ZPG como en APG TBL.
- Las configuraciones con distribuciones de β aproximadamente constante convergen hacia un estado canónico después de una distancia de desarrollo suficientemente larga ($\sim 10\delta_{99}$), esto se puede comprobar utilizando el factor de defecto de forma, G. Estos casos presentan curvas de fricción y factor de forma que parecen seguir las leyes empíricas propuestas por Vinuesa *et al.* (2017) para casos con β constante. Estas leyes son similares a aquellas propuestas previamente por Nagib *et al.* (2007) para ZPG TBLs.
- La densidad espectral de la potencia multiplicada por la frecuencia de la velocidad en la dirección del flujo, $f^+\Phi^+_{uu}$, muestra estructuras de gran escala en la región exterior cuando el gradiente de presión crece. Además, para los casos con alto número de Reynolds estas estructuras son más energéticas y aparecen otras estructuras de gran escala en el medio de la zona logarítmica que recuerdan a las que aparecen en los casos de ZPG TBLs con alto número de Reynolds.
- El análisis de los datos utilizando una descomposición de escalas muestra como la componente que corresponde a las escalas pequeñas de la velocidad en la dirección del flujo no escala como en los casos de ZPG TBL. Por ello, deberían de realizarse estudios adicionales para entender mejor si se puede seguir usando la longitud adimensionalizada del hilo caliente L^+ como referencia para comparar bases de datos o correcciones de medidas de anemometría de hilo caliente.
- La modulación de las escalas grandes aumenta con β, esto se ve reflejado con una distribución de las fluctuaciones correspondientes a la componente de escalas grandes u^+_L que se hace más amplia y fuerte. Además, el punto de modulación cero en APG TBLs se desplaza hacia regiones más exteriores de la capa límite comparado con ZPG TBLs.
- El incremento de fluctuaciones correspondientes a la componente de escalas grandes u^+_L contribuye a incrementar la varianza asociada a las escalas pequeñas en toda la capa límite. También parece que las escalas pequeñas se hacen más fuertes por el efecto del gradiente de presión, incluso si no hay fluctuaciones de escala grande.
- Se ha propuesto un método nuevo que localiza el pico externo de la varianza de la componente de la velocidad en la dirección del flujo. Esta posición está relacionada con

los efectos del gradiente de presión. El método propuesto esta basado en las interacciones entre los momentos de alta y baja velocidad en flujos APG. La posición del pico exterior y el valor correspondiente de la varianza en la dirección del flujo es analizado en la base de datos presentada y los resultados sirven para complementar evoluciones para altos valores de β presentadas previamente en Maciel *et al.* (2018).

- Los escalados propuestos en Kitsios *et al.* (2017) y Maciel *et al.* (2018) son probados con los datos de la base de datos presentada. Los resultados muestran que no existe una completa autosemejanza de los perfiles dentro de los casos con β aproximadamente constante. Estos resultados confirman lo observado en el estudio de Townsend (1956), donde se mostró que los flujos internos (canal y tubería) son las únicas capas límite turbulentas que pueden exhibir autosemejanza.

Bibliography

Agüera, N., Cafiero, G., Astarita, T. & Discetti, S. 2016 Ensemble 3D PTV for high resolution turbulent statistics. *Meas. Sci. Technol.* **27**, 124011.

Alfredsson, P. H. & Örlü, R. 2010 The diagnostic plot – a litmus test for wall bounded turbulence data. *Eur. J. Mech. B/Fluids* **29**, 403–406.

Alfredsson, P. H., Örlü, R. & Segalini, A. 2012 A new formulation for the streamwise turbulence intensity distribution in wall-bounded turbulent flows. *Eur. J. Mech. B/Fluids* **36**, 167–175.

Alfredsson, P. H., Segalini, A. & Örlü, R. 2011 A new scaling for the streamwise turbulence intensity in wall-bounded turbulent flows and what it tells us about the "outer" peak. *Phys. Fluids* **23**, 041702.

Alving, A. E. & Fernholz, H. H. 1995 Mean-velocity scaling in and around a mild, turbulent separation bubble. *Phys. Fluids* **7**, 1956–1969.

Astarita, T. 2007 Analysis of weighting windows for image deformation methods in PIV. *Exp. Fluids* **43** (6), 859–872.

Astarita, T. & Cardone, G. 2005 Analysis of interpolation schemes for image deformation methods in PIV. *Exp. Fluids* **38**, 233–243.

Avallone, F., Discetti, S., Astarita, T. & Cardone, G. 2015 Convergence enhancement of single-pixel PIV with symmetric double correlation. *Exp. Fluids* **56**, 71.

Bandyopadhyay, P. R. & Hussain, A. K. M. F. 1984 The coupling between scales in shear flows. *Phys. Fluids* **27** (9), 2221–2228.

Berkooz, G., Holmes, P. & Lumley, J. L. 1993 The proper orthogonal decomposition in the analysis of turbulent flows. *Annu. Rev. Fluid Mech.* **25**, 539–575.

Bobke, A., Vinuesa, R., Örlü, R. & Schlatter, P. 2017 History effects and near equilibrium in adverse-pressure-gradient turbulent boundary layers. *J. Fluid Mech.* **820**, 667–692.

Boussinesq, J. 1877 Essai sur la théorie des eaux courantes. *Mém. Acad. Sci. Paris* **22**, 1–680.

Bradshaw, P. 2013 *An introduction to turbulence and its measurement: thermodynamics and fluid mechanics series*. Elsevier.

Bruun, H. H. 1995 *Hot-wire Anemometry: Principles and Signal Analysis*. Oxford University Press Inc., New York, USA.

Chauhan, K. A., Monkewitz, P. A. & Nagib, H. M. 2009 Criteria for assessing experiments in zero pressure gradient boundary layers. *Fluid Dyn. Res.* **41**, 021404.

Clauser, F. H. 1954 Turbulent boundary layers in adverse pressure gradients. *J. Aero. Sci.* **21**, 91–108.

Clauser, F. H. 1956 The turbulent boundary layer. *Adv. Appl. Mech.* **4**, 1–51.

Coles, D. E. 1956 The law of the wake in the turbulent boundary layer. *J. Fluid Mech.* **1**, 191–226.

Coles, D. E. 1968 The young person's guide to the data. In *AFOSR-IFP-Stanford Conf. on Computation of turbulent boundary layers*, pp. 1–45. (e.d. D. E. Coles and E. A. Hirst).

Cowen, E. & Monismith, S. 1997 A hybrid digital particle tracking velocimetry technique. *Exp. Fluids* **22**, 199–211.

Cutler, A. D. & Johnston, J. P. 1989 The relaxation of a turbulent boundary layer in an adverse pressure gradient. *J. Fluid Mech.* **200**, 367–387.

Cuvier, C., Srinath, S., Stanislas, M., Foucaut, J. M., Laval, J. P., Kähler, C. J., Hain, R., Scharnowski, S., Schröder, A., Geisler, R., Agocs, J., Röse, A., Willert, C., Klinner, J., Amili, O., Atkinson, C. & Soria, J. 2017 Extensive characterisation of a high reynolds number decelerating boundary layer using advanced optical metrology. *J. Turbul.* **18**, 929–972.

Dengel, P. & Fernholz, H. 1990 An experimental investigation of an incompressible turbulent boundary layer in the vicinity of separation. *J. Fluid Mech.* **212**, 615–636.

Doering, C. R. 2009 The 3D Navier-Stokes Problem. *Annu. Rev. Fluid Mech.* **41** (1), 109–128.

Dogan, E., Örlü, R., Gatti, D., Vinuesa, R. & Schlatter, P. 2019 Quantification of amplitude modulation in wall-bounded turbulence. *Fluid Dyn. Res.* **51**, 011408.

East, L. F. & Sawyer, W. 1980 An investigation of the structure of equilibrium turbulent boundary layers. In *Turbulent Boundary Layers: Experiment, Theory and Modelling, CP-271, AGARD*, p. 6.1–6.19.

Eitel-Amor, G., Örlü, R. & Schlatter, P. 2014 Simulation and validation of a spatially evolving turbulent boundary layer up to $Re_\theta = 8300$. *Int. J. Heat Fluid Flow* **47**, 57–69.

Felsch, K. O., Geropp, D. & Walz, A. 1968 Method for turbulent boundary layer prediction. *In: Proceedings of the Stanford Conference on the Computation of Turbulent Boundary Layers* pp. 170–176.

Fernholz, H. H. & Finley, P. J. 1996 The incompressible zero-pressure-gradient turbulent boundary layer: An assessment of the data. *Prog. Aero. Sci.* **32**, 245–311.

Ganapathisubramani, B., Hutchins, N., Monty, J. P., Chung, D. & Marusic, I. 2012 Amplitude and frequency modulation in wall turbulence. *J. Fluid Mech.* **712**, 61–91.

George, W. K. 2007 Is there a universal log law for turbulent wall-bounded flows? *Phil. Trans. R. Soc. Lond. A* **365** (1852), 789–806.

George, W. K. & Castillo, L. 1997 Zero-pressure-gradient turbulent boundary layer. *Appl. Mech. Rev.* **50** (12), 689–729.

Gungor, A., Maciel, Y., Simens, M. & Soria, J. 2016 Scaling and statistics of large-defect adverse pressure gradient turbulent boundary layers. *Int. J. Heat Fluid Flow* **59**, 109–124.

Harun, Z., Monty, J. P., Mathis, R. & Marusic, I. 2013 Pressure gradient effects on the large-scale structure of turbulent boundary layers. *J. Fluid Mech.* **715**, 477–498.

Hinze, J. O. 1975 *Turbulence*. McGraw-Hill, 2nd. Ed.

Holmes, P., Lumley, J. L., Berkooz, G. & Rowley, C. W. 2012 *Turbulence, coherent structures, dynamical systems and symmetry*. Cambridge University Press, Cambridge, UK.

Hultmark, M., Bailey, S. C. C. & Smits, A. J. 2010 Scaling of near-wall turbulence in pipe flow. *J. Fluid Mech.* **649**, 103–113.

Jiménez, J. 2012 Cascades in wall-bounded turbulence. *Annu. Rev. Fluid Mech.* **44**, 27–45.

Kähler, C. J., Scharnowski, S. & Cierpka, C. 2012 On the resolution limit of digital particle image velocimetry. *Exp. Fluids* **52**, 1629–1639.

Kajishima, T. & Taira, K. 2017 Reynolds-Averaged Navier–Stokes Equations. In *Computational Fluid Dynamics*, pp. 237–268. Springer.

von Kármán, T. 1930 Mechanische Ähnlichkeit und Turbulenz. In *Proceedings of the 3rd International Congress on Applied Mechanics*, pp. 85–93.

von Kármán, T. 1937 The fundamentals of statistical theory of turbulence. *J. Aero. Sci.* **4**, 131–138.

Keane, R., Adrian, R. & Zhang, Y. 1995 Super-resolution particle imaging velocimetry. *Meas. Sci. Technol.* **6**, 754–768.

Kim, J. 2011 Physics and control of wall turbulence for drag reduction. *Phil. Trans. R. Soc. A* **369** (1940), 1396–1411.

Kitsios, V., Atkinson, C., Sillero, J., Borrell, G., Gungor, A., Jiménez, J. & Soria, J. 2016 Direct numerical simulation of a self-similar adverse pressure gradient turbulent boundary layer. *Int. J. Heat Fluid Flow* **61**, 129–136.

Kitsios, V., Sekimoto, A., Atkinson, C., Sillero, J. A., Borrell, G., Gungor, A. G., Jiménez, J. & Soria, J. 2017 Direct numerical simulation of a self-similar adverse pressure gradient turbulent boundary layer at the verge of separation. *J. Fluid Mech.* **829**, 392–419.

Knopp, T., Buchmann, N. A., Schanz, D., Eisfeld, B., Cierpka, C., Hain, R., Schröder, A. & Kähler, C. J. 2015 Investigation of scaling laws in a turbulent boundary layer flow with adverse pressure gradient using PIV. *J. Turbul.* **16**, 250–272.

Kolmogorov, A. N. 1941 Energy dissipation in locally isotropic turbulence. *Dokl. Akad. Nauk. SSSR* **32**, 19–21.

Lee, J. H. & Sung, H. J. 2008 Effects of an adverse pressure gradient on a turbulent boundary layer. *Int. J. Heat Fluid Flow* **29**, 568–578.

Lindgren, B. & Johansson, A. V. 2002 Evaluation of the flow quality in the MTL wind-tunnel. *Tech. Rep., Royal Institute of Technology (KTH), Stockholm, Sweden* .

Maciel, Y., Rossignol, K. & Lemay, J. 2006 A study of a turbulent boundary layer in stalled-airfoil-type flow conditions. *Exp. Fluids* **41** (4), 573–590.

Maciel, Y., Wei, T., Gungor, A. G. & Simens, M. P. 2018 Outer scales and parameters of adverse-pressure-gradient turbulent boundary layers. *J. Fluid Mech.* **844**, 5–35.

Marusic, I., McKeon, B. J., Monkewitz, P. A., Nagib, H. M., Smits, A. J. & Sreenivasan, K. R. 2010 Wall-bounded turbulent flows at high Reynolds numbers: Recent advances and key issues. *Phys. Fluids* **22**, 065103.

Marusic, I., Monty, J. P., Hultmark, M. & Smits, A. J. 2013 On the logarithmic region in wall turbulence. *J. Fluid Mech.* **716**, R3.

Marušić, I. & Perry, A. E. 1995 A wall-wake model for the turbulence structure of boundary layers. Part 2. Further experimental support. *J. Fluid Mech.* **298**, 389–407.

Mathis, R., Hutchins, N. & Marusic, I. 2009 Large-scale amplitude modulation of the small-scale structures in turbulent boundary layers. *J. Fluid Mech.* **628**, 311–337.

Mathis, R., Marusic, I., Hutchins, N. & Sreenivasan, K. 2011 The relationship between the velocity skewness and the amplitude modulation of the small scale by the large scale in turbulent boundary layers. *Phys. Fluids* **23**, 121702.

Mellor, G. & Gibson, D. 1966 Equilibrium turbulent boundary layers. *J. Fluid Mech.* **24**, 225–253.

Mendez, M. A., Raiola, M., Masullo, A., Discetti, S., Ianiro, A., Theunissen, R. & Buchlin, J. M. 2017 POD-based background removal for particle image velocimetry. *Exp. Therm. Fluid Sci.* **80**, 181–192.

Millikan, C. B. 1939 A critical discussion of turbulent flow in channels and circular tubes. In *Proceedings of the 5th International Congress on Applied Mechanics*, pp. 386–392. Wiley.

Moin, P. & Mahesh, K. 1998 Direct numerical simulation: a tool in turbulence research. *Annu. Rev. Fluid Mech.* **30** (1), 539–578.

Monkewitz, P. A., Chauhan, K. A. & Nagib, H. M. 2007 Self-consistent high-Reynolds-number asymptotics for zero-pressure-gradient turbulent boundary layers. *Phys. Fluids* **19**, 115101.

Monty, J. P., Harun, Z. & Marusic, I. 2011 A parametric study of adverse pressure gradient turbulent boundary layers. *Int. J. Heat Fluid Flow* **32**, 575–585.

Morrison, J. F., McKeon, B. J., Jiang, W. & Smits, A. J. 2004 Scaling of the streamwise velocity component in turbulent pipe flow. *J. Fluid Mech.* **508**, 99–131.

Nagano, Y., Tagawa, M. & Tsuji, T. 1993 Effects of adverse pressure gradients on mean flows and turbulence statistics in a boundary layer. In *Turbulent Shear Flows 8*, pp. 7–21. Springer.

Nagano, Y., Tsuji, T. & Houra, T. 1998 Structure of turbulent boundary layer subjected to adverse pressure gradient. *Int. J. Heat Fluid Flow* **19**, 563–572.

Nagib, H. M. & Chauhan, K. A. 2008 Variations of von Kármán coefficient in canonical flows. *Phys. Fluids* **20**, 101518.

Nagib, H. M., Chauhan, K. A. & Monkewitz, P. A. 2007 Approach to an asymptotic state for zero pressure gradient turbulent boundary layers. *Phil. Trans. R. Soc. A.* **365**, 755–770.

Nagib, H. M., Christophorou, C. & Monkewitz, P. A. 2004 High Reynolds number turbulent boundary layers subjected to various pressure-gradient conditions. In *IUTAM Symposium on one hundred years of boundary layer research*, pp. 383–394. (ed. G. E. A. Meier and K. R. Sreenivasan).

Nickels, T. B. 2004 Inner scaling for wall-bounded flows subject to large pressure gradients. *J. Fluid Mech.* **521**, 217–239.

Örlü, R. 2009 Experimental studies in jet flows and zero pressure-gradient turbulent boundary layers. *Ph. D. thesis, Royal Institute of Technology, Stockholm, Sweden* .

Örlü, R., Fransson, J. H. M. & Alfredsson, P. H. 2010 On near wall measurements of wall bounded flows – the necessity of an accurate determination of the wall position. *Prog. Aero. Sci.* **46**, 353–387.

Örlü, R., Segalini, A., Klewicki, J. & Alfredsson, P. H. 2016 High-order generalisation of the diagnostic scaling for turbulent boundary layers. *J. Turbul.* **17**, 664–677.

Örlü, R. & Vinuesa, R. 2017 Thermal Anemometry. In *Experimental Aerodynamics* (ed. S. Discetti & A. Ianiro). CRC Press Taylor & Francis Group, Boca Raton, FL.

Österlund, J. M. 1999 Experimental studies of zero pressure-gradient turbulent boundary layer flow. *Ph. D. thesis, Royal Institute of Technology, Stockholm, Sweden* .

Perry, A. 1966 Turbulent boundary layers in decreasing adverse pressure gradients. *J. Fluid Mech.* **26** (3), 481–506.

Pope, S. 2000 *Turbulent Flows*. Cambridge University Press, Cambridge, UK.

Prandtl, L. 1904 Über flussigkeitsbewegung bei sehr kleiner reibung. In *Verhandlungen des III Intl Math. Kongr Heidelberg*, pp. 484–491. Teubner.

Prandtl, L. 1925 Bericht uber untersuchungen zur ausgebildeten turbulenz. *Zs. angew. Math. Mech.* **5**, 136–139.

Raffel, M., Willert, C. E., Scarano, F., Kähler, C. J., Wereley, S. T. & Kompenhans, J. 2018 *Particle image velocimetry: a practical guide*. Springer.

Reynolds, O. 1883 An experimental investigation of the circumstances which determine whether the motion of water shall he direct or sinuous, and of the law of resistance in parallel channels. *Phil. Trans. R. Soc. Lond. A* **174**, 935–982.

Reynolds, O. 1895 On the dynamical theory of incompressible viscous fluids and the determination of the criterion. *Phil. Trans. R. Soc. Lond. A* **186**, 123–164.

Richardson, L. F. 1920 The supply of energy from and to atmospheric eddies. *Proc. R. Soc. Lond. A* **97** (686), 354–373.

Rotta, J. 1962 Turbulent boundary layers in incompressible flow. *Prog. Aero. Sci.* **2**.

Rowley, C. W. & Dawson, S. T. 2017 Model reduction for flow analysis and control. *Annu. Rev. Fluid Mech.* **49**, 387–417.

Sagaut, P. 2006 *Large eddy simulation for incompressible flows: an introduction*. Springer Science & Business Media.

Samuel, A. & Joubert, P. 1974 A boundary layer developing in an increasingly adverse pressure gradient. *J. Fluid Mech.* **66** (3), 481–505.

Sanmiguel Vila, C., Örlü, R., Vinuesa, R., Schlatter, P., Ianiro, A. & Discetti, S. 2017*a* Adverse-pressure-gradient effects on turbulent boundary layers: Statistics and flow-field organization. *Flow Turbul. Combust.* **99**, 589–612.

Sanmiguel Vila, C., Vinuesa, R., Discetti, S., Ianiro, A., Schlatter, P. & Örlü, R. 2017*b* On the identification of well-behaved turbulent boundary layers. *J. Fluid Mech.* **822**, 109–138.

Sanmiguel Vila, C., Vinuesa, R., Discetti, S., Ianiro, A., Schlatter, P. & Örlü, R. 2019 Large-scale motions and amplitude modulation in adverse-pressure-gradient turbulent boundary layers. *J. Fluid Mech.* **Under Revision**.

Scarano, F. 2001 Iterative image deformation methods in PIV. *Meas. Sci. Technol.* **13**, R1–R19.

Scharnowski, S., Hain, R. & Kähler, C. J. 2012 Reynolds stress estimation up to single-pixel resolution using PIV-measurements. *Exp. Fluids* **52**, 985–1002.

Schlatter, P. & Örlü, R. 2010*a* Assessment of direct numerical simulation data of turbulent boundary layers. *J. Fluid Mech.* **659**, 116–126.

Schlatter, P. & Örlü, R. 2010*b* Quantifying the interaction between large and small scales in wall-bounded turbulent flows: A note of caution. *Phys. Fluids* **22**, 051704.

Schlatter, P. & Örlü, R. 2012 Turbulent boundary layers at moderate Reynolds numbers: inflow length and tripping effects. *J. Fluid Mech.* **710**, 5–34.

Schmid, P. J. 2010 Dynamic mode decomposition of numerical and experimental data. *of fluid mechanics* **656**, 5–28.

Sillero, J. A., Jiménez, J. & Moser, R. D. 2013 One-point statistics for turbulent wall-bounded flows at Reynolds numbers up to $\delta^+ \simeq 2000$. *Phys. Fluids* **25**, 105102.

Skåre, P. E. & Krogstad, P. 1994 A turbulent equilibrium boundary layer near separation. *J. Fluid Mech.* **272**, 319–348.

Skote, M. 2001 Studies of turbulent boundary layer flow through direct numerical simulation. *Ph. D. thesis, Royal Institute of Technology, Stockholm, Sweden* .

Skote, M., Henningson, D. & Henkes, R. 1998 Direct numerical simulation of self-similar turbulent boundary layers in adverse pressure gradients. *Flow Turbul. Combust.* **60**, 47–85.

Soria, J. 1996 An investigation of the near wake of a circular cylinder using a video-based digital cross-correlation particle image velocimetry technique. *Exp. Therm. Fluid Sci.* **12**, 221–233.

Spalart, P. R. & Watmuff, J. H. 1993 Experimental and numerical study of a turbulent boundary layer with pressure gradients. *J. Fluid Mech.* **249**, 337–371.

Stratford, B. S. 1959 An experimental flow with zero skin friction throughout its region of pressure rise. *J. Fluid Mech.* **5**, 17–35.

Tani, I. 1969 Boundary-layer transition. *Annu. Rev. Fluid Mech.* **1**, 169–196.

Taylor, G. I. 1915 I. eddy motion in the atmosphere. *Phil. Trans. R. Soc. Lond. A* **215** (523-537), 1–26.

Taylor, G. I. 1922 Diffusion by continuous movements. *Proc. Lond. Math. Soc.* **2** (1), 196–212.

Tennekes, H. & Lumley, J. L. 1972 *A First Course in Turbulence*. MIT Press, Cambridge, Massachusetts.

Titchener, N., Colliss, S. & Babinsky, H. 2015 On the calculation of boundary-layer parameters from discrete data. *Exp. Fluids* **56** (8), 159.

Townsend, A. 1956*a* The properties of equilibrium boundary layers. *J. Fluid Mech.* **1**, 561–573.

Townsend, A. A. 1956*b* *The Structure of Turbulent Shear Flow*. Cambridge University Press.

Tropea, C. & Yarin, A. L. 2007 *Springer Handbook of Experimental Fluid Mechanics*. Springer Science & Business Media.

Vinuesa, R., Bobke, A., Örlü, R. & Schlatter, P. 2016 On determining characteristic length scales in pressure-gradient turbulent boundary layers. *Phys. Fluids* **28**, 055101.

Vinuesa, R., Negi, P. S., Atzori, M., Hanifi, A., Henningson, D. S. & Schlatter, P. 2018 Turbulent boundary layers around wing sections up to $Re_c = 1,000,000$. *Int. J. Heat Fluid Flow* **72**, 86–99.

Vinuesa, R., Örlü, R., Sanmiguel Vila, C., Ianiro, A., Discetti, S. & Schlatter, P. 2017 Revisiting history effects in adverse-pressure-gradient turbulent boundary layers. *Flow Turbul. Combust.* **99**, 565–587.

Vinuesa, R., Rozier, P. H., Schlatter, P. & Nagib, H. M. 2014 Experiments and computations of localized pressure gradients with different history effects. *AIAA J.* **52** (2), 368–384.

Wei, T. & Maciel, Y. 2018 Derivation of Zagarola-Smits scaling in zero-pressure-gradient turbulent boundary layers. *Phys. Rev. Fluids* **3**, 012601.

Westerweel, J., Geelhoed, P. & Lindken, R. 2004 Single-pixel resolution ensemble correlation for micro-PIV applications. *Exp. Fluids* **37**, 375–384.

Westerweel, J. & Scarano, F. 2005 Universal outlier detection for PIV data. *Exp. Fluids* **39**, 1096–1100.

Willert, C. & Gharib, M. 1991 Digital particle image velocimetry. *Exp. Fluids* **10**, 181–193.

Yoon, M., Hwang, J. & Sung, H. J. 2018 Contribution of large-scale motions to the skin friction in a moderate adverse pressure gradient turbulent boundary layer. *J. Fluid Mech.* **848**, 288–311.

Zagarola, M. V. & Smits, A. J. 1998 A new mean velocity scaling for turbulent boundary layers. In *Proceedings of ASME Fluids Engineering Division Summer Meeting, June 21–25, Washington DC*.

Part II

Papers

1

Paper 1

On the identification of well-behaved turbulent boundary layers

Carlos Sanmiguel Vila[1], Ricardo Vinuesa[2], Stefano Discetti[1], Andrea Ianiro[1], Philipp Schlatter[2] and Ramis Örlü[2]

[1] Aerospace Engineering Group, Universidad Carlos III de Madrid, Leganés, Spain
[2] Linné FLOW Centre, KTH Mechanics, SE-100 44 Stockholm, Sweden

Journal Fluid Mechanics (2017), vol. **822**, 109–138

The present paper introduces a new method based on the diagnostic plot (Alfredsson *et al.*, Phys. Fluids, **23**:041702, 2011) to assess the convergence towards a well-behaved zero-pressure-gradient (ZPG) turbulent-boundary layer (TBL). The most popular and well understood methods to assess the convergence towards a well-behaved state rely on empirical skin-friction curves (requiring accurate skin-friction measurements), shape-factor curves (requiring full velocity profile measurements with an accurate wall position determination) or wake-parameter curves (requiring both of the previous quantities). On the other hand, the proposed diagnostic-plot method only needs measurements of mean and fluctuating velocities in the outer region of the boundary layer at arbitrary wall-normal positions. To test the method, six tripping configurations, including optimal setups as well as both under and over-tripped cases, are used to quantify the convergence of zero-pressure-gradient turbulent boundary layers towards well-behaved conditions in the Reynolds-number range covered by recent high-fidelity direct-numerical simulation (DNS) data up to a Re_θ of around 4,000 (corresponding up to 2.5 m from the leading edge). Additionally, recent high Re data sets have been employed to validate the method. Results show that weak tripping configurations lead to deviations in the mean flow and the velocity fluctuations within the logarithmic region with respect to optimally-tripped boundary layers. On the other hand, a strong trip leads to a more energized outer region, manifested in the emergence of an outer peak in the velocity-fluctuation profile and in a more prominent wake region. While established criteria based on skin-friction and shape-factor correlations yield generally equivalent results with the diagnostic-plot method in terms of convergence towards a well-behaved state, the proposed method has the advantage of being a practical surrogate that is a more efficient tool when designing the set-up for TBL experiments, since it diagnoses the state of the boundary layer without the need to perform extensive velocity profile measurements.

Key words: Turbulent boundary layers, turbulent flows

1. Introduction

Turbulent boundary layers (TBLs) are of paramount importance given their ubiquitous presence in many relevant fluid-flow problems such as the flow over wings, land and sea vehicles, turbines, compressors, etc. Due to the complex physics present in these flows, simplified scenarios such as the zero pressure gradient (ZPG) TBL developing over a flat plate are investigated to understand the fundamental aspects of wall-bounded turbulence. In experimental ZPG TBL studies, the transition to turbulence of a laminar boundary layer is commonly induced using an external perturbation, since natural transition requires long development lengths, and is significantly affected by external disturbances (Tani 1969). The perturbation used to trigger transition in experimental studies is typically a trip (Klebanoff & Diehl 1954; Erm & Joubert 1991), and it is important to carefully design it, in accordance with the inflow conditions, since an inadequate

choice of this perturbation may condition the results of the study (Hutchins 2012). Effects such as inflow conditions, tripping devices and development length, which may lead to local non-equilibrium conditions producing flows that are no longer representative of the *canonical* ZPG TBL, have started to receive some renewed attention in recent years. Consequently, criteria and methods to determine if a TBL can be considered as *well-behaved*, (*i.e.*, not in a post-transitional state or affected by non-equilibrium effects), have been the object of increasing interest. In the context of this study, the term *well-behaved* refers to a state in which the TBL is independent of the tripping conditions and flow history, as defined in the work by Chauhan *et al.* (2009). In particular, the well-behaved state corresponds to that of a canonical ZPG TBL, which is a particular case of near-equilibrium boundary layer in which the mean velocity defect is self-similar in the outer region at high Reynolds numbers as discussed for instance by Marusic *et al.* (2010).

A number of different trip devices, including wires, distributed grit and cylindrical pins, were studied by Erm & Joubert (1991) in the Reynolds number range $715 \leq Re_\theta \leq 2,815$, where the subscript θ denotes the momentum thickness. In their work, Erm & Joubert (1991) designed the trip devices to obtain a correct stimulation of the flow at a specific velocity, adapting the trip height iteratively until the measured value of ΔU^+ (proportional to the so-called wake parameter Π), which is the maximum deviation of a given profile from the logarithmic law, would agree with the empirical relation between ΔU^+ and Re_θ proposed by Coles (1962). Note that in the present study the superscript '+' denotes scaling with the friction velocity u_τ and the viscous length $\ell_* = \nu/u_\tau$ (where $u_\tau = \sqrt{\tau_w/\rho}$, τ_w, being the mean wall-shear stress, ρ the fluid density and ν the kinematic viscosity). Additionally, Erm & Joubert (1991) have shown that for varying free-stream velocities the ΔU^+ versus Re_θ curves would not agree with the one proposed by Coles (1962, 1968) at Reynolds numbers below $Re_\theta \simeq 3,000$, which manifests the flow sensitivity to the particular tripping device, especially at early development stages. Moreover, when the flow is not properly stimulated, the initial evolution of parameters such as the shape factor $H = \delta^*/\theta$ (where δ^* is the displacement thickness) and the skin friction coefficient $C_f = 2\tau_w/\left(\rho U_\infty^2\right)$ (where U_∞ is the free-stream velocity) may differ in the low-Re range below $Re_\theta \simeq 3,000$. In this context, Castillo & Johansson (2002) studied the effect of the upstream conditions on low Reynolds number ZPG TBLs by varying the wind tunnel speed while maintaining the trip wire size and its location. They reported that the evolution of parameters such as the growth rate of the boundary layer or the Reynolds shear stresses were affected by the different inflow conditions. The fact that the upstream conditions play such an important role in the downstream flow implies that experiments with the same local Reynolds number may produce different results depending on the particular tripping strategy adopted. As a consequence, discrepancies between different experimental studies can be found in the literature. In order to discern which ZPG TBL can be considered *"well-behaved"*, Chauhan *et al.* (2009), taking up the seminal works by Coles (1968) and Fernholz & Finley (1996), analyzed and compared in detail a large number of experimental databases with significant discrepancies among them. They fitted a wide range of velocity profiles to a composite profile formulation (Chauhan *et al.* 2009) in order to obtain the wake parameter Π (Coles 1956) and the shape factor H, besides the skin-friction coefficient. By comparing the streamwise evolution of the measured values of C_f, H and Π with respect to the ones predicted through numerical integration of the composite profile, Chauhan *et al.* (2009) identified *well-behaved* profiles.

Marusic *et al.* (2015) further investigated on the evolution of ZPG TBLs tripped with different tripping devices. In their study the trip strength was varied in an incremental fashion from weak tripping up to over-tripping with all other parameters kept constant, including local Reynolds number, pressure-gradient conditions, etc. The aim of their work was to compare TBL evolutions from various tripping configurations at matched local Reynolds numbers. The trip strength was modified by considering a standard sandpaper trip, together with two threaded rods of different diameters designed to overstimulate the boundary layer. They reported the evolution of the different flows until their equilibrium state, and observed that the effects of the particular trip persisted up to streamwise distances of the order of $2,000$ trip heights. However, this conclusion

is only valid for their particular setup and trip method. The trip effects were especially evident on the large-scale motions (residing in the outer layer) in the flow, which are effectively energized by the overstimulating tripping configurations.

With the aim of generating canonical high-Reynolds number TBLs in short wind tunnels, a study of tripping configurations was carried out by Rodríguez-López *et al.* (2016). A sawtooth serrated fence and different spanwise arrays of cylinders were employed to obtain a uniform wall-normal blockage distribution case and a non-uniform one. In their study, Rodríguez-López *et al.* (2016) have shown how tripping configurations with a uniform blockage ratio can be used to obtain canonical high-Reynolds number TBLs with an increase of up to 150% in momentum thickness with respect to a standard sandpaper trip. It was also shown that, after an adaptation region, tripping configurations with uniform blockage ratio eventually lead to a canonical state in contrast with configurations with non-uniform blockage ratio, which do not generate canonical TBLs even after a long recovery distance.

The choice of tripping strategy and inflow conditions also affects significantly the results from numerical simulations, as shown by Schlatter & Örlü (2010). Their results shown that the impact of transitional effects through the boundary layer development and the slow convergence of the outer layer can lead to important differences, as shown through the comparison of a wide number of direct numerical numerical simulation (DNS) databases of ZPG TBLs. The estimated values of parameters such as H and C_f may differ up to 5% and 20%, respectively. In a follow-up study, Schlatter & Örlü (2012) reported that if transition is initiated at Reynolds numbers based on momentum thickness $Re_\theta < 300$, then comparisons between different numerical and experimental databases can be made for $Re_\theta > 2,000$ if the flow is not over or under-tripped. Thus, under these conditions the ZPG TBL can be considered as *canonical*, and does not exhibit features reminiscent of its particular inflow condition. Along the lines of these studies, the importance of selecting an adequate trip condition for producing a canonical TBL was highlighted by Hutchins (2012).

Whereas Schlatter & Örlü (2012) considered a laminar boundary layer as inflow for their simulations, and used a tripping method based on wall-normal volume forcing which emulates the effect of experimental tripping devices, Sillero *et al.* (2013) used a recycling method based on the one proposed by Lund *et al.* (1998) to generate synthetic inflow conditions for their DNS of a ZPG TBL. Simens *et al.* (2009) suggested that when considering synthetic inflow conditions, the turnover length may be a better measure than Re_θ of how quickly the boundary layers recover from a specific inflow condition. The turnover length $\tilde{x}$ is the distance the eddies are advected during a turnover time δ/u_τ (δ being the boundary-layer thickness), as defined through:

$$\tilde{x} = \int^{x} \mathrm{d}x / \left(\delta U_\infty^+\right), \tag{1}$$

where x is the streamwise coordinate. Sillero *et al.* (2013) reported that in their simulations the parameters connected to the small scales, such as the maximum Reynolds stress, require a recovery distance of $\tilde{x} \simeq 1$. The variables connected to the larger scales, on the other hand, require longer recovery distances (in agreement with the observations by Schlatter & Örlü 2012), *viz.* as much as $\tilde{x} \simeq 3-4$ in the case of H or δ/θ, and $\tilde{x} \simeq 4-5$ for Π. Note that this may lead to the fact that the computational domain is not long enough to allow full development of the large-scale motions in the TBL, as it was the case in one of the preliminary simulations reported by Sillero *et al.* (2013).

In another recent study, Kozul *et al.* (2016) studied a temporally-developing turbulent boundary layer through DNS, in a setup where the lower plate is suddenly set into motion, as in the case of TBLs developing on a flat plate in towing-tank experiments (Lee *et al.* 2014). The initial velocity profile they used is similar to that of the wake after a wall-mounted trip wire used in wind tunnels. They also assessed how different trip conditions affected the results in terms of a "trip Reynolds number" based on the trip-wire diameter. In their study it is shown that as the ratio of momentum thickness to trip-wire diameter approaches unity, the flow converges towards a state free from the

Tripping case	Characteristics and location	Color code	Description
①	DYMO "V" at $x = 75$ mm	Red	Weak tripping
②	DYMO "V" at $x = 75$, 90, 115 mm and 5 mm square bar at $x = 85$ mm	Black	Strong over-tripping
③	DYMO "V" at $x = 90$, 115 mm and 2.4 mm height turbulator	Blue	Optimal tripping 1
④	DYMO "V" at $x = 90$, 115 mm and 1.6 mm height turbulator	Magenta	Optimal tripping 2
⑤	DYMO "V" at $x = 90$ mm	Green	Weak, late tripping
⑥	DYMO "V" at $x = 230$ mm	Brown	Weak, very late tripping

Table 1: Specifications of the tripping configurations including location and respective color coding for symbols. The embossed (DYMO) letter "V" points downstream and has a nominal height of 0.3 mm.

effects of its starting trip Reynolds number. This is an interesting conclusion due to the connection between experimental trip devices, and numerical characterization of temporally-developing TBLs.

In the present study the primary objective is to investigate whether there exists a criterion to identify a well-behaved boundary layer for both experiments and simulations without the need of acquiring huge amount of data and without relying on quantities difficult to be measured (such as the wall distance or the wall shear stress). The present investigation revisits the early experimental studies on the history effects of tripping devices on turbulence characteristics at low Re (see *e.g.* Erm & Joubert 1991) in light of the recent numerical as well as high Re experimental studies with the aim to a) assess the various criteria proposed in the literature to discern a *canonical* ZPG TBL and b) propose a practical method that can be employed prior to extensive measurements and/or DNS.

The article is organized as follows: the experimental setup is described in §2, upon which the boundary-layer development from the various inflow conditions are compared and presented in §3. A method to assess the boundary-layer development based on the diagnostic-plot method (Alfredsson *et al.* 2011) is presented in §4, and its outcomes are compared with those of other available criteria. Prior to the summary and conclusions in §5, the proposed method is demonstrated to be a practically feasible and efficient tool when designing the set-up for TBL experiments.

2. Experimental set-up

2.1. *Wind tunnel and boundary-layer flow conditions*

Experiments were carried out in the *Minimum Turbulence Level* (MTL) closed-loop wind tunnel located at KTH Royal Institute of Technology in Stockholm. The test section is 7 m long with a cross-sectional area of 0.8×1.2 m^2 (height $\times$ width). This tunnel is capable of reaching a maximum speed of 70 m/s with a streamwise velocity disturbance level of approximately 0.025% of the free-stream velocity at a test speed of 25 m/s. The air temperature can be controlled with an accuracy of ± 0.05°C by means of a heat exchanger. More details on the MTL can be found in Lindgren & Johansson (2002). Measurements of the turbulent boundary layer developing over the flat plate were performed at a nominal free-stream velocity of 12 m/s. The aluminum flat plate of 6 m length and 26 mm thickness, spanned the entire width of the wind tunnel and was suspended 25 cm above the tunnel floor. The flat plate has a leading edge following the shape of a modified super ellipse and is equipped with a trailing-edge flap plate to modify the position of the stagnation point on the leading edge. For a more detailed description the reader is referred to Österlund (1999).

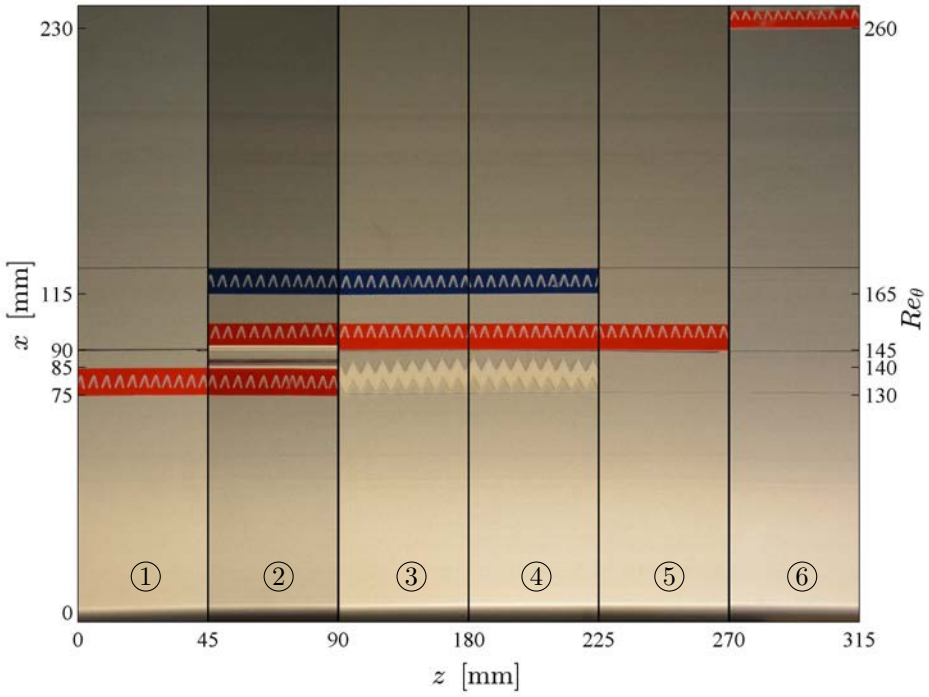

Figure 1: Schematic view of the tripping configurations used in the present study and summarized in Table 1, with streamwise direction from bottom to top. The indicated momentum-thickness Reynolds number Re_θ is related to the laminar boundary layer in absence of the trip. Note that the difference between ③ and ④ is the height of the turbulator, and is hence not visible in the present two-dimensional view. The scale in mm is included in order to provide a reference for the size of the "V" and the turbulator pattern.

The boundary layer was tripped close to the leading edge with a set of tripping devices in order to obtain a range of different tripping conditions. Using as a reference the cases studied numerically by Schlatter & Örlü (2012), a combination of weak, late, optimal and strong trippings were tested. In this study, the nomenclature *optimal* is referred to cases in which the boundary layer is neither overstimulated nor underestimulated by the tripping and that the profiles would lead to a common state within the streamwise distance considered here. With this aim, *DYMO* tapes (with the embossed letter 'V' pointing in the flow direction and a nominal height of 0.3 mm) in various combinations with and without turbulators were used to establish 5 different initial evolutions of the TBL. Additionally, a square bar with a side length of 5 mm was used to obtain a strongly over-tripped case. The 6 different tripping cases under consideration are summarized in Table 1, which also reports the color coding used for such tripping condition, through the remainder of the paper, and represented in Figure 1. All the tripping configurations were placed spanning the full spanwise length of the plate and at a streamwise location in the range $75 < x\,[\mathrm{mm}] < 230$ from the leading edge, corresponding to the range $130 < Re_\theta < 260$ in terms of the laminar boundary layer as can be observed in Figure 1.

An initial set of 4 streamwise locations were selected for measurements on each tripping configuration. Additional stations were added to match Re_θ, covering a final Reynolds number range of $440 < Re_\theta < 4,070$ as shown in Table 3. The streamwise pressure-gradient distribution was controlled by adjusting the wind tunnel ceiling, which comprises a total of six panels allowing

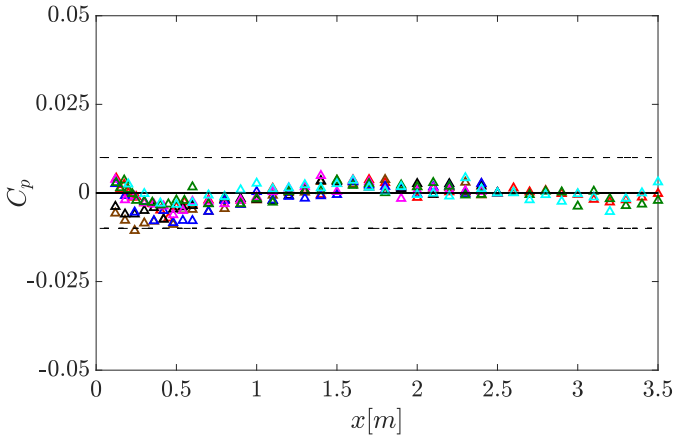

Figure 2: Streamwise variation of the pressure coefficient C_p for the 6 tripping configurations considered in the present study. See Table 1 for the used color code. The additional cyan symbols correspond to a case in which no tripping was used. Reference dash lines at $C_p = \pm 0.010$ are included.

vertical displacement. The evolution of the pressure coefficient C_p from the leading edge ($x = 0$ m) down to $x = 3.5$ m is shown in Figure 2 for the 6 tripping cases under consideration, as well as for an additional case where no tripping was used (and where the boundary layer remained laminar). This figure shows the quality of the ZPG established in the test section, with C_p values between -0.01 and 0.01, and deviations in U_∞ below 0.5%, which is comparable in quality with related studies, see *e.g.* Marusic *et al.* (2015). From Figure 2 it can be observed that the changes in displacement thickness δ^* due to the different tripping configurations have a very small influence in the pressure distribution. This is due to the large ratio between the distance from the flat plate and the tunnel ceiling (around 0.55 m), and the maximum displacement thickness, which is below around 1%.

2.2. *Hot-wire anemometry measurements*

Streamwise velocity measurements were performed by means of a home-made single hot-wire probe resembling a standard *Dantec* boundary-layer probe, *i.e.*, a 55P15. The hot-wire probe was etched in-house using a stubless Platinum wire of 560 μm length and nominal diameter of 2.5 μm, which was soldered to conical prongs with diameter of around 30 μm. Voltage signals from the hot-wire were recorded using a *Dantec StreamLine* 90N10 frame in conjunction with a 90C10 constant-temperature anemometer module operated at a resistance overheat ratio of 80%. An offset and gain were applied to the top-of-the-bridge voltage in order to match the voltage range of the 16-bit A/D converter used. All the measurements were recorded using a sampling frequency of 20 kHz and acquisition time of 30 s, and a low-pass filter of 10 kHz cut-off frequency was used prior to the data acquisition in order to avoid aliasing. Calibration of the hot-wire was performed in situ using as reference a Prandtl tube located parallel to the incoming free stream. The Prandtl tube was connected to a micromanometer of type *FC0510 (Furness Control Limited)*, which was also employed to record the ambient temperature and pressure during the calibration and the experiments. Data acquired in the calibration was fitted to a fourth-order polynomial curve, which is a rather common procedure in the wall-turbulence community (see *e.g.* Morrison *et al.* 2004; Hultmark *et al.* 2010). Hot-wire measurements were acquired with a sufficiently large number of points within the sublayer and buffer region in order to correct for the absolute wall position and determine the friction velocity (Örlü & Vinuesa 2017) without relying on log-law constants. The composite profile given by Chauhan *et al.* (2009) is used to fit the experimental

Quantity	Notation	Uncertainty (±)
Temperature	T	0.2%
Dynamic pressure	Δp	0.4%
Atmospheric pressure	p_∞	0.1%
Air density	ρ	0.2%
Kinematic viscosity	ν	0.2%
Velocity	U	1.0%
Wall position	Δy	15 μm
Friction velocity	u_τ	0.8%
Momentum thickness	θ	0.5%
Displacement thickness	δ^*	0.5%
Wake parameter	Π	2.5%

Table 2: Uncertainty estimates for various measured quantities.

data and correct the absolute wall position as well as to obtain the friction velocity, which has been shown to be a robust method whenever near-wall measurements are at hand (Örlü *et al.* 2010; Rodríguez-López *et al.* 2015). Additional oil-film interferometry measurements, described in §2.3, were performed for some selected conditions and were utilized to validate the aforementioned procedure to determine the friction velocity. The experimental uncertainties associated with the measurements were determined through an approach based on a Monte Carlo simulation, assuming random errors in the velocity measurements, viscosity and absolute wall position with the following uncertainties: 1%, 0.2% and 15 μm, respectively (see *e.g.* Bailey *et al.* 2013). A summary of the resulting uncertainties is shown in Table 2.

2.3. *Oil-film interferometry measurements*

Oil-film interferometry (OFI) was used to measure the wall-shear stress, and validate the process to determine the friction velocity based on near-wall velocity measurements described in §2.2. To this end, the OFI measurements were carried out a the same positions as the hot-wire. Silicon oil with a nominal viscosity of 200 cSt at 25°C was used. The oil viscosity was calibrated by means of a capillary-suspended level viscometer. Black Mylar films were attached to the flat plate in order to obtain better contrast for the fringe patterns from the oil-film light reflections. The oil film was illuminated using a low-pressure sodium lamp which had a power of 55 W and a nominal wavelength of 589 nm and was placed on the wind tunnel roof. A handhold digital thermocouple *Fluke* was attached to the flat plate close to the recording station to control the oil temperature. The equipment used to obtain the pictures consisted of a digital single-lens reflex camera *Nikon D7100*, and telephoto zoom lens *Nikon Nikkor 200 mm f4*. The camera was placed on the roof of the wind tunnel with an angle of 15° normal to the plate, and was controlled remotely via a USB cable. For further details on the performed oil-film interferometry measurements, as well as on the post-processing of the data, the reader is referred to Örlü & Schlatter (2013) and Vinuesa & Örlü (2017), respectively. Also note that we do not expect the very small local pressure gradient observed at around $x \simeq 0.4$ m in Figure 2 to impact the OFI results, since this technique has been used in other studies dealing with pressure-gradient TBLs (Monty *et al.* 2011; Vinuesa *et al.* 2014), where no effects that would produce a significant bias were observed.

3. TBL evolution for various tripping configurations

In this section, we analyze streamwise mean velocity and velocity fluctuation profiles, as well as spectra, to assess the evolution of the TBL from the various tripping devices described in Table 1. All the velocity profiles under consideration are summarized in Table 3, where, following the procedure proposed by Schlatter & Örlü (2010), the composite profile by Nickels (2004) was used

to obtain the free-stream velocity U_∞ and the 99% boundary-layer thickness δ_{99} in a consistent manner, upon which the Reynolds numbers, integral quantities and boundary layer parameters were then computed. The summary in this table will also serve as an identification sheet for the data sets made available with this paper. As shown in Table 3, all the velocity profiles were measured in the range $0.24 < x$ [m] < 2.5 from the flat-plate leading edge. In terms of spatial resolution, the hot-wire probe length can be considered nominally matched in terms of viscous length to approximately 20, while the temporal resolution is as well sufficiently well-resolved based on the criteria set by Hutchins *et al.* (2009, 2015).

3.1. *Comparison of TBLs at the same streamwise location*

Mean streamwise velocity and velocity fluctuation profiles are shown at four streamwise measuring stations, for the six tripping cases, in Figure 3. For the tripping configurations from ① to ⑤, the near-wall region collapses in all the stations, in agreement with the conclusions from Schlatter & Örlü (2012) who showed that this region is expected to adapt quickly to a canonical TBL development. Interestingly, case ⑥ (weak, very late trip; subplot k)) in which the tripping is located at $x = 0.23$ m, corresponding to $Re_\theta = 260$, the boundary layer remains essentially laminar for $x < 1.8$ m, as apparent from the linear profile ($U^+ = y^+$) that extends far beyond the usual bound of $y^+ \lesssim 5$. The two optimal cases, ③ and ④ (subplots e) and g)), exhibit similar developments in the buffer and overlap regions, with similar increase in U_∞^+ at the same streamwise measurement stations, which indicates that the development of the outer region is adequate (note that the missing point in the freestream present in one of the profiles from Figure 3e) is due to the fact that the traverse file erroneously was missing this point). The weak tripping case ① (subplot a)) shows that the first profile, at $x = 0.24$ m, is slightly underdeveloped in comparison with the equivalent profile in the optimal tripping cases ③ and ④: although the U_∞^+ value is similar to that of case ④, the overlap region deviates from the higher Re profiles earlier (at $y^+ \simeq 100$) compared with the optimal cases. The case ⑤ (subplot i)) exhibits a similar behavior at $x = 0.24$, with an even lower value of the inner-scaled free-stream velocity related to the late transition and consequently lower friction Reynolds number Re_τ. The profiles downstream of this station are, in cases ① and ⑤, in good agreement with the optimal configurations ③ and ④. With respect to the strong trip case ② (subplot c)), the first profile at $x = 0.24$ m shows a more prominent wake region than the optimal cases, whereas at this first station the overlap region from case ② is beneath the optimal ones. These effects become attenuated downstream, where the profiles from the strong trip case progressively converge towards the optimal ones.

Regarding the streamwise variance profiles, the two optimal cases ③ and ④ also show an adequate development of the TBL, *i.e.* the inner and outer layers growth monotonically along the streamwise direction with only apparent differences in the first station. The mean flow deviation from the overlap region at around $y^+ \simeq 100$, observed at the first station of case ①, is also observed in the variance profile; at this location the variance decays faster than in the optimal case ④. Case ⑤ also shows fluctuation amplitudes below the optimal cases in the outer region, but, interestingly, cases ① and ⑤ progressively converge towards the variance profiles of the optimal cases, suggesting adequately that they recover from the weak tripping. With respect to case ⑥, the first profiles up to $x \simeq 1.8$ m also indicate the disturbance level is not sufficiently high to trigger transition to turbulence, as evinced from the fluctuation values close to zero throughout the whole boundary layer. The streamwise coordinate $x = 1.8$ m is the first one at which case ⑥ exhibits a near-wall fluctuation peak, although it clearly exhibits deviations with respect to the optimal cases. The first fluctuation profile from the strong tripping case ② is interesting in that respect since, in addition to an enhanced value of the near-wall peak, it also shows the emergence of an outer peak at $y^+ \simeq 250$, although the wall-normal location is clearly beyond the inner layer as is the case for a canonical high Re ZPG TBL (Alfredsson *et al.* 2011). These effects in the outer region of the boundary layer, reminiscent of adverse-pressure-gradient TBLs (Monty *et al.* 2011; Hosseini *et al.* 2016), were also observed by Tang *et al.* (2016) in their measurements of

Case	x [m]	Re_θ	Re_τ	u_τ [m/s]	δ_{99} [mm]	θ [mm]	δ^* [mm]	H	Π	ν/u_τ [μm]	L^+	Δt^+	TU_∞/δ_{99}
① Weak	**0.24**	540	210	0.58	5.82	0.69	1.09	1.59	0.38	26.2	21	1.11	61,800
① Weak	**0.60**	1,200	430	0.53	13.09	1.52	2.23	1.47	0.37	28.4	20	0.94	27,500
① Weak	**1.10**	1,950	650	0.50	19.81	2.48	3.56	1.44	0.44	30.5	18	0.82	18,100
① Weak	**1.80**	2,900	910	0.47	28.68	3.70	5.25	1.42	0.55	32.4	17	0.72	12,400
② Strong	**0.24**	1,770	620	0.53	20.96	2.25	3.17	1.41	-0.03	28.4	20	0.93	17,000
② Strong	**0.60**	2,330	1,120	0.52	31.45	2.96	3.90	1.32	-0.21	28.8	19	0.91	11,300
② Strong	**1.10**	3,040	1,240	0.49	36.53	3.86	5.17	1.34	0.09	30.5	18	0.81	9,700
② Strong	**1.80**	4,070	1,390	0.46	51.13	5.20	7.03	1.35	0.35	32.6	17	0.71	6,900
③ Optimal 1	**0.24**	1,030	420	0.55	11.39	1.32	1.91	1.45	0.12	27.3	21	1.01	31,100
③ Optimal 1	**0.60**	1,600	580	0.51	16.74	2.03	2.90	1.43	0.31	29.3	19	0.88	21,200
③ Optimal 1	0.90	2,040	690	0.49	22.47	2.60	3.70	1.42	0.40	30.5	18	0.81	15,700
③ Optimal 1	**1.10**	2,340	760	0.48	24.81	2.98	4.24	1.42	0.46	31.2	18	0.78	14,300
③ Optimal 1	**1.80**	3,290	1,000	0.46	35.94	4.19	5.91	1.41	0.45	32.6	17	0.71	9,900
④ Optimal 2	**0.24**	700	300	0.58	7.87	0.89	1.33	1.49	0.09	25.8	22	1.12	45,200
④ Optimal 2	**0.60**	1,360	490	0.52	13.90	1.72	2.49	1.45	0.31	28.7	20	0.91	25,600
④ Optimal 2	0.95	1,910	640	0.49	18.68	2.42	3.48	1.44	0.46	30.3	18	0.82	19,100
④ Optimal 2	**1.10**	2,140	700	0.49	22.47	2.71	3.88	1.43	0.44	30.7	18	0.80	15,800
④ Optimal 2	**1.80**	3,090	960	0.46	30.31	3.92	5.56	1.42	0.55	32.3	17	0.72	11,700
⑤ Weak, late	**0.24**	440	190	0.61	4.60	0.55	0.87	1.59	0.24	24.6	23	0.41	78,100
⑤ Weak, late	**0.60**	1,190	410	0.52	12.04	1.48	2.21	1.49	0.45	28.5	20	0.31	29,800
⑤ Weak, late	**1.10**	1,950	630	0.49	20.61	2.44	3.53	1.44	0.51	30.4	18	0.27	17,400
⑤ Weak, late	**1.80**	2,900	910	0.47	30.44	3.64	5.16	1.42	0.52	31.7	18	0.25	11,800
⑥ Weak, very late	**0.60**	480	70	0.24	4.10	0.60	1.24	2.06	0.0	62.3	9	0.19	87,000
⑥ Weak, very late	**1.10**	600	90	0.22	6.33	0.76	1.54	2.03	0.0	68.8	8	0.16	56,300
⑥ Weak, very late	**1.80**	1,440	520	0.52	17.27	1.82	2.62	1.43	0.35	29	19	0.89	20,600
⑥ Weak, very late	2.10	1,930	680	0.50	21.87	2.48	3.51	1.41	0.29	30.2	19	0.83	16,000
⑥ Weak, very late	2.50	2,500	830	0.48	30.23	3.22	4.51	1.40	0.37	31.3	18	0.77	11,600

Table 3: Experimental parameters for all the profiles in the present study. The measurement stations x that are common to all the trip configurations are highlighted in bold. The hot-wire length is denoted by L, Δt is the time between samples and T is the total sampling time.

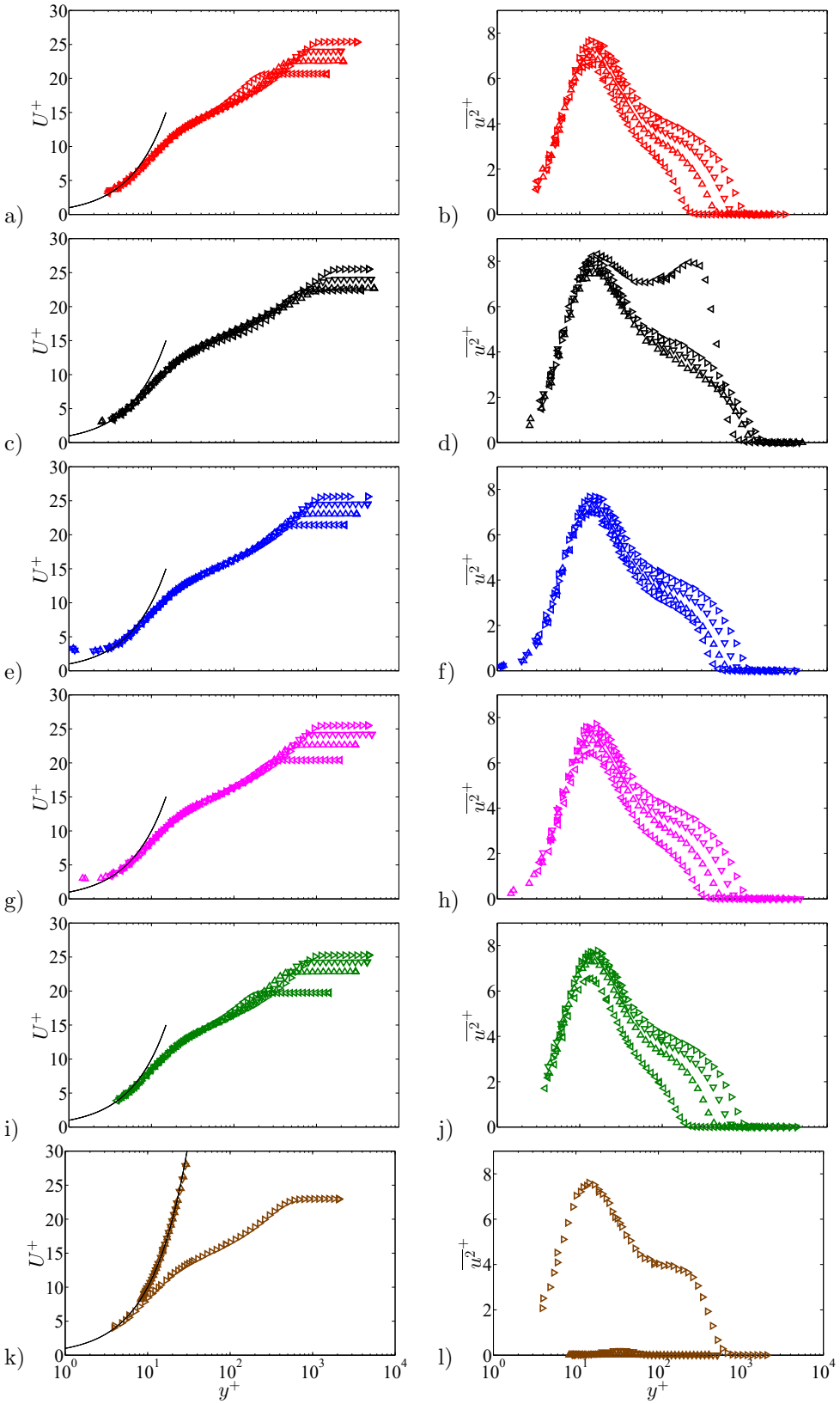

Figure 3: Evolution of inner-scaled mean streamwise velocity (left panels) and variance (right panels) profiles at ($\triangleleft$) $x = 0.24$ m, ($\triangle$) $x = 0.6$ m, ($\triangledown$) $x = 1.1$ m and ($\triangleright$) $x = 1.8$ m. Colors correspond to the various tripping configurations described in Table 1, while the solid lines depicts the linear profile $U^+ = y^+$.

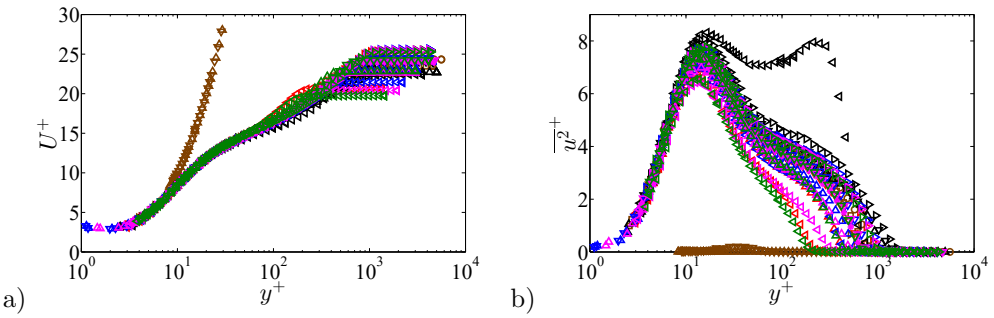

Figure 4: Inner-scaled a) mean streamwise velocity and b) variance profiles. Colors and symbols as in Figure 3, and additional measurement stations are represented by: (×) $x = 0.9$ m, (∗) $x = 0.95$ m, (□) $x = 2.1$ m and (○) $x = 2.5$ m.

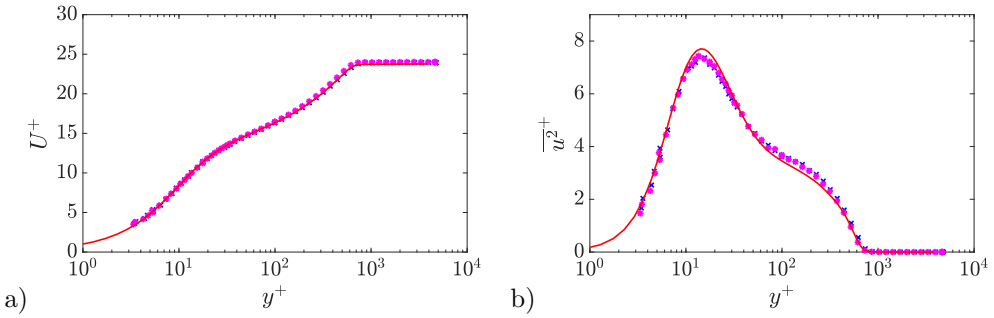

Figure 5: Inner-scaled a) mean streamwise velocity and b) variance profiles corresponding to the two optimal cases, *i.e.*, cases ③ and ④, at $Re_\theta \simeq 2,000$. Colors and symbols as in Figure 4, with the addition of the solid red line which represents the DNS results by Schlatter & Örlü (2010).

TBLs perturbed by a cylindrical roughness element. The outer peak in the fluctuations profiles progressively diminishes downstream of this location, as also observed by Tang *et al.* (2016), even if there is no complete convergence towards the optimal tripping profiles within the development lengths considered in the present study. These, effects, together with the ones observed in the mean flow, can be further examined in Figure 4, where all the mean and variance profiles for all stations shown in Table 3, including the ones not shown in Figure 3, are presented. Moreover, the two optimal cases, *i.e.*, cases ③ and ④, are compared at a matched Reynolds number of $Re_\theta \simeq 2,000$ with the DNS ZPG TBL data by Schlatter & Örlü (2010) in Figure 5. Note that the experimental profiles are obtained at slightly different streamwise locations, *i.e.*, at $x \simeq 0.90$ m in case ③ and at $x \simeq 0.95$ m in case ④, in order to obtain the matched value of Re_θ. This figure shows that both cases with optimal tripping are in excellent agreement with the numerical data, a conclusion that is observed both in the mean velocity and in the streamwise velocity fluctuation profiles. The results shown in Figure 5 are in agreement with the conclusions reported by Schlatter & Örlü (2012), in particular regarding the minimum value of $Re_\theta \simeq 2,000$ necessary to converge towards canonical ZPG TBL conditions.

3.2. *Comparison of TBLs at matched Reynolds number*

In order to emphasize the differences induced by the various tripping configurations under consideration, a comparison between cases at matched local momentum-thickness Reynolds numbers is shown. Figure 6 shows nominally matched $Re_\theta \approx 1,850$ cases of ①, ②, ④ and ⑥.

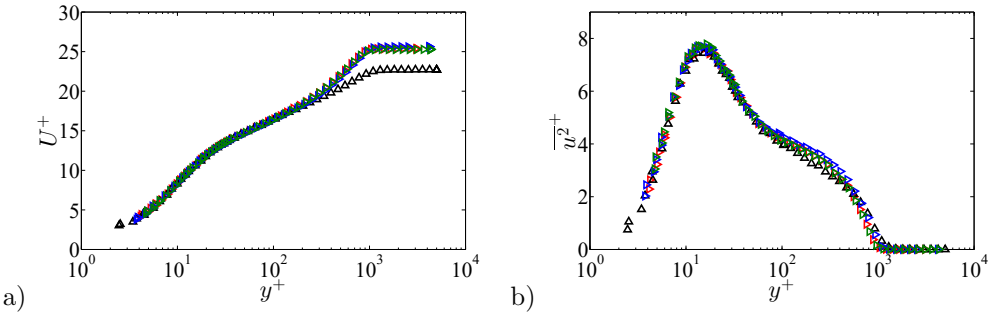

Figure 6: Inner-scaled a) mean streamwise velocity and b) velocity fluctuation profiles at matched $Re_\theta \approx 1,850$ for cases ①, ②, ④ and ⑥. Colors and symbols as in Figure 3, and streamwise locations reported in Table 1.

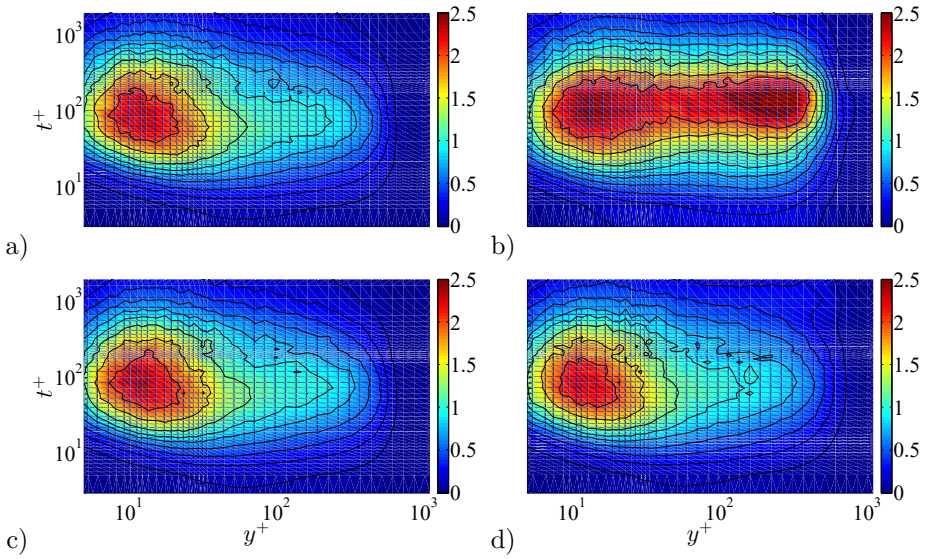

Figure 7: Inner-scaled streamwise premultiplied power spectral density of the streamwise velocity $f^+\Phi^+_{uu}$, at matched $Re_\theta \approx 1,850$. The following cases are shown: a) trip ① at $x = 1.1$ m, b) trip ② at $x = 0.24$ m, c) trip ④ at $x = 0.95$ m and d) trip ⑥ at $x = 2.1$ m. Contour levels are also highlighted at $f^+\Phi^+_{uu}$= 0.1, 0.25, 0.4, 0.575, 0.775, 0.95, 1.2, 1.6, 2 by black lines.

For the mean streamwise velocity and variance, the profiles of cases ①, ④ and ⑥ are nearly identical. In the strong trip case ②, the profile exhibits a reduced wake region which shows that the influence of the initial condition, in form of a strong over-tripping, is still present. Regarding the pre-multiplied spectra of the streamwise velocity $f^+\Phi^+_{uu}$, which is shown in Figure 7, good agreement between all the cases, except ②, can be observed in the near-wall region where the inner peak is located at $y^+ \simeq 15$ and at a streamwise wavelength of $\lambda^+_x \simeq 1,000$ (when the period t^+ is converted into a wavelength through the local mean velocity as convection velocity). In the strong trip case ② the large-scale motions are clearly energized by the bar; since a strong outer peak is present in the spectra. Similar results of agreement between cases ①, ④ and ⑥ are observed also for $Re_\theta > 3,000$. While the mean and variance profile for case ② for $Re_\theta > 3,000$ is

nearly indistinguishable from the other cases, differences remain in the spectral energy distribution in the outer layer when compared to the other tripping cases.

4. Establishing criteria for identifying "well-behaved" profiles

In this section a study on the canonical behaviour of the profiles and their identification is presented. In §4.1 the criteria suggested by previous studies (Chauhan *et al.* 2009; Schlatter & Örlü 2012) are described, upon which a new method to identify well-behaved TBLs based on the diagnostic plot (Alfredsson *et al.* 2011) is proposed in §4.2, and is then finally applied in §4.3 to already existing DNS datasets combined with the criteria outlined in §4.1 to identify, with minimal ambiguity, which profiles can be considered as canonical, and to validate the method.

4.1. *Existing criteria*

In order to discern which profiles can be considered as canonical, the evolution of the shape factor H, the skin-friction coefficient C_f, and the wake parameter Π, are considered as references. According to Chauhan *et al.* (2009), the wake parameter and the shape factor can be used as diagnostic quantities to assess whether a particular TBL can be considered to be canonical, since they have a high sensitivity to different boundary and inflow conditions. These quantities provide, in particular, an estimation of the degree of distortion in the outer part of the TBL, and require a long recovery distance to become independent of upstream disturbances (see also Schlatter & Örlü 2012). In this study, the reference curve chosen to characterise the shape factor is the one proposed by Monkewitz *et al.* (2007), which is obtained from asymptotic arguments, based on a vast number of experimental profiles covering a wide range of Reynolds numbers: $450 < Re_\theta < 125,000$. The equation proposed by Monkewitz *et al.* (2007) relates to H and Re_θ as follows:

$$H = 1 + \frac{\kappa I_{WW}}{\ln(Re_\theta)} + \frac{\kappa^2 I_{WW}(I_{WW} - C)}{\ln^2(Re_\theta)} + \frac{\kappa^2 I_{WW}\left(\kappa I_{WW}^2 - I_{WW} - 2\kappa I_{WW} C + \kappa C^2\right)}{\ln^3(Re_\theta)}, \quad (2)$$

with $\kappa = 0.384$, $I_{WW} = 7.11$ and $C = 3.3$. Regarding the evolution of the skin-friction coefficient C_f, the following Coles–Fernholz relation is considered:

$$C_f = 2\left[\frac{1}{\kappa}\ln(Re_\theta) + C'\right]^{-2}, \quad (3)$$

where the value of the von Kármán coefficient κ is also 0.384 and the constant C' takes the value 4.127. This choice of constants is due to Nagib *et al.* (2007), who established them based on a comprehensive analysis of experimental databases. Finally, the baseline streamwise-evolution of the wake parameter Π is obtained following the methodology proposed by Chauhan *et al.* (2009), based on the integration of the composite profile.

4.2. *Diagnostic-plot criterion*

The previous criteria rely on the computation of integral quantities, which often requires previous knowledge of other variables such as an accurate determination of the absolute wall position y and the friction velocity u_τ. These parameters are typically highly sensitive to experimental errors (Örlü *et al.* 2010). Moreover, the Reynolds-number evolution of other reference quantities such as H or Π can be defined in terms of several empirical curves. Furthermore, the application of the criteria described in §4.1 requires also an extensive experimental campaign (in terms of skin-friction and detailed mean velocity profile measurements), as well as intensive data processing, to identify whether and from which streamwise location on the TBL can be considered as well-behaved. For these reasons, here we propose an alternative method based on the so-called diagnostic-plot scaling introduced by Alfredsson *et al.* (2011). In this scaling, the root mean square of the streamwise velocity fluctuation u' is plotted against the mean velocity U, both normalised by the free-stream velocity U_∞. This plot has been shown to scale canonical ZPG TBL data over a wide range of Re

Case	Re_θ range	Color code
Schlatter & Örlü (2010)	600 – 4,300	Red
Eitel-Amor *et al.* (2014)	1,200 – 8,300	Brown
Jiménez *et al.* (2010)	1,100 – 2,000	Black
Sillero *et al.* (2013)	4,000 – 6,500	Blue
Wu *et al.* (2014)	650 – 3,100	Magenta
Khujadze & Oberlack (2004)	400 – 2,600	Green

Table 4: Summary of numerical databases under consideration in the present study, together with Re_θ ranges and color code.

throughout the logarithmic and outer region of ZPG TBLs (Alfredsson *et al.* 2012; Örlü *et al.* 2016). The diagnostic-plot was also found to scale pressure-gradient turbulent boundary layers (Drózdz *et al.* 2015) and thereby provide a robust method to determine the boundary layer thickness and the edge velocity in these flows (Vinuesa *et al.* 2016), as well as scale rough-wall boundary layers (Castro *et al.* 2013) as well as a variety of wall-bounded and free-shear flows (Castro 2015). One of the greatest advantages of this scaling is the fact that according to Alfredsson *et al.* (2011), the data of canonical ZPG TBL collapse in the outer region, especially in the range $0.7 \leq U/U_\infty \leq 0.9$ (the lower limit further decreases with increasing Re, see Örlü *et al.* 2016), following a linear relation,

$$\frac{u'}{U} = \alpha - \beta \frac{U}{U_\infty}, \tag{4}$$

where α and β are fitting parameters. This means that the profiles that follow equation (4) in the outer region give "a good indication whether the boundary layer is in a natural state" (Alfredsson & Örlü 2010); although this was suggested in the first work on the diagnostic plot, it has not been systematically investigated with the focus on tripping and inflow effects as in the present work. The effect of Re_θ in the value of the parameters α and β is analysed in the following and is used to assess whether a boundary layer is considered well-behaved or not. Note that the only data required to use this method are U and u' in the outer region, and U_∞. These measurements can be obtained easily at numerous stations from a simple hot-wire scan, without the need of any additional measurement such as y, u_τ, etc. Furthermore, measurements of turbulence quantities in the outer region are generally not subjective to spatial or temporal resolution issues. Therefore, this approach could be suitable to assess the development of turbulent boundary layers in a robust and efficient manner.

4.3. *Validation of the diagnostic plot method with numerical data*

In order to evaluate the ability of the method described in §4.2 to assess the convergence towards a canonical state of TBLs, here the method is applied to a number of ZPG TBL DNS datasets, namely the ones by Schlatter & Örlü (2010), Jiménez *et al.* (2010), Sillero *et al.* (2013), Wu *et al.* (2014) and Khujadze & Oberlack (2004), and to the well-resolved large-eddy simulation (LES) database by Eitel-Amor *et al.* (2014). Note that the particular Re_θ ranges of the various databases can be found in Table 4. The values of the free-stream velocity U_∞, the 99% boundary-layer thickness δ_{99} as well as other boundary-layer parameters have been recomputed following the procedure as outlined for the tripping experiments. In Figure 8 the numerical data are plotted in the diagnostic-plot form: subplot a) reports the profiles at all stations, while subplot b) reports only the profiles which fit to the diagnostic-plot outer scaling. In order to identify which profiles follow the diagnostic plot, only the profiles complying with both the H and C_f criteria to within $\pm 2\%$ and 3% tolerance, respectively, have been considered, and fitting curves for α and β as function of Re_θ have been computed with the remaining data points. Then only the profiles

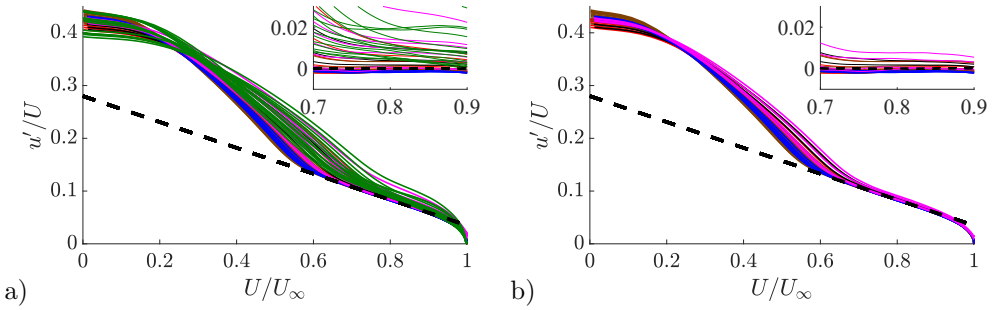

Figure 8: Diagnostic plot for a) all the numerical datasets and b) the numerical datasets that are considered well-behaved. Colors correspond to the cases summarized in Table 4. Dashed line represents equation (4) with $\alpha = 0.280$ and $\beta = 0.245$. Insets depict the difference between the data and equation (4) with the aforementioned constants.

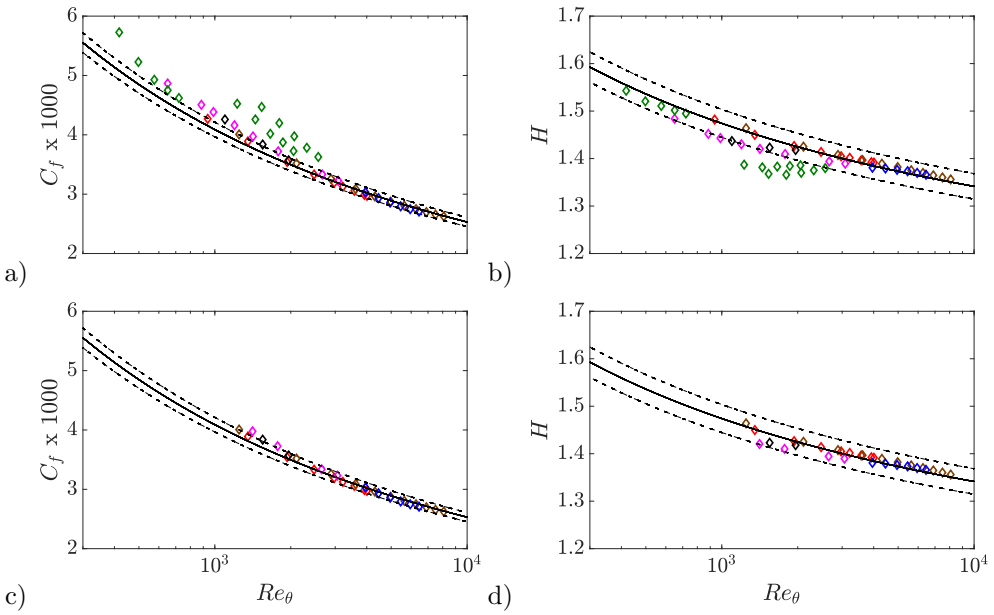

Figure 9: Skin-friction coefficient evolution with Re_θ for a) all the numerical datasets and c) the numerical profiles that follow the diagnostic-plot scaling given by equation (4), where the solid line is the reference given by equation (3) and ±3% deviation is represented by the dashed lines. Reynolds-number evolution of the shape factor H is given for b) all the numerical cases and d) the numerical profiles that follow (4), where the solid line shows the reference trend given by equation (2) and the dashed lines show ±2% deviation. Colors correspond to the cases summarized in Table 4.

with α, β and β/α complying with the fitting relations to within ±5%, ±5%, and ±2% tolerance, respectively, have been considered to properly fit the diagnostic plot (cf. §4.4). On the other hand, the H and C_f evolutions corresponding to all the numerical datasets are shown in Figure 9, together with the reference curves given by equations (2) and (3), respectively, as described in §4.1. It is interesting to note that the profiles that satisfy the diagnostic-plot criterion, *i.e.*, the

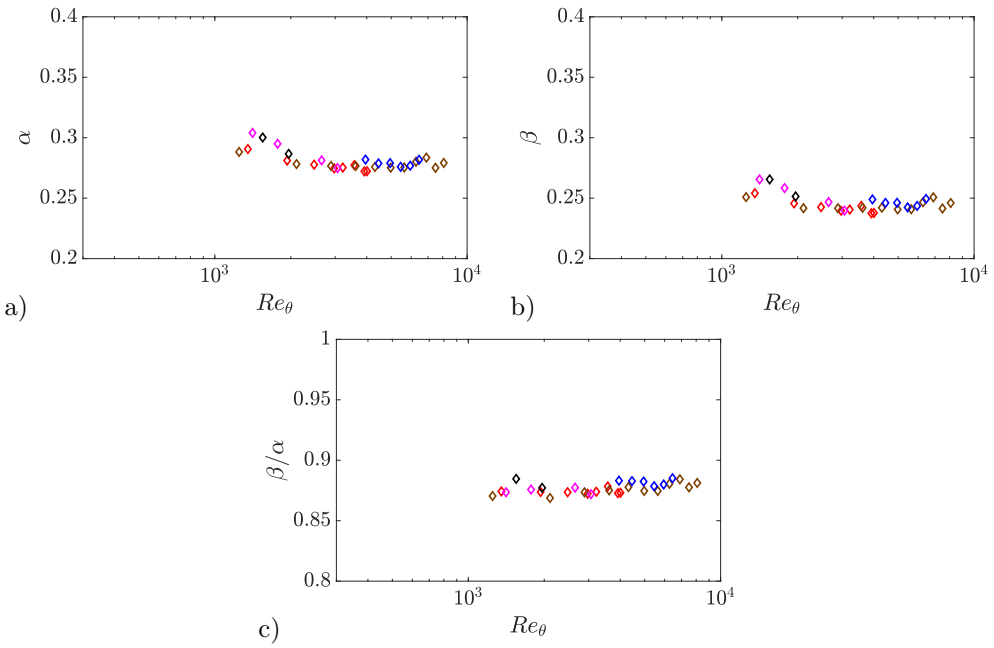

Figure 10: Evolution of the diagnostic-fit coefficients a) α and b) β, as well as the ratio c) β/α, with Re_θ. These coefficients are obtained from fits to equation (4), from the numerical databases described in Table 4, where the color code is also given.

ones shown in Figure 8b), are identical to the ones that follow the reference H and C_f curves within $\pm 2\%$ and 3% tolerances, respectively, as shown in Figure 9. In accordance with previous studies (Schlatter & Örlü 2010, 2012), the diagnostic plot indicates, that all of the profiles from Khujadze & Oberlack (2004) exhibit non-canonical behaviour. The general agreement between the results from the inspection of the diagnostic plot and the criteria by Chauhan *et al.* (2009) is an argument in favour for the diagnostic-plot criterion described in §4.2 as a robust tool to assess whether a particular boundary layer exhibits canonical ZPG TBL conditions. In fact, the diagnostic plot can be used not only to discern well-behaved profiles, but also to recognize if a profile is fully-developed. From the insets of Figure 8, it can be observed that with increasing Re_θ the profiles tend to collapse. This fact can be better understood when the coefficients α and β of equation (4) are plotted as a function of Re_θ, as done in Figure 10. Note that these coefficients, obtained through fitting each individual profile to equation (4), exhibit an asymptotic behavior with Re, *i.e.*, α and β converge towards values around 0.280 and 0.245, respectively, for $Re_\theta > 2,000$. This observation is in accordance with the results by Schlatter & Örlü (2012), who established $Re_\theta \simeq 2,000$ as a threshold beyond which canonical features are exhibited by the ZPG TBL profiles, for cases in which transition was initiated at $Re_\theta < 300$. Moreover, Sillero *et al.* (2013) also claimed that the profiles with $Re_\theta < 2,000$ could not be considered fully developed. Interestingly, Figure 10 also shows that the ratio β/α shows an approximately constant value of around 0.876 for $Re_\theta > 1000$, which is the ratio of the asymptotic values of the two coefficients; note that values are rounded to two decimal places.

4.4. *Determination of the canonical boundary layer from experimental data*

After showing the ability of the diagnostic-plot method described in §4.2 to discern which numerical profiles exhibited canonical ZPG TBL conditions, we apply the same methodology to the experimental measurements to assess whether its results are in agreement with the other

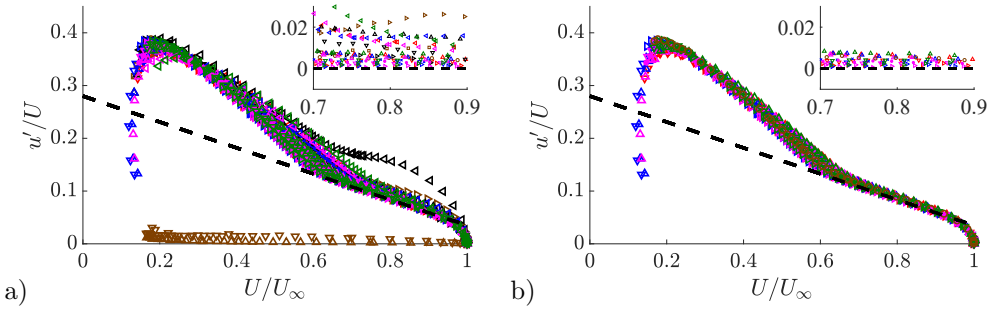

Figure 11: Diagnostic plot for a) all the experimental profiles and b) the experimental profiles that follow the diagnostic-plot scaling given by equation (4). Colors correspond to the cases summarized in Table 1. Dashed line represents equation (4) with $\alpha = 0.280$ and $\beta = 0.245$. Insets depict the difference between the data and equation (4) with the aforementioned constants.

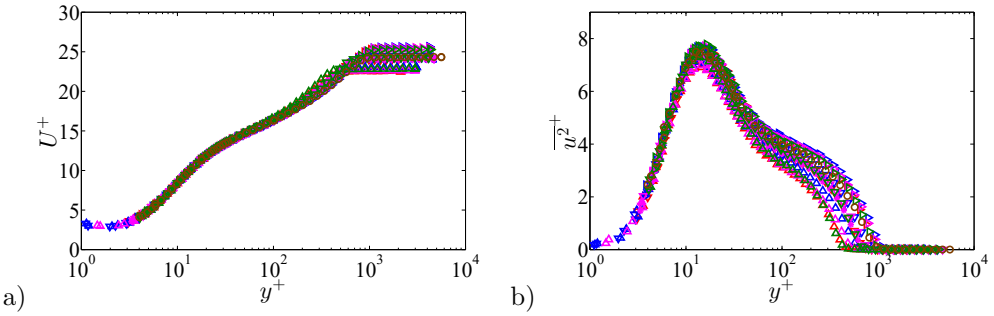

Figure 12: Inner-scaled a) mean streamwise velocity and b) variance profiles. Same data as in Figure 4, with the difference that profiles not passing the diagnostic-plot criteria are omitted.

criteria described in §4.1. In Figure 11 all the experimental profiles summarized in Table 1 are presented in the diagnostic-plot form: subplot a) reports all cases, while subplot b) only reports the cases that follow the diagnostic scaling. Plotting now the profiles that remain in Figure 11b) in classical inner-scaling for the mean and variance, Figure 4 reduces to Figure 12, which exhibits the expected clear Reynolds-number trends in the wake profile for the mean velocity profile as well as the increase of the near-wall peak in the variance profile and the monotonic increase of the turbulence level in the outer layer.

Figure 13 depicts the Reynolds-number evolution of both C_f and H, and it is interesting to observe that, as in the numerical databases, the experimental profiles that follow the diagnostic-plot scaling are the ones consistent with the reference curves for both skin-friction coefficient and shape factor, as described in §4.1. All profiles which do not follow the diagnostic-plot criterion either fail according to the C_f or the H based criteria. For example, it can be observed that the cases which fulfil the H criterion (such as the lowest Re profile from the strong over-tripping case ②) but not the C_f criterion are clearly discarded by the diagnostic-plot approach. Therefore, the proposed methodology can also be used in experimental databases to assess the degree of convergence towards canonical conditions of a particular TBL configuration. Further support for this statement is given in Figure 14, where the coefficients from the diagnostic-plot equation (4) are calculated and shown as a function of Re_θ. Also in this case the profiles with $Re_\theta > 2,000$ exhibit coefficients which asymptote to $\alpha \simeq 0.280$ and $\beta \simeq 0.245$. Interestingly, also in the experimental

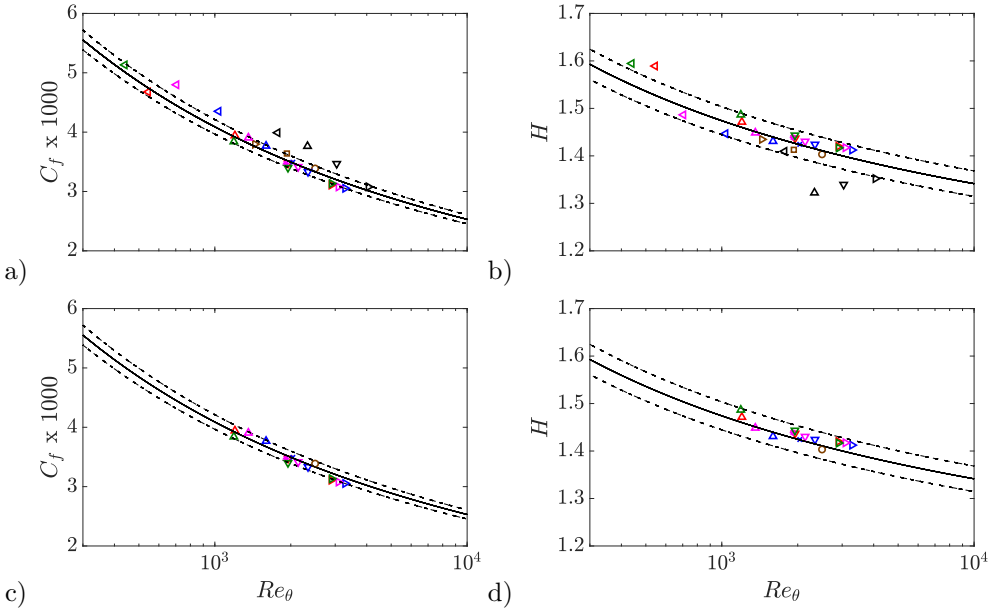

Figure 13: Skin-friction coefficient evolution with Re_θ for a) all the experimental profiles and c) the experimental profiles that follow the diagnostic-plot scaling given by equation (4), where the solid line is the reference given by equation (3) and ±3% tolerances are represented by the dashed lines. Reynolds-number evolution of the shape factor H is given for b) all the experimental cases and d) the experimental profiles that follow (4), where the solid line shows the reference trend given by equation (2) and the dashed lines show ±2% deviation. Colors correspond to the cases summarized in Table 3.

profiles the ratio β/α exhibits an approximately constant value of around 0.876 throughout the whole Reynolds-number range, as in the numerical databases shown in §4.3.

The evolution of the α and β coefficients is extended to higher Reynolds numbers by including in the analysis the experimental datasets by Bailey *et al.* (2013), Örlü & Schlatter (2013) and Vincenti *et al.* (2013) (except its highest Re data due to scatter and limited number of data points in the region in which α and β is determined). Note that in the extended database the maximum Re_θ is around 40,000. Following the same approach as in Figure 14, the diagnostic-plot coefficients are calculated for all the datasets from Tables 3 and 4, and for the three additional high-Re experimental datasets. In Figure 15 the Reynolds-number evolution of the coefficients α and β, together with the one of the ratio β/α, are shown for all the cases under consideration. The left panels show the cases where the particular profile follows the diagnostic-plot scaling, and the right panels the cases where the profiles do not follow it. It is interesting to note that all the high-Re datasets exhibit asymptotic values of α, β and β/α, which are consistent with the conclusions drawn from the previous, lower-Re datasets. Excluding the profiles on the right panels, which do not follow the diagnostic scaling, it is possible to establish the following empirical fits defining the Re_θ evolutions of α and β:

$$\alpha = 0.280 + 20/Re_\theta, \tag{5}$$

$$\beta = 0.245 + 17.5/Re_\theta. \tag{6}$$

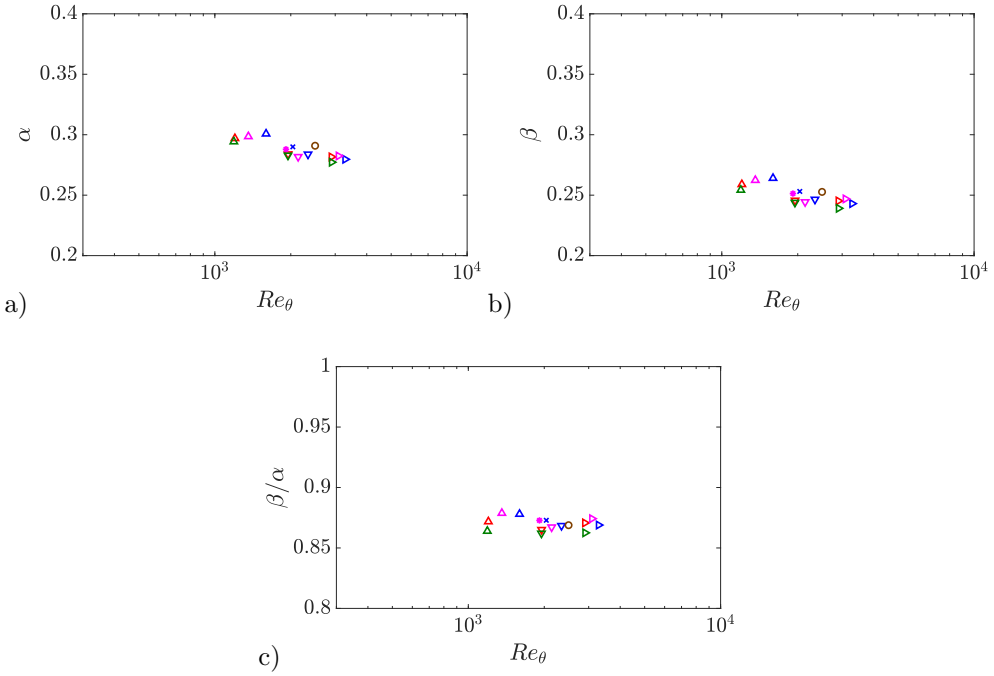

Figure 14: Evolution of the diagnostic-plot coefficients a) α and b) β, as well as c) the ratio β/α, with Re_θ. These coefficients are obtained from fits to equation (4), from the experimental databases described in Table 3, where the color code is also given.

These curves are also shown in Figure 15, where it can be observed that all the profiles in subplots a) and c) follow these trends within $\pm 5\%$. Moreover, Figure 15e) shows that the ratio β/α is approximately constant and equal to $\simeq 0.876$ for the whole Re-range in all the profiles following the diagnostic scaling. All the profiles in this subplot exhibit deviations in β/α within $\pm 2\%$ with respect to 0.876, which is an interesting conclusion regarding the applicability of the diagnostic-plot method for assessment of well-behaved profiles at low Re. With respect to the profiles shown in the right panels of Figure 15, it is clear that α and β do not follow the relations given by equations (5) and (6), and the ratio β/α deviates from 0.876. Interestingly, the cases that do not satisfy the diagnostic-plot scaling are not consistent with the C_f and H equations (3) and (2) presented above either, which shows additional support for the use of the methodology based on the diagnostic-plot method, and additionally highlights the consistency of the various approaches to characterize the TBL development. In fact, there are few cases in Figure 15 (right) in which the trend of a particular coefficient is followed, but only the profiles for which the evolution of the two coefficients is consistent with the empirical fits also satisfy both the skin-friction and shape-factor criteria.

The discussion above shows that the diagnostic-plot criterion, which only requires measurements of the streamwise mean velocity and turbulence intensity is consistent with other methods such as the skin-friction coefficient curve, which requires accurate measurements of the wall-shear stress, or the shape-factor curve for which full velocity profile measurements are required. Note that it may not be straightforward to determine the location of the wall directly and/or accurately in hot-wire measurements, especially at high Reynolds numbers where the viscous length scale becomes progressively smaller (Örlü *et al.* 2010; Vinuesa *et al.* 2016*b*). For this reason, in the present work we propose a methodology based on the diagnostic plot given by equation (4), and the evolution with Re of its parameters. In order to discern if a ZPG TBL is well-behaved, it

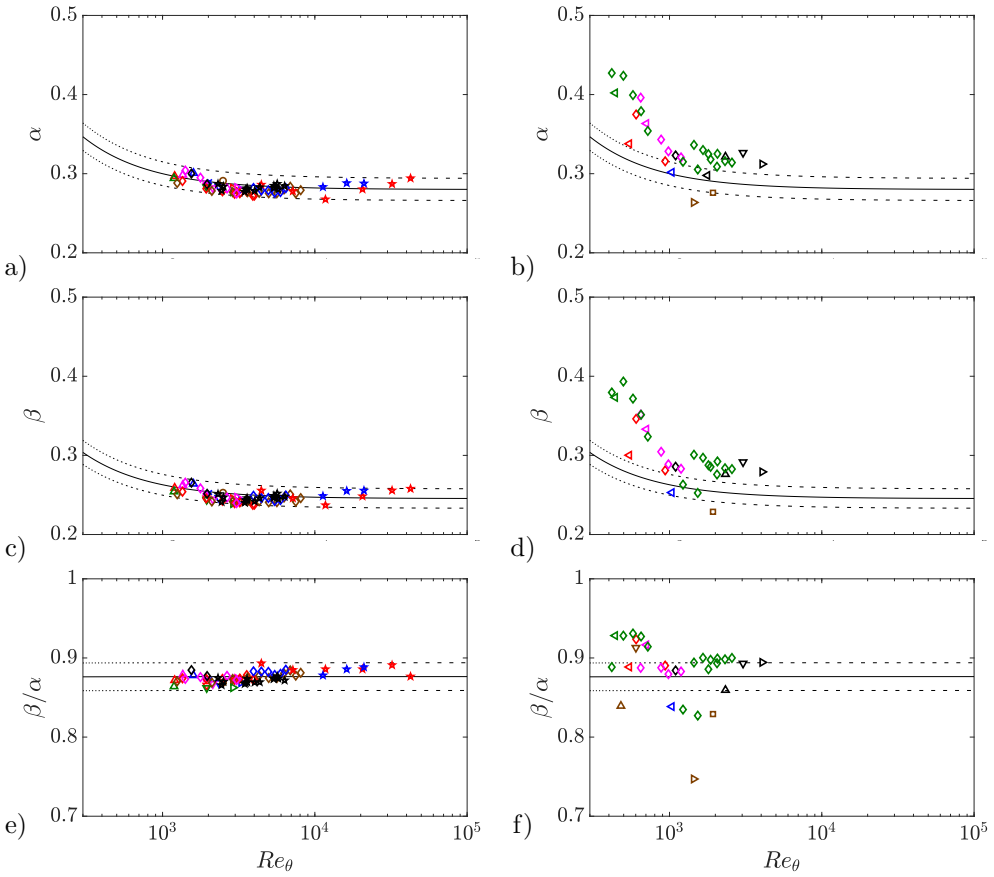

Figure 15: Evolution with Re_θ of diagnostic-plot coefficients a–b) α and c–d) β from equation (4), as well as e–f) their ratio β/α, for all experimental and numerical (indicated by $\diamond$) datasets summarised in Tables 3 and 4, respectively. Additional, high-Re experimental datasets are represented by the following symbols: (blue star) Bailey *et al.* (2013), (black star) Örlü & Schlatter (2013) and (red star) Vincenti *et al.* (2013). Left panels show the profiles that follow the diagnostic-plot scaling (4), whereas the data shown in the right panels do not follow it. Black solid lines represent the empirical fits for α and β given by equations (5) and (6), respectively, as well as the ratio $\beta/\alpha \simeq 0.876$. Dashed lines represent $\pm 5\%$ deviation with respect to equations (5) and (6), and $\pm 2\%$ deviation with respect to $\beta/\alpha \simeq 0.876$.

is only necessary to analyze the mean velocity and turbulence intensity profiles in the range $0.7 < U/U_\infty < 0.9$, where a linear fit can be used to obtain the values of α, β and β/α. These parameters can be compared with equations (5) and (6) for α and β, and with the value 0.876 for the ratio β/α. As shown in Figure 15, if the values of α and β lie within $\pm 5\%$ of the values predicted by equations (5) and (6), and if β/α is within $\pm 2\%$ of 0.876, the ZPG TBL profile can be considered to be well-behaved. Note that since the trends discussed above are valid for $Re_\theta > 1,000$, in cases where Re_θ is unknown the procedure to ensure convergence towards a canonical state is to obtain α, β and β/α at several streamwise locations and study the convergence of these values towards the predicted asymptotic values, *i.e.*, $\alpha \simeq 0.280$ and $\beta \simeq 0.245$. The use of the diagnostic-plot methodology proposed here shows the advantage with respect to the shape-factor method of relying only on the scaling of mean velocity and turbulence intensity in the outer region of the TBL. Moreover, the method proposed by Chauhan *et al.* (2009) based on

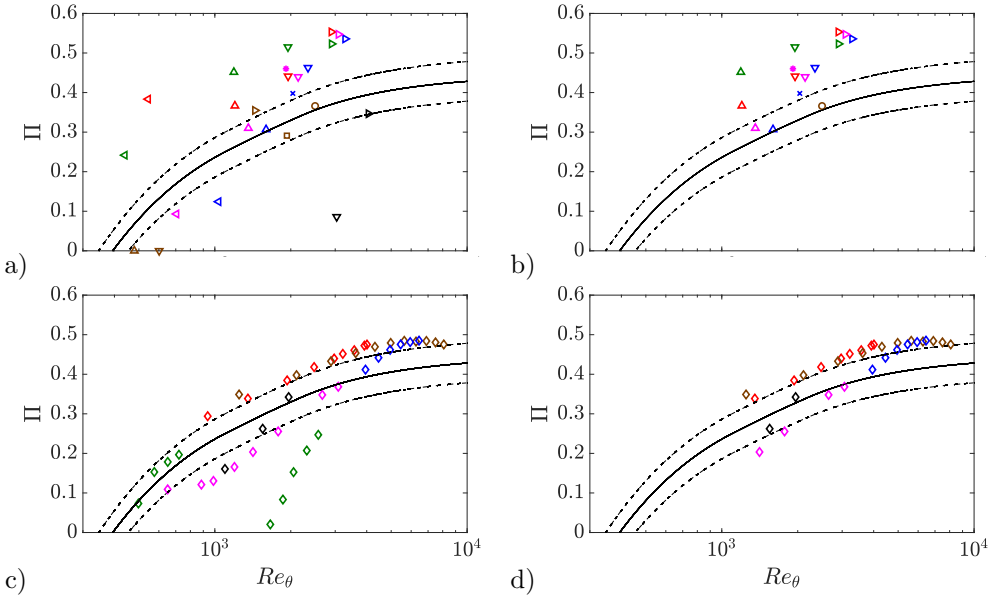

Figure 16: Reynolds-number evolution of the wake parameter Π from a) all the experimental profiles summarized in Table 3, b) the profiles that follow the diagnostic-plot scaling (4), c) all the numerical datasets and d) the numerical datasets that follow the diagnostic-plot scaling given by equation (4). Solid line is obtained through integration of the composite profile as in Chauhan *et al.* (2009), and dashed lines represent ±0.05 deviation.

the wake parameter Π is also tested here, and compared with the outcome of the other methods discussed above. Note that the wake parameter is a very sensitive quantity, which requires accurate measurements of the inner-scaled mean velocity profile (including u_τ and y), relies on composite fits to calculate the value of Π and is directly dependent on the log-law constants/coefficients; an issue of ambiguity on its own for low-Re data sets. In Figure 16a) we show the evolution with Re of the wake parameter calculated from all the experimental profiles; note that the calculation of Π was performed based on the method proposed by Chauhan *et al.* (2009), and the reference Π evolution with Re_θ was determined through integration of the composite profile proposed in the same work. On the other hand, in Figure 16b) we show the Π curve from the profiles that satisfy the diagnostic-plot criterion (which also satisfy the skin-friction and shape-factor criteria as discussed above). As expected, the profiles that do not satisfy the diagnostic-plot method also deviate from the Π curve proposed by Chauhan *et al.* (2009), and do not exhibit any consistent trend with Reynolds number. Furthermore, the profiles that follow the diagnostic-plot method exhibit an increasing trend of Π with Re_θ, similar to the one shown by the curve from Chauhan *et al.* (2009), although they appear consistently shifted upwards by around $\simeq 0.1$. This shows that, although the wake parameter is also a good indicator of the state of the boundary layer, and in particular of its convergence towards canonical ZPG TBL conditions, it is very sensitive to a number of factors and experimental uncertainties, including details of the tripping mechanism and of the fit, and therefore shows more difficulties when used to assess in detail the conditions of the TBL. It should also be noted that the Π values given here (in accordance with Chauhan *et al.* 2009) are obtained with fixed log-law parameters, which explains that very low and even negative values can be obtained; cf. values in table 3. To underline this point, subplots c) and d) depict the same plots for the DNS data discussed in §4.3 which besides removing data points with low

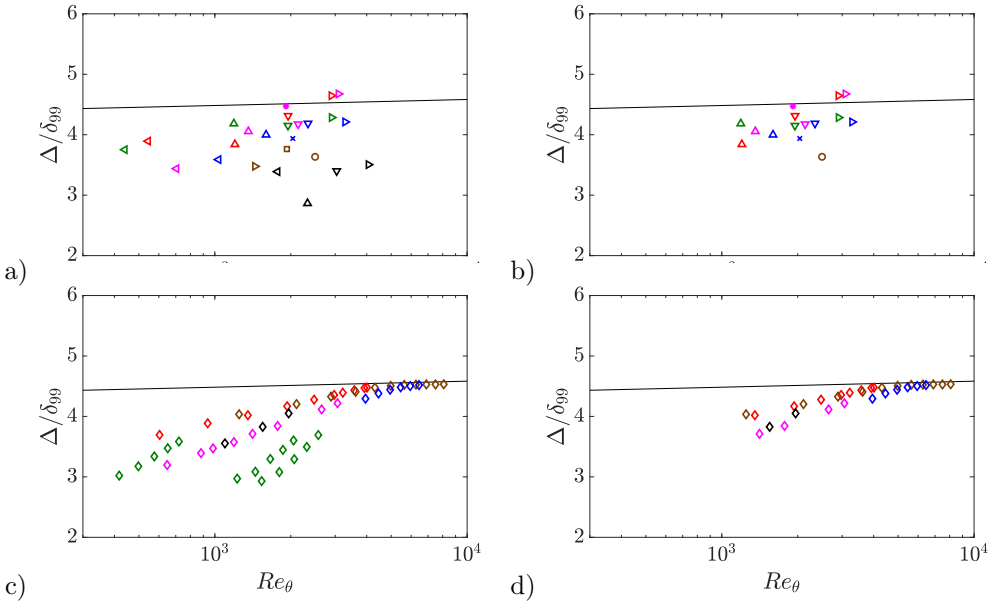

Figure 17: Reynolds-number evolution of Δ/δ_{99} from a) all the experimental profiles summarized in Table 3, b) the experimental profiles that follow the diagnostic-plot scaling (4), c) all the numerical datasets and d) the numerical datasets that follow the diagnostic-plot scaling given by equation (4). Solid line shows the reference trend given by Nagib *et al.* (2007).

Re-effects also indicates that most of the data sets lie actually above, but parallel to, the curve from Chauhan *et al.* (2009) in accordance with the experimental data shown in subplots a) and b).

In addition to the Π criterion, the evolution of the Rotta-Clauser length scale $\Delta = U_\infty \delta^*/u_\tau$ normalized with the boundary-layer thickness defined here as δ_{99} is also studied. According to the work by Nagib *et al.* (2007), the ratio Δ/δ_{99} can also be used to assess the evolution of a TBL towards a well-behaved state independent of the inflow conditions. In Figures 17a) and c) we show the Reynolds-number evolution of Δ/δ_{99} for all the experimental and numerical cases under consideration, where it can be observed that a number of profiles exhibit Δ/δ_{99} values below the trend reported by Nagib *et al.* (2007). This is associated with profiles which have not reached a state independent of the inflow conditions, and therefore subjected to non-equilibrium effects. In Figures 17b) and d) we only show the experimental and numerical profiles that follow the diagnostic-plot scaling given by equation (4). It can be observed that the profiles above $Re_\theta \simeq 2,000$ are in good agreement with the curve developed by Nagib *et al.* (2007), whereas the ones below this Reynolds number follow a similar trend, with slightly lower values. Also note that the higher-*Re* profiles exhibit a value of Δ/δ_{99} approximately equal to 4.5, which is consistent with the observations by Nagib *et al.* (2007). Therefore, the method proposed in the present work based on the diagnostic plot is in reasonably good agreement with the approach to assess well-behaved profiles based on Δ/δ_{99}, proposed by Nagib *et al.* (2007).

4.5. *Diagnostic-plot methodology as a design tool*

The previous sections have shown that the proposed diagnostic-plot methodology is a reliable technique to evaluate the development of ZPG TBLs towards canonical conditions, which only requires measurements of the streamwise mean and turbulence intensity in the outer region of the boundary layer. Since neither the skin-friction coefficient, shape factor or wake parameter, nor full velocity profile measurements are required, the idea to assess the streamwise development with a

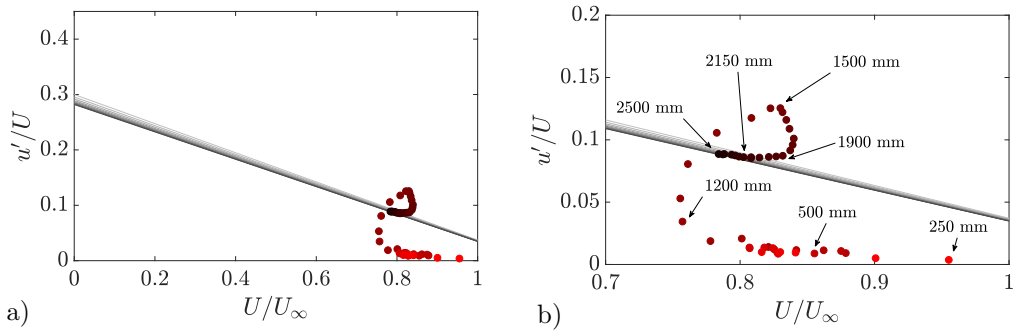

Figure 18: a) Diagnostic-plot methodology as a design tool demonstrated using the ZPG TBL with the tripping configuration ⑥, *i.e.* the weak, very late tripping. Solid lines correspond to equation (5)–(6) with $Re_\theta = 1,000$ (light grey) to 10,000 (dark grey) (10 logarithmically spaced cases). b) Zoom-in of a) with indicated streamwise locations of the measurement points taken with equidistanc streamwise spacings of $\Delta x = 50$ mm.

scan through the outer part of the TBL arose. More specifically, here we demonstrate that by placing a hot-wire probe within the outer part of the boundary layer and traversing it downstream by keeping it within the outer region of the TBL, the streamwise location from where on the TBL can be considered genuine and well-behaved is estimated to be when the measured turbulence intensity falls on relation (4) with the established constants. Figure 18 shows the results from a streamwise traverse while keeping (through an iterative procedure) the probe within the velocity range $0.7 < U/U_\infty < 0.9$ through the outer part of a ZPG TBL corresponding to the tripping configuration ⑥. As apparent from the color-coded measurement points, indicating the streamwise distance from the leading edge (from lighter to darker symbols with increasing streamwise distance), the boundary layer is first laminar and then undergoes transition to turbulence with the associated overshoot in turbulence intensity (in accordance with figures 3k–l) somewhere between the 1.1 m and 1.8 m stations. Since the measurement points are taken with an equidistant streamwise spacing, it is apparent from the accumulation of measurement points that the outer layer requires long development lengths to overcome the post-transitional stage and behave in accordance with the diagnostic scaling. It is interesting to note that the profiles in the post-transitional regime for $x \geq 1.8$ m actually agree very well with the empirical curves for the skin-friction coefficient, shape factor and wake parameter. According to the diagnostic plot, the first point that complies with the diagnostic scaling corresponds to x =1.90 m, which agrees sufficiently well with the results shown in figure 13. Note that albeit the exact location of the range $0.7 < U/U_\infty < 0.9$ is not known a priory, the traverse can still be taken in an automated way by iterating until the measured mean velocity is within the desired percentage of the free-stream velocity.

5. Summary and Conclusions

The impact of tripping devices on the development of zero-pressure-gradient turbulent boundary layers is assessed in the present study by means of hot-wire anemometry measurements. To that end, a total of six tripping configurations, including optimal set-ups and both under and over-tripping cases, are used. A total of 27 velocity profiles are measured over the Reynolds number range $440 < Re_\theta < 4,070$, and their evolutions from the various inflow conditions are compared at matched streamwise locations from the flat-plate leading edge, and also at matched Re_θ conditions. Our results show that the weak tripping cases lead to deviations in the logarithmic region of the inner-scaled mean flow (at around $y^+ \simeq 100$) with respect to the optimum tripping, whereas the over-tripping case leads to a more prominent wake. Regarding the effect in the streamwise variance profile, the weak trip cases also lead to small deviations with respect to the optimum

tripping at around $y^+ \simeq 100$, where the fluctuation levels are lower. The strong tripping case leads to an enhanced inner peak as well as to the development of an outer peak in the variance profile. This effect was also observed in the experiments by Tang *et al.* (2016), and suggests that the strong tripping energizes the large-scale motions in the outer part of the boundary layer, as in adverse-pressure-gradient TBLs (Monty *et al.* 2011; Hosseini *et al.* 2016), and supported by spectral analysis.

Development of TBLs towards canonical conditions have from early days of turbulent-boundary-layer research (Coles 1968) been assessed based on the streamwise evolution of quantities such as the skin-friction coefficient C_f, the shape factor H and the wake parameter Π and this is still the common way in the literature (Chauhan *et al.* 2009; Marusic *et al.* 2015). Extensive analysis of a wide range of experimental databases has led to a number of empirical relations for these evolution of the three parameters, as discussed in §4.1, and convergence towards canonical conditions can be assessed with respect to such reference curves. It is important to note that accurate measurements of the friction velocity u_τ are necessary for an assessment based on C_f, and that an accurate location of the wall y is required to obtain the shape-factor curve. Furthermore, the wake parameter relies on measurements of the inner-scaled mean velocity profile and is a very sensitive parameter that requires the use of composite profiles in order to be calculated. In the present study we assess the possibility of using the diagnostic-plot method (Alfredsson *et al.* 2011). The advantage of this method is that it only relies on measurements of the streamwise mean velocity and turbulence intensity at arbitrary wall-normal distances, and therefore uncertainties from u_τ or y, among others, are eliminated with its use. The measurements conducted as part of this experimental campaign, as well as several numerical databases up to $Re_\theta = 8,300$, show that the diagnostic-plot method proposed here, while extremely simple in its application, provides results equivalent to the C_f and H curves when assessing the convergence of a TBL towards canonical conditions. It is important to note that the current diagnostic-plot approach is based on a limited Re-range, in which a completely developed overlap layer cannot be observed yet. However, the assessment of whether a particular profile can be considered canonical or not is consistent with the C_f and H correlations, obtained over wider Reynolds-number ranges. Moreover, none of these methods would guarantee convergence towards canonical conditions in the limit of infinite Reynolds number. In addition to this, analysis of the α and β coefficients from the diagnostic-plot curve (4) from the canonical profiles shows that they reach approximately constant values of $\alpha \simeq 0.280$ and $\beta \simeq 0.245$ for $Re_\theta > 2,000$. Although additional data at higher Reynolds numbers would be required to assess whether these are the asymptotic values of α and β, they allow to formulate a robust criterion to assess the initial development of the boundary layer. In fact, this is in good agreement with the results by Schlatter & Örlü (2012), who established $Re_\theta \simeq 2,000$ as a threshold beyond which canonical features are exhibited by the ZPG TBL profiles, *i.e.*, below which low Re-effects need to be accounted for. Empirical relations for the evolution of α and β with Re_θ are provided in order to extend the diagnostic-plot criterion also to the low Re_θ range. The ratio β/α is practically independent of Re, once $Re_\theta > 1000$, and approximately equal to 0.876 for well-behaved profiles. Note that although the empirical relations have been additionally verified with high-Re datasets (up to $Re_\theta \simeq 40000$), the conclusions in the present work are based on low-Re data, as well as on streamwise mean and fluctuating velocity profiles.

The diagnostic-plot methodology proposed in the present study is therefore a reliable technique to evaluate the development of ZPG TBLs towards canonical conditions, which only requires measurements of the streamwise mean and turbulence intensity, in the outer region of the boundary layer. This is a great advantage in comparison to methods based on skin-friction coefficient, shape factor or wake parameter, which require more involved measurements of friction velocity, accurate wall position and use of composite profiles. The mentioned features of the diagnostic-plot methodology can be exploited to determine the streamwise location from where on the ZPG TBL is well-behaved, by simply traversing the measurement probe through a portion of the outer region

until the measured turbulence intensity falls on top of the diagnostic scaling. Equivalently, the method is shown to provide a quick diagnostic tool to assess the quality of numerical data as well.

Acknowledgements

CSV acknowledges the financial support from Universidad Carlos III de Madrid within the program "Ayudas para la Movilidad del Programa Propio de Investigación". RÖ, RV and PS acknowledge the financial support from the Swedish Research Council (VR) and the Knut and Alice Wallenberg Foundation. CSV, SD and AI were partially supported by the COTURB project (Coherent Structures in Wall-bounded Turbulence), funded by the European Research Council (ERC), under grant ERC-2014.AdG-669505. AI, CSV and SD have been partially supported by grant DPI2016-79401-R of the Spanish Mineco.

References

Alfredsson, P. H. & Örlü, R. 2010 The diagnostic plot — a litmus test for wall bounded turbulence data. *Eur. J. Mech. B/Fluids* **29**, 403–406.

Alfredsson, P. H., Örlü, R. & Segalini, A. 2012 A new formulation for the streamwise turbulence intensity distribution in wall-bounded turbulent flows. *Eur. J. Mech. B/Fluids* **36**, 167–175.

Alfredsson, P. H., Segalini, A. & Örlü, R. 2011 A new scaling for the streamwise turbulence intensity in wall-bounded turbulent flows and what it tells us about the "outer" peak. *Phys. Fluids* **23**, 041702.

Bailey, S. C. C., Hultmark, M., Monty, J. P., Alfredsson, P. H., Chong, M. S., Duncan, R. D., Fransson, J. H. M., Hutchins, N., Marusic, I., Mckeon, B. J., Nagib, H. M., Örlü, R., Segalini, A., Smits, A. J. & Vinuesa, R. 2013 Obtaining accurate mean velocity measurements in high Reynolds number turbulent boundary layers using pitot tubes. *J. Fluid Mech.* **715**, 642–670.

Castillo, L. & Johansson, T. G. 2002 The effects of the upstream conditions on a low Reynolds number turbulent boundary layer with zero pressure gradient. *J. Turbul.* **3**, 1–19.

Castro, I. A. 2015 Turbulence intensity in wall-bounded and wall-free flows. *J. Fluid Mech.* **770**, 289–304.

Castro, I. A., Segalini, A. & Alfredsson, P. H. 2013 Outer-layer turbulence intensities in smooth- and rough-wall boundary layers. *J. Fluid Mech.* **727**, 119–131.

Chauhan, K. A., Monkewitz, P. A. & Nagib, H. M. 2009 Criteria for assessing experiments in zero pressure gradient boundary layers. *Fluid Dyn. Res.* **41**, 021404.

Coles, D. E. 1956 The law of the wake in the turbulent boundary layer. *J. Fluid Mech.* **1**, 191–226.

Coles, D. E. 1962 The turbulent boundary layer in a compressible fluid. *Rand. Rep. R-403-PR.*

Coles, D. E. 1968 The young person's guide to the data. *AFOSR-IFP-Stanford Conf. on Computation of turbulent boundary layers, D. E. Coles and E. A. Hirst (Eds.), pp. 1–45.*

Drózdz, A., Elsner, W. & Drobniak, S. 2015 Scaling of streamwise Reynolds stress for turbulent boundary layers with pressure gradient. *Eur. J. Mech. B-Fluid* **49**, 137–145.

Eitel-Amor, G., Örlü, R. & Schlatter, P. 2014 Simulation and validation of a spatially evolving turbulent boundary layer up to $Re_\theta = 8300$. *Int. J. Heat Fluid Flow* **47**, 57–69.

Erm, L. P. & Joubert, P. N. 1991 Low-Reynolds-number turbulent boundary layers. *J. Fluid Mech.* **230**, 1–44.

Fernholz, H. H. & Finley, P. J. 1996 The incompressible zero-pressure-gradient turbulent boundary layer: An assessment of the data. *Prog. Aero. Sci.* **32**, 245–311.

Hosseini, S. M., Vinuesa, R., Schlatter, P., Hanifi, A. & Henningson, D. S. 2016 Direct numerical simulation of the flow around a wing section at moderate Reynolds number. *Int. J. Heat Fluid Flow* **61**, 117–128.

Hultmark, M, Bailey, S. C. C. & Smits, A. J. 2010 Scaling of near-wall turbulence in pipe flow. *J. Fluid Mech.* **649**, 103–113.

Hutchins, N. 2012 Caution: tripping hazards. *J. Fluid Mech.* **710**, 1–4.

Hutchins, N., Monty, J. P., Hultmark, M. & Smits, A. J. 2015 A direct measure of the frequency response of hot-wire anemometers: temporal resolution issues in wall-bounded turbulence. *Exp. Fluids* **56**, 18.

Hutchins, N., Nickels, T. B., Marusic, I. & Chong, M. S. 2009 Hot-wire spatial resolution issues in wall-bounded turbulence. *J. Fluid Mech.* **635**, 103–136.

Jiménez, J., Hoyas, S., Simens, M. P. & Mizuno, Y 2010 Turbulent boundary layers and channels at moderate Reynolds numbers. *J. Fluid Mech* **657**, 335–360.

Khujadze, G. & Oberlack, M. 2004 DNS and scaling laws from new symmetry groups of ZPG turbulent boundary layer flow. *Theor. Comput. Fluid Dyn.* **18**, 391–411.

Klebanoff, P. S. & Diehl, W. S. 1954 Some features of artificially thickened fully developed turbulent boundary layers with zero pressure gradient. *NACA Tech. Rep. 1110*.

Kozul, M., Chung, D. & Monty, J. P. 2016 Direct numerical simulation of the incompressible temporally developing turbulent boundary layer. *J. Fluid Mech.* **796**, 437–472.

Lee, J. H., Kwon, Y. S., Monty, J. P. & Hutchins, N. 2014 Time-resolved PIV measurement of a developing zero pressure gradient turbulent boundary layer. *In Proceedings of the 19th Australasian Fluid Mechanics Conference, 8th-11th December 2014 (ed. P. A. Brandner B. W. Pearce). Australasian Fluid Mechanics Society.*

Lindgren, Björn & Johansson, A. V. 2002 Evaluation of the flow quality in the MTL wind-tunnel. *Tech. Rep., Royal Institute of Technology (KTH), Stockholm, Sweden*.

Lund, T., Wu, X. & Squires, K. 1998 Generation of turbulent inflow data for spatially-developing boundary layer simulations. *J. Comput. Phys.* **140**, 233–258.

Marusic, I., Chauhan, K. A., Kulandaivelu, V. & Hutchins, N. 2015 Evolution of zero-pressure-gradient boundary layers from different tripping conditions. *J. Fluid Mech.* **783**, 379–411.

Marusic, I., McKeon, B. J., Monkewitz, P. A., Nagib, H. M., Smits, A. J. & Sreenivasan, K. R. 2010 Wall-bounded turbulent flows at high Reynolds numbers: Recent advances and key issues. *Phys. Fluids* **22**, 065103.

Monkewitz, P. A., Chauhan, K. A. & Nagib, H. M. 2007 Self-consistent high-Reynolds-number asymptotics for zero-pressure-gradient turbulent boundary layers. *Phys. Fluids* **19**, 115101.

Monty, J. P., Harun, Z. & Marusic, I. 2011 A parametric study of adverse pressure gradient turbulent boundary layers. *Int. J. Heat Fluid Flow* **32**, 575–585.

Morrison, Jonathan F, McKeon, B. J., Jiang, W & Smits, A. J. 2004 Scaling of the streamwise velocity component in turbulent pipe flow. *J. Fluid Mech.* **508**, 99–131.

Nagib, H. M., Chauhan, K. A. & Monkewitz, P. A. 2007 Approach to an asymptotic state for zero pressure gradient turbulent boundary layers. *Phil. Trans. R. Soc.* **365**, 755–770.

Nickels, T. B. 2004 Inner scaling for wall-bounded flows subject to large pressure gradients. *J. Fluid Mech.* **521**, 217–239.

Örlü, R., Fransson, J. H. M. & Alfredsson, P. H. 2010 On near wall measurements of wall bounded flows — the necessity of an accurate determination of the wall position. *Prog. Aero. Sci.* **46**, 353–387.

Örlü, R. & Schlatter, P. 2013 Comparison of experiments and simulations for zero pressure gradient turbulent boundary layers at moderate Reynolds numbers. *Exp. Fluids* **54**, 1547.

Örlü, R., Segalini, A., Klewicki, J. & Alfredsson, P. H. 2016 High-order generalisation of the diagnostic scaling for turbulent boundary layers. *J. Turbulence* **17**, 664–677.

Örlü, R. & Vinuesa, R. 2017 Thermal anemomentry. In *Experimental Aerodynamics* (ed. S. Discetti & A. Ianiro). CRC Press. pp. 257–303.

Österlund, J. M. 1999 Experimental studies of zero pressure-gradient turbulent boundary layer flow. *Ph. D. thesis, Royal Institute of Technology, Stockholm, Sweden*.

Rodríguez-López, E., Bruce, P. J. K. & Buxton, O. R. H. 2015 A robust post-processing method to determine skin friction in turbulent boundary layers from the velocity profile. *Exp. Fluids* **56**, 68.

Rodríguez-López, E., Bruce, P. J. K. & Buxton, O. R. H. 2016 On the formation mechanisms of artificially generated high Reynolds number turbulent boundary layers. *Boundary-Layer Meteor.* **160**, 201–224.

Schlatter, P. & Örlü, R. 2010 Assessment of direct numerical simulation data of turbulent boundary layers. *J. Fluid Mech.* **659**, 116–126.

Schlatter, P. & Örlü, R. 2012 Turbulent boundary layers at moderate reynolds numbers: inflow length and tripping effects. *J. Fluid Mech.* **710**, 5–34.

Sillero, J. A., Jiménez, J. & Moser, R. D 2013 One-point statistics for turbulent wall-bounded flows at Reynolds numbers up to $\delta^+ \simeq 2000$. *Phys. Fluids* **25**, 105102.

Simens, M., Jiménez, J., Hoyas, S. & Mizuno, Y. 2009 A high-resolution code for turbulent boundary layers. *J. Comput. Phys.* **228**, 4218–4231.

Tang, Z., Jiang, N., Zheng, X. & Wu, Y. 2016 Bursting process of large- and small-scale structures in turbulent boundary layer perturbed by a cylinder roughness element. *Exp. Fluids* **57**, 79.

Tani, I. 1969 Boundary-layer transition. *Annu. Rev. Fluid Mech.* **1**, 169–196.

Vincenti, P., Klewicki, J., Morrill-Winter, C., White, C. M. & Wosnik, M. 2013 Streamwise velocity statistics in turbulent boundary layers that spatially develop to high Reynolds number. *Exp. Fluids* **54**, 1629.

Vinuesa, R., Bobke, A, Örlü, R. & Schlatter, P. 2016*a* On determining characteristic length scales in pressure-gradient turbulent boundary layers. *Phys. Fluids* **28**, 055101.

Vinuesa, R., Duncan, R. D. & Nagib, H, M. 2016*b* Alternative interpretation of the Superpipe data and motivation for CICLoPE: The effect of a decreasing viscous length scale. *Eur. J. Mech. B/Fluids* **58**, 109–116.

Vinuesa, R. & Örlü, R. 2017 Measurement of wall shear stress. In *Experimental Aerodynamics* (ed. S. Discetti & A. Ianiro). CRC Press. pp. 393–428.

Vinuesa, R., Rozier, P. H., Schlatter, P. & Nagib, H. M. 2014 Experiments and computations of localized pressure gradients with different history effects. *AIAA J.* **52**, 368–384.

Wu, X, Moin, P. & Hickey, J.-P. 2014 Boundary layer bypass transition. *Phys. Fluids* **26**, 091104.

2

Paper 2

Revisiting history effects in adverse-pressure-gradient turbulent boundary layers

Ricardo Vinuesa[1], Ramis Örlü[1], Carlos Sanmiguel Vila[2], Andrea Ianiro[2], Stefano Discetti[2] and Philipp Schlatter[1]

[1] Linné FLOW Centre, KTH Mechanics, S-100 44 Stockholm, Sweden
[2] Aerospace Engineering Group, Universidad Carlos III de Madrid, Leganés, Spain

Flow, Turbulence and Combustion (2017), vol. **99**, 565–587

The goal of this study is to present a first step towards establishing criteria aimed at assessing whether a particular adverse-pressure-gradient (APG) turbulent boundary layer (TBL) can be considered *well-behaved*, *i.e.*, whether it is independent of the inflow conditions and is exempt of numerical or experimental artifacts. To this end, we analyzed several high-quality datasets, including in-house numerical databases of APG TBLs developing over flat-plates and the suction side of a wing section, and five studies available in the literature. Due to the impact of the flow history on the particular state of the boundary layer, we developed three criteria of convergence to well-behaved conditions, to be used depending on the particular case under study. (i) In the first criterion, we develop empirical correlations defining the Re_θ-evolution of the skin-friction coefficient and the shape factor in APG TBLs with constant values of the Clauser pressure-gradient parameter $\beta = 1$ and 2 (note that $\beta = \delta^*/\tau_w \mathrm{d}P_e/\mathrm{d}x$, where δ^* is the displacement thickness, τ_w the wall-shear stress and $\mathrm{d}P_e/\mathrm{d}x$ the streamwise pressure gradient). (ii) In the second one, we propose a predictive method to obtain the skin-friction curve corresponding to an APG TBL subjected to any streamwise evolution of β, based only on data from zero-pressure-gradient TBLs. (iii) The third method relies on the diagnostic-plot concept modified with the shape factor, which scales APG TBLs subjected to a wide range of pressure-gradient conditions. These three criteria allow to ensure the correct flow development of a particular TBL, and thus to separate history and pressure-gradient effects in the analysis.

Key words: Turbulent boundary layer, Pressure gradient, Flow history, Numerical simulation

1. Introduction

Fundamental studies of wall-bounded turbulence require accurate representations of the flow case under consideration. The main three *canonical* flow cases of wall-bounded turbulence, namely the zero-pressure-gradient (ZPG) turbulent boundary layer (TBL), the channel and the pipe, have the advantage of exhibiting simple, well-defined geometries and operating conditions. This allows to isolate the physics of wall-bounded turbulence from other effects present in more complicated configurations, such as for instance the secondary flows in ducted geometries (Marin *et al.* 2016). It is essential to obtain reliable databases, where the flow case under study is independent of the inflow conditions and is exempt of numerical or experimental artifacts. In the context of the present work, we will denote such a flow case as *well-behaved*. Thus, a well-behaved ZPG experiment or simulation would be representative of a canonical ZPG TBL. Possible effects leading to deviations from the well-behaved state have received some attention in the recent years (Hutchins 2012). For instance, Marusic *et al.* (2015) have assessed the impact of tripping devices on the development of TBLs in wind-tunnel experiments and Schlatter & Örlü (2012) have investigated the effect of tripping in numerical simulations of wall-bounded turbulence. As stated by Chauhan *et al.* (2009), among the three canonical cases stated above the ZPG TBL is the most challenging case

to establish experimentally, due to its requirements in terms of tripping, a carefully-controlled pressure-gradient distribution, as well as the impact of local non-equilibrium conditions on the history of the flow. The fact that channels and pipes are fully-developed flows reduces slightly the complexity of the experimental setups, albeit a considerable development length is required (as well as a large aspect ratio in the channel case).

Motivated by the need to characterize well-behaved TBLs, Chauhan *et al.* (2009) developed criteria based on the wake parameter Π (Coles 1956) and on the shape factor $H = \delta^*/\theta$ (where δ^* and θ denote the displacement and momentum thicknesses, respectively). They provided empirical relations describing the canonical ZPG TBL evolution of these parameters with Reynolds number, and established that the boundary layers satisfying such criteria exhibit inner-scaled mean velocity and defect profiles exempt of experimental artifacts. Note that the work by Chauhan *et al.* (2009) expanded the previous studies by Coles (1968) and Fernholz & Finley (1996). Schlatter & Örlü (2010) showed that numerical ZPG TBLs can also be affected by the inflow conditions and the tripping method, and documented differences up to 5% in H among direct numerical simulation (DNS) databases, and interestingly up to 20% in the skin-friction coefficient $C_f = 2\,(u_\tau/U_e)^2$ (note that U_e is the velocity at the boundary-layer edge, and $u_\tau = \sqrt{\tau_w/\rho}$ is the friction velocity; τ_w is the mean wall-shear stress and ρ is the fluid density). These differences, attributed to inflow and tripping conditions, were supported by a follow-up study (Schlatter & Örlü 2012), where it is shown that various ZPG TBLs would converge onto the same state in terms of integral quantities and turbulence statistics for Reynolds numbers based on momentum thickness $Re_\theta > 2,000$ if the tripping is performed at $Re_\theta < 300$. Under these conditions, a particular boundary layer can be considered to be well-behaved, and therefore representative of a canonical ZPG TBL.

Marusic *et al.* (2015) later considered three different tripping configurations in their wind-tunnel experiments. In addition to the standard sand-paper trip, which yields canonical ZPG TBL conditions, they also tested two threaded rods as tripping devices, which produce different levels of over-stimulation in the developing boundary layer. Based on a simplified approach of the work by Perry *et al.* (2002), applied to the particular case of ZPG TBLs, they derived evolution equations to define the well-behaved development of the boundary layer, leading to curves relating C_f, H and Π, among others, with Reynolds number. They also documented the effect of the tripping, in particular the over-stimulation of the boundary layer, on the large-scale motions of the flow. Another relevant work where the effect of various tripping configurations, including cylindrical pins, distributed grit and wires, was considered is the study by Erm & Joubert (1991).

It is also relevant to mention the recent work by Rodríguez-López *et al.* (2016), who also analyzed various tripping conditions, in their case with the aim of achieving well-behaved high-Re TBLs. They used a sawtooth serrated fence, together with a number of arrays of cylinders in the spanwise direction, leading to various configurations with uniform and non-uniform blockage in the wall-normal direction. Their results show that when using tripping devices with uniform wall-normal blockage, it is possible to increase the momentum thickness of the TBL by 150% in comparison with standard tripping conditions, which effectively leads to the same increase in Reynolds number. Moreover, using tripping devices with non-uniform blockage in the wall-normal direction and 100% blockage at the wall leads to TBLs that are not well-behaved, even after very long distances downstream of the trip. They also identified the impact of the different trippings on the characteristics of the near-wall structures and their formation mechanisms, which explains the observed differences in the boundary layers.

As documented by Schlatter & Örlü (2012), numerical databases are also subjected to effects related to the inflow conditions and the tripping mechanism, and it is therefore essential to ensure that the simulated flow is well-behaved. Regarding the impact of the mechanism used to generate the inflow conditions, it is interesting to highlight the difference between the approach by Schlatter & Örlü (2010, 2012), who considered a laminar boundary layer as inflow, and the method adopted by Sillero *et al.* (2013), who generated synthetic inflow conditions based on the recycling method by Lund *et al.* (1998). One of the observations by Sillero *et al.* (2013) was the fact that the

turnover length might be the appropriate way of assessing whether the TBL was independent of the inflow or not when such synthetic conditions were used. Note that the turnover length is defined as the streamwise distance traveled by the eddies during a turnover time δ/u_τ, where δ is the boundary-layer thickness. They also reported that quantities related to the large-scale motions of the flow required much longer distances to become independent of the inflow conditions, a conclusion that is in agreement with other studies such as the one by Schlatter & Örlü (2012). Another interesting numerical study is the work by Kozul *et al.* (2016), who simulated a temporal boundary layer, and drew interesting connections between spatially- and temporally-developing boundary layers, as well as with experimental trip devices.

The aforementioned studies have highlighted the recent efforts with respect to the required development length in ZPG TBLs in order to establish well-behaved conditions. The situation for PG TBLs is even more complicated due to the additional effects of the local pressure gradient and of the pressure-gradient history. The practical relevance of TBLs under PG conditions explains the large interest, in particular when it comes to APG TBLs. Numerical simulations have been used to study the characteristics of PG TBLs, starting from the early work by Spalart & Watmuff (1993), followed by the simulations by Skote *et al.* (1998), and more recently by Lee & Sung (2008) and Gungor *et al.* (2016). The effect of pressure gradient on the coherent structures in TBLs has been studied, among others, by Marquillie *et al.* (2011) (who focused on near-wall streaks) and by Maciel *et al.* (2017) (who analyzed two-point correlations of the streamwise velocity).

Based on wind-tunnel experiments, Sanmiguel Vila *et al.* (2017) pointed out the fact that widely used methods to assess convergence towards well-behaved conditions rely on either accurate wall-shear stress measurements or full velocity profiles with accurate wall-position determination; or even on both. Since obtaining these quantities at a number of streamwise positions to assess such convergence in an experiment may be problematic, they introduced an alternative method based on the diagnostic-plot scaling (Alfredsson *et al.* 2011). The method relies on measurements of the streamwise mean velocity and local turbulence intensity within the outer region of the boundary layer, and does not require an accurate wall-position determination or knowledge of the friction velocity, therefore allowing to perform scans in the streamwise direction in order to assess with more robustness and less tedious procedures the region of convergence. Sanmiguel Vila *et al.* (2017) evaluated their method with various tripping configurations, and also characterized the development length under such different inflow conditions in wind-tunnel experiments of ZPG TBLs. In the present article, we extend their work to adverse-pressure-gradient (APG) TBLs where, as discussed by Bobke *et al.* (2017), the effect of the flow history is crucial, and develop the corresponding criteria to assess whether a particular TBL can be considered well-behaved or not. These criteria are, in particular, important in the case of wind-tunnel experiments, where the lack of accurate measurements everywhere in the domain of interest requires the use of such methods in order to ensure an adequate boundary-layer development.

As discussed below, in the present study we develop a number of criteria based on several in-house numerical databases, together with five high-quality sets of data available in the literature. In particular, we will consider the numerical work by Kitsios *et al.* (2016), Lee (2017) and Spalart & Watmuff (1993), together with the experimental databases by Monty *et al.* (2011) and Nagib *et al.* (2006). The various conditions present in the different databases lead to a variety of pressure-gradient evolutions, ranging from moderate-pressure-gradient cases to the strongly decelerated TBL on the suction side of a wing. The reason to limit the present work to these data sets is that not only the statistics at various streamwise positions (and hence Reynolds numbers) are required, but also their particular pressure-gradient history needs to be at hand. The latter was at our disposal only for some of the selected data sets. These data have allowed us to analyze the convergence to well-behaved conditions in scenarios with moderately complicated flow histories, and although some criteria are based on relatively low Reynolds-number ranges, the experimental measurements by Monty *et al.* (2011) up to $Re_\theta = 18,700$ and by Nagib *et al.* (2006) up to

$Re_\theta = 56,100$ were used to establish the higher-Re behavior in one of the criteria discussed below.

It is important to stress that, unlike the ZPG TBL case, which is uniquely defined by the Reynolds number with a constant value of $\beta = 0$ (defined below), there are infinitely many possible realizations of well-behaved PG TBLs defined by their particular $\beta(x)$ history and Reynolds number. In the present study we use a total of 11 databases of PG TBLs, which include cases with constant β, and relatively simple $\beta(x)$ evolutions, including both increasing and decreasing β trends. Therefore, the criteria proposed in the present work are aimed at assessing whether a particular PG TBL is well-behaved or not, although their applicability is limited to the relatively simple $\beta(x)$ configurations under study.

The article is structured as follows: in §2 we introduce the various in-house numerical databases under study in the present work and discuss their flow histories; we also introduce the five datasets from the literature analyzed in the following. In §3 we present convergence criteria based on empirical correlations for cases of constant and non-constant pressure-gradient magnitudes. In §4 we also present criteria for constant and non-constant pressure-gradient magnitudes, but in this case based on the diagnostic-plot scaling. Finally, in §5, we summarize the conclusions of the present work.

2. Description of the databases analyzed in the present study

As discussed in the introduction, there are a number of criteria in the literature to assess the convergence of ZPG TBLs towards well-behaved conditions. Most of these criteria rely on empirical relations defining the evolution of the skin-friction coefficient, the shape factor or the wake parameter. However, it is more problematic to define criteria based on empirical correlations for general PG TBLs due to the effect of flow history, *i.e.,* besides inflow and tripping as in the case of ZPG TBLs, also the additional dependence on the streamwise pressure-gradient history has to be taken into consideration (Bobke *et al.* 2017). The goal of the present study is to develop several convergence criteria for APG TBLs, extending some of the ideas and techniques previously developed for ZPG TBLs (Sanmiguel Vila *et al.* 2017). To this end, we will analyze several numerical and experimental databases of PG TBLs with very different flow histories. In Table 1 we summarize various in-house numerical databases analyzed in the present study. These include five flat-plate APG TBLs (Bobke *et al.* 2017), all of them in what was denoted by Marusic *et al.* (2010) as near-equilibrium conditions. These TBLs would only exhibit self-similarity at very high Reynolds numbers, and only in the outer region. As reported by Townsend (1956) or Mellor & Gibson (1966), this can be obtained when the freestream velocity U_∞ is described by a power-law relation as $U_\infty(x) = C\,(x - x_0)^m$, where x is the streamwise coordinate, x_0 is the power-law virtual origin, and m has to be larger than $-1/3$ in order to obtain near-equilibrium conditions. All the flat-plate APG cases in Table 1 were defined with power-law freestream velocity distributions, and are therefore in near-equilibrium conditions. Note that additional discussions and interpretations regarding equilibrium in APG TBLs can be found in the studies reported in Aubertine & Eaton (2005); Maciel *et al.* (2006); Skåre & Krogstad (1994), in particular when it comes to scaling laws and their Reynolds-number evolution. Regarding the cases shown in Table 1, two of them exhibit long regions of constant values of the Clauser pressure-gradient parameter $\beta = \delta^*/\tau_w \mathrm{d}P_e/\mathrm{d}x$, where $\mathrm{d}P_e/\mathrm{d}x$ is the streamwise pressure gradient. The constant-β cases are of great importance, since as discussed by Bobke *et al.* (2017) they allow to study the effect of the pressure gradient on TBLs, isolating it from the effect of the flow history. In fact, the widely studied ZPG TBL is a particular case of near-equilibrium TBL with a constant value of $\beta = 0$. It could therefore be stated that an APG TBL is *canonical* when it is subjected to a constant value of β. Another in-house numerical database analyzed in the present work is the TBL developing on the suction side of a NACA4412 wing section reported by Hosseini *et al.* (2016). The interest of this latter flow case lies in the fact that the APG increases exponentially in the streamwise direction, and therefore the TBL is subjected to extreme pressure-gradient conditions, although it

Table 1: Summary of numerical databases analyzed in the present study, including the color that will be used to identify each cases throughout the article. Note that the setup corresponding to the $m13$, $m16$, $m18$ and the constant-β cases $b1$ and $b2$ is given by Bobke *et al.* (2017); the setup corresponding to the wing configuration can be found in Hosseini *et al.* (2016). The reference ZPG TBL data is reported by Schlatter & Örlü (2010).

Case	Range of Re_θ under study	Range of β	Color
$m13$	$1,610 < Re_\theta < 3,100$	$0.96 < \beta < 1.51$	
$m16$	$1,740 < Re_\theta < 3,620$	$1.95 < \beta < 2.78$	
$m18$	$1,750 < Re_\theta < 4,010$	$3.15 < \beta < 4.47$	
$b1$	$1,470 < Re_\theta < 2,980$	$\simeq 1$	
$b2$	$1,760 < Re_\theta < 3,200$	$\simeq 2$	
Wing	$750 < Re_\theta < 2,800$	$0.60 < \beta < 85$	
ZPG	$1,000 < Re_\theta < 4,060$	$\simeq 0$	

remains attached in the mean up to the trailing edge. Additional details regarding the numerical aspects are given in the respective references, but note that the flat-plate APG cases are obtained through well-resolved large-eddy simulations (LESs) using the Fourier–Chebyshev code SIMSON (Chevalier *et al.* 2007), and DNS was used for the wing, with the spectral-element code Nek5000 (Fischer *et al.* 2008). The DNS of ZPG TBL simulated by Schlatter & Örlü (2010) with SIMSON is also included in Table 1, since it will be used in a number of comparisons in the present work.

In order to develop robust criteria of convergence to well-behaved conditions, we also analyzed the five additional databases from the literature summarized in Table 2. In the DNS by Kitsios *et al.* (2016) a region of constant $\beta = 1$ is established, over a higher Reynolds-number range than that of our $b1$ case shown in Table 1. Since both simulations are performed using high-order codes, their accuracy should be comparable, and therefore we will be able to define a more robust criterion for APG TBLs subjected to a constant value of $\beta = 1$, as discussed below. The DNS dataset by Lee (2017) also includes APG TBLs with constant values of β, in their case equal to 0.73, 2.2 and 9. Note that the boundary-layer profiles for $\beta \simeq 2.2$ and 9 are located at the beginning of the constant-β region, and are therefore not considered in the following to establish constant-β criteria. However, since the $\beta(x)$ evolution is reported, the results could be used to develop more robust criteria for flows with varying pressure-gradient magnitudes. With respect to the DNS TBL reported by Spalart & Watmuff (1993), their flow is subjected to a pressure-gradient distribution ranging from a mild favorable pressure gradient (FPG) of $\beta = -0.3$ to a strong APG of $\beta = 2$. This database will be used in the determination of skin-friction criteria. Finally, the experimental profiles by Monty *et al.* (2011) and Nagib *et al.* (2006) span a higher Reynolds-number range than that of the other datasets, and therefore will be used to assess the high-Re trends in one of our criteria. However, due to the fact that the $\beta(x)$ evolutions were not available in these cases, these databases can only be used in one of the criteria discussed below.

2.1. *Characterization of the in-house APG TBLs*

The in-house numerical databases introduced in §2 and summarized in Table 1 are briefly characterized here. In Figure 1 (top) we show the evolution of the Clauser pressure-gradient parameter β with Re_θ for the various APG cases under consideration. The first observation is the fact that the $b1$ and $b2$ cases exhibit long regions of constant values of β, with average values of $\beta = 1.0$ and $\beta = 2.1$, respectively. Note that positive values of β are associated with APGs, *i.e.*, with decelerated boundary layers. This deceleration produces an increase in the wall-normal velocity, which in turn leads to larger boundary-layer thicknesses in APG TBLs. As argued, among others, by Bobke *et al.* (2017) and discussed in §3.2, the state of a particular APG TBL is not uniquely determined by the Reynolds number and the local value of β, but also by its pressure-gradient

Table 2: Summary of additional databases available in the literature analyzed in the present study, including the symbol that will be used to identify them throughout the article.

Reference	Type of data	Range of Re_θ under study	Range of β	Symbol
Kitsios *et al.*	DNS	3,500–4,800	$\simeq 1$	
Lee	DNS	1,605–2,840	$\simeq 0.73$, $\simeq 2.2$ and $\simeq 9$	
Spalart & Watmuff	DNS	640–1,600	-0.3–2	
Monty *et al.*	Exp	6,100–18,700	0.91–4.73	
Nagib *et al.*	Exp	11,600–56,100	-0.2–0.3	

history $\beta(x)$. The $m13$ and $m16$ cases, which constitute also near-equilibrium APG TBLs, exhibit a slightly decreasing trend in β. They start from stronger APG conditions than the $b1$ and $b2$ configurations, and progressively reach very similar pressure-gradient magnitudes. On the other hand, the stronger flat-plate APG case $m18$, starts with an increasing β trend from around 3.5 up to approximately 4.5 (a value of β achieved at $Re_\theta \simeq 2,700$). Beyond this point, it also exhibits a decreasing trend in β, with a final value of around 3.2 (corresponding to strong APG conditions), at $Re_\theta \simeq 4,010$. The β in the wing shows an exponential increase as Re_θ increases, a trend significantly different from that exhibited by the near-equilibrium boundary layers. Note that although a very large value of $\beta \simeq 85$ is observed close to the trailing edge of the wing, the boundary layer on the suction side only exhibits up to around 30% instantaneous reversed flow (Vinuesa *et al.* 2017), and the boundary layer remains attached in the mean. Figure 1 (bottom) includes, for reference, the Reynolds-number evolution of the Clauser pressure-gradient parameter of the five databases from the literature listed in Table 2. Note that in the two databases containing regions of constant β, namely the ones by Kitsios *et al.* (2016) and Lee (2017), only the β values from the profiles analyzed here are shown.

The different development of the boundary layers are illustrated in Figure 2, where the various boundary-layer thicknesses are documented. As discussed by Vinuesa *et al.* (2016), the boundary-layer thickness is a rather ambiguous quantity in APG TBLs compared to the ZPG case. This is due to the fact that, in the former, the streamwise velocity is not necessarily constant beyond the boundary-layer edge, a fact that explains some of the irregularities observed in the boundary-layer parameters shown in Figures 1 and 2. In the present work, the 99% boundary-layer thickness δ_{99} is calculated following the procedure by Vinuesa *et al.* (2016), which is based on the diagnostic-plot concept by Alfredsson *et al.* (2011). In Figure 2 (top) we show the evolution of the ratios δ_{99}/δ^* and δ_{99}/θ, which are sensitive indicators of the boundary-layer growth (Schlatter & Örlü 2012). Lower values of these ratios are associated with velocity profiles exhibiting lower velocities in the near-wall region, as it is the case in APGs due to the increased wall-normal momentum transfer. As expected, the values of δ_{99}/δ^* from the APG cases are below the ones of the ZPG, with the ratio decreasing for increasing values of β. Interestingly, cases $b1$ and $b2$ show a slightly increasing behavior, approximately parallel to the trend from the ZPG boundary layer. The rest of the flat-plate cases also show a slightly increasing trend, although not parallel to the one described by the ZPG TBL case. Moreover, the $m18$ boundary layer, with the strongest APG magnitude, shows almost no growth for $Re_\theta > 3,500$. On the other hand, the APG on the suction side of the wing shows a decreasing trend throughout the whole domain of interest, a manifestation of the progressively stronger APG conditions it is subjected to, and connected to the fact that this boundary layer is clearly not in near-equilibrium conditions. Also note that the APG increases the thickness of the boundary layer, which explains the larger values of δ^* at higher β. Similar conclusions can be drawn from the δ_{99}/θ ratios, also presented in the same figure.

The Reynolds number based on momentum and displacement thickness is shown, as a function of the friction Reynolds number $Re_\tau = \delta_{99}u_\tau/\nu$ (where ν is the fluid kinematic viscosity), in Figure 2 (bottom) for all the cases. In this figure it can be observed that stronger APGs lead

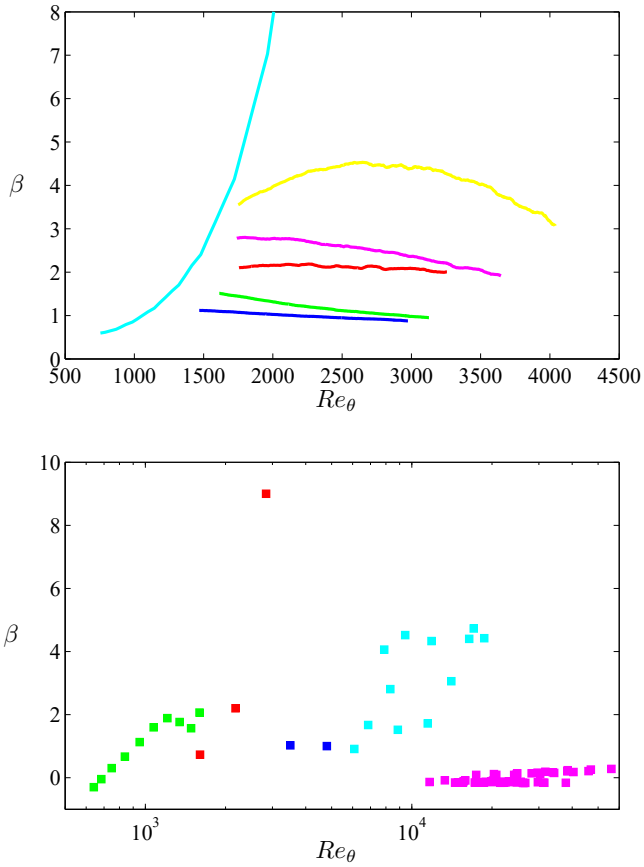

Figure 1: Evolution of the Clauser pressure-gradient parameter with Re_θ for (top) the various in-house APG cases, and (bottom) five additional databases available in the literature. Colors and symbols given in Tables 1 and 2.

to higher values of Re_{δ^*} and Re_θ. Note that these Reynolds numbers are formed with the local values of the the edge velocity U_e and either δ^* or θ. This implies that although U_e decreases in APG TBLs due to the streamwise deceleration, the increase in δ^* and θ is larger than the velocity decrease, thus yielding a significant increase in both Reynolds numbers for progressively stronger APG conditions. The $b1$ and $b2$ cases also show trends approximately parallel to the ZPG ones (except the lower-Re range in the $\beta = 2$ case, which exhibits smaller values of Re_{δ^*}), and as expected the $m18$ configuration shows the largest values among the flat-plate cases. The APG boundary layer on the suction side of the wing section exhibits an interesting trend, with progressively increasing values of Re_{δ^*} and Re_θ in the streamwise direction, but with a maximum value of $Re_\tau \simeq 373$. This value is reached at a streamwise distance of 80% of the chord length on the suction side of the wing, and corresponds to $Re_{\delta^*} = 2,990$ and $Re_\theta = 1,720$. This trend in Re_τ is produced by the progressively increasing APG magnitude, which leads to an increase in δ_{99}, but also to a decrease in the friction velocity u_τ. At 80% of the chord length the decrease in u_τ overcomes the increase in δ_{99}, a fact that leads to the decrease in Re_τ. This also shows that Re_τ is not a good quantity to study the asymptotic behavior of strongly decelerated APG TBLs, and Re_{δ^*} or Re_θ would be preferable instead as shown in Figure 2 (bottom). On the other hand, the parallel evolution of Re_θ and Re_{δ^*} with Re_τ for the flat-plate boundary layers studied here, indicates that for the mild APG conditions investigated here, any of the aforementioned Reynolds

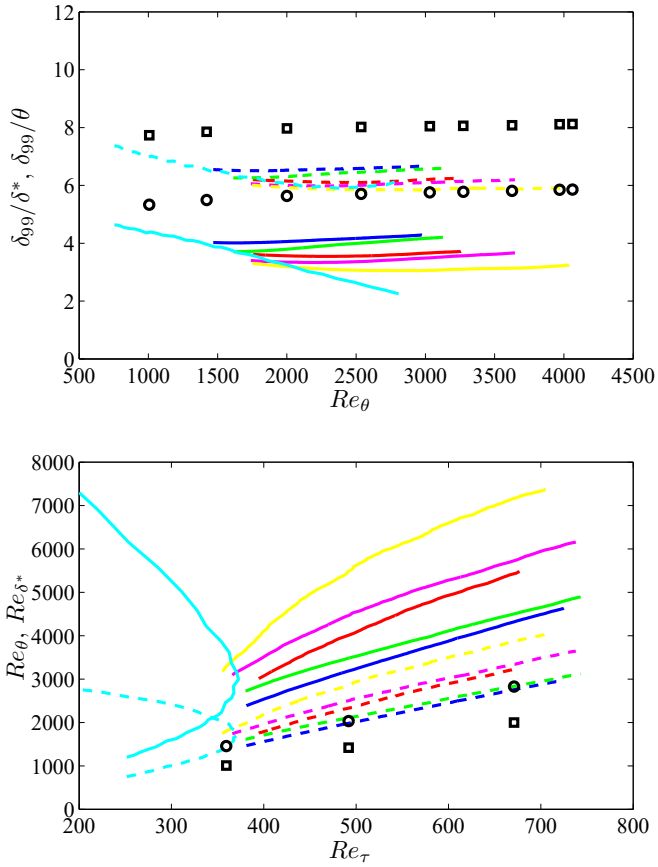

Figure 2: (Top) Evolution of the ratio between boundary-layer thickness and (——) displacement and (– –) momentum thickness with Re_θ for the various APG cases. (Bottom) Reynolds number based on (——) displacement and (– –) momentum thickness for the various APG cases, as a function of friction Reynolds number. The colors are given in Table 1, and the ZPG results are represented by (○) and (□) for displacement and momentum thickness, respectively.

numbers is appropriate to study Reynolds-number effects. For the following discussion, which includes the APG TBL on the suction side of the wing, the momentum-loss Reynolds number Re_θ is preferred.

After discussing the development of the various APG TBLs under study, it is clear that the very different flow histories (defined by the various β distributions in Figure 1) lead to significant differences in the evolution of the boundary layers. In §3 and 4 we will discuss the possibilities to define criteria to discern whether an APG TBL can be considered as well-behaved or not, using both the mentioned in-house databases and the five additional datasets from the literature summarized in Table 2.

3. Criteria to identify "well-behaved" APG TBLs

3.1. *Cases with constant β*

In the introduction we discussed the importance of developing criteria to ensure that the flow cases under investigation can be considered to be well-behaved, *i.e.*, independent of the inflow conditions and exempt of any numerical or experimental artifacts. Chauhan *et al.* (2009) proposed empirical

correlations describing the Re-evolution of the shape factor and the wake parameter, in the context of ZPG TBLs. The advantage of the ZPG configuration is the fact that the well-behaved cases are not affected by (streamwise pressure-gradient) history effects, since this boundary layer is defined by a constant value of $\beta = 0$. Therefore, any deviation from the proposed empirical correlations can be attributed to local non-equilibrium effects or problems with the development of the boundary layer (*e.g.* due to strong over- or under-tripping), which would basically imply that the particular flow case cannot be considered to be a canonical ZPG TBL. Nevertheless, general PG TBLs are greatly affected by history effects, as can be observed in Figures 1 and 2. This adds some difficulty when establishing criteria of convergence towards well-behaved conditions. There would be as many well-behaved evolutions of H, Π or C_f as possible pressure-gradient histories, and therefore it is not possible to use such criteria for general PG TBLs. It is also interesting to note that the $b1$ and $b2$ cases, with constant value of β, are subjected to the same well-defined pressure-gradient magnitude throughout a considerable streamwise extent. In the present section we will focus on the $b1$ and $b2$ cases, together with the APG TBL with constant value of $\beta = 1$ by Kitsios *et al.* (2016), and report empirical curves that can be used to assess whether a particular APG TBL, with constant $\beta = 1$ or 2, can be considered to be well-behaved. Note that given the relatively low Reynolds number available for the present databases, we will focus on the skin-friction coefficient and shape factor, and therefore we will not provide an empirical curve for the wake parameter, which would require higher Reynolds numbers in order to not be affected by low-Re effects.

The skin-friction coefficient C_f can be written as follows, assuming that the overlap region follows the logarithmic law (Nagib *et al.* 2007):

$$C_f = 2\left[\frac{1}{\kappa}\ln\left(Re_\theta\right) + C\right]^{-2}, \tag{1}$$

where κ is the von Kármán coefficient, and C is a constant. As discussed by Chauhan *et al.* (2009), this skin-friction relation is the leading-order term of a high-Re expansion of C_f, and higher-order terms can be added to account for low-Re effects. Although Chauhan *et al.* (2009) expressed C_f in terms of Re_{δ^*}, here we express it in terms of Re_θ and retain the same higher-order terms, leading to the following relation:

$$C_f = 2\left[\frac{1}{\kappa}\ln\left(Re_\theta\right) + C + \frac{D_0\ln\left(Re_\theta\right)}{Re_\theta} + \frac{D_1}{Re_\theta}\right]^{-2}, \tag{2}$$

where D_0 and D_1 are also constants. Note that the logarithmic skin-friction relation and its low-Re correction have found widespread preference compared to other empirical relations since the early work by Rotta (1953). The values of the various coefficients in the correlations (1) and (2) used in the present work for the ZPG, and the APG cases with constant $\beta = 1$ (including Kitsios *et al.* (2016)) and 2, are given in Table 3. In order to obtain the various coefficients, the data with $Re_\theta > 2,000$ was first fit to equation (1), which led to the values of κ and C. Then, the full Re-range was fit to equation (2), using the previously obtained values of κ and C, to determine the coefficients in the higher-order terms. The ZPG values $\kappa = 0.384$ and $C = 4.127$ were also reported by Nagib *et al.* (2007), and the coefficients D_0 and D_1 are of the same order as the ones obtained by Chauhan *et al.* (2009) in their Re_{δ^*}-based correlation. Regarding the APG cases, note that the values of κ decrease with increasing APG magnitude, as reported for instance by Nagib & Chauhan (2008) or Nickels (2004).

Using the definitions of δ^* and θ it is possible to derive the following equation for the shape factor H (Tennekes & Lumley 1972):

$$H = \frac{1}{1 - \left(C'/U_e^+\right)}, \tag{3}$$

where $U_e^+ = U_e/u_\tau$ is the inner-scaled boundary-layer edge velocity, $C' = \int_0^\infty W^{+2}\,\mathrm{d}\left(y/\Delta\right)$, $W^+ = U_e^+ - U^+$ and $\Delta = U_e^+\delta^*$ is the Rotta–Clauser length scale. As in the case of equation (1),

Table 3: Summary of coefficients used in the C_f and H correlations (1)–(4), for the various cases in the present study.

Case	κ	C	D_0	D_1	C'	E_1
ZPG	0.384	4.127	220	$-1,945$	7.135	-19.12
APG with constant $\beta = 1$	0.361	5.300	250	$-2,100$	9.932	-2.415
APG with constant $\beta = 2$	0.349	6.886	260	$-2,500$	12.53	-88.41

it is possible to extend this relation to include low-Re effects by considering an additional term of $O(1/Re_\theta)$, similarly to what was done by Chauhan *et al.* (2009) with Re_{δ^*}, as follows:

$$H = \frac{1}{1 - \left(C'/U_e^+\right)} + \frac{E_1}{Re_\theta}, \tag{4}$$

where E_1 is a constant. The values used in the present work for the different cases in equations (3) and (4) are also summarized in Table 3. Note that, as in the C_f correlations, the C' value was obtained by fitting the data with $Re_\theta > 2,000$ to equation (3), and then using that value to obtain the higher-order coefficient E_1 from the complete dataset using (4). Moreover, the inner-scaled edge velocity was obtained from equation (1), through the relation $U_e^+ = \sqrt{2/C_f}$. Interestingly, the $b1$ and Kitsios *et al.* (2016) cases with $\beta = 1$ led to a very small value of $E_1 = -2.415$, which means that the high-Re version of the H correlation is almost capable of representing the complete Reynolds-number range. Note that the value from the ZPG case $C' = 7.135$ was also reported by Nagib *et al.* (2007), and that the values of C' from the cases with constant $\beta = 1$ and 2, are 9.932 and 12.53 respectively, are close to the values obtained by integrating the inner-scaled mean velocity defect profiles (with average values over the datasets of 9.87 and 12.09, respectively). The small deviations between the C' values obtained from the curve fit to H and from the individual velocity profiles can be associated to low-Re effects.

Figure 3 shows the boundary-layer parameters in terms of Re_θ, compared with the empirical correlations (1)–(4). In Figure 3 (left) we show the skin-friction coefficient C_f, which as expected exhibits values progressively smaller as the APG magnitude increases. This figure shows that the evolution with Re_θ of the skin-friction coefficients from the constant $\beta = 0$, 1 and 2 cases are in very good agreement with equation (1) for $Re_\theta > 2,000$, thus providing a possible criterion to assess whether a particular boundary layer exhibits well-behaved conditions beyond this Reynolds number. It can also be observed that using the low-Re correction in equation (2), the complete dataset is well reproduced by the empirical relation, and therefore this constitutes a more complete criterion of convergence to well-behaved conditions. Regarding the evolution of the shape factor shown in Figure 3 (right), it can be observed that stronger APG boundary layers exhibit larger values of H. This is due to the fact that the APG increases the thickness of the boundary layer, with the consequent reduction in wall-shear stress. The high-Re correlation (3) shown for the ZPG case again represents the data well for $Re_\theta > 2,000$, although the low-Re correction improves the agreement with the numerical data below this Reynolds number. Note that for the cases with constant $\beta = 1$ and 2 we only show the correlation with the low-Re correction (4), which represents very well the full range of data, with the exception of the lowest Reynolds number in the $b2$ case. The results presented here show that the empirical correlations (2) and (4), for C_f and H respectively, can be used as convergence criteria in APG TBLs with constant values of $\beta = 1$ and 2. This is an important conclusion, because it also highlights the fact that it is possible to define specific APG conditions in which the TBL is subjected to a constant magnitude of the pressure gradient, analogously to ZPG TBL cases.

The interesting theoretical work by Mellor & Gibson (1966) also led to expressions for the skin-friction coefficient and the shape factor in PG TBLs subjected to constant values of β. In particular, they proposed a skin-friction relation of the same type as (1), defined in terms of Re_{δ^*}

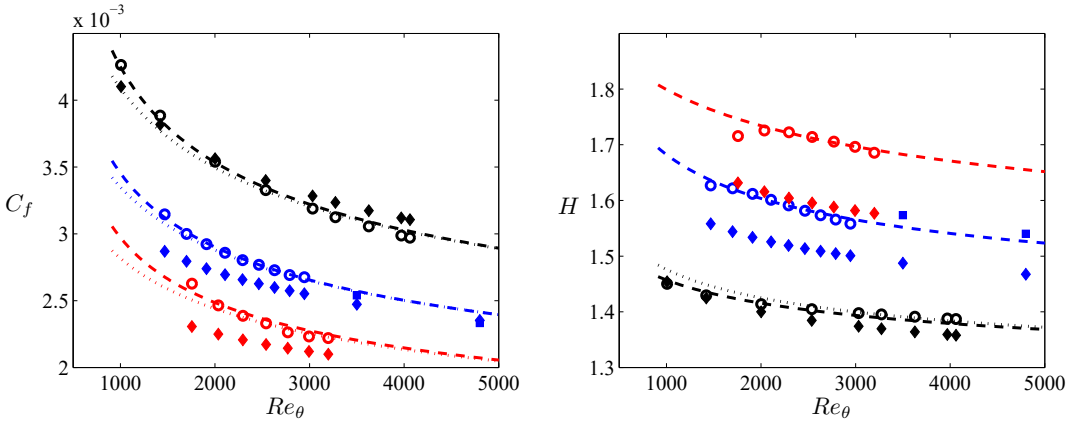

Figure 3: (Left) Evolution of the skin-friction coefficient with Reynolds number based on momentum thickness. (○) represents values from the individual profiles corresponding to the various in-house simulations, (· · ·) corresponds to the high-Re correlation (1) and (– –) to the low-Re curve given by (2). (Right) Evolution with Re_θ of the shape factor, where again (○) represent values from individual profiles, (· · ·) corresponds to equation (3) and (– –) to (4). Colors represent the constant-β cases defined in Table 1. As shown in Table 2, (■) corresponds to data from Kitsios *et al.* (2016). Predictions from the correlations by Mellor & Gibson (1966), at the same Reynolds numbers as those of the cases presented here, are represented by (♦) and the colors are according to the cases described in Table 1.

instead of Re_θ. However, the most relevant difference with respect to the present study is the fact that they proposed a constant value of $\kappa = 0.41$ regardless of the pressure-gradient magnitude, and a value of C related to the particular β. Thus, in their analysis they considered the slope of the logarithmic region to be independent of the pressure gradient, with different intercepts according to the PG magnitude. Predictions from the skin-friction relation proposed by Mellor & Gibson (1966) at the same Reynolds numbers as the ones discussed for the $\beta = 0$, 1 and 2 cases are shown in Figure 3 (left). Note that although the results are shown in terms of Re_θ, the corresponding Re_{δ^*} values were used to calculate C_f. Due to the fact that it is necessary to have the relation between Re_{δ^*} and Re_θ (*i.e.*, the shape factor) to compare the skin-friction relation proposed in the present study and the one by Mellor & Gibson (1966), we only show the predictions from the latter over the Reynolds-number range spanned by the available constant-β datasets. Firstly, note that the value of κ used by Mellor & Gibson (1966), even for the ZPG case, is higher than the value of $\kappa = 0.384$ recently reported by Nagib *et al.* (2007) among others. This could explain the small deviations between our ZPG data and the correlation by Mellor & Gibson (1966). At low Reynolds number the Mellor & Gibson (1966) correlation is in good agreement with equation (1), *i.e.*, our skin-friction correlation for ZPG TBLs without the low-Re correction. At higher Reynolds numbers the correlation from Mellor & Gibson (1966) slightly overestimates the skin-friction trend. On the other hand, in the $\beta = 1$ and 2 cases the correlation from Mellor & Gibson (1966) underestimates the skin-friction trends from the $b1$ and $b2$ cases, up to Re_θ values of around 3,000. However, the C_f predictions from Mellor & Gibson (1966) for $\beta = 1$ at higher Reynolds numbers are in very good agreement with the values reported by Kitsios *et al.* (2016). Due to the fact that we do not have H values beyond this Reynolds number, we cannot predict whether the curve from Mellor & Gibson (1966) would be in good agreement with (2) at higher Reynolds numbers for $\beta = 1$. Nevertheless, it appears that the use of a constant value of κ for the whole pressure-gradient range, as it is the case of the correlation by Mellor & Gibson (1966), could lead to inaccuracies in boundary-layer predictions as reported, for instance, by Nagib &

Chauhan (2008) or Vinuesa *et al.* (2014). In this context, Dixit & Ramesh (2009) developed a modified Clauser-chart method to predict the wall-shear stress in PG TBLs, based on variable values of κ according to the pressure-gradient conditions. It is also important to mention that in the definition of the freestream boundary condition from the simulation by Kitsios *et al.* (2016), the evolution of the displacement thickness in the streamwise direction is prescribed according to the work by Mellor & Gibson (1966). However, an assessment of the impact of this on the results is beyond the scope of the present work.

In addition to the skin-friction correlation, Mellor & Gibson (1966) also provided the theoretical background to estimate the Reynolds-number evolution of the shape factor H in PG TBLs subjected to constant values of β. In particular, they provided the evolution of the defect shape factor G with β, a quantity that can then be used to calculate the shape factor through the relation: $G = (H-1)\,/\left(H\sqrt{C_f/2}\right)$. Since this quantity relies on C_f, it can be expressed in terms of Re_{δ^*} and then represented as a function of Re_θ as shown in Figure 3 (right). Note that Mellor & Gibson (1966) introduced an additional Reynolds-number correction for G, which was also considered in the present study. In this figure it can be observed that although the shape-factor equation by Mellor & Gibson (1966) is in good agreement with the low-Re ZPG data, it underestimates the values of H at higher Reynolds numbers. Regarding the $\beta = 1$ and 2 cases, the trends predicted by Mellor & Gibson (1966) are below the expected values, a deviation that appears to increase at higher values of β. This discrepancy could again be connected to the fact that a constant value of κ is considered in the log-law description over the whole pressure-gradient range.

3.2. *Cases with arbitrary $\beta(Re_\theta)$ distributions*

Although the convergence criteria given by equations (2) and (4) are useful when used for APG TBLs with constant β, it is not practical to define a different criterion for each possible $\beta(Re_\theta)$ history. On the other hand, it would be interesting to have a criterion to be used for general APG TBLs. In Figure 4 (left) we show the skin-friction curves from all the in-house APG boundary layers in the present study, together with the ZPG case. As observed in Figures 3 (left) and 4 (left), the C_f curves of the $b1$ and $b2$ cases are similar to the one of the ZPG TBL, although shifted towards lower wall-shear values for increasing β. In particular, Figure 4 (left) shows that the C_f curves from the constant-β cases can be reproduced empirically from the ZPG DNS data as follows:

$$C_{f,b1} \approx \frac{C_{f,\mathrm{ZPG}}}{H_{\mathrm{ZPG}}^{0.5}}, \tag{5}$$

$$C_{f,b2} \approx \frac{C_{f,\mathrm{ZPG}}}{H_{\mathrm{ZPG}}}, \tag{6}$$

where $C_{f,b1}$ and $C_{f,b2}$ are the skin-friction coefficients from the $b1$ and $b2$ cases, and $C_{f,\mathrm{ZPG}}$ and H_{ZPG} are the skin-friction coefficient and shape factor from the ZPG DNS, all of them at the same value of Re_θ. This result can be generalized to constant-β cases in the moderate range of pressure-gradient magnitudes investigated in the present study as follows:

$$C_{f,\beta} = \frac{C_{f,\mathrm{ZPG}}}{H_{\mathrm{ZPG}}^{\beta/2}}, \tag{7}$$

where $C_{f,\beta}$ is the skin-friction coefficient of an APG TBL with a constant value of β. This is a very interesting result, because it implies that it appears possible to reproduce skin-friction curves from constant-β APG TBLs, based uniquely on ZPG TBL results. In fact, and since the estimation of $C_{f,\beta}$ is done at the same Re_θ as the ZPG TBL, equation (7) can be interpreted as a "correction" to the ZPG trend, through the shape factor (which increases with the APG) and the pressure-gradient magnitude. Moreover, in Figure 4 (left) we also show that it is possible to reproduce the skin-friction curve of an APG TBL with a certain $\beta(Re_\theta)$ distribution based only

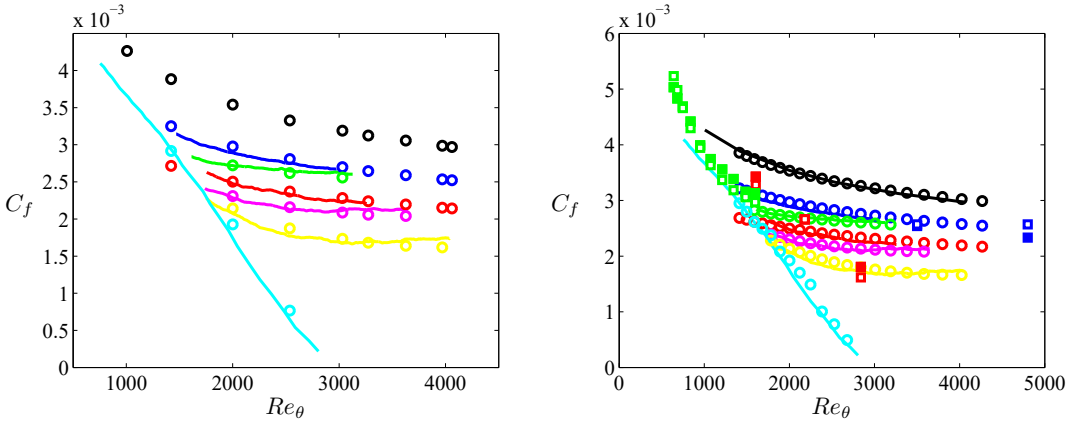

Figure 4: (Left) Evolution of the skin-friction coefficient with Re_θ, where the colored (—) represent the various in-house APG cases, and the black (○) the ZPG curve. Colored (○) represent estimations of the C_f values from the various APG boundary layers using equation (8), and the ZPG DNS data. (Right) Evolution of the skin-friction coefficient with Re_θ, where the colored (—) represent the various in-house boundary-layer cases, including the ZPG. Colored (○) represent estimations of C_f using equation (8), evaluated based on the ZPG correlations (2) and (4). Note that the DNS data is not used in this panel, and that although the ZPG correlations are continuous, the values of $\overline{\beta}$ are evaluated at the discrete set of Re_θ values indicated by (○). Colors given in Table 1. Filled (■) correspond to the cases summarized in Table 2, whereas empty (□) denotes estimations of C_f using equation (8), together with the ZPG correlations (2) and (4) for the same cases.

on ZPG DNS results as follows:

$$C_{f,\mathrm{APG}} = \frac{C_{f,\mathrm{ZPG}}}{H_{\mathrm{ZPG}}^{\overline{\beta}/2}}, \tag{8}$$

where $C_{f,\mathrm{APG}}$ is the skin-friction coefficient of an APG TBL subjected to a known $\beta(Re_\theta)$ pressure-gradient distribution. In order to incorporate the effect of the flow history into this relation, we used the averaged $\overline{\beta}$, calculated as:

$$\overline{\beta}(Re_\theta) = \frac{1}{Re_\theta - Re_{\theta,0}} \int_{Re_{\theta,0}}^{Re_\theta} \beta(Re_\theta)\, \mathrm{d}Re_\theta, \tag{9}$$

where $\overline{\beta}(Re_\theta)$ represents the average value of β up to a certain Reynolds number. Note that $Re_{\theta,0}$ is the point where the averaging is started, and in the case of the results in Figure 4 it was set to the first available Re_θ value in the dataset above $1,000$. Figure 4 (left) reflects a quite remarkable agreement, *i.e.*, it is possible to reproduce the C_f curves from all the APG TBLs under consideration in this work, using only the ZPG TBL DNS data and the β evolution. The flow histories from the various APG cases are encapsulated in the $\overline{\beta}$ parameter, calculated through relation (9). Note that not only the C_f curves from the moderately complicated flow histories in the three near-equilibrium flat-plate cases ($m13$, $m16$ and $m18$) are very well reproduced in Figure 4 (left), but also the extreme pressure-gradient distribution exhibited by the wing profile (see Figure 1). Ignoring the pressure-gradient history by utilizing the local value of β instead would result in curves that deviate up to 100% with respect to the reference data in the wing case. It is important to note that the results shown in Figure 4 (left) were obtained using the ZPG DNS data, at the particular Re_θ values where those profiles are available. Moreover, in Figure 4 (right) we test the possibility of reproducing the C_f curve of any APG TBL using the ZPG correlations for C_f and H, *i.e.,* relations (2) and (4), respectively. Using the correlations instead of the DNS

data significantly extends the applicability of the method proposed here. Interestingly, the C_f curves estimated using the ZPG correlations of C_f and H also agree very well with the reference in-house cases, as observed in Figure 4 (right). Note, however, the slight over-prediction of the C_f curve from the wing at around $Re_\theta \simeq 2,000$. In addition to the fact that the method proposed above is only based on empirical observations, other additional aspects may contribute to this. Firstly, small inaccuracies in the ZPG correlations around this Reynolds number, magnified by the larger pressure-gradient magnitude in comparison with the flat-plate APGs. A second factor that could explain this small over-prediction comes from the method used to calculate the average β, which essentially integrates in Re_θ to account for the history effects. Further work is required to develop a more sophisticated method to incorporate the history, possibly performing some windowing technique in order to attribute a larger weight to the local value of β.

This method is further tested in Figure 4 (right) with the additional numerical databases by Spalart & Watmuff (1993), Kitsios *et al.* (2016) and Lee (2017). The APG TBL by Kitsios *et al.* (2016) is subjected to a constant value of $\beta = 1$ and, as can be observed in Figure 4 (right), the agreement with the predictions from equation (8) is very good. This equation is also able to capture the three points extracted from the three constant-β APG TBLs by Lee (2017), which span a lower Reynolds-number range but a wider range of β values up to 9. Moreover, the skin-friction coefficient from the boundary layer by Spalart & Watmuff (1993), which is in fact subjected to a more complex pressure-gradient history (starting with a mild FPG leading to a strong APG), is also well reproduced by equation (8). Note that in this case, the negative values of β would lead to a skin-friction coefficient larger than the one of a ZPG TBL (as expected for accelerated boundary layers), a fact that is also reproduced by equation (8). Therefore, the method proposed here to estimate the skin-friction coefficient provides very good agreement with the PG TBL results, over a wide range of pressure-gradient conditions. The only knowledge required to obtain the C_f curve is the $\beta(Re_\theta)$ distribution of the APG boundary layer. Then, the ZPG correlations (2) and (4) can be used to construct a reference skin-friction curve for any APG TBL (as well as several mild FPG cases, which were well reproduced by this method).

4. Convergence criteria based on the diagnostic-plot scaling

4.1. *Cases with arbitrary $\beta(Re_\theta)$ distributions*

In §3.1 we discussed criteria to assess the convergence to well-behaved conditions of constant-β TBLs, based on empirical curves for C_f and H. Then, a criterion based on C_f for general APG TBLs with any β distribution was presented in §3.2. Although the criteria based on C_f gives a good indication of whether a particular boundary-layer profile can be considered well-behaved or not, if the goal is to assess the location after which the flow exhibits well-behaved conditions in a wind-tunnel experiment then these criteria are not practical. This is due to the fact that in order to accurately determine the wall-shear stress experimentally it is necessary to perform direct measurements, using for instance the oil-film interferometry (OFI) technique described, for example, by Vinuesa & Örlü (2017). It is usually not possible to perform OFI measurements at a large number of streamwise locations, and therefore the C_f criteria is not suitable to assess the location of convergence to well-behaved conditions.

An alternative to the use of C_f curves was explored by Sanmiguel Vila *et al.* (2017), who employed the diagnostic-plot scaling (Alfredsson *et al.* 2011) to assess the convergence to well-behaved conditions in ZPG TBLs. This scaling collapses data when the turbulence intensity, u'/U, is plotted against the local mean velocity normalized with the edge velocity, U_e. The apparent advantage of this scaling is that it is independent of indirectly measured quantities such as the wall-shear stress and the absolute wall distance, or other integral parameters, and is solely based on directly measured quantities, thereby excluding additional measurement uncertainties. It turns out that this plot exhibits an extended linear behavior in the outer region of ZPG TBLs (including

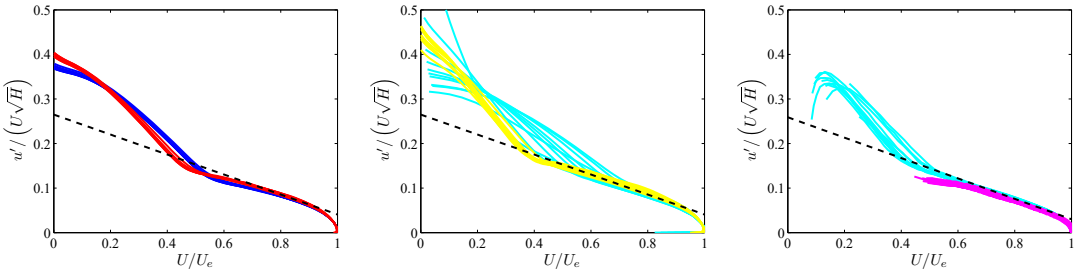

Figure 5: Diagnostic-plot scaling modified with the shape factor H, applied to several PG TBL cases. Colors are given in Table 1 for the in-house databases shown in (left) and (middle), whereas the colors from the high-Re cases shown in (right) are given in Table 2. (**– –**) represents the linear relation (11). In (left) and (middle), the values $\alpha_H = 0.264$ and $\beta_H = 0.227$ (obtained from equations (12) and (13) at $Re_\theta = 4,000$) are used, whereas in (right) the asymptotic values $\alpha_H = 0.259$ and $\beta_H = 0.223$ are considered. Three different panels are used in order to clearly show all the curves.

the logarithmic region). In particular, this region follows the relation:

$$\frac{u'}{U} = \alpha_d - \beta_d \frac{U}{U_e}, \tag{10}$$

where α_d and β_d are fitting parameters. Note that the linear region extends with increasing Re towards lower U/U_e-values (Alfredsson *et al.* 2011). Regarding PG TBLs, Drózdz *et al.* (2015) and Vinuesa *et al.* (2016) showed that the diagnostic scaling also collapsed boundary layers subjected to a wide range of pressure-gradient conditions when introducing the shape factor on the left-hand-side of relation (10) as: $u'/\left(U\sqrt{H}\right)$. In Figure 5 (left) and (middle) we show this scaling applied to several of the in-house APG TBLs considered in the present study, where it can be observed that despite the different pressure-gradient magnitudes and flow histories, all the profiles collapse in the outer region. In particular, a linear behavior is observed in the range $0.8 \leq U/U_e \leq 0.9$ in all the cases. Note that the reduced range of the linear region is probably attributed to the relatively low Re-range considered here, since the higher-Re cases shown in Figure 5 (right) exhibit longer regions of linear behavior. This observation will be exploited in the present work to define a criterion of convergence to well-behaved conditions, by inspecting the region of the boundary layer between $U/U_e = 0.8$ and 0.9, and fitting it to the relation:

$$\frac{u'}{U\sqrt{H}} = \alpha_H - \beta_H \frac{U}{U_e}, \tag{11}$$

where α_H and β_H are different fitting parameters valid for PG TBLs, when using the diagnostic plot scaled with H. The collapse observed in Figure 5 motivates the development of another convergence criterion, valid for any APG TBL regardless of the flow history. The idea is to measure profiles of the streamwise mean velocity and streamwise velocity fluctuations, use the diagnostic-plot scaling modified with the shape factor, and assess whether they follow the linear behavior given by equation (11). Note that in general it is easier to perform profile measurements than to accurately measure wall-shear stress at a number of streamwise locations, and therefore this method has a wider range of applicability from an experimental point of view. Furthermore, the region adhering to equation (11) will extend with increasing Re, as observed in studies from ZPG TBLs (Alfredsson *et al.* 2011).

A convergence criterion can therefore be defined by using the in-house APG TBL data presented in this study, together with the numerical databases by Kitsios *et al.* (2016) and Lee (2017) and the experimental results by Monty *et al.* (2011) and Nagib *et al.* (2006). The experimental results

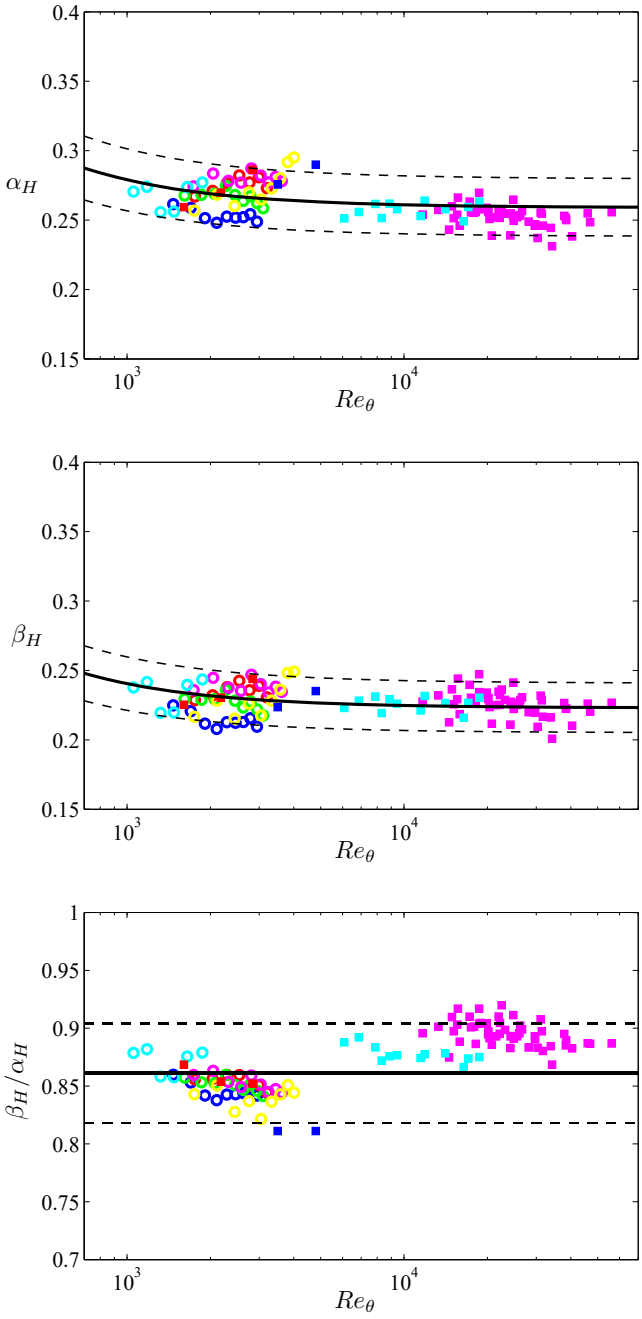

Figure 6: Evolution with Re_θ of the diagnostic-scaling parameters in equation (11), namely (top) α_H, (middle) β_H and (bottom) their ratio β_H/α_H. (——) represents (top) equation (12) $\pm 8\%$, (middle) equation (13) $\pm 8\%$ and (bottom) $0.861 \pm 5\%$. Color code is given in Tables 1 and 2.

are used to define the present criterion in a more robust way, up to $Re_\theta = 18,700$ and 56,100, respectively. The present criterion does not rely on the specific flow history, but on the local state of the boundary layer, which is manifested in the local value of the shape factor H. By fitting all the profiles to equation (11) in the linear region, approximately given by $0.8 \leq U/U_e \leq 0.9$, one

obtains the values of α_H and β_H shown in Figure 6 for all the cases under consideration. The following empirical correlations can be used to describe the evolution with Re_θ of the coefficients α_H and β_H:

$$\alpha_H = 0.259 + \frac{20}{Re_\theta}, \tag{12}$$

$$\beta_H = 0.223 + \frac{17.5}{Re_\theta}. \tag{13}$$

As also observed in Figure 6 (bottom), the ratio β_H/α_H shows an approximately constant value of around 0.861. Thus, a criterion based on calculating the values of α_H and β_H, comparing them with the correlations (12) and (13), and with the ratio 0.861, can be defined. It is interesting to note that when considering the ZPG TBL data analyzed by Sanmiguel Vila *et al.* (2017), and recomputing their ratio β_H/α_H, a value very close to the one found here, *i.e.* 0.861, is obtained. Note that the boundary layer by Spalart & Watmuff (1993) also exhibits a linear region when represented in the diagnostic scaling following equation (11). However, due to the low Reynolds number and complicated flow history, this region was observed over a narrow range, and therefore the values of α_H and β_H from this profile were not included in Figure 6. This is a similar method to the one proposed by Sanmiguel Vila *et al.* (2017) for ZPG TBLs, with the novelty that it can be applied to general PG TBLs, regardless of their particular flow history. The advantage of using this criterion over the ones based on skin-friction curves is the fact that it only relies on velocity profile measurements, but not on direct measurements of τ_w. Note, however, that these profile measurements require an accurate determination of the wall position, due to the fact that the shape factor H is necessary to obtain the diagnostic-plot scaling in relation (11). In the following section we will discuss the possibility of using another convergence criterion based on the diagnostic-plot scaling, which does not require an accurate determination of the wall position.

4.2. *Possibility of defining a criterion for cases with constant β and x-scans*

Although the criterion presented in §4.1 represents an advantage with respect to the approaches based on C_f curves, it still requires the measurement of velocity profiles at a number of streamwise locations. In fact, since the shape factor has to be determined from these profiles, it is also necessary to obtain an accurate estimation of the wall position, which could be problematic especially in hot-wire anemometry measurements (see, for instance, the work by Örlü & Vinuesa (2017)). This is the technique preferred when near-wall measurements are required. An alternative to the full profile measurements was proposed by Sanmiguel Vila *et al.* (2017) for ZPG TBLs, consisting in x-scans in the outer region of the boundary layer. In this method, the probe is moved in the streamwise direction, measuring u' and U, and these values are then compared to equation (10) in order to assess the location of convergence towards canonical ZPG conditions. Unfortunately, the x-scan approach cannot be used with the method discussed in §4.1, due to the fact that it is necessary to measure the full profile in order to obtain H. On the other hand, the diagnostic scaling (10) applied to APG TBLs also leads to a linear region, in this case between $0.7 \leq U/U_e \leq 0.9$ (Vinuesa *et al.* 2016), although the particular values of α_d and β_d depend on the magnitude of the APG and the flow history. Therefore, as it was the case in §3.1, it is not possible to define a general criterion for any APG TBL, due to the fact that any flow history would produce a different evolution of α_d and β_d with Re_θ.

As we did in §3.1, it is in principle possible to define reference curves for particular boundary layers with a prescribed flow history (for instance, for APG TBLs with constant values of β). Note that in this case the Reynolds-number evolution of α_d and β_d for a certain constant-β APG could also be used as a criterion to identify well-behaved TBLs. Thus, a probe can be located in the outer region of the boundary layer (in particular, in $0.7 \leq U/U_e \leq 0.9$, which covers a large part of the boundary layer in terms of the boundary-layer thickness) and traversed horizontally in the streamwise direction to obtain measurements of u' and U. As in the work by Sanmiguel Vila *et al.* (2017), these x-scans can then be compared with the values obtained from the empirical

relations for α_d and β_d, potentially producing a convergence criterion for wind-tunnel experiments of constant-β APG TBLs. However, additional databases spanning wider Reynolds-number ranges would be required to accurately define such a criterion.

5. Conclusions

In the present work we analyze a total of six in-house APG TBLs and five additional high-quality databases of PG TBLs available in the literature (Kitsios *et al.* 2016; Lee 2017; Monty *et al.* 2011; Nagib *et al.* 2006; Spalart & Watmuff 1993). These TBLs, which exhibit very different albeit relatively simple flow histories, are used to define several criteria to assess the convergence of APG TBLs to well-behaved conditions. These criteria can be used for numerical databases, but are also useful in experimental design in order to assess if local effects in the wind tunnel have an impact on the development of the boundary layer. The assessment of whether a particular boundary layer can be considered as *well-behaved*, *i.e.*, it is independent of the inflow conditions and is exempt of numerical or experimental artifacts, has received some attention in the past years. In particular, Chauhan *et al.* (2009) proposed empirical fits for the shape factor H and the wake parameter Π, and Sanmiguel Vila *et al.* (2017) developed a method based on the diagnostic-plot scaling, all of them in the context of ZPG TBLs. In this article we aim at extending some of these criteria to APG TBLs, with the additional complexity introduced by the pressure gradient and thus the flow history. Note that it is simpler to define such criteria for the ZPG TBL, due to the fact that this flow case is uniquely defined by the Reynolds number. However, arbitrary $\beta(x)$ evolutions can define specific PG TBLs, a fact that significantly complicates the possibility of establishing criteria for well-behaved PG TBLs. It must be highlighted that the criteria presented in this study have been developed using APG flows with simple $\beta(x)$ evolutions, including constant, increasing and decreasing $\beta(x)$ trends. Therefore, we proposed the following three convergence criteria, to be used depending on the particular boundary layer under consideration, as long as the flow exhibits a relatively simple flow history as discussed above:

1. *Empirical curves of C_f and H for constant-β APG TBLs.* These criteria are based on the empirical correlations (2) and (4) for C_f and H, respectively. The coefficients corresponding to the various cases under consideration are given in Table 3. The advantage of these criteria is that they are relatively easy to evaluate, although they require direct measurements of wall-shear stress and profile measurements with accurate wall position, respectively. Moreover, they cannot be used for APGs with general $\beta(Re_\theta)$ distributions. The correlations given in the present work correspond to APG TBLs with constant values of $\beta = 1$ and 2. It is therefore apparent that a large database of constant-β PG TBLs needs to be compiled before general criteria for a wide range of Re and β conditions can be established.
2. *Empirical curve of C_f for general $\beta(Re_\theta)$ PG TBLs.* This criterion is based on the observation that it is possible to obtain the C_f curve of any PG TBL by using only ZPG TBL data, and the $\beta(Re_\theta)$ curve. The reference C_f curve of the particular PG boundary layer is obtained from equation (8), where $C_{f,\mathrm{ZPG}}$ and H_{ZPG} can be determined from the curves (2) and (4), and $\overline{\beta}$ is computed from relation (9). This is a very flexible method, with the only drawback of requiring direct measurements of the wall-shear stress at a number of locations, which may be impractical in wind-tunnel experiments.
3. *Diagnostic-plot scaling for general $\beta(Re_\theta)$ PG TBLs.* This method relies on the collapse observed in the region $0.8 \leq U/U_e \leq 0.9$ when using the diagnostic-plot scaling (modified with H), over a wide range of pressure-gradient conditions. The idea behind this criterion is to perform a linear fit to equation (11) in the region $0.8 \leq U/U_e \leq 0.9$, and to compare the obtained values of α_H and β_H to the empirical curves (12) and (13). The only disadvantage of this method is the fact that it requires profile measurements at a number of locations, with an accurate determination of the wall position and the boundary-layer thickness (to compute H).

A fourth criterion, based on the diagnostic-plot scaling and x-scans, could be also defined for constant-β APG TBLs. This would be an extension of the idea proposed by Sanmiguel Vila *et al.* (2017) of using x-scans to assess the convergence of ZPG TBLs. Given the empirical observation that APG TBLs exhibit a linear region following equation (10) for $0.7 \leq U/U_e \leq 0.9$, it is in principle possible to measure values of u' and U at a particular height, and traverse the probe downstream within the outer layer in order to assess beyond which point they follow the Reynolds-number trend of α_d and β_d described by the proposed criterion. The approach with the x-scans would allow a more accurate determination of the point of convergence to well-behaved conditions.

This work constitutes a first step towards developing convergence criteria to evaluate whether a particular APG exhibits well-behaved conditions or not, when subjected to relatively simple $\beta(x)$ evolutions. A first step in assessing the effect of PGs on TBLs consists of separating the effect of flow history and APG magnitude, as discussed by Bobke *et al.* (2017), Monty *et al.* (2011) or Vinuesa *et al.* (2014). Given the different flow histories exhibited by the boundary layers discussed in the present work (see Figures 1 and 2), it is crucial to use robust criteria to ensure that the boundary layer under consideration is in fact subjected to the desired flow history. This is especially relevant in experimental studies, where it is usually not possible to obtain accurate measurements everywhere in the domain of interest, and therefore the methods described above may be quite relevant to ensure adequate flow conditions. Also note that although the specific applicability of some of the aforementioned criteria is limited to $\beta = 0$, 1 or 2, it should be noted that there is a lack of APG TBL data in the literature with significant regions of constant β and a documented flow history. Future work will be devoted to extend these criteria to obtain general expressions for α_d and β_d as a function of the APG magnitude. This will also require datasets up to higher Reynolds numbers, over a wider range of constant-β values. In addition to these, additional high-quality numerical and experimental studies of PG TBLs with more complex flow histories, at sufficiently high Reynolds numbers, are required to test and extend the criteria presented in this study. Note that, although these criteria provide robust results in the APG cases with relatively simple flow histories under study here, they may not be accurate when considering more complex $\beta(x)$ evolutions. Therefore the methods described here should be considered as a first attempt to establish criteria to identify well-behaved APGs.

Acknowledgments

RV, RÖ and PS acknowledge the funding provided by the Swedish Research Council (VR) and from the Knut and Alice Wallenberg Foundation. CSV acknowledges the financial support from Universidad Carlos III de Madrid within the program "Ayudas para la Movilidad del Programa Propio de Investigación". CSV, SD and AI were partially supported by the COTURB project (Coherent Structures in Wall-bounded Turbulence), funded by the European Research Council Coturb Grant No. ERC-2014.AdG-669505. The simulations were performed on resources provided by the Swedish National Infrastructure for Computing (SNIC) at PDC (KTH Stockholm).

References

Alfredsson, P. H., Segalini, A. & Örlü, R. 2011 A new scaling for the streamwise turbulence intensity in wall-bounded turbulent flows and what it tells us about the "outer" peak. *Phys. Fluids* **23**, 041702.

Aubertine, C. D. & Eaton, J. K. 2005 Turbulence development in a non-equilibrium turbulent boundary layer with mild adverse pressure gradient. *J. Fluid Mech.* **532**, 345–364.

Bobke, A., Vinuesa, R., Örlü, R. & Schlatter, P. 2017 History effects and near equilibrium in adverse-pressure-gradient turbulent boundary layers. *J. Fluid Mech.* **820**, 667–692.

Chauhan, K. A., Monkewitz, P. A. & Nagib, H. M. 2009 Criteria for assessing experiments in zero pressure gradient boundary layers. *Fluid Dyn. Res.* **41**, 021404.

Chevalier, M., Schlatter, P., Lundbladh, A. & Henningson, DS 2007 A pseudospectral solver for incompressible boundary layer. Technical Report TRITA-MEK 2007:07. KTH Mechanics.

Coles, D. 1956 The law of the wake in the turbulent boundary layer. *J. Fluid Mech.* **1**, 191–226.

Coles, D. 1968 The young person's guide to the data. *AFOSR-IFP-Stanford Conf. on Computation of turbulent boundary layers, D. E. Coles and E. A. Hirst (Eds.)* pp. 1–45.

Dixit, S. A. & Ramesh, O. N. 2009 Determination of skin friction in strong pressure-gradient equilibrium and near-equilibrium turbulent boundary layers. *Exp. Fluids* **47**, 1045–1058.

Drózdz, A., Elsner, W. & Drobniak, S. 2015 Scaling of streamwise Reynolds stress for turbulent boundary layers with pressure gradient. *Eur. J. Mech. B-Fluid* **49**, 137–145.

Erm, L. P. & Joubert, P. N. 1991 Low-Reynolds-number turbulent boundary layers. *J. Fluid Mech.* **230**, 1–44.

Fernholz, H. H. & Finley, P. J. 1996 The incompressible zero-pressure-gradient turbulent boundary layer: An assessment of the data. *Prog. Aero. Sci.* **32**, 245–311.

Fischer, P. F., Lottes, J. W. & Kerkemeier, S. G. 2008 NEK5000: Open source spectral element CFD solver. Available at: `http://nek5000.mcs.anl.gov` .

Gungor, A. G., Maciel, Y., Simens, M. P. & Soria, J. 2016 Scaling and statistics of large-defect adverse pressure gradient turbulent boundary layers. *Int. J. Heat Fluid Flow* **59**, 109–124.

Hosseini, S. M., Vinuesa, R., Schlatter, P., Hanifi, A. & Henningson, D. S. 2016 Direct numerical simulation of the flow around a wing section at moderate Reynolds number. *Int. J. Heat Fluid Flow* **61**, 117–128.

Hutchins, N. 2012 Caution: Tripping hazards. *J. Fluid Mech.* **710**, 1–4.

Kitsios, V., Atkinson, C., Sillero, J. A., Borrell, G., Gungor, A. G. & Jiménez, J. 2016 Direct numerical simulation of a self-similar adverse pressure gradient turbulent boundary layer. *Int. J. Heat Fluid Flow* **61**, 129–136.

Kozul, M., Chung, D. & Monty, J. P 2016 Direct numerical simulation of the incompressible temporally developing turbulent boundary layer. *J. Fluid Mech.* **796**, 437–472.

Lee, J. H. 2017 Large-scale motions in turbulent boundary layers subjected to adverse pressure gradients. *J. Fluid Mech.* **810**, 323–361.

Lee, J.-H. & Sung, H. J. 2008 Effects of an adverse pressure gradient on a turbulent boundary layer. *Int. J. Heat Fluid Flow* **29**, 568–578.

Lund, T., Wu, X. & Squires, K. 1998 Generation of turbulent inflow data for spatially-developing boundary layer simulations. *J. Comput. Phys.* **140**, 233–258.

Maciel, Y., Rossignol, K.-S. & Lemay, J. 2006 Self-similarity in the outer region of adverse-pressure-gradient turbulent boundary layers. *AIAA J.* **44**, 2450–2464.

Maciel, Y., Simens, M. P. & Gungor, A. G. 2017 Coherent structures in a non-equilibrium large-velocity-defect turbulent boundary layer. *Flow Turbul. Combust.* **98**, 1–20.

Marin, O., Vinuesa, R., Obabko, A. V. & Schlatter, P. 2016 Characterization of the secondary flow in hexagonal ducts. *Phys. Fluids* **28**, 125101.

Marquillie, M., Ehrenstein, U. & Laval, J.-P. 2011 Instability of streaks in wall turbulence with adverse pressure gradient. *J. Fluid Mech.* **681**, 205–240.

Marusic, I., Chauhan, K. A., Kulandaivelu, V. & Hutchins, N. 2015 Evolution of zero-pressure-gradient boundary layers from different tripping conditions. *J. Fluid Mech.* **783**, 379–411.

Marusic, I., Mckeon, B. J., Monkewitz, P. A., Nagib, H. M., Smits, A. J. & Sreenivasan, K. R. 2010 Wall-bounded turbulent flows at high Reynolds numbers: Recent advances and key issues. *Phys. Fluids* **22**, 065103.

Mellor, G. L. & Gibson, D. M. 1966 Equilibrium turbulent boundary layers. *J. Fluid Mech.* **24**, 225–253.

Monty, J. P., Harun, Z. & Marusic, I. 2011 A parametric study of adverse pressure gradient turbulent boundary layers. *Int. J. Heat Fluid Flow* **32**, 575–585.

Nagib, H. M. & Chauhan, K. A. 2008 Variations of von Kármán coefficient in canonical flows. *Phys. Fluids* **20**, 101518.

Nagib, H. M., Chauhan, K. A. & Monkewitz, P. A. 2007 Approach to an asymptotic state for zero pressure gradient turbulent boundary layers. *Phil. Trans. R. Soc. A* **365**, 755–770.

Nagib, H. M., Christophorou, C. & Monkewitz, P. A. 2006 High Reynolds number turbulent boundary layers subjected to various pressure-gradient condition. *In Proc. IUTAM Symposium on One Hundred Years of Boundary Layer Research, G. E. A. Meier and K. R. Sreenivasan (eds.)* pp. 383–394.

Nickels, T. B. 2004 Inner scaling for wall-bounded flows subject to large pressure gradients. *J. Fluid Mech.* **521**, 217–239.

Örlü, R. & Vinuesa, R. 2017 Thermal Anemometry. *In Experimental Aerodynamics (ed. S. Discetti and A. Ianiro). CRC Press* .

Perry, A.E., Marusic, I. & Jones, M.B. 2002 On the streamwise evolution of turbulent boundary layers in arbitrary pressure gradients. *J. Fluid Mech.* **461**, 61–91.

Rodríguez-López, E., Bruce, P. J. K. & Buxton, O. R. H. 2016 On the formation mechanisms of artificially generated high Reynolds number turbulent boundary layers. *Boundary-Layer Meteor.* **160**, 201–224.

Rotta, J. C. 1953 On the theory of the turbulent boundary layer. *NACA Technical Report 1344* .

Sanmiguel Vila, C., Vinuesa, R., Discetti, S., Ianiro, A., Schlatter, P. & Örlü, R. 2017 On the identification of well-behaved turbulent boundary layers. *J. Fluid Mech.* **822**, 109–138.

Schlatter, P. & Örlü, R. 2010 Assessment of direct numerical simulation data of turbulent boundary layers. *J. Fluid Mech.* **659**, 116–126.

Schlatter, P. & Örlü, R. 2012 Turbulent boundary layers at moderate Reynolds numbers. Inflow length and tripping effects. *J. Fluid Mech.* **710**, 5–34.

Sillero, J. A., Jiménez, J. & Moser, R. D. 2013 One-point statistics for turbulent wall-bounded flows at Reynolds numbers up to $\delta^+ \simeq 2000$. *Phys. Fluids* **25**, 105102.

Skote, M., Henningson, D. S. & Henkes, R. A. W. M. 1998 Direct numerical simulation of self-similar turbulent boundary layers in adverse pressure gradients. *Flow Turbul. Combust.* **60**, 47–85.

Skåre, P. E. & Krogstad, P.-A. 1994 A turbulent equilibrium boundary layer near separation. *J. Fluid Mech.* **272**, 319–348.

Spalart, P. R. & Watmuff, J. H. 1993 Experimental and numerical study of a turbulent boundary layer with pressure gradients. *J. Fluid Mech.* **249**, 337–371.

Tennekes, H. & Lumley, J. L. 1972 A First Course in Turbulence. *Cambridge, MA: The MIT Press.* .

Townsend, A. A. 1956 The Structure of Turbulent Shear Flow. *Cambridge Univ. Press, Cambridge* .

Vinuesa, R., Bobke, A., Örlü, R. & Schlatter, P. 2016 On determining characteristic length scales in pressure-gradient turbulent boundary layers. *Phys. Fluids* **28**, 055101.

Vinuesa, R. & Örlü, R. 2017 Measurement of Wall-Shear Stress. *In Experimental Aerodynamics (ed. S. Discetti and A. Ianiro). CRC Press* .

Vinuesa, R., Örlü, R. & Schlatter, P. 2017 Characterisation of backflow events over a wing section. *J. Turbul.* **18**, 170–185.

Vinuesa, R., Rozier, P. H., Schlatter, P. & Nagib, H. M. 2014 Experiments and computations of localized pressure gradients with different history effects. *AIAA J.* **52**, 368–384.

Paper 3

3

Adverse-pressure-gradient effects on turbulent boundary layers: statistics and flow-field organization

Carlos Sanmiguel Vila[1], Ramis Örlü[2], Ricardo Vinuesa[2], Philipp Schlatter[2] Andrea Ianiro[1] and Stefano Discetti[1]

[1] Aerospace Engineering Group, Universidad Carlos III de Madrid, Leganés, Spain
[2] Linné FLOW Centre, KTH Mechanics, S-100 44 Stockholm, Sweden

Flow, Turbulence and Combustion (2017), vol. **99**, 589–612

This manuscripts presents a study on adverse-pressure-gradient turbulent boundary layers under different Reynolds-number and pressure-gradient conditions. In this work we performed Particle Image Velocimetry (PIV) measurements supplemented with Large-Eddy Simulations in order to have a dataset covering a range of displacement-thickness-based Reynolds-number 2,300< Re_{δ^*} <34,000 and values of the Clauser pressure-gradient parameter β up to 2.4. The spatial resolution limits of PIV for the estimation of turbulence statistics have been overcome via ensemble-based approaches. A comparison between ensemble-correlation and ensemble Particle Tracking Velocimetry was carried out to assess the uncertainty of the two methods. The effects of β, Re and of the pressure-gradient history on turbulence statistics were assessed. A modal analysis via Proper Orthogonal Decomposition was carried out on the flow fields and showed that about 20% of the energy contribution corresponds to the first mode, while 40% of the turbulent kinetic energy corresponds to the first four modes with no appreciable dependence on β and Re within the investigated range. The topology of the spatial modes shows a dependence on the Reynolds number and on the pressure-gradient strength, in line with the results obtained from the analysis of the turbulence statistics. The contribution of the modes to the Reynolds stresses and the turbulence production was assessed using a truncated low-order reconstruction with progressively larger number of modes. It is shown that the outer peaks in the Reynolds-stress profiles are mostly due to large-scale structures in the outer part of the boundary layer.

Key words: Wall turbulence, PTV, PIV, POD

1. Introduction

The quest for a better understanding of turbulent boundary layers (TBLs) is one of the main research goals of the turbulence community since many decades, as stated for instance in Marusic *et al.* (2010). Wall-bounded turbulence is present in many relevant fluid-flow problems such as the flow around wings, land and sea vehicles, or in turbines, compressors, etc. Simplified scenarios, such as the zero-pressure-gradient (ZPG) TBL developing over a flat plate, have been investigated to understand the fundamental aspects of wall-bounded turbulence. Unfortunately, ZPG conditions are nearly never encountered in real-life applications; instead, the majority of flow problems are under the effect of complex pressure gradients. In particular, adverse pressure gradients might produce flow separation with the consequent losses in performances. Under these conditions, the applicability of the knowledge from ZPG TBLs to decelerating boundary layers is still rather limited (Bobke *et al.* 2017; Monty *et al.* 2011). Despite the existence of a number of simulations and experiments on adverse-pressure-gradient (APG) TBLs (among many others, see *e.g.* Kitsios *et al.* (2016); Bobke *et al.* (2017); Knopp *et al.* (2014); Mellor & Gibson (1966); Monty *et al.* (2011); Nagano *et al.* (1998); Skåre & Krogstad (1994); Vinuesa *et al.* (2014)), there is still no clear understanding of the isolated effects of the imposed pressure-gradient, of

its upstream history and of the Reynolds number. The wider parametric space with respect to ZPG TBLs and the importance of history effects in the development of the flow are some of the reasons which make the study of these flows challenging. In an attempt to reduce the number of parameters which characterize the history effects, most of the APG studies are performed in a state of near-equilibrium. This implies that the mean velocity deficit in the outer part is self-similar at sufficiently high Reynolds numbers as discussed, among others, in Marusic *et al.* (2010). The streamwise evolution of the free-stream velocity $U_\infty(x)$ in an APG TBL under near-equilibrium conditions follows a power-law relation such that $U_\infty = C(x - x_0)^m$. Here C is a constant, x_0 is a virtual origin and the exponent m ranges between $-1/3 < m < 0$ (Townsend 1956).

Some important features of APG flows have already been clarified in the past decades. The most recognisable feature of an APG TBL is the more prominent wake of streamwise mean velocity profile (Nagano *et al.* 1993). The strengthened wake reflects the local state of the boundary layer as a consequence of the impact of history effects experienced by the flow. The wake strength is connected to the Clauser pressure-gradient parameter β (Clauser 1954), which is defined as $\beta = (\delta^*/\tau_w)(\mathrm{d}P/\mathrm{d}x)$, where δ^* is the displacement thickness, τ_w is the mean wall-shear stress, and $\mathrm{d}P/\mathrm{d}x$ is the derivative of the static pressure along the streamwise coordinate. As β increases, the mean velocity profile develops a larger wake region and the streamwise variance profile exhibits an outer peak, which is related to the development of more energetic large-scale motions (Monty *et al.* 2011). The appearance of more energetic structures in the outer region is also accompanied by larger values of the inner peak of the streamwise variance profile (Harun *et al.* 2013; Lee & Sung 2008).

On the other hand, there is some controversy on whether the logarithmic law of the wall still holds in APG TBL flows (Alving & Fernholz 1995; Knopp *et al.* 2015). There are studies where it is claimed that the law of the wall is still valid, but that the region occupied by the logarithmic law is progressively reduced when the pressure gradient is increased. Furthermore some studies report that the logarithmic region shifts with increasing pressure gradient strength below the one for canonical ZPG TBLs (Nagano *et al.* 1993; Nagib & Chauhan 2008). The streamwise velocity profile normalized with respect to the friction velocity is below the ZPG profile in the buffer region for progressively stronger APGs. Consequently the U^+ slope is found to increase with increasing APG, leading to lower values of the von Kármán constant κ (Bobke *et al.* 2017; Spalart & Watmuff 1993). Some authors, on the other hand, propose a dependence of the constants in terms of the pressure-gradient parameter in inner units $p_x^+ = (\nu/\rho u_\tau^3)(dP/dx)$ (Nickels 2004). In other works it is argued that the existence of the law of the wall is conditioned to the near-equilibrium state (Gungor *et al.* 2016).

The effect of the pressure gradient on statistical properties poses thus a challenge far from being assessed. One pathway to obtain a better understanding of APG TBLs is based on the dynamics of the coherent structures. Large-scale features are indeed known to provide a significant contribution to the turbulent kinetic energy and Reynolds stress production in wall-bounded flows (Balakumar & Adrian 2007). It is thus expectable that a better understanding of the pressure-gradient effects on the large-scale features in TBL flows will allow to improve the current turbulence models and flow control strategies. The influence of the pressure gradient can be observed in Marušić & Perry (1995), which documents that attached-eddy-based models, which reproduce well ZPG TBLs statistical properties, fail when they are used to reconstruct the shear-stress distributions in the outer layer of APG TBLs. Consequently, it is concluded that large-scale motions in the outer layer have to be taken into account when modelling the turbulence production. Spectral and scale-decomposition analyses (Harun *et al.* 2013) confirm that the large scales are more energized throughout the entire adverse-pressure-gradient boundary layer, especially in the outer region. Harun *et al.* (2013) reports that the spectral distribution of energy in the wake region of APG TBLs is similar to that of the ZPG TBLs; nevertheless, the three-dimensional spatial correlations reported in Maciel *et al.* (2017) show that large-scale structures in the outer region of large-defect boundary layers are shorter in the streamwise direction and more inclined with respect to the wall.

In the present study, APG TBLs developing on a flat plate are experimentally studied in order to shed some light on the effect of the large-scale motions on the Reynolds stresses via combined analysis of statistics and modal decomposition. To this end, an experimental campaign was carried out by means of Particle Image Velocimetry (PIV) in a streamwise/wall-normal plane. Flow conditions were characterised in terms of the displacement-thickness-based Reynolds number Re_{δ^*} and pressure-gradient parameter β by means of hot-wire anemometry (HWA) measurements performed in the Reynolds-number range $8,000 < Re_{\delta^*} < 34,000$, and for pressure-gradient magnitudes of $\beta = 1.3$ and 2.4. Turbulence statistics were compared with Large-Eddy Simulation (LES) results of ZPG TBLs at similar Reynolds numbers (Eitel-Amor *et al.* 2014) and LES from APG TBLs at comparable values of the Clauser pressure-gradient parameter β (Bobke *et al.* 2017). The effects of APGs on the large-scale structures are addressed with Proper Orthogonal Decomposition (POD) of the flow-fields.

The structure of the article is as follows: in §2 we report a description of the experimental setup, providing details on the streamwise evolution of β; in §2 we also assess the accuracies of different PIV approaches ranging from Ensemble Particle Tracking Velocimetry (EPTV) to single-pixel and standard PIV, using as a reference well-resolved hot-wire anemometry measurements. In §3 the discussion focuses on the comparison of flow statistics, taking into account also the effect of the streamwise evolution of β. Section §4 reports the modal decomposition of the flow allowing to assess the effect of β on the large-scale organization. Following an approach similar to Wu & Christensen (2010), the instantaneous fluctuating velocities are decomposed into large-scale and small-scale features using POD modes in the streamwise/wall-normal planes.

2. Experimental setup

2.1. *Wind-tunnel and boundary-layer flow conditions*

The experiments were performed in the *Minimum Turbulence Level* (MTL) closed-loop wind tunnel located at KTH Royal Institute of Technology in Stockholm. The test section is 7 m long with a cross-sectional area of 0.8×1.2 m^2 (height $\times$ width). The MTL is capable of reaching a maximum speed of 70 m/s with a streamwise velocity fluctuation intensity of approximately 0.025% of the free-stream velocity at a test speed of 25 m/s. The air temperature can be controlled with an accuracy of ± 0.05 K by means of a heat exchanger. More details regarding the MTL can be found in (Lindgren & Johansson 2002; Österlund 1999).

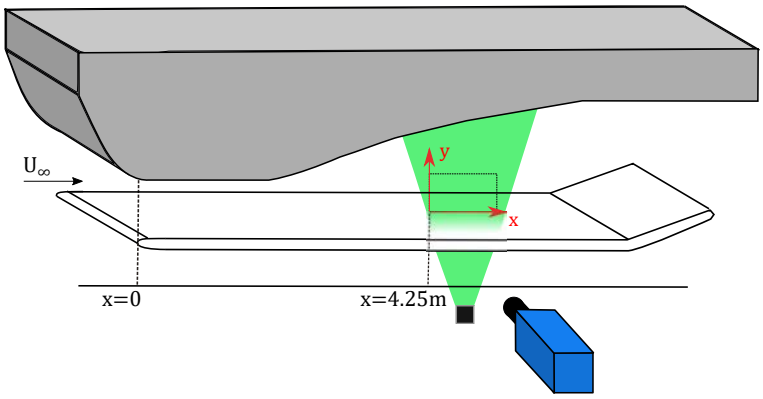

Figure 1: Description of the roof geometry and schematic view of the experimental setup. The wall insert to obtain the desired pressure-gradient evolution is indicated in grey. Note that both the upstream and downstream ends are flash-mounted with the tunnel roof.

The desired streamwise evolution of the pressure gradient was established by means of wall inserts made of foam and hung by threaded rods. The roof shape could be further modified by adjusting the wind tunnel ceiling, which comprises a total of six panels allowing vertical displacement The wall inserts were designed iteratively. The first trial shape of the ceiling was designed by performing Reynolds-Averaged Navier–Stokes (RANS) computations. From this geometry the final shape was iterated using as a reference the β distribution obtained from hot-wire measurements. As described in Vinuesa *et al.* (2014), the RANS computations were carried out by considering the two-equation Shear-Stress Transport (SST) model (Menter 1994), implemented in the CFD code Fluent (v.6.3).

The turbulent boundary layers developed on a smooth aluminium flat plate of 6 m length and 26 mm thickness, spanning the entire width of the wind tunnel and suspended 15 cm above the wind-tunnel floor. The ceiling geometry was designed with a converging-diverging shape (as schematically shown in Figure 1), thus resulting in an initially accelerated flow (*i.e.* a favourable pressure gradient), a region of nearly zero-pressure-gradient conditions and finally a region of adverse pressure gradient. The flow was initially accelerated by reducing the tunnel test section height from 0.80 m to approximately 0.60 m. The flat plate was placed at a vertical distance of 0.42 m from the roof at the throat. The leading edge of the flat plate was located right at the beginning of the roof throat. Downstream of the leading edge of the flat plate, the ceiling geometry was designed such that a ZPG was maintained for approximately 1.0 m. From that location on, two different adverse-pressure-gradient conditions were imposed by changing the roof geometry in the divergent part.

The pressure distribution is expressed in terms of the pressure coefficient C_p, which is defined for an incompressible flow as $C_p = (P - P_{ref})/(1/2\rho U_{ref}^2) = 1 - (U_\infty/U_{ref})^2$, where P is the local static pressure, P_{ref} is the static pressure in the ZPG region (measured at $x = 0.6$ m), U_∞ is the local free-stream velocity and U_{ref} is the reference free-stream velocity at $x = 0.6$ m. The experiments were carried out for three different inflow velocities, *i.e.* $U_{ref} = 6$, 12 and 30 m/s. The evolution of C_p along the streamwise direction for the two aforementioned roof geometries is presented in Figure 2.

The flat plate has a leading edge following the shape of a modified super ellipse and is equipped with a 1.5 m long trailing-edge flap in order to modify the position of the stagnation point. In the present experimental campaign, the flap position was set to 10°. For a more detailed description the reader is referred to Österlund (1999). The boundary layer was tripped close to the leading edge with *DYMO* tapes (with the embossed letter 'V' pointing in the flow direction and a nominal height of 0.3 mm) in combination with a 1.6 mm height turbulator. Care was taken to ensure that the turbulent boundary layer at the measurement location was not affected by tripping effects (Sanmiguel Vila *et al.* 2017*b*). The values of the Reynolds numbers and β for the various cases under consideration are reported in Table 1. The corresponding values of the shape factor $H_{12} = \delta^*/\theta$ (with θ being the momentum thickness) and of the viscous length $l^* = \nu/u_\tau$ (with ν being the kinematic viscosity and u_τ being the friction velocity) are also indicated for reference. In order to calculate δ^* and θ, the boundary-layer thickness needs to be determined, since it is the upper limit of integration. This quantity is rather ambiguous in APG TBLs owing to possible gradients of the streamwise velocity beyond the boundary-layer edge (Vinuesa *et al.* 2016). In this work, δ_{99} has been calculated according to the procedure reported in Vinuesa *et al.* (2016), which is based on the diagnostic-plot concept (Alfredsson *et al.* 2011).

Empirical evidence covering a wide range of Reynolds number and pressure-gradient parameters (Vinuesa *et al.* 2016) has established that the classical boundary-layer edge corresponding to U/U_∞ equal to 0.99 is found where $u'/(U_\infty\sqrt{H_{12}}) = 0.02$. This allows to calculate U_∞ in an iterative way (since the shape factor H_{12} is not known *a priori*), and once the value of U_∞ is estimated, the value of δ_{99} can be obtained from the definition $\delta_{99} = y(U = 0.99U_\infty)$. The mean wall-shear stress has been deduced from hot-wire measurements in the sublayer (viscous sublayer and buffer region). The composite profile given by Chauhan *et al.* (2009) is used to fit the experimental data

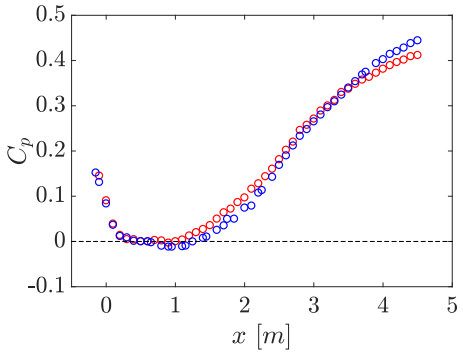

Figure 2: Distributions of pressure coefficient C_p along the streamwise direction for two wall-insert configurations where (○) corresponds to the roof configuration 1 and (○) to the roof configuration 2. Note that the reference pressure for C_p is taken at $x = 0.6$ m.

up to $y^+ = 15$ and correct the absolute wall position. The resulting distributions of β along the streamwise direction are reported in Figure 3 for both roof configuration 1 and 2. Note that the β distributions reported in Figure 3 are relative to $Re_\tau = 1,920$ and 1,880, respectively; however, the streamwise evolution of β has shown very weak dependence on U_{ref}.

2.2. *Particle Image Velocimetry*

Particle Image Velocimetry was used to perform velocity field measurements in a streamwise/wall-normal plane at a streamwise location of $x = 4.25$ m from the leading edge of the flat plate. In order to enable laser illumination for the PIV measurements an aluminium section of the flat plate was replaced with a transparent acrylic glass (polymethyl metacrilate) insert. The flow was seeded with 1 μm diameter Di-Ethyl-Hexyl-Sebacate (DEHS) droplets produced with a smoke generator. Seeding particles were injected into the flow at the end of the test section to minimize flow perturbation and were then recirculated through the wind tunnel. The seeded flow was illuminated by a Quanta Ray double cavity Nd:YAG laser with a pulse energy of 400 mJ at 15 Hz. Laser light passed through the transparent section of the flat plate. The thickness of the laser sheet was approximately 1 mm.

The acquisition of the PIV images was performed with an *ANDOR Zyla sCMOS 5.5MP* camera (2560 × 2160 pixel array, 6.5 μm × 6.5 μm pixel size). The camera was equipped with a Tokina 100 mm lens. The lens aperture was set to $f/\# = 11$ and the objective was slightly set out of focus in order to obtain large particle images and avoid peak locking. The field of view was designed to fit the entire boundary-layer thickness with a spatial resolution of 16 pixels/mm. With the provided optical setup, the diffraction-limited particle image diameter was 15.7 μm, and the depth of field was 38 mm. An ensemble of 1,150 image couples was acquired for each experiment. Image quality was improved by removing laser reflections and illumination background using the POD-based approach described in Mendez *et al.* (2017).

A custom made PIV software developed at University of Naples Federico II was used to perform digital cross-correlation analysis of the particle images (Willert & Gharib 1991) to calculate the velocity fields. The interrogation strategy is an iterative multi-grid/multi-pass (Soria 1996) image deformation algorithm (Scarano 2001), with final interrogation windows of 40 × 40 pixels with 75% overlap (the final vector spacing is equal to 10 pixels, *i.e.* 0.6 mm, which results in at least 140 vectors throughout the boundary layer thickness). B-spline interpolation schemes were used to improve the accuracy of the PIV processing (Astarita & Cardone 2005). The vector validation to identify invalid vectors was carried out with a universal median test (Westerweel & Scarano 2005) on a 3 × 3 vectors kernel and an error threshold equal to 2. Discarded vectors were replaced with a distance-weighted average of neighbouring valid vectors.

Table 1: Boundary-layer parameters of the various cases in the present experimental database.

β [−]	U_∞ [m/s]	Re_{δ^*} [−]	Re_θ [−]	Re_τ [−]	δ_{99} [mm]	H_{12} [−]	l^* [μm]	Symbol Color	Roof Configuration
1.3	9.4	13,940	9,070	1,920	98.9	1.54	51.6	●	1
1.3	24.1	29,950	20,450	4,130	90.1	1.46	21.8	■	1
2.4	4.8	8,640	5,340	1,070	108.4	1.62	101.1	★	2
2.4	9.1	15,850	9,790	1,880	104.3	1.62	55.4	●	2
2.4	23.4	33,770	22,240	4,200	95.6	1.52	22.8	■	2

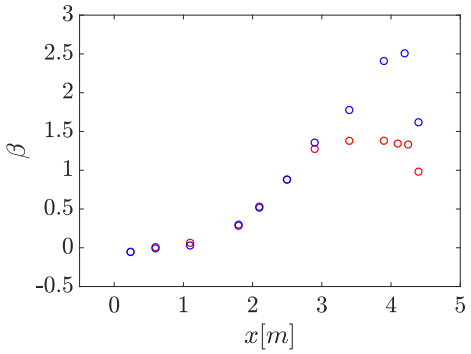

Figure 3: Streamwise distribution of the Clauser pressure-gradient parameter β where (○) corresponds to the roof configuration 1 and (○) to the roof configuration 2.

2.3. *Hot-wire anemometry measurements*

Hot-wire anemometry measurements were carried out to assess the quality of the PIV data and to characterise the pressure distribution along the streamwise direction. The measurements were performed by means of a home-made single hot-wire probe resembling a standard *Dantec* boundary-layer probe, *i.e.*, a 55P15. The hot-wire probe consists of a fully-etched Platinum wire of 525 μm length and nominal diameter of 2.5 μm, which was soldered to conical prongs with diameters of around 30 μm. Voltage signals from the hot-wire were recorded using a *Dantec StreamLine* 90N10 frame in conjunction with a 90C10 constant-temperature anemometer module operated at a resistance overheat ratio of 80%. An offset and gain were applied to the top-of-the-bridge voltage in order to match the voltage range of the 16-bit A/D converter. A low-pass filter of 30 kHz cut-off frequency was used prior to the data acquisition in order to avoid aliasing. The calibration of the hot-wire was performed in-situ using as reference a Prandtl tube located parallel to the incoming freestream. The Prandtl tube was connected to a micromanometer of type *FC0510 (Furness Control Limited)*, which was also employed to record the ambient temperature and pressure during the calibration and the experiments. Data acquired in the calibration was fitted to a fourth-order polynomial curve (Örlü & Vinuesa 2017). The uncertainty of hot-wire measured mean velocity and turbulence intensity is estimated to be 1% and 2%, respectively.

Hot-wire measurements were acquired with a sufficiently large number of points within the viscous sublayer and the buffer region in order to correct for the absolute wall position and determine the friction velocity (Örlü *et al.* 2010) without relying on log-law constants.

2.4. *Spatial resolution effects of PIV on turbulence statistics*

The turbulence statistics evaluated with PIV can be affected by limited spatial resolution issues due to the finite size of the interrogation window (Adrian & Westerweel 2011; Foucaut & Stanislas

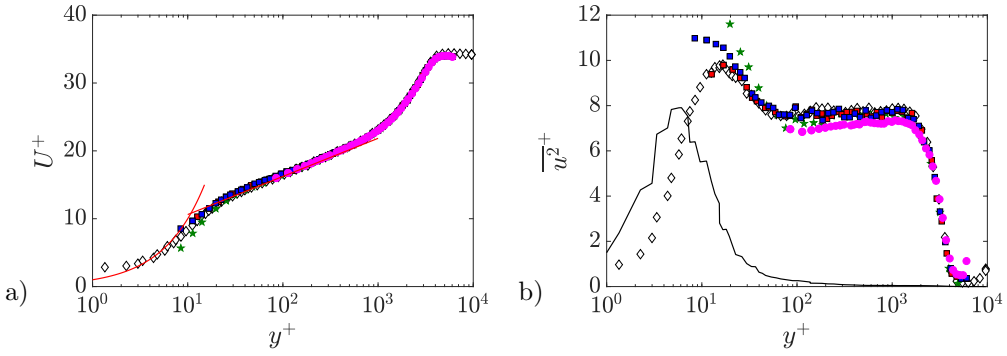

Figure 4: Comparison between HWA (◇), standard-PIV (●), *single-pixel* (★), Ensemble Particle Tracking Velocimetry (EPTV) with top-hat (■) and polynomial fit approach (■) for the case with $Re_\tau = 4,130$ and $\beta = 1.3$. a) Mean streamwise velocity in inner scaling and b) streamwise normal Reynolds stress in inner scaling. Additionally, red lines (-) depict the linear profile $U^+ = y^+$ and the logarithmic profile $U^+ = \frac{y^+}{0.41} + 5$ in a) and the black line (-) depicts the wall-normal velocity gradient $10 \cdot \partial U^+/\partial y^+$ profile in b).

2002; Foucaut *et al.* 2004; Lee *et al.* 2016). This induces systematic errors on the mean velocity in the presence of a mean velocity gradient. The second-order statistics are similarly affected by limited resolution issues, since small-scale features are filtered out in the PIV processing, and so is their energy content. On the other hand, the effect of random noise on the shape of the cross-correlation peaks is to produce a white noise distribution over the whole spectrum (Raiola *et al.* 2015), which under certain conditions might fictitiously compensate the previous modulation effect (Atkinson *et al.* 2014).

In this section two different approaches to improve the spatial resolution and accuracy of turbulence statistics are compared:

- Ensemble-correlation using the probability density function (pdf) deconvolution approach outlined in Scharnowski *et al.* (2012) to extract second-order statistics. The interrogation region size was equal to 41×11 pixels. A symmetric double-correlation method (Avallone *et al.* 2015) was used to improve convergence. Additionally, the correlation maps were spatially averaged over a region of 400×4 pixels (in the streamwise and wall-normal directions).
- Ensemble Particle Tracking Velocimetry (EPTV), as in Agüera *et al.* (2016); Cowen & Monismith (1997); Kähler *et al.* (2012*a*), with biased search using PIV as a predictor Keane *et al.* (1995). The bin is performed on 400×4 pixels regions. The computation of turbulence statistics is carried out with a standard *top-hat* bin averaging and with a polynomial-fit-based method (Agüera *et al.* 2016), which estimates the statistical moments around a second-order polynomial fit applied on the velocity vectors within each bin. This method is here assessed for the first time in wall-bounded flows, and it has demonstrated in shear-free flows to reduce systematic errors due to unresolved mean velocity gradients.

The accuracy of the various approaches is tested on a case with $\beta = 1.3$ and $Re_\tau = 4,130$; the results are presented in Figure 4. Hot-wire measurements are included for reference. No spatial resolution effects are expected in the overlap region since the viscous-scaled wire length of the hot-wire, defined as $L^+ = L/l^*$ (where L is the active hot-wire length), is $L^+ \approx 24$ (Hutchins *et al.* 2009; Segalini *et al.* 2011). The PIV results reported in Figure 4 are in good agreement with the mean velocity profile measured by means of hot-wire anemometry from the wake region down to the overlap region ($y^+ \approx 100$). The inner-scaled streamwise variance profile $\overline{u^2}^+$ exhibits an intensity

Table 2: Boundary-layer parameters for the LES dataset.

β	Re_{δ^*}	Re_θ	Re_τ	H_{12}	Case	Reference	Symbol/Color
0	8,705	6,380	1,940	1.36	ZPG	Eitel-Amor *et al.* (2014)	
2.4	2,290	1,330	315	1.72	increasing β	Bobke *et al.* (2017, 2016)	
2.4	5,130	2,930	580	1.75	decreasing β	Bobke *et al.* (2017, 2016)	

reduction of about 10% from $y^+ \approx 100$ to $y^+ \approx 2,000$. Nevertheless, the shape of the profile is correctly estimated if compared with the hot-wire profile. The attenuation is thus to be ascribed to modulation of the small-scale fluctuations. Nonetheless, considering that the modulation appears to be almost independent of the wall-normal position, it can be hypothesized that the spectral content of energy of the small scales exhibits small changes for $100 \leq y^+ \leq 2,000$ if compared to the large-scales contribution (as in Figure 6 of Monty *et al.* (2011)). Thus, the energy spatial distribution obtained from PIV data is only weakly affected by non-uniform modulation effects.

The ensemble-correlation and ensemble-PTV methods lead to a very good agreement with the reference mean velocity profile from hot-wire measurements down to approximately $y^+ = 10$. It has to be underlined here that the case under analysis is one of the two cases with higher Re_τ, and thus one of the most challenging of the dataset from the standpoint of the spatial resolution. Within the inner layer the ensemble-correlation approach is biased towards smaller velocity values than the reference profile measured by the hot-wire. This bias can be attributed to the residual reflections present on the images after pre-processing, which affect the computed correlation maps by stretching them along the wall-parallel direction, as well as biasing their peak towards zero-displacement. A thorough assessment of bias errors in ensemble correlation near walls is reported in Kähler *et al.* (2012*b*), in which it is suggested to use ensemble correlation or PTV for wall distances below half the PIV interrogation window size, while PTV is superior for wall distances smaller than the particle image diameter. Both ensemble-correlation and ensemble-PTV measurements of the $\overline{u^2}^+$ are in good agreement with the hot-wire data in the outer layer. The ensemble-correlation approach overestimates $\overline{u^2}^+$ for $y^+ < 100$. Similarly to the bias in the mean velocity profile, this error can be attributed to the stretching of the correlation peak along the wall-parallel direction due to the residual reflections on the pre-processed images. The ensemble-PTV approach is able to follow the reference profile well within the inner layer with a remarkable improvement when using the polynomial fit approach (Agüera *et al.* 2016). Indeed, in the regions where $\partial U^+/\partial y^+$ attains its larger values the residual unresolved velocity gradient within the interrogation window might lead to significant overestimation of the normal Reynolds stresses (Agüera *et al.* 2016).

On the basis of this assessment, in the following sections statistics obtained exclusively using the ensemble-PTV approach with polynomial fit (Agüera *et al.* 2016) will be shown. The data obtained from standard-PIV will be used only for the purpose of analyzing the large-scale flow-field organization using Proper Orthogonal Decomposition, as discussed in §4.

3. Turbulence statistics

In this section the influence of β and Re on the turbulence statistics is addressed. The main focus is on the effect of different local β values and streamwise evolutions of β on first- and second-order statistics while the discussion of the impact on the flow organization is postponed to §4. Data from well-resolved LESs of a ZPG TBL (Eitel-Amor *et al.* 2014) and APG TBLs (Bobke *et al.* 2017, 2016) are included to further support the discussion. The simulation parameters for these cases are reported in Table 2. The evolution of β in the two APG LES cases as a function of Re_τ is reported in Figure 5.

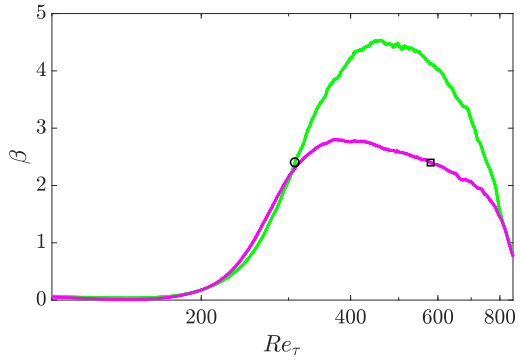

Figure 5: Streamwise distributions of the Clauser pressure-gradient parameter β for the two APG LES cases. Colours are reported in Table 2. Circle symbol ($\circ$) indicates conditions of the increasing-β case and square symbol ($\square$) indicates those of the decreasing-β case, as reported in Table 2.

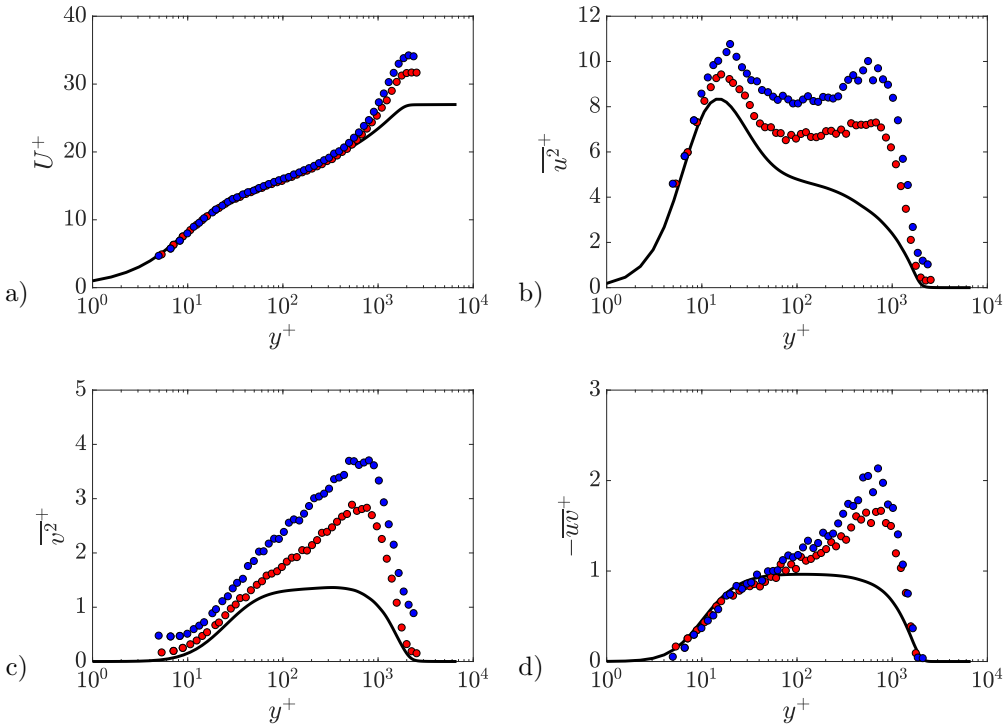

Figure 6: Inner-scaled profiles for a ZPG ($-$), and APG TBLs with $\beta = 1.3$ (●) and $\beta = 2.4$ (●) at $Re_\tau \simeq 1,900$. a) Mean streamwise velocity, b) streamwise normal Reynolds stress, c) wall-normal Reynolds stress and d) Reynolds shear stress.

3.1. *Effect of β at matched Reynolds number*

In Figure 6 a comparison between inner-scaled turbulence statistics for $\beta = 1.3$ (●) and $\beta = 2.4$ (●) at matched friction Reynolds number $Re_\tau \approx 1,900$ is reported. At this point a comment on the choice of the definition of the Reynolds number is appropriate. In the case of strongly-decelerated APG TBLs, the friction velocity (and hence the friction Reynolds number Re_τ) would approach

zero, and would therefore be inappropriate to define the state of the boundary layer. However, for the present rather mild pressure-gradient conditions, both Re_θ and Re_{δ^*} develop similarly to Re_τ (Bobke *et al.* 2017; Vinuesa *et al.* 2017*b*); thus, Re_τ is an appropriate Reynolds number to study the Re-dependence of the cases analyzed here. As a baseline for comparison, Figure 6 also reports velocity and Reynolds-stress profiles from a ZPG TBL simulation at matched $Re_\tau \approx 1,900$ (Eitel-Amor *et al.* 2014). Doing so, the effect of the imposed pressure gradient can be assessed. The APG mean velocity profiles collapse with the ZPG profile from the wall up to $y^+ \approx 200$, thus showing no significant discrepancy with the law of the wall. A more prominent wake is observed in APG TBLs when comparing with the ZPG case. This is due to the reduced wall-shear stress present in APGs, which is connected to the increased wall-normal convection. The increase of momentum defect in the wake, reported for instance in Gungor *et al.* (2016); Harun *et al.* (2013); Kitsios *et al.* (2016); Monty *et al.* (2011); Skåre & Krogstad (1994), strongly depends on the flow history and accumulated effect of the APG, as discussed in Bobke *et al.* (2017).

The Reynolds normal-stress profiles in the APG TBLs exhibit an outer peak located at around $500 \leqslant y^+ \leqslant 700$, which is not present in the ZPG case. The amplitude of the outer peak increases with β. As addressed in Harun *et al.* (2013), the increase of the inner-scaled Reynolds stresses is not just due to the lower value of the friction velocity used to scale the profile, but it is ascribed to enhanced large-scale motions in the outer region. This is further supported by the distribution of the Reynolds shear stress $-\overline{uv}^+$, which plays a leading role in the turbulence production, as discussed in §3.3. It is worth noting that the inner-scaled edge velocity increases with β, a fact that is connected to the presence of the additional mean shear in the outer region due to the pressure gradient (Gungor *et al.* 2016; Maciel *et al.* 2006).

3.2. *Effect of Reynolds number at matched β*

Turbulence statistics are compared at fixed $\beta \approx 2.4$ for Re_τ values of 1,070, 1,880 and 4,200. The profiles are shown in inner scaling in Figure 7. Statistics from LES of APG TBL at matched local β (Bobke *et al.* 2017, 2016) at Re_τ values of 315 and 580 are also included for comparison. Note that, in the cases under consideration, although the local value of β is matched, the $\beta(x)$ evolution is not the same for all cases (see Figures 3 and 5). The streamwise velocity variance profiles for the experimental cases are characterized by inner and outer peaks with limited intensity variation in the investigated Reynolds-number range. This is in agreement with Hutchins & Marusic (2007), which reported that the large-scale contribution increases weakly with the Reynolds number. The Reynolds-number range under investigation is, however, not large enough to draw firm conclusions about the amplitude of the outer peak documented in Aubertine & Eaton (2006).

Considering the relatively weak influence of the Reynolds number at matched β on the magnitude of inner/outer peaks, the differences observed between LES and experimental data can be attributed mostly to the different flow histories present in the various cases (see Figures 3 and 5). For the case of decreasing β, all the Reynolds stresses have a larger outer peak, as a result of a stronger accumulated β history experienced throughout its development (see Bobke *et al.* (2017)). Moreover, as reported in Vinuesa *et al.* (2017*a*), low-Re TBLs are more sensitive to APG effects, especially when it comes to the development of energetic structures in the outer region of the boundary layer. This therefore justifies the stronger outer peak in the low-Re TBL. Similarly, the LES case with increasing β shows an attenuated outer peak in the $\overline{u^2}^+$ profile, due to reminiscence of lower pressure-gradients. The LES and experimental data at matched local β support the conclusion that the outer-layer features are strongly dependent on the streamwise evolution of β, thus hindering a comparison of APG TBLs at matched Reynolds number and β if the upstream history is not known, as it is often the case in several (comparative) studies in the literature.

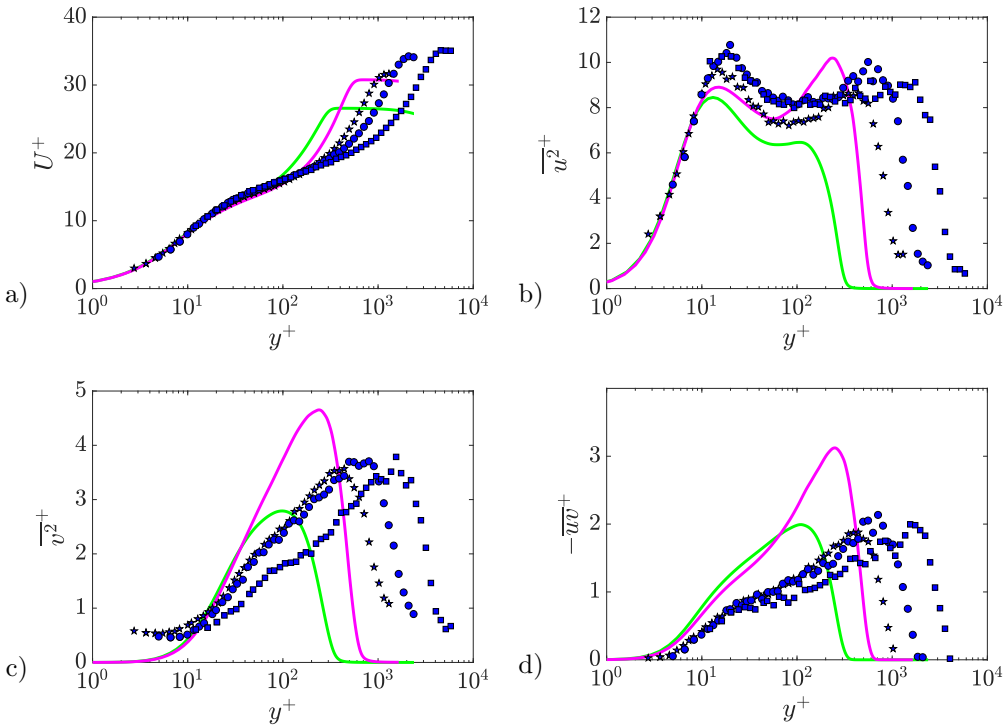

Figure 7: Inner-scaled profiles for $\beta = 2.4$ at varying Reynolds number. PIV measurements are represented with symbols: (★) $Re_\tau = 1,070$, (●) $Re_\tau = 1,880$ and (■) $Re_\tau = 4,200$. LES profiles are represented with solid lines: (−) $Re_\tau = 315$ and (−) $Re_\tau = 580$. a) Mean streamwise velocity, b) streamwise normal Reynolds stress, c) wall-normal Reynolds stress and d) Reynolds shear stress.

3.3. *Turbulence production*

Further insight on the effect of the APG on the large-scale dynamics can be obtained via analysis of the turbulence production. The general equation for turbulence production in inner scaling, assuming a mean spanwise velocity of zero (Pope 2000), can be written as follows:

$$P^+ = -\overline{uv}^+ \frac{\partial U^+}{\partial y^+} - \left(\overline{u^2}^+ - \overline{v^2}^+\right) \frac{\partial U_\infty^+}{\partial x^+} - \overline{uv}^+ \frac{\partial V^+}{\partial x^+}. \tag{1}$$

Through an order-of-magnitude analysis it can be shown that in ZPG or in mild pressure-gradient TBLs, the second and third terms of the right-hand side of Eq. 1 are negligible with respect to the first one (Harun *et al.* 2013). This allows for a simplified estimation of the turbulence production as:

$$P^+ \approx -\overline{uv}^+ \frac{\partial U^+}{\partial y^+}. \tag{2}$$

The inner-scaled turbulence production in premultiplied form (calculated from Eq. 1) is reported in Figure 8 a) for all the cases under study. The visual advantage of the premultiplied form P^+y^+ is that, when represented in semi-logarithmic form, equal areas correspond to equal contributions to the production (Marusic *et al.* 2010). While the ZPG TBL is characterized by a relatively flat P^+y^+ distribution, in the case of the APG TBL an increasing production is observed in the outer layer, in agreement with Bradshaw (1967); Harun *et al.* (2013). This depicts

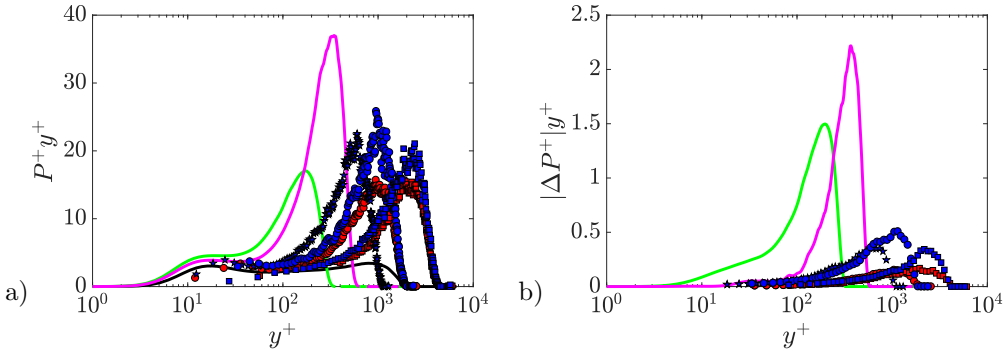

Figure 8: Premultiplied turbulence production in inner scaling. Colours and symbols are reported in Tables 1 and 2: a) turbulence production estimated according to Eq. 1 and b) error in the estimation of the turbulent production due to Eq. 2. Note that the ordinate in b) is zoomed in to enhance the minor differences.

a scenario of increasingly more energetic large-scale motions in the outer layer (Harun *et al.* 2013). Interestingly, the position of the production peak corresponds to the location of the peak in the $\overline{uv}$ profile and is weakly dependent on β at fixed Re_τ when scaled in inner units. This means that the main effect of the pressure gradient is to change the distribution of energy through the boundary layer, displacing large energetic structures from the near-wall region to the outer region (as it will be further highlighted in §4). This originates from the fact that the scale separation is fixed when considering TBLs at matched Re_τ. The APG thickens the boundary layer and convects flow in the wall-normal direction, but, when carrying out the comparisons at fixed Re_τ, the outer peak is at approximately the same location.

The effect of Re_τ is to shift the production peak towards higher y^+. LES data again confirm the importance of history effects: even though both cases are for $\beta \approx 2.4$, the producion peak intensity for the case of increasing β is similar to the experimental case at $\beta = 1.3$. Conversely, for the case with decreasing β, the observed production peak intensity would be compatible with a case with constant β higher than 2.4.

As stated above, the use of Eq. 2 results in an approximation to P^+, and the difference between the production obtained from Eqs. 1 and 2 is denoted by ΔP^+. Inner-scaled profiles of ΔP^+ in premultiplied form are reported in Figure 8 b). Since the turbulence production peaks are located at the same position as those of $\overline{uv}^+$, the maximum error in the estimation of the turbulent production (due to the use of. Eq. 2) is located at the position where the maximum values of P^+y^+ are observed in Figure 8a). Note that the third term on the right-hand side in Eq. 2, which involves $\overline{uv}^+$, becomes progressively larger with increasing values of β. The maximum values of ΔP^+y^+ reach around 6% and 10% of the maxima in P^+y^+ in the two LES cases. This is reduced to around 2% in the higher-Re, experimental cases. Therefore, the approximation incurred in Eq. 2 appears to be reliable at moderately-high Reynolds numbers, and with mild pressure-gradient magnitudes.

4. POD and modal contribution to turbulence statistics

In this section a modal analysis by means of Proper Orthogonal Decomposition (Berkooz *et al.* 1993) is carried out using data from standard PIV analysis. The effect of β and of the Reynolds number on the modal energy distribution and on the topology of the spatial modes is investigated and discussed. The modes are used to perform a low-rank approximation of the flow fields and to address the relative importance of large and small scales on the turbulence statistics.

4.1. *POD fundamentals*

Consider the streamwise wall-parallel and crosswise wall-normal fluctuating velocity components, both functions of space $\underline{x} = (x, y)$ and time t, $u(\underline{x}, t)$ and $v(\underline{x}, t)$. These quantities can be approximated as a linear combination of basis functions $\phi_n(\underline{x})$ as:

$$u(\underline{x}, t) \approx \sum_{n=1}^{N_m} a_n(t)\phi_n(\underline{x}), \tag{3}$$

where $a_n(t)$ are time-dependent coefficients. Note that an equivalent expression can be written for v. The symbol N_m is used to indicate the number of basis functions used. In the limit $N_m \to \infty$ the approximation becomes exact. Proper Orthogonal Decomposition identifies orthonormal basis functions, *i.e.* the scalar product between whichever pair of functions of the set is $(\phi_n(\underline{x}), \phi_p(\underline{x})) = \delta_{np}$, with δ_{np} being the Kronecker delta (equal to 1 for $n = p$ and to 0 elsewhere). POD can be used to extract information regarding the coherent structures in turbulent flows since it sorts the spatial basis functions $\phi_n(\underline{x})$ according to its mean square projections $\lambda_n = \langle (u(\underline{x}, t), a_n(t)\varphi_n(\underline{x}))\rangle$, with $\langle ...\rangle$ indicating an ensemble average. The identification of the basis functions corresponds to the solution of the integral eigenvalue problem having with kernel the two-point correlation tensor of u, with λ_n being the eigenvalues and $\phi_n(\underline{x})$ being the eigenvectors.

Consider a set of N_t realizations, each one consisting of N_p values along the spatial coordinate $\underline{x}$, with $N_t < N_p$. The integral equation has a discrete set of solutions: N_t eigenvalues λ_n of the two-point correlation matrix and N_t basis functions $\phi_n(\underline{x})$. Following the snapshot method (Sirovich 1987), each realization can be treated as a N_p-dimensional vector and the data can be arranged in a $N_t \times N_p$ snapshot matrix:

$$\underline{\underline{u}} = \begin{bmatrix} u(x_1, t_1) \cdots u(x_{N_p}, t_1) \\ \vdots \quad \ddots \quad \vdots \\ u(x_1, t_{N_t}) \cdots u(x_{N_p}, t_{N_t}) \end{bmatrix}; \; \underline{\underline{v}} = \begin{bmatrix} v(x_1, t_1) \cdots v(x_{N_p}, t_1) \\ \vdots \quad \ddots \quad \vdots \\ v(x_1, t_{N_t}) \cdots v(x_{N_p}, t_{N_t}) \end{bmatrix}. \tag{4}$$

Since the focus of this analysis is on the Reynolds stresses, it is suitable to extract a basis which is optimal in terms of turbulent kinetic energy, *i.e.* which maximizes both the u and v energy content. It is important to underline that, since planar PIV only provides two components of the velocity field, the analysis here is limited to the turbulent kinetic energy associated to streamwise and wall-normal velocity fluctuations. From this point on this would be referred as in-plane turbulent kinetic energy or simply TKE. The two-point correlation matrix can be written as $\underline{\underline{C}} = \underline{\underline{u}}\,\underline{\underline{u}}^T + \underline{\underline{v}}\,\underline{\underline{v}}^T$, where the superscript ^{T} refers to the matrix transpose. Solving the eigenvalue problem of $\underline{\underline{C}}$ returns the eigenvalues λ_n and the left and right eigenvector matrices. The left and right eigenvector matrices are respectively the matrix $\underline{\underline{\psi}}$ containing in its columns the normalized temporal modes $\underline{a_n}/|\underline{a_n}|$ (which are orthonormal vectors of length N_t and unitary norm) and its inverse (*i.e.* its transpose). Note that the columns of $\underline{\underline{\psi}}$ form a basis of rank N_t and that the eigenvalues λ_n are representative of the in-plane turbulent kinetic energy contribution of each mode. The orthonormal spatial modes $\phi_n(\underline{x})$ can then easily be computed as $\underline{\underline{\Sigma_u}}\,\underline{\underline{\phi_u}} = \underline{\underline{\psi}}^T\,\underline{\underline{u}}$ and $\underline{\underline{\Sigma_v}}\,\underline{\underline{\phi_v}} = \underline{\underline{\psi}}^T\,\underline{\underline{v}}$ where $\underline{\underline{\Sigma_u}}$ and $\underline{\underline{\Sigma_v}}$ are diagonal matrix which in each n^{th} diagonal elements contain the streamwise and wall-normal Reynolds-stress contribution of the n^{th} mode.

4.2. *POD modes*

The eigenspectral distribution of energy of the POD modes is reported in Figure 9. The eigenvalues distributions from the entire PIV dataset are superposed. The modal energy content is normalized with the corresponding total energy content $\sum_{i=1}^{N_t} \lambda_i$ of each case. Interestingly, the mode energy distribution is not appreciably affected neither by the Reynolds number nor by the pressure

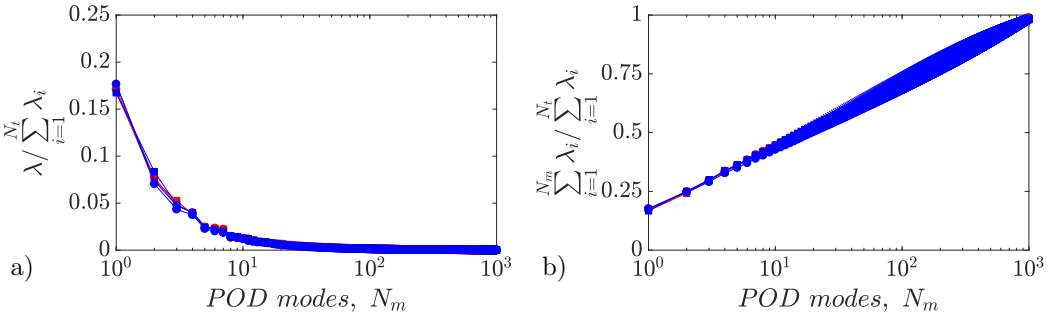

Figure 9: a) POD spectrum of the eigenvalues λ_i; b) Cumulative sum of the eigenvalues. Colours and symbols are reported in Table 1.

gradient magnitude. In particular, the mode energy distribution is in good agreement with the ZPG data presented in Wu (2014) at $Re_\theta = 8,200$, suggesting that in the considered range the energy share between large-scale and small-scale features is independent of both Re and β. About 20% of the energy contribution is ascribed to the first mode, 10% is ascribed to the second mode and barely 5% to the third and the fourth modes. It is thus possible to model up to 40% of the in-plane turbulent kinetic energy with only four modes, as shown in Figure 9b). Consequently these modes, which are related to the large-scale motions, are discussed in detail in the following.

It has to be underlined here that the first POD modes relate to the large-scale motions, which populate the outer part of the boundary layer. Such motions scale with the outer length scale and typically have a streamwise length much larger than the measurement domain assessed in the current experiment. Consequently, the streamwise length of these large-scale motions cannot be fully characterized. Recent studies aiming at the characterization of streamwise extent of outer-scale features have exploited multiple cameras (Cuvier *et al.* 2017) or temporal resolution (Kerherve *et al.* 2017). Nonetheless, snapshot POD allows to estimate the characteristic shape of these structures in the observed measurement domain since it is purely based on the two-point temporal correlation. In the following, the POD modes are compared with those reported in Wu (2014) for a ZPG TBL, which were obtained with a flow domain with similar size in outer scaling.

The streamwise velocity contours and vector fields of the spatial modes are plotted for $\beta \approx 1.3$ and 2.4 and $Re_\tau \approx 1{,}900$ and 4,200 in Figure 10 (which reports modes 1 and 3) and in Figure 11 (modes 2 and 4). This particular choice is due to the similar spatial organization of these mode pairs in all tested cases. The spatial coordinates are scaled using the boundary-layer thickness δ_{99}. The first spatial mode represents an event with positive streamwise velocity and negative wall-normal velocity. According to the quadrant analysis reported for instance in Wallace (2016), such an event is a "sweep", and is denoted as a Q4 event which brings high-momentum flow towards the wall. It has to be noted, however, that fluctuating instantaneous flow fields are obtained as a linear combination of the spatial modes, each one multiplied by their respective time coefficient as in Eq. 3: if multiplied by a negative time coefficient, the first spatial mode will instead represent a Q2 event ($u < 0$, $v > 0$), *i.e.* an ejection. This result appears to confirm the result in Lozano-Durán & Jiménez (2014) that sweeps and ejections should be essentially mirror images of one another. The shape of the first mode is similar to that shown in Wu (2014) for a ZPG TBL. By increasing β, however, the location of the region affected by more intense streamwise velocity fluctuations (*i.e.* sweeps/ejections) is moved farther from the wall. In Wu (2014) the streamwise velocity is reported to be stronger below $y = 0.6\delta_{99}$ while here it is found to extend well beyond $y = 0.75\delta_{99}$ and $y = 0.8\delta_{99}$ for $\beta = 1.3$ and 2.4, respectively. This finding

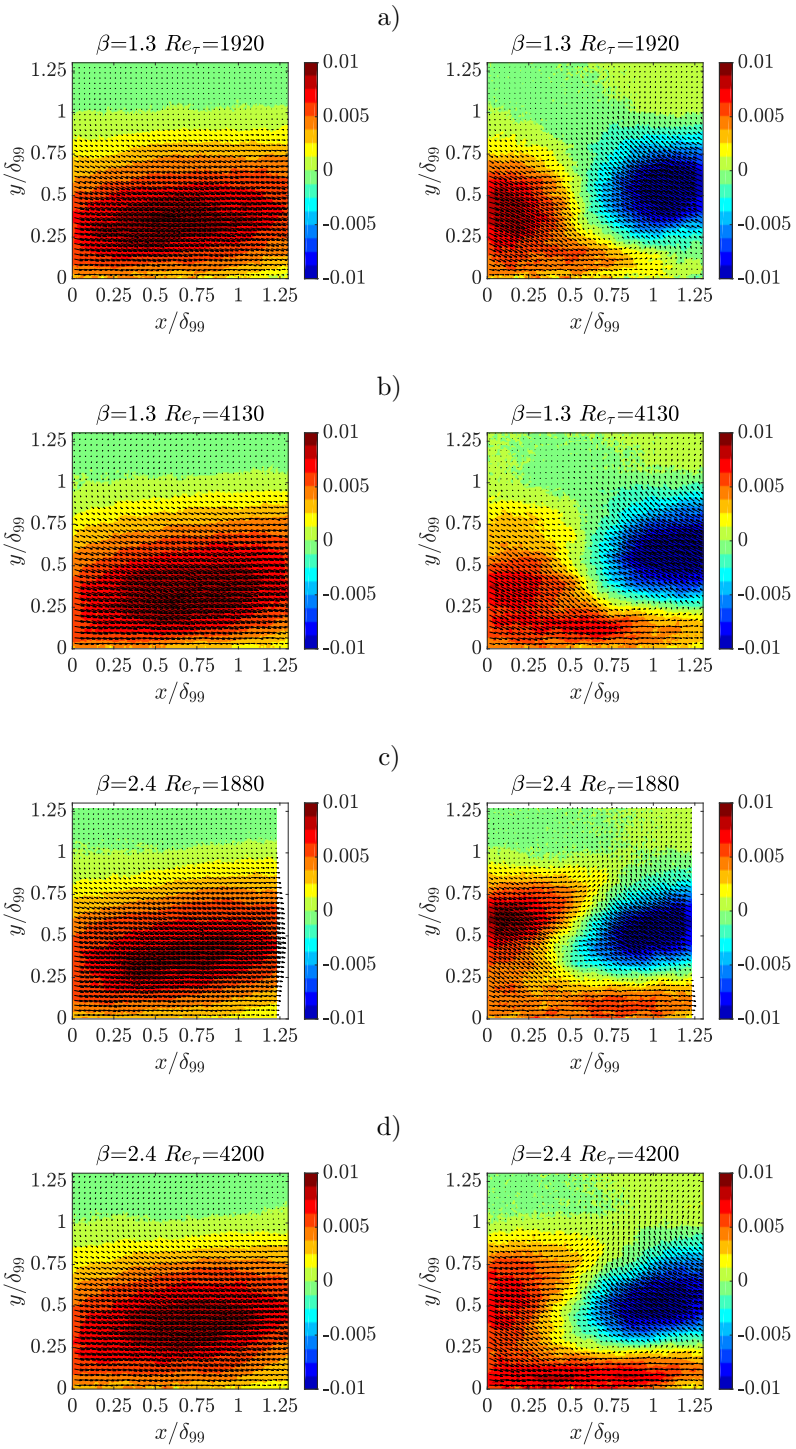

Figure 10: Contour plot with superimposed vector arrows of POD spatial modes ϕ_1 (left column) and ϕ_3 (right column) of the streamwise velocity fluctuations for: a) $\beta = 1.3$ and $Re_\tau = 1,920$, b) $\beta = 1.3$ and $Re_\tau = 4,130$, c) $\beta = 2.4$ and $Re_\tau = 1,880$, d) $\beta = 2.4$ and $Re_\tau = 4,200$.

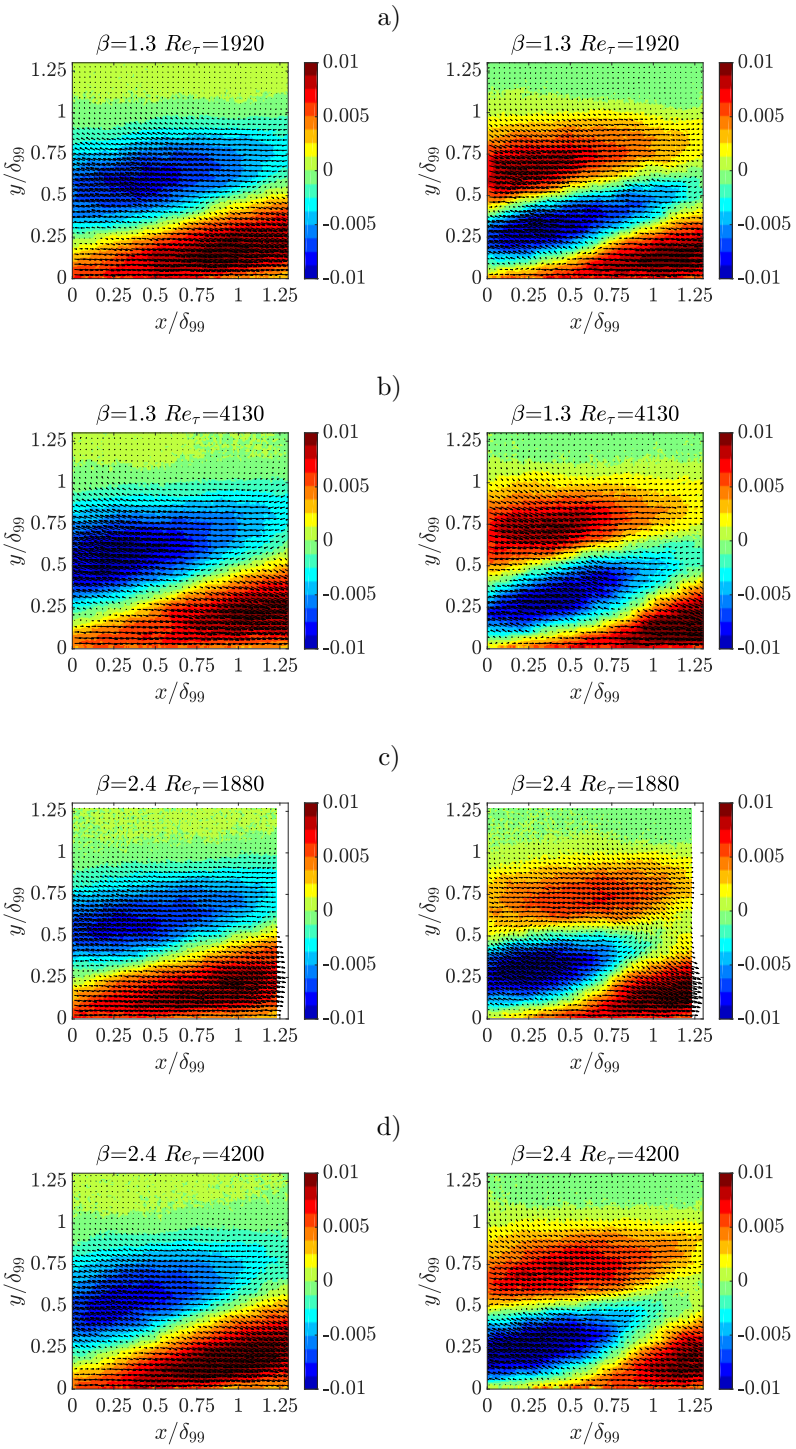

Figure 11: Contour plot with superimposed vector arrows of POD spatial modes ϕ_2 (left column) and ϕ_4 (right column) of the streamwise velocity fluctuations for: a) $\beta = 1.3$ and $Re_\tau = 1,920$, b) $\beta = 1.3$ and $Re_\tau = 4,130$, c) $\beta = 2.4$ and $Re_\tau = 1,880$, d) $\beta = 2.4$ and $Re_\tau = 4,200$.

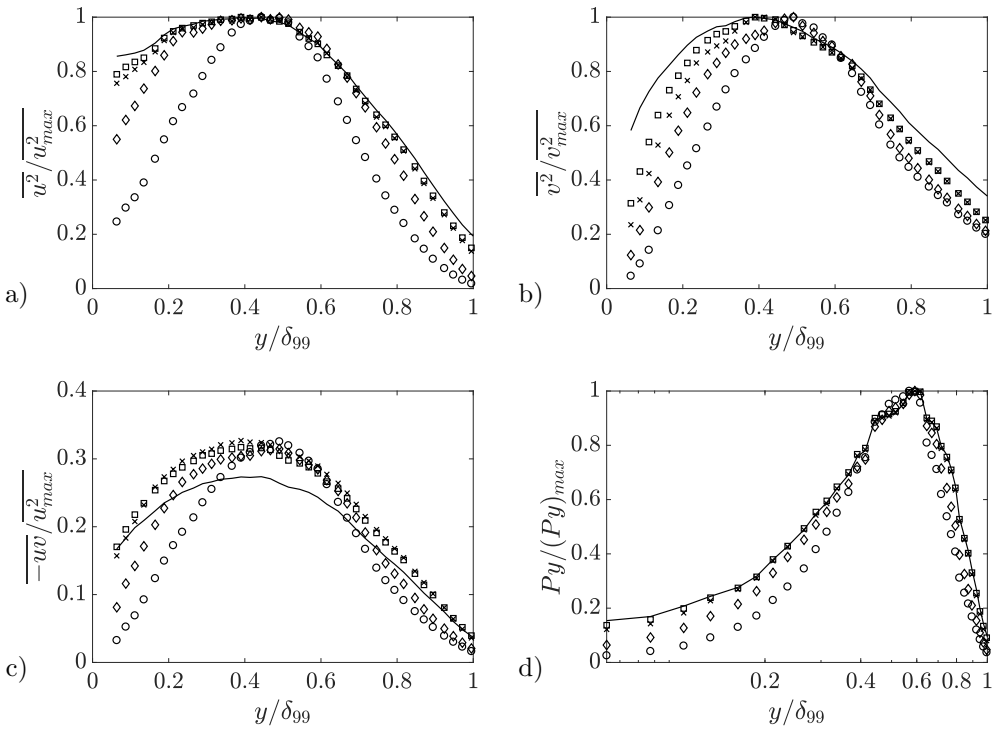

Figure 12: Comparative plot of profiles reconstructed with POD modes for $\beta = 1.3$ at $Re_\tau = 1,010$. a) Streamwise Reynolds normal stress; b) Wall-normal Reynolds normal stress; c) Reynolds shear-stress; d) Pre-multiplied turbulence production. The number of modes used in the reconstruction is represented with the following legend: ($\circ$) 1 mode, ($\diamond$) 2 modes, ($\times$) 4 modes, ($\square$) 50 modes and solid line 1,150 modes.

confirms the claim in Maciel *et al.* (2017) according to which, in APG TBLs, wall-attached large sweeps and ejections are less numerous than in ZPG TBLs.

Modes 1 and 3 (Figure 10) are coupled: mode 3 represents a phase-quadrature term which is needed to correctly represent the low/high momentum coherent motions being convected inside or outside of the measurement domain. As shown by mode 3, the passage of high/low-momentum coherent motions results also in promoting high/low-momentum streaks close to the wall; this shows a connection between the outer-layer fluctuations and the near-wall dynamics. The effect of the Reynolds number is similar to the β effect since the mode spatial distribution is slightly changed with an increased outer fluctuation peak. It is also interesting to note (see mode 3, Figure 10) that the increase of β intensifies the near-wall velocity fluctuations connected with the passage of the low/high momentum coherent motions. Modes 2 and 4 are reported in Figure 11. Mode 2 represents a shear layer spanning through the boundary layer and going from $y/\delta_{99} \approx 0.1$ on the left of the domain to $y/\delta_{99} \approx 0.5$ on the right of the domain. Although the inclination of the shear layer seems to slightly decrease with β, the investigated range is not large enough to draw firm conclusions. Note that the inclination is just slightly smaller than that reported in Wu (2014) for a ZPG TBL. Modes 2 and 4 seem to determine the location of the high/low-momentum coherent motions through the boundary layer. The effect of the Reynolds number is to increase the magnitude of the fluctuation maxima as for mode 1 and 3 and to move the maxima closer to the wall. The effect of β appears to be an overall increase in the penetration of sweeps/ejections from the outer layer towards the wall. Although the shear layer inclination is only weakly dependent

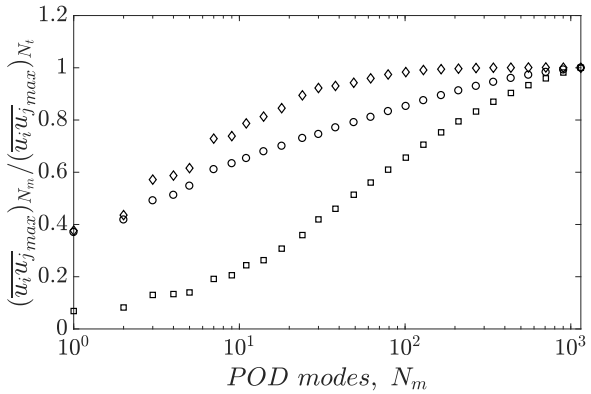

Figure 13: Comparative plot of the maximum value of the Reynolds stresses reconstructed with POD modes for $\beta = 1.3$ at $Re_\tau = 1,010$. ($\circ$) Corresponds to streamwise normal Reynolds stress, ($\square$) to wall-normal Reynolds stress and diamond symbols ($\diamond$) to Reynolds shear stress. Values are normalized with the maximum Reynolds stress value.

on β and Re, the inclination of the coherent motions is changed, especially in presence of larger β, an observation that is particularly evident for mode 4.

In order to understand the modal contribution to the Reynolds stresses, a low-order reconstruction of rank N_m of $\underline{u}$ and $\underline{v}$ is performed retaining the first N_m modes in Eq. 3, as a counterpart of the results shown in Monty *et al.* (2011), where hot-wire measurements were decomposed into small/large-wavelength contributions to observe the effect of the large-scale motions on $\overline{u^2}$. Here POD is used as a filter and allows to emphasize the role of the large-scale phenomena in the Reynolds stresses. For a discrete dataset as the present one, if the number of modes N_m used for the low-order representation is equal to the number of realizations N_t the reconstruction is exact and accounts for the exact representation of the in-plane turbulent kinetic energy and Reynolds stresses. It has to be remarked that this reconstruction will be optimal for what concerns the in-plane turbulent kinetic energy, although we have checked that for the present problem it approximates satisfactorily the reconstruction of all the in-plane components of the Reynolds-stress tensor. A low-order representation allows also to separate scale contributions, as shown in Wu & Christensen (2010), since large-scale features correspond to the higher-energy modes, while small scales are contained in the higher-order modes; thus, performing a low-rank reconstruction allows to separate and highlight the contribution of large-scale structures in building up the Reynolds stresses.

Figure 12 shows the profiles of $\overline{u^2}$, $\overline{v^2}$, Py (which is the pre-multiplied turbulence production) and $-\overline{uv}$. The first three quantities are normalized with their respective maximum value obtained from the reconstructed profile. The Reynolds shear stress $-\overline{uv}$ is instead normalized with the maximum $\overline{u^2}$ from the reconstructed profile; this choice is due to the fact that the two-point correlation matrix $\underline{\underline{C}}$ does not take into account the covariance of u and v. The profiles are reported for $N_m = 1,\ 2,\ 50,\ 1,150$ (the latter corresponds to the ensemble of all modes and represents the complete statistics). Consistently with the observations from modes 1–4, the first mode is already able to locate the fluctuation peaks, thus showing that the wall-normal locations of the maxima of Reynolds stresses and turbulence production are highly influenced by the large-scale features. The peak position is slightly adjusted by the pair formed by the second and the fourth mode, while all the following modes contribute practically uniformly to the generation of Reynolds stresses and turbulence production. The latter statement is further confirmed by the observation of Figure 13, which shows that the maxima constantly increase with increasing number of modes. The peaks in the streamwise and Reynolds shear-stress profiles are mostly due to large-scale motions, whereas

the peak in the wall-normal Reynolds stress is mostly due to smaller-scale features. In the case of the streamwise Reynolds normal stress it is also clear that the highest-order modes contribute in building up the inner peak of the variance profile. The first two POD modes contribute in building up the Reynolds-stress distributions more strongly at $y/\delta_{99} \approx 0.4$, which is within the outer layer. Adding more modes spreads out the distribution, but the peak location is unaffected. Interestingly, the production profiles peak at approximately the same location, *i.e.* $y/\delta_{99} \approx 0.4$, when using only the first mode, while the inclusion of more modes (and thus of small-scale contributions) shifts the peak towards larger wall-normal positions. This might be indicative of an interaction between small-scale and large-scale structures in producing turbulence in APG TBLs.

5. Conclusions

In this work a study on APG TBLs under different Reynolds-number and pressure-gradient conditions has been carried out using PIV measurements which were supplemented by APG TBL LES data. The combination of both datasets allowed us to cover a wide Reynolds-number range: 2,300$< Re_{\delta^*} <$34,000.

Different PIV approaches for the measurement of turbulence statistics have been assessed against hot-wire measurements. Ensemble PTV with polynomial fits, as proposed in Agüera *et al.* (2016), has shown superior performances, with an excellent agreement also in second-order turbulence statistics from the wake region down to $y^+ \simeq 10$ for the TBL at the highest Reynolds number tested. In-plane Reynolds stresses have thus been estimated with ensemble PTV, allowing to assess experimentally the effect of the APG on the various components of the Reynolds-stress tensor. The increase of β is accompained by the strengthening of the wake and by a larger velocity defect, together with the appearance of an outer peak in the streamwise Reynolds stress profile at $500 \leqslant y^+ \leqslant 700$ and of a peak, approximately at the same location, of the Reynolds wall-normal and shear stresses. The experiments at matched β with different values of the Reynolds number show that the main effect is to displace these peaks farther away from the wall (when scaled in wall units) without altering significantly the peaks intensities while, conversely, changing β at fixed Re_τ has little effect on the peak location and strong effect on the peak magnitude. This is also evident from inspection of the turbulence production profile.

LES data with matched β but different flow history support the conclusion that the turbulence statistics are significantly affected by the streamwise evolution of β. For instance, for a decreasing β, the boundary layer exhibits features of an effectively larger β (stronger peak intensity), while for increasing β the opposite occurs. This suggests that APG TBL features should be interpreted in terms of the accumulated effect of β (for instance, defining an average of the streamwise β evolution as in Vinuesa *et al.* (2017*b*)), rather than in terms of the local value of β. This result is further supported by the analysis of turbulence production, which increases for larger values of β, while the production peak is moved towards higher y^+ for increasing Re_τ. Eq. 2, commonly used to estimate the turbulence production, has been assessed both with LES and PIV data, showing that the terms related to streamwise flow derivatives are non-negligible for cases at lower Reynolds number and greater β. Also in this case the accumulated β history represents an important parameter, more than the local value.

POD is used to show the effect of the large scales on the flow features. The energy eigenspectrum of the POD modes is apparently not affected by the Reynolds number nor by β in the ranges under study. The most energetic modes reflect the interaction between the outer and near-wall regions. In particular, the first POD mode represents a sweep or an ejection depending on the sign of the time coefficient in a certain snapshot. Q4 events are connected to high-speed-flow coherent motions and Q2 events to low-speed-flow ones, both being mirror images of one another. The mode organization is however affected by both the pressure gradient and the Reynolds number, and in agreement with Maciel *et al.* (2017) sweeps/ejections are moved farther from the wall. The contribution of the modes to the Reynolds stresses and turbulence production is analysed by reconstructing these quantities with different numbers of modes. Our results show that the first

mode is able to reconstruct the outer peak and reproduce the location of the fluctuation peak, while the following modes slightly adjust the position of the peaks and contribute to build the inner peak.

Acknowledgements

CSV acknowledges the financial support from Universidad Carlos III de Madrid within the program "Ayudas para la Movilidad del Programa Propio de Investigación". RÖ, RV and PS acknowledge the financial support from the Swedish Research Council (VR) and the Knut and Alice Wallenberg Foundation. CSV, SD and AI were partially supported by the COTURB project (Coherent Structures in Wall-bounded Turbulence), funded by the European Research Council (ERC), under grant ERC-2014.AdG-669505. CSV, SD and AI have been partially supported by Grant DPI2016-79401-R funded by the Spanish State Research Agency (SRA) and European Regional Development Fund (ERDF).

References

Adrian, R. J. & Westerweel, J. 2011 *Particle Image Velocimetry*. Cambridge University Press.

Agüera, N., Cafiero, G., Astarita, T. & Discetti, S. 2016 Ensemble 3D PTV for high resolution turbulent statistics. *Meas. Sci. Technol.* **27**, 124011.

Alfredsson, P. H., Segalini, A. & Örlü, R. 2011 A new scaling for the streamwise turbulence intensity in wall-bounded turbulent flows and what it tells us about the "outer" peak. *Phys. Fluids* **23**, 041702.

Alving, A. E. & Fernholz, H. H. 1995 Mean-velocity scaling in and around a mild, turbulent separation bubble. *Phys. Fluids* **7**, 1956–1969.

Astarita, T. & Cardone, G. 2005 Analysis of interpolation schemes for image deformation methods in PIV. *Exp. Fluids* **38**, 233–243.

Atkinson, C., Buchmann, N. A., Amili, O. & Soria, Julio 2014 On the appropriate filtering of piv measurements of turbulent shear flows. *Exp. Fluids* **55**, 1654.

Aubertine, C. D. & Eaton, J. K. 2006 Reynolds number scaling in a non-equilibrium turbulent boundary layer with mild adverse pressure gradient. *Int. J. Heat Fluid Flow* **27**, 566–575.

Avallone, F., Discetti, S., Astarita, T. & Cardone, Gennaro 2015 Convergence enhancement of single-pixel PIV with symmetric double correlation. *Exp. Fluids* **56**, 71.

Balakumar, B. J. & Adrian, R. J. 2007 Large-and very-large-scale motions in channel and boundary-layer flows. *Phil. Trans. R. Soc. A.* **365**, 665–681.

Berkooz, G., Holmes, P. & Lumley, J. L. 1993 The proper orthogonal decomposition in the analysis of turbulent flows. *Annu. Rev. Fluid Mech.* **25**, 539–575.

Bobke, A., Vinuesa, R., Örlü, R. & Schlatter, P. 2016 Large-eddy simulations of adverse pressure gradient turbulent boundary layers. *J. Phys.: Conf. Ser.* **708**, 012012.

Bobke, A., Vinuesa, R., Örlü, R. & Schlatter, P. 2017 History effects and near equilibrium in adverse-pressure-gradient turbulent boundary layers. *J. Fluid Mech.* **820**, 667–692.

Bradshaw, P. 1967 The turbulence structure of equilibrium boundary layers. *J. Fluid Mech.* **29**, 625–645.

Chauhan, K. A., Monkewitz, P. A. & Nagib, H. M. 2009 Criteria for assessing experiments in zero pressure gradient boundary layers. *Fluid Dyn. Res.* **41**, 021404.

Clauser, F. H. 1954 Turbulent boundary layers in adverse pressure gradients. *J. Aero. Sci.* **21**, 91–108.

Cowen, E. A. & Monismith, S. G. 1997 A hybrid digital particle tracking velocimetry technique. *Exp. Fluids* **22**, 199–211.

Cuvier, C., Srinath, S., Stanislas, M., Foucaut, J. M., Laval, J. P., Kähler, C. J., Hain, R., Scharnowski, S., Schröder, A., Geisler, R., Agocs, J., Röse, A., Willert, C., Klinner, J., Amili, O., Atkinson, C. & Soria, J. 2017 Extensive characterisation of a high reynolds number decelerating boundary layer using advanced optical metrology. *Journal of Turbulence* **18**, 929–972.

Eitel-Amor, G., Örlü, R. & Schlatter, P. 2014 Simulation and validation of a spatially evolving turbulent boundary layer up to $Re_\theta = 8300$. *Int. J. Heat Fluid Flow* **47**, 57–69.

Foucaut, J. M., Carlier, J. & Stanislas, M. 2004 Piv optimization for the study of turbulent flow using spectral analysis. *Meas. Sci. Technol.* **15**, 1046.

Foucaut, J. M. & Stanislas, M. 2002 Some considerations on the accuracy and frequency response of

some derivative filters applied to particle image velocimetry vector fields. *Meas. Sci. Technol.* **13**, 1058–1071.

Gungor, A. G., Maciel, Y., Simens, M. P. & Soria, J. 2016 Scaling and statistics of large-defect adverse pressure gradient turbulent boundary layers. *Int. J. Heat Fluid Flow* **59**, 109–124.

Harun, Z., Monty, J. P., Mathis, R. & Marusic, I. 2013 Pressure gradient effects on the large-scale structure of turbulent boundary layers. *J. Fluid Mech.* **715**, 477–498.

Hutchins, N. & Marusic, I. 2007 Large-scale influences in near-wall turbulence. *Phil. Trans. R. Soc. A.* **365**, 647–664.

Hutchins, N., Nickels, T. B., Marusic, I. & Chong, M. S. 2009 Hot-wire spatial resolution issues in wall-bounded turbulence. *J. Fluid Mech.* **635**, 103–136.

Kähler, C. J., Scharnowski, S. & Cierpka, C. 2012*a* On the resolution limit of digital particle image velocimetry. *Exp. Fluids* **52**, 1629–1639.

Kähler, C. J., Scharnowski, S. & Cierpka, C. 2012*b* On the uncertainty of digital piv and ptv near walls. *Experiments in fluids* **52** (6), 1641–1656.

Keane, R. D., Adrian, R. J. & Zhang, Y. 1995 Super-resolution particle imaging velocimetry. *Meas. Sci. Technol.* **6**, 754–768.

Kerherve, F., Roux, S. & Mathis, R. 2017 Combining time-resolved multi-point and spatially-resolved measurements for the recovering of very-large-scale motions in high reynolds number turbulent boundary layer. *Exp. Therm. Fluid Sci.* **82**, 102–115.

Kitsios, V., Atkinson, C., Sillero, J. A., Borrell, G., Gungor, A. G. & Jiménez, J. 2016 Direct numerical simulation of a self-similar adverse pressure gradient turbulent boundary layer. *Int. J. Heat Fluid Flow* **61**, 129–136.

Knopp, T., Buchmann, N. A., Schanz, D., Eisfeld, B, Cierpka, C., Hain, R., Schröder, A. & Kähler, C. J. 2015 Investigation of scaling laws in a turbulent boundary layer flow with adverse pressure gradient using PIV. *J. Turbul.* **16**, 250–272.

Knopp, T., Schanz, D., Schröder, A., Dumitra, M., Cierpka, C., Hain, R. & Kähler, C. J. 2014 Experimental investigation of the log-law for an adverse pressure gradient turbulent boundary layer flow at $Re_\theta = 10000$. *Flow Turbul. Combust.* **92**, 451–471.

Lee, J. H., Monty, J. P. & Hutchins, N. 2016 Validating under-resolved turbulence intensities for PIV experiments in canonical wall-bounded turbulence. *Exp. Fluids* **57**, 129.

Lee, J. H. & Sung, H. J. 2008 Effects of an adverse pressure gradient on a turbulent boundary layer. *Int. J. Heat Fluid Flow* **29**, 568–578.

Lindgren, B. & Johansson, A. V. 2002 Evaluation of the flow quality in the MTL wind-tunnel. *Tech. Rep., Royal Institute of Technology (KTH), Stockholm, Sweden* .

Lozano-Durán, A. & Jiménez, J. 2014 Time-resolved evolution of coherent structures in turbulent channels: characterization of eddies and cascades. *J. Fluid Mech.* **759**, 432–471.

Maciel, Y., Rossignol, K. S. & Lemay, J. 2006 Self-similarity in the outer region of adverse-pressure-gradient turbulent boundary layers. *AIAA J.* **44**, 2450–2464.

Maciel, Y., Simens, M. P. & Gungor, A. G. 2017 Coherent structures in a non-equilibrium large-velocity-defect turbulent boundary layer. *Flow, Turbul. Combust.* **98**, 1–20.

Marusic, I., McKeon, B. J., Monkewitz, P. A., Nagib, H. M., Smits, A. J. & Sreenivasan, K. R. 2010 Wall-bounded turbulent flows at high Reynolds numbers: Recent advances and key issues. *Phys. Fluids* **22**, 065103.

Marusic, I. & Perry, A. E. 1995 A wall-wake model for the turbulence structure of boundary layers. Part 2. Further experimental support. *J. Fluid Mech.* **298**, 389–407.

Mellor, G. L. & Gibson, D. M. 1966 Equilibrium turbulent boundary layers. *J. Fluid Mech.* **24**, 225–253.

Mendez, M. A., Raiola, M., Masullo, A., Discetti, S., Ianiro, A., Theunissen, R. & Buchlin, J. M. 2017 POD-based background removal for particle image velocimetry. *Exp. Therm. Fluid Sci.* **80**, 181–192.

Menter, F. R. 1994 Two-equation eddy-viscosity turbulence models for engineering applications. *AIAA J.* **32**, 1598–1605.

Monty, J. P., Harun, Z. & Marusic, I. 2011 A parametric study of adverse pressure gradient turbulent boundary layers. *Int. J. Heat Fluid Flow* **32**, 575–585.

Nagano, Y., Tagawa, M. & Tsuji, T. 1993 Effects of adverse pressure gradients on mean flows and turbulence statistics in a boundary layer. In *Turbulent Shear Flows 8*, pp. 7–21. Springer.

Nagano, Y., Tsuji, T. & Houra, T. 1998 Structure of turbulent boundary layer subjected to adverse pressure gradient. *Int. J. Heat Fluid Flow* **19**, 563–572.

Nagib, H. M. & Chauhan, K. A. 2008 Variations of von Kármán coefficient in canonical flows. *Phys. Fluids* **20**, 101518.

Nickels, T. B. 2004 Inner scaling for wall-bounded flows subject to large pressure gradients. *J. Fluid Mech.* **521**, 217–239.

Örlü, R., Fransson, J. H. M. & Alfredsson, P. H. 2010 On near wall measurements of wall bounded flows – the necessity of an accurate determination of the wall position. *Prog. Aero. Sci.* **46**, 353–387.

Örlü, R. & Vinuesa, R. 2017 Thermal Anemometry. In *Experimental Aerodynamics* (ed. Stefano Discetti & Andrea Ianiro). CRC Press.

Österlund, J. M. 1999 Experimental studies of zero pressure-gradient turbulent boundary layer flow. *Ph. D. thesis, Royal Institute of Technology, Stockholm, Sweden* .

Pope, S 2000 Turbulent Flows. *Cambridge University Press, Cambridge, UK* .

Raiola, M., Discetti, S. & Ianiro, A. 2015 On PIV random error minimization with optimal POD-based low-order reconstruction. *Exp. Fluids* **56**, 75.

Sanmiguel Vila, C, Vinuesa, Ricardo, Discetti, S, Ianiro, A, Schlatter, Philipp & Örlü, R 2017 On the identification of well-behaved turbulent boundary layers. *J. Fluid Mech.* **822**, 109–138.

Scarano, F. 2001 Iterative image deformation methods in PIV. *Meas. Sci. Technol.* **13**, R1–R19.

Scharnowski, S., Hain, R. & Kähler, C. J. 2012 Reynolds stress estimation up to single-pixel resolution using PIV-measurements. *Exp. Fluids* **52**, 985–1002.

Segalini, A., Örlü, R., Schlatter, P., Alfredsson, P. H., Rüedi, J.-D & Talamelli, Alessandro 2011 A method to estimate turbulence intensity and transverse taylor microscale in turbulent flows from spatially averaged hot-wire data. *Exp. Fluids* **51**, 693–700.

Sirovich, L. 1987 Turbulence and the dynamics of coherent structures. II. symmetries and transformations. *Quart. Appl. Math.* **45**, 573–582.

Skåre, P. E. & Krogstad, P. 1994 A turbulent equilibrium boundary layer near separation. *J. Fluid Mech.* **272**, 319–348.

Soria, J. 1996 An investigation of the near wake of a circular cylinder using a video-based digital cross-correlation particle image velocimetry technique. *Exp. Therm. Fluid Sci.* **12**, 221–233.

Spalart, P. R. & Watmuff, J. H. 1993 Experimental and numerical study of a turbulent boundary layer with pressure gradients. *J. Fluid Mech.* **249**, 337–371.

Townsend, A. A. 1956 *The Structure of Turbulent Shear Flow*. Cambridge University Press.

Vinuesa, R., Bobke, A., Örlü, R. & Schlatter, P. 2016 On determining characteristic length scales in pressure-gradient turbulent boundary layers. *Phys. Fluids* **28** (5), 055101.

Vinuesa, R., Negi, P., Hanifi, A., Henningson, D. S. & Schlatter, P. 2017*a* High-fidelity simulations of the flow around wings at high Reynolds numbers. *Proc. Intern. Symp. on Turbulence & Shear Flow Phenomena (TSFP-10), Chicago, USA*.

Vinuesa, R, Örlü, R, Sanmiguel Vila, C, Ianiro, A, Discetti, S & Schlatter, P 2017*b* Revisiting history effects in adverse-pressure-gradient turbulent boundary layers. *Flow Turbul. Combust.* **99**, 565–587.

Vinuesa, R., Rozier, P. H., Schlatter, P. & Nagib, H. M. 2014 Experiments and computations of localized pressure gradients with different history effects. *AIAA J.* **52**, 368–384.

Wallace, J. M. 2016 Quadrant analysis in turbulence research: history and evolution. *Annu. Rev. Fluid Mech.* **48**, 131–158.

Westerweel, J. & Scarano, F. 2005 Universal outlier detection for PIV data. *Exp. Fluids* **39**, 1096–1100.

Willert, C. E. & Gharib, M. 1991 Digital particle image velocimetry. *Exp. Fluids* **10**, 181–193.

Wu, Y. 2014 A study of energetic large-scale structures in turbulent boundary layer. *Phys. Fluids* **26**, 045113.

Wu, Y. & Christensen, K. T. 2010 Spatial structure of a turbulent boundary layer with irregular surface roughness. *J. Fluid Mech.* **655**, 380–418.

Paper 4

4

Large-scale motions and amplitude modulation in adverse-pressure-gradient turbulent boundary layers

Carlos Sanmiguel Vila[1], Ricardo Vinuesa[2], Stefano Discetti[1], Andrea Ianiro[1], Philipp Schlatter[2] and Ramis Örlü[2]

[1] Linné FLOW Centre, KTH Mechanics, S-100 44 Stockholm, Sweden
[2] Aerospace Engineering Group, Universidad Carlos III de Madrid, Leganés, Spain

Journal Fluid Mechanics (2019), vol. **Under Revision**

Adverse-pressure-gradient (APG) turbulent boundary layers (TBLs) are studied using a new extensive hot-wire database which covers a range of Reynolds number based on momentum thickness $450 < Re_\theta < 23,450$ and a Clauser pressure-gradient-parameter range up to $\beta \approx 2.4$. Increasing and approximately constant β distributions with the same upstream history are characterised. Turbulence statistics are compared among the different pressure-gradient distributions and additional numerical and experimental zero-pressure-gradient (ZPG) TBL data at matched values of β and friction Reynolds number Re_τ. Cases at approximately constant β, which can be considered as "canonical" representations of the boundary layer under a certain pressure-gradient magnitude, exhibit skin-friction and shape-factor curves consistent with the ones proposed by Vinuesa *et al.* (*Flow Turbul. Combust.*, 99, 565–587, 2017). These curves resemble the ones proposed by Nagib *et al.* (*Phil. Trans. R Soc. A.*, 365, 755–770, 2007) for ZPG TBLs. The pre-multiplied power-spectral density is employed to study the differences in the large-scale energy content throughout the boundary layer. Two different large-scale phenomena are identified, the first one due to the pressure gradient and the second one (also present in high-Re ZPG TBLs) due to the Reynolds number. A decomposition of the streamwise velocity fluctuations using a spatial filter shows that the small-scale velocity fluctuations do not scale in APG TBL flows since the effect of the large-scale features extends all the way down to the near-wall region, resulting in a stronger modulation of the fluctuations. The large-scale modulation is further studied using the methodology proposed by Ganapathisubramani *et al.* (*J. Fluid Mech.*, 712, 61–91, 2012). This analysis provides a picture of more intense fluctuations of the large scales and of enhanced influence on the small scales as the pressure-gradient strength increases. Based on the interaction between high/low-speed events, a method to locate the outer peak due to pressure-gradient effects is assessed. Recently proposed scaling laws by Kitsios *et al.* (*Int. J. Heat Fluid Flow*, 61, 129–136, 2016) and Maciel *et al.* (*J. Fluid Mech.*, 844, 5–35, 2018) are tested over a wider Reynolds-number range and for different β cases. The mean velocity and streamwise velocity fluctuation profiles are found to be dependent on the upstream development. The mean velocity profile is found to be self-similar only in the outer region, in agreement with classical theory. The evolution of the outer peak location and its corresponding streamwise variance magnitude is also presented. The outer peak location, when scaled in outer units, is found to be weakly dependent on the Reynolds number and more influenced by pressure-gradient effects. The mean and higher-order statistics of the new APG TBL database are available under the following URL: www.flow.kth.se.

Key words: Turbulent boundary layer, Turbulent Flows

1. Introduction

The advent of high-quality simulations and high-Reynolds-number experiments is progressively paving the way towards the understanding of flow conditions which are representative of real-life

applications (Jiménez 2018). Among others, the development of a turbulent boundary layer (TBL) under the effect of a streamwise pressure gradient has recently captured much attention in high-fidelity numerical simulations (Bobke *et al.* 2017; Kitsios *et al.* 2017; Maciel *et al.* 2018; Yoon *et al.* 2018). These studies, together with recent experimental campaigns at higher Reynolds numbers (Cuvier *et al.* 2017; Sanmiguel Vila *et al.* 2017*a*), are focused on extending the knowledge of the TBL under pressure-gradient effects since the applicability of the theory from zero-pressure-gradient (ZPG) TBLs to decelerating boundary layers is still rather limited (Clauser 1954; Monty *et al.* 2011; Bobke *et al.* 2017). Part of the complexity associated with the study of adverse-pressure-gradient (APG) TBL flows is due to the broader parametric space with respect to the ZPG (Monty *et al.* 2011). The pressure-gradient parameter β, proposed by Clauser (1954, 1956), is widely accepted as the most relevant non-dimensional number. This quantity is defined as $\beta = (\delta^*/\tau_w)(\mathrm{d}P/\mathrm{d}x)$, where δ^* is the displacement thickness, τ_w is the mean wall-shear stress, and $\mathrm{d}P/dx$ is the pressure gradient along the streamwise coordinate. An additional difficulty is that the local state of APG TBLs is strongly affected by their streamwise history as shown by Bobke *et al.* (2017). APG TBLs have a memory of their upstream conditions, thus the local value of β does not suffice for a full characterization; the accumulated effect of β, for instance, should also be taken into account, as suggested in Sanmiguel Vila *et al.* (2017*a*) and Vinuesa *et al.* (2017). To overcome these difficulties, Clauser (1954) proposed to study APG TBLs in which the value of β is maintained constant, therefore fixing the ratio of the forces acting (per unit spanwise length) on a fluid element due to the pressure gradient ($\delta^*\mathrm{d}P$) and to the wall-shear stress ($\tau_w\mathrm{d}x$). According to Rotta (1962) and Mellor & Gibson (1966), this condition is required to reach a near-equilibrium state in which the mean velocity deficit in the outer part is expected to be self-similar at sufficiently high Reynolds numbers (Marusic *et al.* 2010). Several theoretical studies deal with the conditions that are necessary to reach the near-equilibrium state. Townsend (1956) and Mellor & Gibson (1966) derived the required streamwise evolution of the freestream velocity U_∞ for a near-equilibrium state, resulting in a power-law relation, $U_\infty = C(x - x_0)^m$, where x is the streamwise coordinate, x_0 is the power-law virtual origin, and m is a constant which has a value in the range $-1/3 < m < 0$.

Near-equilibrium APG TBLs with constant β are flow cases of paramount importance since these TBLs can be considered as the counterpart of the representative "canonical" ZPG TBL (Schlatter & Örlü 2012) and allow to characterise Re-effects under a certain pressure-gradient strength. Despite this relevance, the complexity of reaching high-Re constant-β APG TBLs has resulted in only few numerical and experimental studies which deal with this flow condition. On the numerical side, the direct numerical simulations (DNS) carried out by Gungor *et al.* (2016), Kitsios *et al.* (2017), Lee & Sung (2008), Lee (2017), the seminal simulation by Skote *et al.* (1998), as well as the well-resolved large-eddy simulation (LES) by Bobke *et al.* (2017) are remarkable. These studies are focused on the differences between ZPG and APG TBLs following different approaches. The simulations carried out by Skote *et al.* (1998) and Kitsios *et al.* (2016, 2017) are focused on the analysis of the statistics and on scaling considerations. In these studies, the authors associated the near-equilibrium state with the possibility of finding a self-similar state. While in the work by Skote *et al.* (1998) the low-Reynolds-number range did not allow to obtain self-similarity in the outer region of the Reynolds shear-stress profiles, Kitsios *et al.* (2016, 2017) reported a self-similar region of the mean velocity deficit and Reynolds-stress profiles for Re_θ from 3,500 to 4,800 with $\beta = 1$. These results should be interpreted with some caution, since complete self-similarity can only be achieved for the case of the sink flow (Townsend 1956). On the other hand, the studies by Lee & Sung (2008) and Lee (2017) are focused on the effect of the APG strength on the large-scale features of the flow. These studies identified that the spatial organisation of the u'-structures (u' being the streamwise velocity fluctuations) is affected by the APG strength, as also found in the experimental study by Sanmiguel Vila *et al.* (2017*a*). In both studies, Q4 and Q2 events are observed and connected to high- and low-speed large-scale motions, respectively.

Regarding the well-resolved LES by Bobke *et al.* (2017), this work analysed different near-equilibrium cases for which the pressure-gradient parameter was kept constant for streamwise distances of 37 and 28 boundary-layer thicknesses δ_{99} at values of $\beta = 1$ and 2, respectively. The results, compared to APG TBLs at matched β and Reynolds number values, but with increasing or decreasing $\beta(x)$ curves, highlight the impact and thus importance of the upstream (pressure gradient) history on the local turbulence statistics. Moreover, Bobke *et al.* (2017) reported that (for their specific cases) a streamwise distance of approximately $7\delta_{99}$ with constant β is needed to obtain a "well-behaved" APG TBL with constant-β conditions. This is particularly critical when performing an analysis which compares cases with the same Reynolds number and β, since – as also shown in Sanmiguel Vila *et al.* (2017*a*) – the cases with a non-constant β distribution need to be analyzed in terms of the accumulated pressure-gradient magnitude. This result is in agreement with the finding of Vinuesa *et al.* (2017), who report that the accumulated value of β, $\bar{\beta}(Re_\theta)$, expressed as

$$\bar{\beta}(Re_\theta) = \frac{1}{Re_\theta - Re_{\theta_0}} \int_{Re_{\theta_0}}^{Re_\theta} \beta(Re_\theta) \mathrm{d}Re_\theta. \tag{1}$$

represents the average value of β (estimated over the momentum-thickness Reynolds-number range $Re_\theta - Re_{\theta_0}$) and provides a good measure to account for the upstream history. It is interesting to note that an integral method for these history effects on the TBL was also proposed in the 1960s by Felsch *et al.* (1968).

Experimental studies of APG TBL flows, on the other side, are rather complex, since the desired pressure-gradient distribution must be imposed by e.g. applying suction or geometrical modifications of the roof of the test section. A typical choice for the study of APG TBLs developing on flat plates is to properly shape the wall opposite to the plate. The pressure-gradient distribution depends on the TBL development on the plate and roof, thus requiring a trial-and-error process to achieve the desired streamwise (pressure-gradient) history. Additionally, the $\beta(x)$ history depends on the local value of the wall-shear stress and of the displacement thickness, thus requiring extensive measurements for its characterization. This might partly explain the lack of information relative to the $\beta(x)$ distribution in numerous previous studies in the literature, which makes difficult a direct comparison between different databases. A summary of the experimental studies available in the literature is found in Table 1. From an experimental point of view, the near-equilibrium state is a challenging condition to be achieved, and there are only very few studies which obtain a relatively long constant-β region as can be observed from Table 1. Some of the most relevant experimental works in these conditions are those by Stratford (1959), in which a TBL with nearly zero skin friction was generated and studied, and by Skåre & Krogstad (1994), where the authors obtained a TBL with a freestream-velocity evolution given by a power-law, with exponent $m = -0.23$, leading to a constant $\beta \approx 20$. In their near-equilibrium region, Skåre & Krogstad (1994) showed self-similarity for all the velocity defect profiles in the outer region (in agreement with classical theory) and reported an increase of the turbulence production in the outer layer.

As a consequence of this increased interest in APG TBLs, classical questions regarding the proper scaling for this type of TBL have been re-examined thanks to new high-quality databases available. In recent studies (Kitsios *et al.* 2017; Wei & Maciel 2018; Maciel *et al.* 2018) different arguments are proposed in order to assess the most appropriate scaling. The outer scaling proposed by Kitsios *et al.* (2017) is based on the freestream velocity U_∞ and the displacement thickness δ^*; based on these parameters the mean velocity and Reynolds-stresses profiles are expected to collapse under conditions of self-similarity. This scaling was tested by Bobke *et al.* (2017) on the downstream evolution of the mean velocity and Reynolds-stresses profiles. Their results showed no self-similarity nor collapse of the profiles in the constant-β region. In the study by Maciel *et al.* (2018) there is no unique pair of scaling variables, but different scaling variables are proposed according to the pressure-gradient intensity. In that study, it is argued that a good scaling does

not need to reveal scale invariance of the mean velocity-defect and Reynolds stresses but should reflect the order of magnitude of the different scaled variables.

The availability of new high-Reynolds-number databases for APG TBLs reveal new interesting features, allowing to use techniques that so far have been employed to characterise the interaction between large and small scales in ZPG TBLs, such as the decomposition of the velocity fluctuations by means of temporal filters (Mathis *et al.* 2011; Dogan *et al.* 2018). These techniques require cases at high enough Reynolds numbers to allow for a sufficient scale separation to study the phenomenon of amplitude modulation between large and small scales. This was done by Harun *et al.* (2013), who reported an increase of the modulation of large scales over the small scales in APGs compared to that in ZPGs; this was later confirmed by Lee (2017) using two-dimensional amplitude-modulation maps. The results of those studies show that the relation between the large and small scales in APG flows is different to that reported for high-Re ZPG TBLs (Mathis *et al.* 2011; Ganapathisubramani *et al.* 2012). In particular, the wall distance of the point in which the amplitude modulation becomes zero in APG TBL flows is larger with respect to that in ZPG TBLs, for which it is located in the middle of the logarithmic region (*i.e.* $y^+ \approx 3.9Re_\tau^{0.5}$). This fact reflects an enhanced activity of the large scales throughout the logarithmic region which need to be further studied by means of high-Re databases.

Despite these recent advances, there is still a need for high-Reynolds-number databases which may help to better discern Re, β and $\beta(x)$ effects in TBLs and allow for a better characterisation of the interaction between the large and small scales in APG flows. For this reason, in the present study a unique experimental database of APG TBL at constant and non-constant β, covering a wide range of Reynolds numbers, is presented. The primary objective is to study and compare near-equilibrium and non-equilibrium APG TBLs developing on a flat plate with different $\beta(x)$ curves, over a wider Reynolds-number range, as the numerical counterpart of the study by Bobke *et al.* (2017). For this purpose, different experimental configurations are considered. Measurements were performed by means of hot-wire anemometry (HWA) and oil-film interferometry (OFI) in the Reynolds-number range $450 < Re_\theta < 23,450$, and for pressure-gradient intensities resulting in values of the Clauser pressure-gradient parameter in the range $0 < \beta < 2.4$. This manuscript is organised as follows: the experimental set-up is described in §2, upon which the boundary-layer development and the turbulence statistics from the various pressure-gradient conditions are compared and presented in §3. In §4, spectral analysis is employed to compare the large-scale organisation at matched Re and β and then, in §5 inner/outer layer interactions are analyzed by means of scale-decomposition and amplitude-modulation analyses in order to identify the effects of APGs on the large- and small-scale energy distribution; additionally a method to identify the outer peak location in APG flows is proposed. Prior to the summary and conclusions, in §6 the scaling laws proposed by Kitsios *et al.* (2017) and Maciel *et al.* (2018) are tested for the velocity profiles and to study the evolution of the outer peak location and streamwise variance value.

2. Experimental set-up

2.1. *Wind tunnel and boundary-layer flow conditions*

The experiments were performed in the Minimum Turbulence Level (MTL) closed-loop wind tunnel located at KTH Royal Institute of Technology in Stockholm. The test section is 7 m long with a cross-sectional area of 0.8×1.2 m^2 (height×width). The MTL is capable of reaching a maximum speed of 70 m/s with a streamwise velocity fluctuation intensity of approximately 0.025% of the free-stream velocity at a nominal speed of 25 m/s. The air temperature is controlled with an accuracy of ± 0.05 K by means of a heat exchanger. More details regarding the MTL can be found in the reports by Österlund (1999) and Lindgren & Johansson (2002), while related flat-plate-boundary-layer experiments in ZPG TBL configurations, here used as reference, are given in Örlü & Schlatter (2013) and Sanmiguel Vila *et al.* (2017*b*).

Three different pressure-gradient distributions were obtained by means of wall inserts made of foam attached to the MTL roof by threaded rods. Additional modifications to the roof shape were

Author(s) (year)	Measurement technique	β-history available	Constant-β region	Range of Re_θ	Range of β	Presented quantities
Clauser (1954)	HWA	–	✓	–	1.8–6.13	U
Stratford (1959)	Pitot	–	✓	–	∞	U
Perry (1966)	Pitot	–	–	15,900–97,200	2.35–71.2	U
Samuel & Joubert (1974)	HWA	–	–	5,000–30,000	0.07–8	U, $\overline{u^2}$, $\overline{v^2}$, $\overline{w^2}$, $\overline{uv}$
East & Sawyer (1980)	HWA	–	–	18,900–34,700	0.47–7.27	U, $\overline{u^2}$, $\overline{v^2}$, $\overline{w^2}$, $\overline{uv}$
Cutler & Johnston (1989)	HWA	–	–	12,000–25,000	2–12	U, V, $\overline{u^2}$, $\overline{v^2}$, $\overline{w^2}$, $\overline{uv}$
Dengel & Fernholz (1990)	HWA	–	–	1,260–11,200	0–∞	U, $\overline{u^2}$, $\overline{uv}$
Nagano *et al.* (1993)	HWA	–	–	1,290–3,350	0.76–4.66	U, $\overline{u^2}$, $\overline{v^2}$, $\overline{w^2}$, $\overline{uv}$
Spalart & Watmuff (1993)	HWA	–	–	<1,600	0–2	U, $\overline{u^2}$, $\overline{v^2}$, $\overline{w^2}$
Skåre & Krogstad (1994)	HWA	✓	✓	25,400–53,970	12.2–21.4	U, $\overline{u^2}$, $\overline{v^2}$, $\overline{w^2}$, $\overline{uv}$
Alving & Fernholz (1995)	HWA	✓	–	2,849–13,305	0.2–324	U
Marušić & Perry (1995)	HWA	✓	–	2,206–19,133	0.65–7.16	U, $\overline{u^2}$, $\overline{v^2}$, $\overline{w^2}$, $\overline{uv}$
Nagano *et al.* (1998)	HWA	–	–	1,070–3,350	0.77–5.32	U, $\overline{u^2}$, $\overline{v^2}$, $\overline{w^2}$
Maciel *et al.* (2006)	PIV	–	–	3,360–14,300	320–∞	U, $\overline{u^2}$, $\overline{v^2}$, $\overline{uv}$
Nagib *et al.* (2004)	HWA	–	–	10,000–70,000	0—0.3	U
Monty *et al.* (2011)	HWA	–	–	6,050–18,500	0.822–4.75	U, $\overline{u^2}$
Harun *et al.* (2013)	HWA	–	–	12,030	1.74	U, $\overline{u^2}$, $\overline{v^2}$, $\overline{uv}$
Vinuesa *et al.* (2014)	Pitot	–	–	13,000–37,000	0.2-0.33	U
Sanmiguel Vila *et al.* (2017*a*) (**Paper 3**)	PIV	✓	–	9,070–22,240	1.3–2.4	U, $\overline{u^2}$, $\overline{v^2}$, $\overline{uv}$

Table 1: Previous experimental studies on adverse pressure gradient turbulent boundary layers developing on flat plates. Streamwise mean velocity component is defined as U, wall-normal mean velocity component is defined as V, variance is defined as $\overline{u^2}$, $\overline{v^2}$, $\overline{w^2}$ for the streamwise, wall-normal and spanwise direction, respectively. Reynolds shear stress is indicated as $\overline{uv}$.

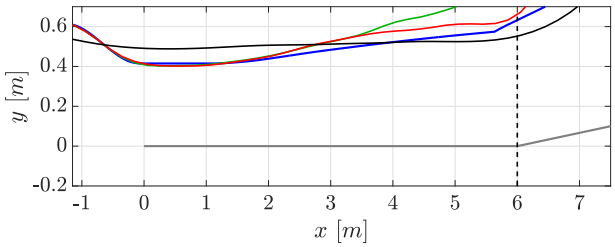

Figure 1: Description of the roof geometry. The wall insert to obtain the desired pressure-gradient evolution is indicated in: red (roof configuration 1), blue (roof configuration 2) and green (roof configuration 3). The gray line represents the aluminium flat plate used in the present experimental campaign. Note that both the upstream and downstream ends are flush-mounted with the tunnel roof. Additionally, a black line which represents the ZPG roof configuration from Sanmiguel Vila *et al.* (2017*b*) is included as a reference. The dashed line indicates the end of the test section. The flow direction is from left to right.

Roof conf.	U_{ref} $[m/s]$	Distribution type	Min. β	Max. β	Color	Symbol
1	6	Approximately constant	0.82	1.11	Red	♢
1	12	Approximately constant	1.00	1.38	Red	◯
1	30	Approximately constant	0.81	1.17	Red	□
2	12	Mildly increasing	0.45	0.80	Blue	◯
2	30	Mildly increasing	0.41	0.74	Blue	□
3	6	Strongly increasing	1.20	2.12	Green	♢
3	12	Strongly increasing	1.32	2.38	Green	◯
3	30	Strongly increasing	1.23	2.19	Green	□

Table 2: Characteristic values for the different configurations in the present experimental database. Maximum and minimum β values are reported in the approximately constant-β region of configuration 1 given by 2.7 m $\leq x \leq$ 4.4 m.

possible by adjusting the wind-tunnel ceiling, which comprises a total of six panels allowing vertical displacement. The design of the different pressure-gradient configurations was performed by an iterative process, starting from a non-constant-β mild pressure gradient ($\beta \approx 0.7$), then modifying this configuration to different non-constant-β cases with a higher peak value of $\beta \approx 2.4$, and eventually reaching a case with an approximately constant value of $\beta \approx 1.1$. Here, the definition of *approximately constant* is used to indicate a configuration with β values that do not exhibit a clear increasing or decreasing trend over several δ_{99} (in the present case bounded within $\pm 15\%$ over at least 15 δ_{99}). Obtaining a completely constant mild value of β is challenging due to the practical difficulty of controlling the streamwise evolution of the different (interacting) boundary layer parameters and the pressure gradient that are inherent in the definition of β. The first trial shape of the ceiling was designed by performing Reynolds-Averaged Navier-Stokes (RANS) computations considering the two-equation Shear-Stress Transport (SST) model (Menter 1994) implemented in the CFD code Fluent (v.6.3), following Vinuesa *et al.* (2014). The turbulent boundary layers developed on a smooth aluminium flat plate of 6 m length and 26 mm thickness, spanning the entire width of the wind tunnel and suspended 15 cm above the wind-tunnel floor.

The flat plate used in the experiments has a leading edge following the shape of a modified superellipse and is equipped with a 1.5 m long trailing-edge flap in order to modify the position of the stagnation point. In the present experimental campaign, the flap position was set to 10°. For

a) b)

Figure 2: Pictures from the experimental campaign carried out in the MTL wind tunnel. a) Hot-wire probe attached to the main traverse. b) Panoramic view from the flat plate with a roof geometry.

a more detailed description, the reader is referred to Österlund (1999). Before this experimental campaign, a tripping study was carried out (Sanmiguel Vila *et al.* 2017*b*) in order to select the appropriate tripping conditions which would not affect the streamwise development of the TBL. Following the results of this study, the boundary layer was tripped close to the leading edge with *DYMO* tapes (with the embossed letter 'V' pointing in the flow direction and a nominal height of 0.3 mm) in combination with a turbulator with height 1.6 mm, corresponding to the tripping denoted as "optimal tripping 2" in Sanmiguel Vila *et al.* (2017*b*), where further details of the tripping conditions can be found.

The desired streamwise evolution of the pressure gradient is divided into three regions: a first region where a favorable pressure gradient (FPG) is imposed, a second one where nearly-ZPG conditions are established in order to obtain a well-behaved TBL (Sanmiguel Vila *et al.* 2017*b*), and finally an APG area which is the region of interest for the present investigation. The coordinates of the different employed geometries are shown in Figure 1, where the converging-diverging shape of the ceilings is depicted. In all the configurations the flow was initially accelerated by reducing the test section height from 0.80 m to approximately 0.60 m. The flat plate was placed at a vertical distance of 0.42 m from the roof at the throat, and the leading edge of the flat plate was located right at the beginning of the roof throat. Downstream of the flat-plate leading edge, the ceiling geometry was designed such that a ZPG was maintained for approximately 1.0 m. From that location on, the different adverse-pressure-gradient conditions were imposed by changing the roof geometry in the divergent part. Modifications in the slope and shape of the divergent part allowed to obtain higher values of β by producing a stronger deceleration. In order to obtain an approximately constant-β case, the slope of the roof geometry was modified in different streamwise locations ($x \approx 3.5$ m and 4 m) in order to limit the possible increasing/decreasing trend in the β evolution. Since the roof comprises several elements, obtaining a constant-β configuration is extremely challenging for the reasons discussed above. On the other hand, in this study we obtained approximately constant-β cases (see Table 2) with variations with respect to the average value lower than 15%. For clarity, Figure 2 from the experimental campaign is presented in which a roof geometry is observed inside the test section.

The resulting pressure distributions are expressed in terms of the pressure coefficient C_p, which is defined for an incompressible flow as $C_p = (P - P_{ref})/(1/2\rho U_{ref}^2) = 1 - (U_\infty/U_{ref})^2$, where P is the local static pressure, P_{ref} is the static pressure in the ZPG region (measured at $x = 0.6$ m), U_∞ is the local free-stream velocity and U_{ref} is the reference freestream velocity at $x = 0.6$ m, in which case the origin of the coordinate system is the leading edge of the flat plate. The evolution of C_p along the streamwise direction for the three aforementioned roof geometries is presented

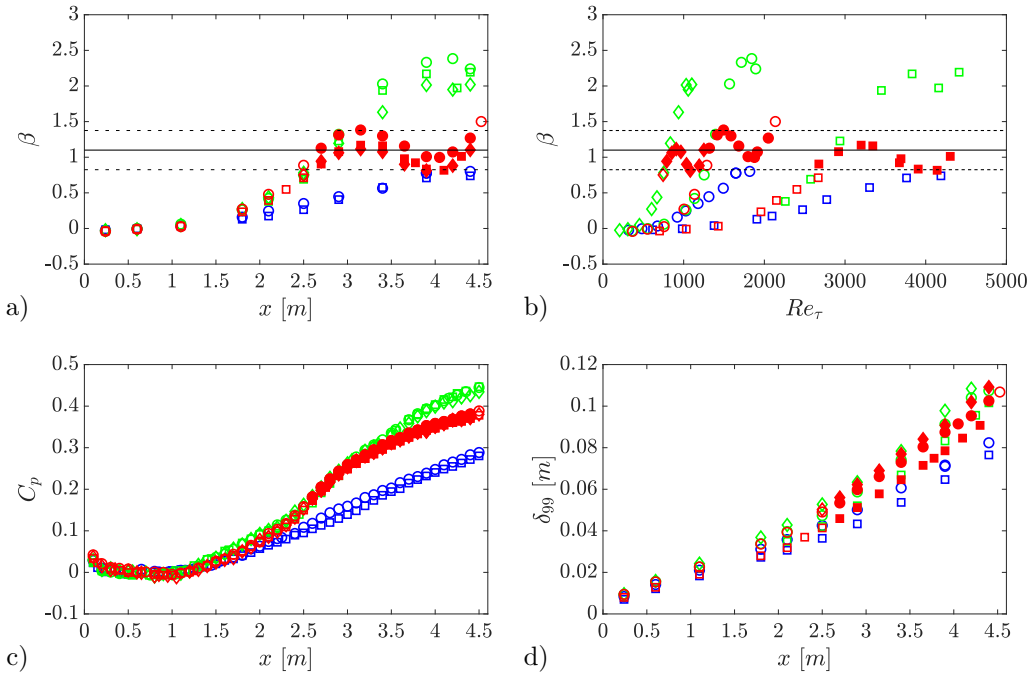

Figure 3: Streamwise evolution of the following quantities for the three ceilings under consideration: a) Clauser pressure-gradient parameter β as a function of the streamwise coordinate (and as a function of the friction Reynolds number Re_τ in panel b)), c) pressure coefficient C_p and d) boundary-layer thickness δ_{99}. The colors and symbols are reported in Table 2. Note that the reference pressure for C_p is taken at $x = 0.6$ m. Reference black dash lines at $\beta = 1.1 \pm 25\%$ are included in panels a) and b). Filled symbols indicated the region bounded by 25% deviation from $\beta \approx 1.1$, which henceforth will be denoted approximately constant-β region.

in Figure 3. Additionally, the Clauser pressure-gradient parameter β and the evolution of the boundary-layer thickness δ_{99} are also shown. The method reported by Vinuesa *et al.* (2016) was used to determine δ_{99} in the present APG TBLs. Since the various roof geometries are identical up to a distance of $x \approx 2$ m, it can be observed that the different quantities collapse up to this location. For the approximately constant-β cases, it can be observed that the changes in the slope of the roof geometry (Figure 1) produced at $x \approx 3.5$ m and 4 m are reflected in the trend changes of the $\beta(x)$ evolution. The experiments were carried out for three different inflow velocities, *i.e.* $U_{ref} = 6$, 12 and 30 m/s. For each value of U_{ref}, the variation of β was below 15% with respect to its approximately constant mean value. In Figure 3 a 25% deviation is reported, enclosing the three test cases of the dataset. A set of ten streamwise locations was selected for measurements on each configuration. Additional stations were added for the configurations with constant β, covering a final Reynolds-number range based on momentum thickness (θ) of $450 < Re_\theta < 23,450$. Table 2 shows a summary of the pressure-gradient distributions for the various cases under consideration.

2.2. *Hot-wire anemometry measurements*

Streamwise velocity measurements were performed by means of home-made single hot-wire probes which resemble a standard *Dantec* boundary-layer probe, *i.e.*, a 55P15. The hot-wire probes were built in-house using a stubless Platinum wire with two lengths of 525 and 275 μm and nominal diameters of 2.5 and 1.25 μm, respectively. The wires were soldered to conical prongs with a diameter of around 30 μm. Voltage signals from the hot wire were recorded using a *Dantec*

StreamLine 90N10 frame in conjunction with a 90C10 constant-temperature anemometer module operated at a resistance overheat of 80%. An offset and a gain were applied to the top of the bridge voltage in order to match the voltage range of the 16-bit A/D converter used. All the measurements were recorded with an acquisition frequency large enough to have $\Delta t^+ < 3$ (where Δt is the time between samples and the superscript + denotes normalisation using viscous units). The total sampling duration T was $TU_\infty/\delta_{99} > 2,700$, and in most cases an order of magnitude larger (as apparent from §Appendix A), thereby ensuring converged statistics in light of the large-scale and very-large-scale features. Additionally, a low-pass filter with cut-off frequency equal to 10 kHz for $U_{ref} = 6, 12$ m/s and 20 kHz for $U_{ref} = 30$ m/s was used prior to the data acquisition in order to avoid aliasing. Calibration of the hot-wire anemometer was performed in situ using as reference a Pitot-static tube located parallel to the incoming freestream. The Pitot-static tube was connected to a micromanometer of type *FC0510 (Furness Control Limited)*, which was also employed to record the ambient temperature and pressure during the calibration and the experiments. Data acquired in the calibration was fitted to a fourth-order polynomial curve, which is a rather common procedure in the wall-turbulence community (Hultmark *et al.* 2010).

2.3. *Oil-film interferometry measurements*

Oil-film interferometry (OFI) was used to measure the wall-shear stress at some locations, and validate the process to determine the friction velocity based on near-wall velocity measurements described in §2.4. To this end, the OFI measurements were carried out at the locations where optical access was possible. Silicon oil with a nominal viscosity of 20, 100 and 200 cSt at 25°C was used, and the oil viscosities were calibrated by means of a Ubbelohde capillary-suspended level viscometer. Black Mylar films were attached to the flat plate in order to obtain better contrast for the pictures. The oil film was illuminated using a low-pressure sodium lamp which had a power of 55 W and a nominal wavelength of 589 nm. The light source was placed on the wind-tunnel roof, aligned with the flow direction. A handheld digital thermocouple *Fluke* was attached to the flat plate close to the recording station to control the oil temperature. The equipment used to obtain the pictures consisted of a digital single-lens reflex camera *Nikon D7100*, and telephoto zoom lens *Nikon Nikkor 200 mm f4*. The camera was placed on the roof of the wind tunnel with an angle of 15° normal to the plate and was controlled remotely via a USB cable. The pictures were acquired at a rate of 0.2 Hz. Before each test, millimetre graph paper was placed on the measurement station and was photographed to calculate the reference length. For further details on the performed oil-film interferometry measurements in pressure-gradient TBLs, as well as on the post-processing of the data, the reader is referred to Vinuesa *et al.* (2014) and Vinuesa & Örlü (2017).

2.4. *Determination of the friction velocity and integral quantities*

Measurements of the wall-shear stress using OFI were limited due to optical access which did not make possible to cover the total streamwise length of the test section. For this reason, the friction velocity for the cases in which no OFI measurements was available is estimated by means of an analytical composite profile. In this work, the composite profile reported in Chauhan *et al.* (2009) was used to fit the experimental data and to correct the absolute wall position, which has been shown to be a robust method whenever near-wall measurements are at hand (Örlü *et al.* 2010; Rodríguez-López *et al.* 2015). This procedure allows to correct possible errors in the absolute wall position due to deflections of the hot-wire probe induced by stronger aerodynamic forces at higher velocities. To this end, hot-wire measurements were acquired with a sufficiently large number of points within the viscous sublayer and buffer region ($y^+ < 12$) in order to fit the data using only data points that do not rely on log-law and wake-function constants. This approach is analogous to the one described in the previous ZPG study by Sanmiguel Vila *et al.* (2017*b*) and in a recent LES APG study reported by Cohen & Gloerfelt (2018). Since the present values of β correspond

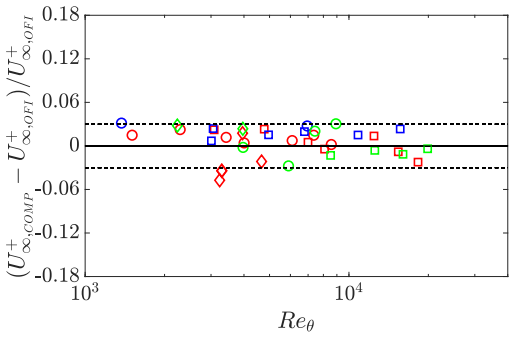

Figure 4: Comparison of the values of U^+_∞ obtained by using the composite profile (Chauhan *et al.* 2009) and oil-film interferometry (OFI). The colors and symbols are reported in Table 2. Dashed error bars at ±3% are included as a reference.

to a moderate pressure gradient, the profiles should not be strongly affected in the inner region (Harun *et al.* 2013; Gungor *et al.* 2016; Bobke *et al.* 2017). To ensure that the approximation is accurate and in order to estimate the uncertainty of the friction-velocity measurements, a comparison between the U^+_∞ values obtained by fitting the near-wall mean velocity profile against the ones measured using OFI is reported in Figure 4. OFI measurements were performed in the range 0.6 m $< x <$ 3.9 m for $U_{ref} = 6$, 12 and 30 m/s. The estimated uncertainty of the OFI measurements is below 2% and the deviation of the u_τ values obtained by means of the composite profile with respect to the OFI measurements is below 3% (see Figure 4).

For consistency purposes, but also because OFI measurements are not available at all measurement stations for all velocitities, the u_τ obtained by using the composite profile (Chauhan *et al.* 2009) is used for the inner normalisation in the present study for all the profiles and integral quantities. As stated above, the estimation of the boundary-layer thickness δ_{99} was performed according to the procedure reported in Vinuesa *et al.* (2016), which is based on the diagnostic-plot concept (Alfredsson *et al.* 2011). Using the value of δ_{99} as the upper limit of integration, δ^* and θ are obtained. With these quantities, the shape factor H_{12} and β are calculated. The Reynolds numbers and the values of β for all the profiles under consideration are reported in §Appendix A.

3. Evolution of the turbulent boundary layer for various adverse-pressure-gradient configurations

In this section, we analyze the evolution of the different APG TBLs along the flat plate. Mean velocity, variance profiles and integral quantities are described. First of all, the streamwise development of each case is assessed, and the comparison between different cases at matched Reynolds-number and pressure-gradient conditions is performed in §4 in an attempt to characterise both effects. All the integral quantities and boundary-layer parameters of the different velocity profiles under consideration are summarised in the tables reported in §Appendix A.

3.1. *Streamwise mean velocity and fluctuations*

The streamwise development of the inner-scaled streamwise mean velocity and streamwise velocity fluctuation profiles is shown for the three APG TBLs configurations for different inlet velocities in Figures 5, 6 and 7. For configuration 1, which exhibits an approximately constant value of β over a significant extent of the test section as shown in Figure 3, we report in Table 3 the corresponding near-equilibrium values of the power law proposed by Townsend (1956); these values were obtained by means of fitting the streamwise velocity distribution to $U^*_\infty = C(x^* - x^*_0)^m$, where $*$ means

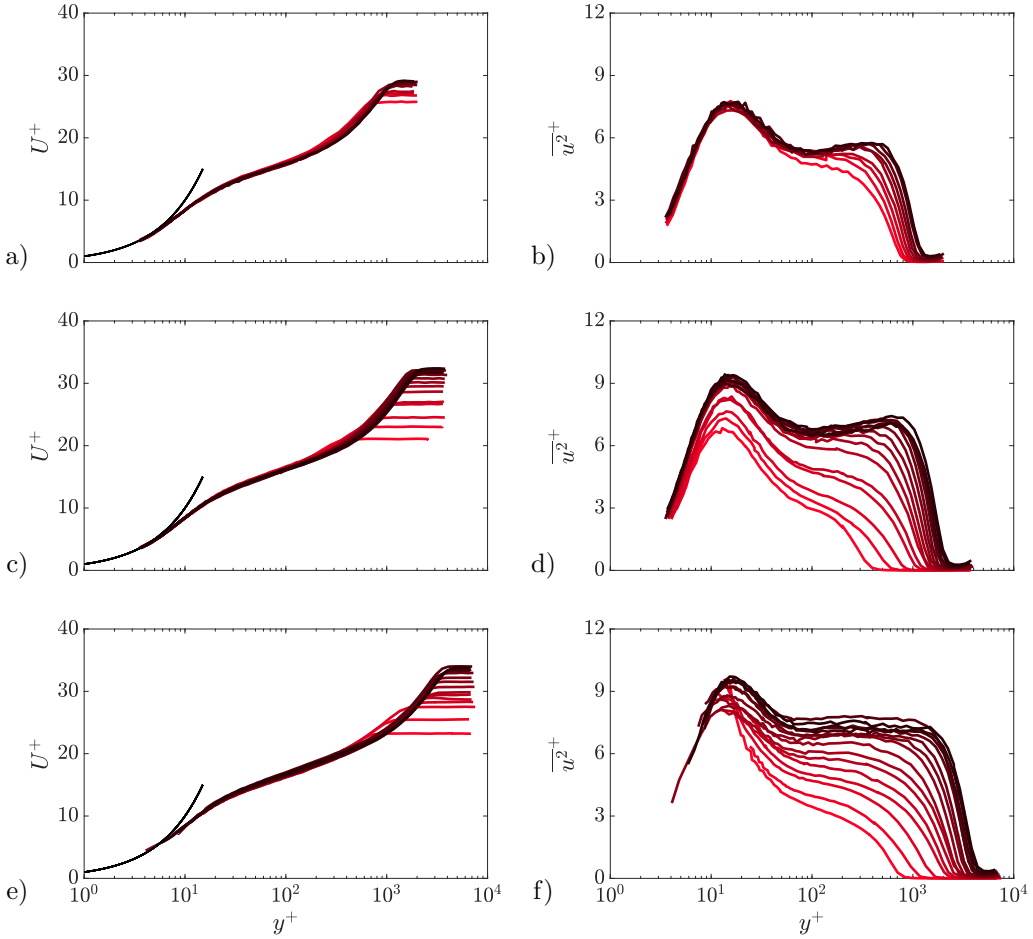

Figure 5: Evolution of the inner-scaled streamwise (a,c,e) mean and (b,d,f) variance profiles for configuration 1 at: (a,b) $U_{ref} = 6$ m/s, (c,d) $U_{ref} = 12$ m/s and (e,f) $U_{ref} = 30$ m/s. Colours vary from light red to dark red with increasing streamwise location. Black line (-) depicts the relation $U^+ = y^+$.

U_{ref} [m/s]	C	x_0^*	m	R^2
6	2.21	48	-0.19	0.9968
12	2.26	51	-0.19	0.9971
30	2.30	59	-0.19	0.9988

Table 3: Values obtained by fitting the data of configuration 1 to the power law $U_\infty^* = C(x^* - x_0^*)^m$ (Townsend 1956), where $*$ means normalization using U_∞ and δ_{99} evaluated at $x = 0.6$m, respectively. The coefficient of determination R^2 is included as a reference of the goodness-of-fit.

normalization using U_∞ and δ_{99} evaluated at $x = 0.6$ m. The value of the exponent $m \approx 0.19$ is consistent with the predicted value according to the non-linear analysis carried out by Skote *et al.*

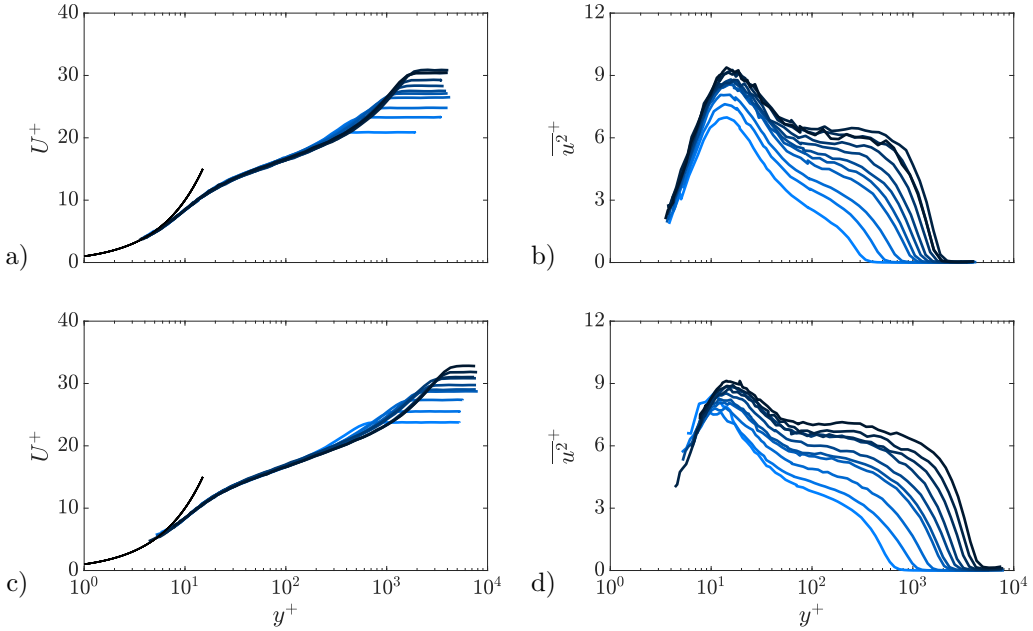

Figure 6: Evolution of the inner-scaled streamwise (a,c) mean and (b,d) variance profiles for configuration 2 at: (a,b) $U_{ref} = 12$ m/s and (c,d) $U_{ref} = 30$ m/s. Colours vary from light blue to dark blue with increasing streamwise location. Black line (-) depicts the relation $U^+ = y^+$.

(1998) with the following expression:

$$m = -\frac{\beta}{H_{12}(1+\beta)+2\beta}. \tag{2}$$

Although in configuration 1 the β distribution still exhibits fluctuations of the order of 15%, the goodness of the fit (see Table 3) allows to consider this configuration as representative of a "near-equilibrium" state. Figures 5, 6 and 7 allow to appreciate the transition from ZPG to APG TBL conditions. The mean velocity profiles collapse from the wall up to $y^+ \approx 200$, thus showing no significant discrepancy with the law of the wall in agreement with Yoon *et al.* (2018). The effect of the pressure gradient starts to become apparent in the outer layer, say starting from $y^+ \approx 200$, where the velocity profiles show higher inner-scaled velocities with increasing β and a more prominent wake which is connected to a decreased wall-shear stress. This is even more evident for configuration 3, where the largest values of β are reached (up to $\simeq 2.4$). These trends are in good agreement with the findings reported in previous studies (Nagano *et al.* 1993; Monty *et al.* 2011; Gungor *et al.* 2016; Vinuesa *et al.* 2018). The effect of increasing β is also evident in the higher value of the inner-scaled edge velocity, a fact that is connected to the lower mean velocity gradient at the wall and thus skin friction due to the adverse pressure gradient. As expected in APGs, the streamwise variance profiles develop an outer peak, whose magnitude becomes comparable to that of the near-wall peak in the larger-β cases from configuration 3. Moreover, the (inner-scaled) value of the inner peak of the velocity variance is also increased when the TBL develops in the streamwise direction. However, while the location of the inner peak remains roughly constant ($y^+ \approx 15$), the inner-scaled wall-distance of the outer peak increases with increasing Re. As reported by Harun *et al.* (2013), the increase of the inner-scaled streamwise variance is not just due to the lower value of the friction velocity used to scale the profile, but it is

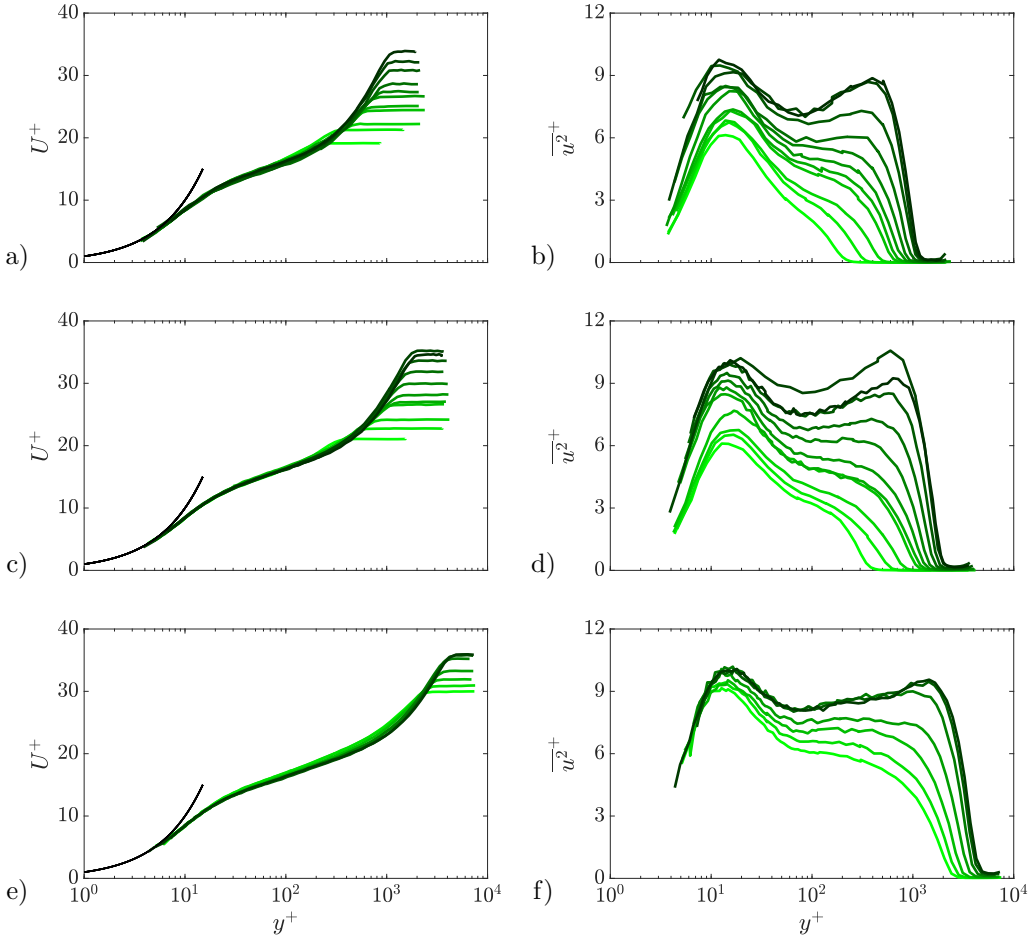

Figure 7: Evolution of the inner-scaled streamwise (a,c,e) mean and (b,d,f) variance profiles for configuration 3 at: (a,b) $U_{ref} = 6$ m/s, (c,d) $U_{ref} = 12$ m/s and (e,f) $U_{ref} = 30$ m/s. Colours vary from light green to dark green with increasing streamwise location. Black line (-) depicts the relation $U^+ = y^+$.

ascribed to enhanced large-scale motions in the outer region. This will be further discussed in section §4 with the spectral analysis in which the energy distribution can be better appreciated.

3.2. *Skewness and flatness factors*

Higher-order statistics for the streamwise velocity fluctuations, in particular the skewness S and flatness F factors, are analysed in Figure 8 for a range of β from 0 to 2.2 at approximately matching $Re_\tau \approx 4,400$ and for the constant-β region from configuration 1, over the streamwise region 2.7 m $< x <$ 4.4 m. The ZPG data from Örlü (2009) (see also Örlü & Schlatter 2013, for a detailed description of data taken under the same conditions) are included in order to highlight the differences induced by the pressure gradient. The skewness factor increases with β in the log-region. These results are in agreement with those reported by Nagano & Houra (2002) and Monty *et al.* (2011), which suggested that the higher values of S are connected with the increased energy of large-scale structures in the APG flows and an increased amplitude modulation of the small scales; such an interrelation has *e.g.* been demonstrated by Schlatter & Örlü (2010). The

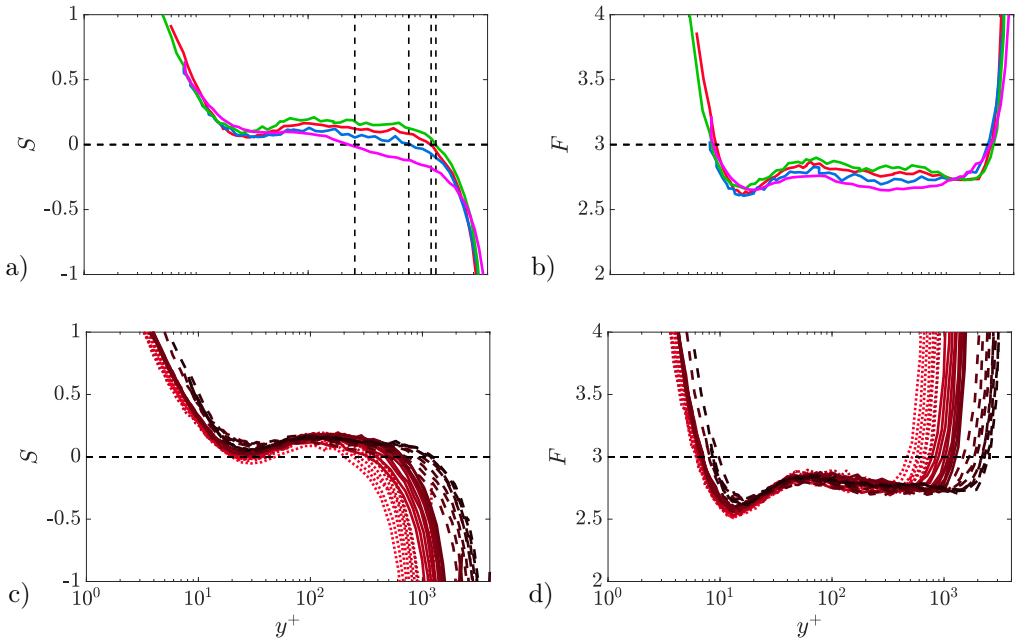

Figure 8: a) Skewness S and b) flatness F factors for $Re_\tau \approx 4,400$. Colours represent – $\beta \approx 0$, – $\beta \approx 0.75$, – $\beta \approx 1.1$, and – $\beta \approx 2.2$. c) Skewness S and d) flatness F factors in the approximately constant-β region given by 2.7 m $\leq x \leq$ 4.4 m, with $\beta \approx 1.1$. Colours vary from light red to dark red with increasing Reynolds number. Line styles correspond to: dotted line $U_{ref} = 6$ m/s, solid line $U_{ref} = 12$ m/s and dashed line $U_{ref} = 30$ m/s. Additionally a vertical line at $y^+_{\text{max,outer}}$ (identified as in §5.2) are located for all the APG cases and $y^+ = 3.9Re_\tau^{0.5}$ for the ZPG case.

skewness exhibits a plateau, *i.e.* an approximately constant value, in the logarithmic region related to the universality of the probability density distribution within the logarithmic layer (Lindgren *et al.* 2004), with an increasing amplitude of the plateau when at higher Re (Figure 8c)). In all the cases it is observed that in the near-wall region there is a sudden increase of the skewness at a location $y^+ \approx 30$ indicative of the strong asymmetry of the probability density distribution in the sublayer caused by the presense of the wall. It is interesting to note that, for all the cases, the location at which the skewness profile crosses the zero line (see Figure 8a)) coincides with the outer peak location (see Figure 12f)). The outer peak location is estimated as $y^+ = 3.9Re_\tau^{0.5}$ for ZPG TBLs and according to method proposed in §5.2 for the APG TBLs.

Regarding the flatness factor, the pressure gradient leads to larger F values in the logarithmic and outer regions. The differences in the behaviour between the ZPG and APG flows are here less significant. At higher Reynolds number, F increases in the inner region but in all the cases the inflexion point is located at $y^+ \approx 15$, see Figure 8b).

Additional insight regarding the connection between high-order moments and the outer-peak location of the streamwise variance is given in Figure 9, where F is plotted against S. This figure suggests that in APG flows there is a connection between the position of the outer maximum of the variance, the zero-crossing of the skewness and the minimum of the flatness. This also is true for the outer peak of the streamwise variance profile in the ZPG cases taken from Örlü (2009). The collapse of the scatter plot of F and S was previously observed in ZPG flows by Eitel-Amor *et al.* (2014), who showed that the inner-scaled wall-normal location of the maximum

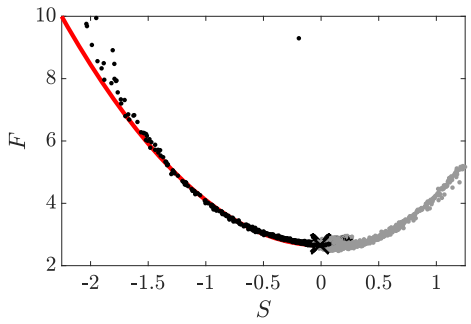

Figure 9: Scatter plot of skewness S and flatness F factors for the APG cases in the region 3.1 m $\leq x \leq$ 4.4 m and the ZPG data from Örlü (2009) and Örlü & Schlatter (2013) (Table 4). Black and grey symbols denote $y^+ > 100$ and $y^+ < 100$, respectively. The thick $\times$ symbol represents the outer peak location, which is calculated according to the method discussed in §5.2. The red line represents the parabola $F = 2.65 + 1.45S^2$ reported in Örlü *et al.* (2016) based on ZPG TBL data.

of the variance, the zero-crossing point of the skewness and the minimum of the flatness coincide. Thus, the present results extend this finding to the outer peak of ZPG and APG TBLs.

3.3. *Integral quantities*

In addition to the results presented in §3.1 and 3.2, the evolution of the boundary-layer integral quantities and pressure-gradient parameters is shown in Figures 10 and 11. In Figure 10, the different parameters are represented in terms of the Reynolds number based on momentum thickness. In order to further characterise the pressure-gradient conditions, the defect shape factor G defined as $G = (H_{12} - 1)/(H_{12}\sqrt{C_f/2})$ (where $C_f = 2(u_\tau/U_\infty)^2$ is the skin-friction coefficient), is represented together with the ratios δ_{99}/θ and δ_{99}/δ^*. Comparing both the β and G curves, it is observed that G is approximately constant for configuration 1, with a value of $G \approx 10$ which is close to the theoretical value of $G \approx 9$ predicted by Mellor & Gibson (1966) and almost identical to the value obtained in the APG simulations of Bobke *et al.* (2017) *i.e.*, $G \approx 9.8$, for $\beta = 1$. Since the mean value of β is slighly higher than 1, it is expected that the G trend falls above the estimated values of a $\beta = 1$ case. Despite this, the behaviour in the trend of G allows to assume that, despite the streamwise deviations in the $\beta(x)$ distribution, the cases with approximately constant β are representative of near-equilibrium conditions. The deviation from the predicted G values from Mellor & Gibson (1966) is explained by considering their proposed evolutions for H_{12} and C_f which will be discussed later. For configurations 2 and 3, G presents progressively larger values with increasing β up to the approximately constant value $G \simeq 12.5$ observed in the last stations of configuration 3. Note that this value is also in good agreement with the ones reported in previous studies (Bobke *et al.* 2017). Comparing the regions of approximately constant β (Figure 3a) and b)) and constant G (Figure 10a)), it can be seen that the beginning of the constant-G region ($x \approx 3.5$ m) is shifted downstream with respect to the approximately constant-β region ($x \approx 2.7$ m). This fact can be attributed to the streamwise distance needed to converge to "near-equilibrium" conditions for the non-constant-β case as was shown by Bobke *et al.* (2017). Figures 10b) and c) reflect the evolution of the ratios δ_{99}/θ and δ_{99}/δ^* respectively, and it can be observed that the effect of β is to decrease both ratios. This result is a consequence of a stronger wake region due to the additional source of shear provided by the pressure gradient (Skåre & Krogstad 1994; Harun *et al.* 2013). This effect is even more evident in the low-Re cases since they

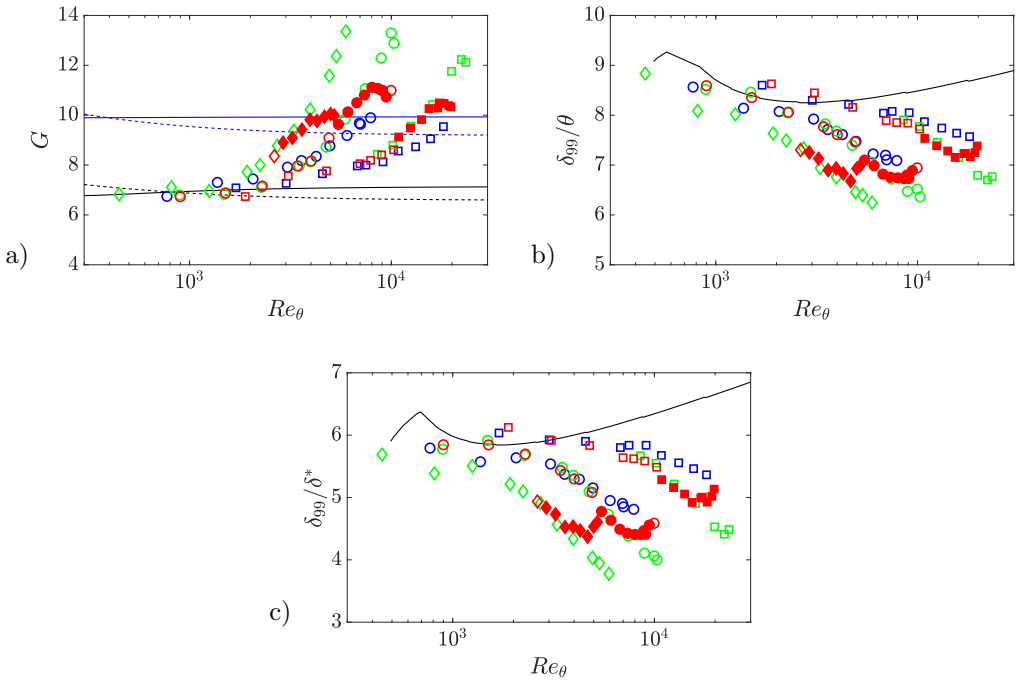

Figure 10: Streamwise evolution in terms of Re_θ of: a) defect shape factor G, b) ratio of boundary-layer and momentum thickness δ_{99}/θ and c) ratio of boundary-layer and displacement thickness δ_{99}/δ^*. Colors and symbols are reported in Table 2. Symbols are filled in the region where β belongs to the approximately constant-β region (Table 2). Black and blue reference lines are correlations for ZPG and $\beta = 1$ given by Chauhan *et al.* (2009) and Vinuesa *et al.* (2017), respectively. Black and blue dashed lines represent the ZPG and $\beta = 1$ relations for G given by Mellor & Gibson (1966).

are more affected by the pressure-gradient effects as was shown in Sanmiguel Vila *et al.* (2017*a*) and Vinuesa *et al.* (2018).

Figure 11 shows the development of the skin-friction coefficient C_f and the shape factor H_{12} as a function of Re_θ. Both quantities are compared with the existing trends for ZPG reported in Nagib *et al.* (2007) and the recently proposed correlations for APG TBLs by Vinuesa *et al.* (2017). For both quantities the transition from a ZPG state to APG conditions can clearly be observed. This transition is reflected in the C_f trend, where the values of C_f fall below the ZPG line, while the opposite trend is exhibited by the H_{12} curve as also reported by Kitsios *et al.* (2017). The values of C_f decay with increasing pressure-gradient magnitude since, as discussed by Bobke *et al.* (2017), the velocity gradient at the wall is reduced as a consequence of the boundary-layer thickening due to the APG. The shape factor H_{12} on the other hand exhibits an increasing trend due to the adverse pressure gradient (Skåre & Krogstad 1994; Monty *et al.* 2011; Bobke *et al.* 2017), and recovers a decreasing trend in the approximately constant-β region, although with a different rate of decay than that of the ZPG. It is interesting to note that the C_f and H_{12} curves of configuration 1 roughly follow the correlations recently proposed by Vinuesa *et al.* (2017). Note, however, that such correlations were developed for a constant $\beta = 1$, and configuration 1 for the intermediate free-stream velocity exhibits values of β slightly larger than 1 ($\beta_{avg} \approx 1.2$), a fact that explains the slightly lower values of C_f. Apart from this, the empirical relations shown here were developed using data at lower Re and the addition of data at higher Re may improve the

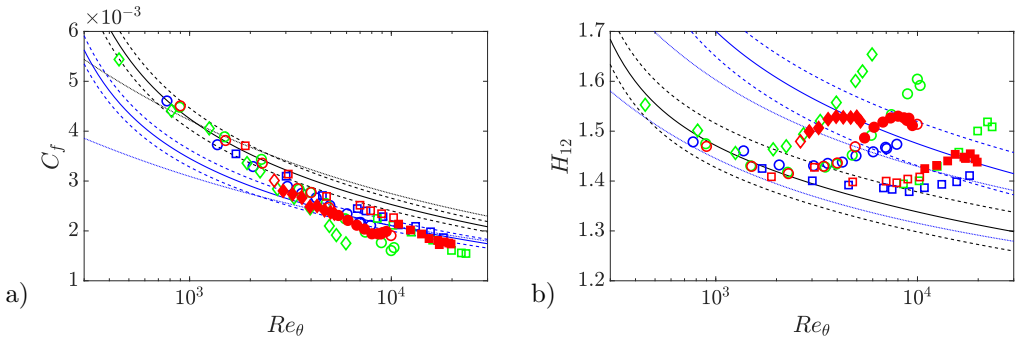

Figure 11: a) Skin-friction coefficient evolution with Re_θ, where the black and blue solid line are the ZPG and $\beta = 1$ references given by Nagib *et al.* (2007) and Vinuesa *et al.* (2017) respectively. Additionally, $\pm 5\%$ deviation are represented by the dashed lines. Black and blue dotted lines represent the ZPG and $\beta = 1$ relations given by Mellor & Gibson (1966). b) Reynolds-number evolution of the shape factor H_{12}, where the black and blue solid lines are the ZPG and $\beta = 1$ references given by Vinuesa *et al.* (2017) and $\pm 3\%$ deviation are represented by the dashed lines. Black and blue dotted lines represent the ZPG and $\beta = 1$ relations given by Mellor & Gibson (1966). The colors and symbols reported in Table 2. Symbols are filled in the region where β belongs to the approximately constant-β region (Table 2).

current trend. The results obtained with the present high-Re experimental database confirm that the functional forms of the empirical curves for H_{12} and C_f are analogous to those in ZPG conditions if the constant-β condition is fulfilled. This is in line with previous observations made by Monty *et al.* (2011). Figure 11 also reports the correlations proposed by Mellor & Gibson (1966) for both H_{12} and C_f. The C_f curve seems to be in good agreement with present data. However, it is apparent that the trend by Mellor & Gibson (1966), which is slightly higher compared to the curve proposed by Vinuesa *et al.* (2017), in the high-Re regime will not follow the evolution of the C_f. In contrast, the H_{12} curve falls below the one proposed by Vinuesa *et al.* (2017) and consequently underestimates the real evolution of H_{12}. These discrepancies may be associated with the fact that a constant value of κ is considered by Mellor & Gibson (1966) in the log-law description of the overlap region over the whole pressure-gradient range, as pointed out by Vinuesa *et al.* (2017). The errors showed in the estimation of H_{12} are associated with the previous trend in G, since a lower value of H_{12} lead to a lower G.

4. Comparison of APG TBLs at matched Reynolds number and Clauser pressure-gradient parameter

In this section we discuss the different effects of the local β and Re using the ZPG data from Örlü (2009), Örlü & Schlatter (2013) and Eitel-Amor *et al.* (2014) which are re-analyzed using the same procedure as in our new APG data. Three different cases at matched Re_τ are used in order to study the pressure-gradient effects. Note that both Re_θ and Re_{δ^*} (which is the Reynolds number based on displacement thickness) develop similarly to Re_τ due to the mild β values for the present study. Therefore, Re_τ is an appropriate Reynolds number to study the β and Re-dependence of the parameters analyzed here (Bobke *et al.* 2017). The boundary-layer parameters for the selected ZPG and APG profiles are reported in Tables 4 - 5. It should be noted that the experimental ZPG data have an inner-scaled hot-wire length $L^+ > 20$, therefore the data suffer from limited attenuation effects in the near-wall region (Hutchins *et al.* 2009).

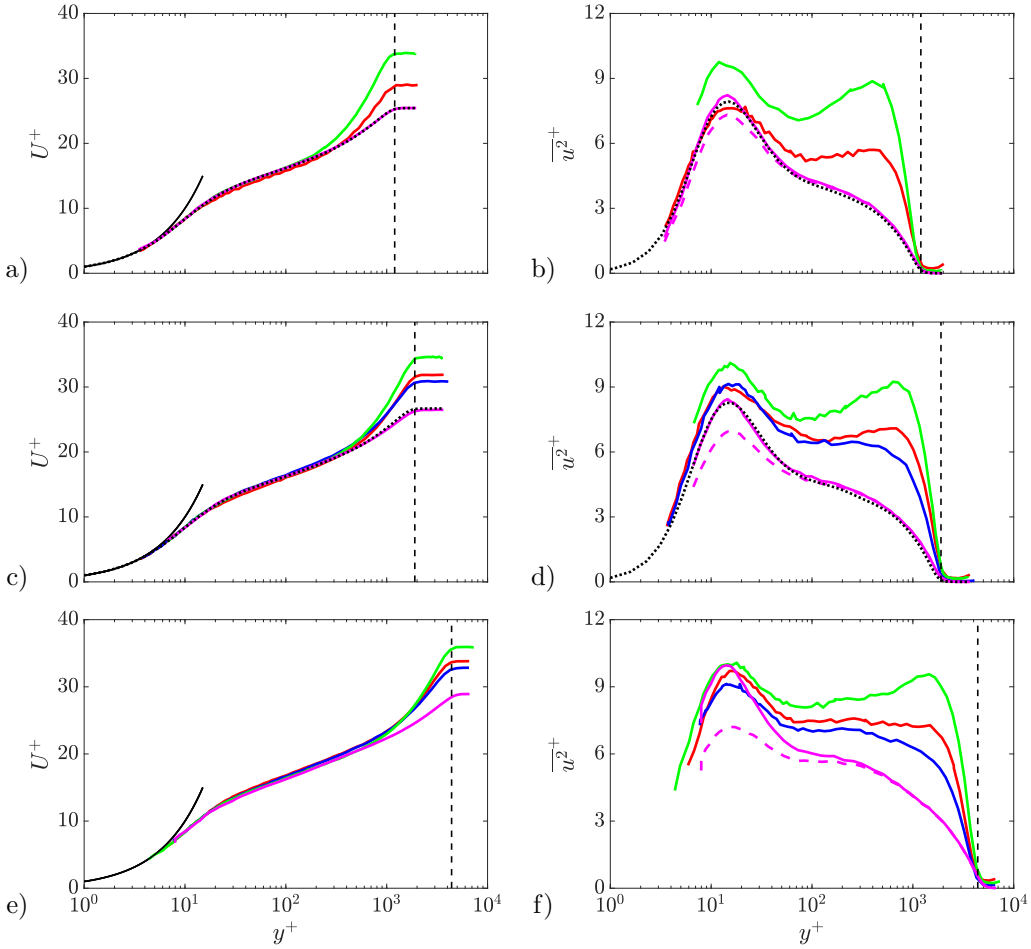

Figure 12: Inner-scaled streamwise (a,c,e) mean and (b,d,f) variance, with approximately matched Re_τ, where colour (–) (dotted) represents $\beta \approx 0$ (LES Eitel-Amor *et al.* (2014)), (–) $\beta \approx 0$ (Experimental data from Örlü (2009) and Örlü & Schlatter (2013)), (–) $\beta \approx 0.75$, (–) $\beta \approx 1.1$, and (–) $\beta \approx 2.2$. The following matched Reynolds numbers are considered: (a,b) $Re_\tau \approx 1,200$, (c,d) $Re_\tau \approx 1,900$, (e,f) $Re_\tau \approx 4,400$. Black dashed line indicates the reference Re_τ for every case. Magenta dashed line indicates raw hot-wire data without applying the correction from Smits *et al.* (2011).

4.1. *Spectral analysis comparison*

Figure 12 shows a comparison between the inner-scaled mean velocity profiles and streamwise variance of the three APG configurations under study and the ZPG reference at matched Re_τ. As apparent from the added LES data by Eitel-Amor *et al.* (2014) at matched Reynolds number, the agreement is exceptional in terms of the mean velocity profile including the wake region. This reinforces the conclusions by Örlü & Schlatter (2013) and those by Schlatter & Örlü (2012) and Sanmiguel Vila *et al.* (2017*b*) that experiments and DNS or well-resolved LES can represent the same flow case if inflow and tripping conditions are matched, which was the case for the present data sets. The differences between the raw hot-wire data instead exhibits a visible attenuation in terms of the near-wall peak of the variance profile, when compared to the LES data (cf. Eitel-Amor *et al.* (2014)). These effects are, however, well documented (Hutchins *et al.* 2009) and several

U_∞ [m/s]	Re_{δ^*}	Re_θ	Re_τ	δ_{99} [cm]	H_{12}	L^+	Colour	Symbol	Dataset
17.14	5,060	3,630	1,150	25.8	1.39	21	Magenta	♢	Örlü & Schlatter
26.42	7,860	5,800	1,810	27.5	1.36	31	Magenta	◯	Örlü & Schlatter
40.03	19,670	15,040	4,480	49.7	1.31	50	Magenta	□	Örlü
-	5,180	3,740	1,170	-	1.38	-	Black	♢	Eitel-Amor *et al.*
-	7,865	5,740	1,750	-	1.37	-	Black	◯	Eitel-Amor *et al.*

Table 4: Boundary-layer parameters for the ZPG datasets from Örlü (2009), Örlü & Schlatter (2013) and Eitel-Amor *et al.* (2014). Note that for the latter, which is a numerical dataset, we do not provide dimensional values of U_∞ and δ_{99}, or any inner-scaled wire length L^+; instead the spanwise grid resolution for these cases is $\Delta z^+ = 8$.

Configuration	β	U_∞ [m/s]	Re_{δ^*}	Re_θ	Re_τ	δ_{99} [mm]	H_{12}	L^+	Colour	Symbol
1	0.88	5.0	7,640	5,000	1,190	102.0	1.53	6	Red	♢
1	1.11	9.5	13,830	9,060	1,910	95.3	1.53	11	Red	◯
1	1.12	24.4	28,440	19,780	4,300	90.7	1.44	13	Red	□
2	0.80	10.3	11,640	7,900	1,820	82.4	1.47	12	Blue	◯
2	0.71	27.0	25,570	18,120	4,190	76.5	1.41	29	Blue	□
3	2.03	4.8	9,850	5,960	1,100	120.4	1.65	5	Green	♢
3	2.25	9.2	16,410	10,310	1,890	107.4	1.59	9	Green	◯
3	2.22	23.2	35,370	23,450	4,410	101.6	1.51	23	Green	□

Table 5: Boundary-layer parameters for the APG dataset, extracted from the present experimental database.

techniques for their compensation are well established in the literature (Segalini *et al.* 2011; Miller *et al.* 2014). In order to compare streamwise variance profiles from APG and ZPG TBLs, here the correction proposed by Smits *et al.* (2011) is employed only on the ZPG data to rectify the attenuated inner peak observed at $Re_\tau \approx 1,900$ and $4,400$ due to the large L^+ in the hot-wire measurements. As one of the results of the present work, as will be apparent from §5, we abstain from applying any correction to the APG TBL data, since the method by Smits *et al.* (2011) (or any other method for that matter) has only been validated empirically under ZPG conditions (or canonical internal flows), but not for flows under the influence of stronger pressure gradients in which the relative importance of small- and large-scale energy is different as under ZPG conditions. It should, however, be noted that most of the APG cases are well-resolved in terms of their spatial and temporal resolution (due to the thicker boundary layer compared to a ZPG); cf §Appendix A. Hence the comparison between the raw and corrected ZPG data gives also confidence that the following discussion on the outer layer turbulence statistics is not biased by spatial resolution effects. Analyzing the inner region it can be observed that the inner peak in the variance profile increases with β, even though this trend is less evident for higher Re_τ. This observation is related to the fact that the low-Re TBLs are more sensitive to APG effects, as reported in Sanmiguel Vila *et al.* (2017*a*) and Vinuesa *et al.* (2018). In the outer region of the variance profiles, progressively larger values can be observed at higher β; note that a prominent outer peak is present at low Re, and for the stronger β cases at higher Re. On the other hand, for the mean velocity profiles a good collapse is observed in the inner region for all the profiles and a progressively stronger wake in the outer region as β increases. Also note that the APG magnitude was not sufficient to produce the reduced inner-scaled velocities in the buffer region, as reported by Spalart & Watmuff (1993) or Vinuesa *et al.* (2018), in any of the cases, which might be related to the fact that the APG effect is less dominant at higher Re.

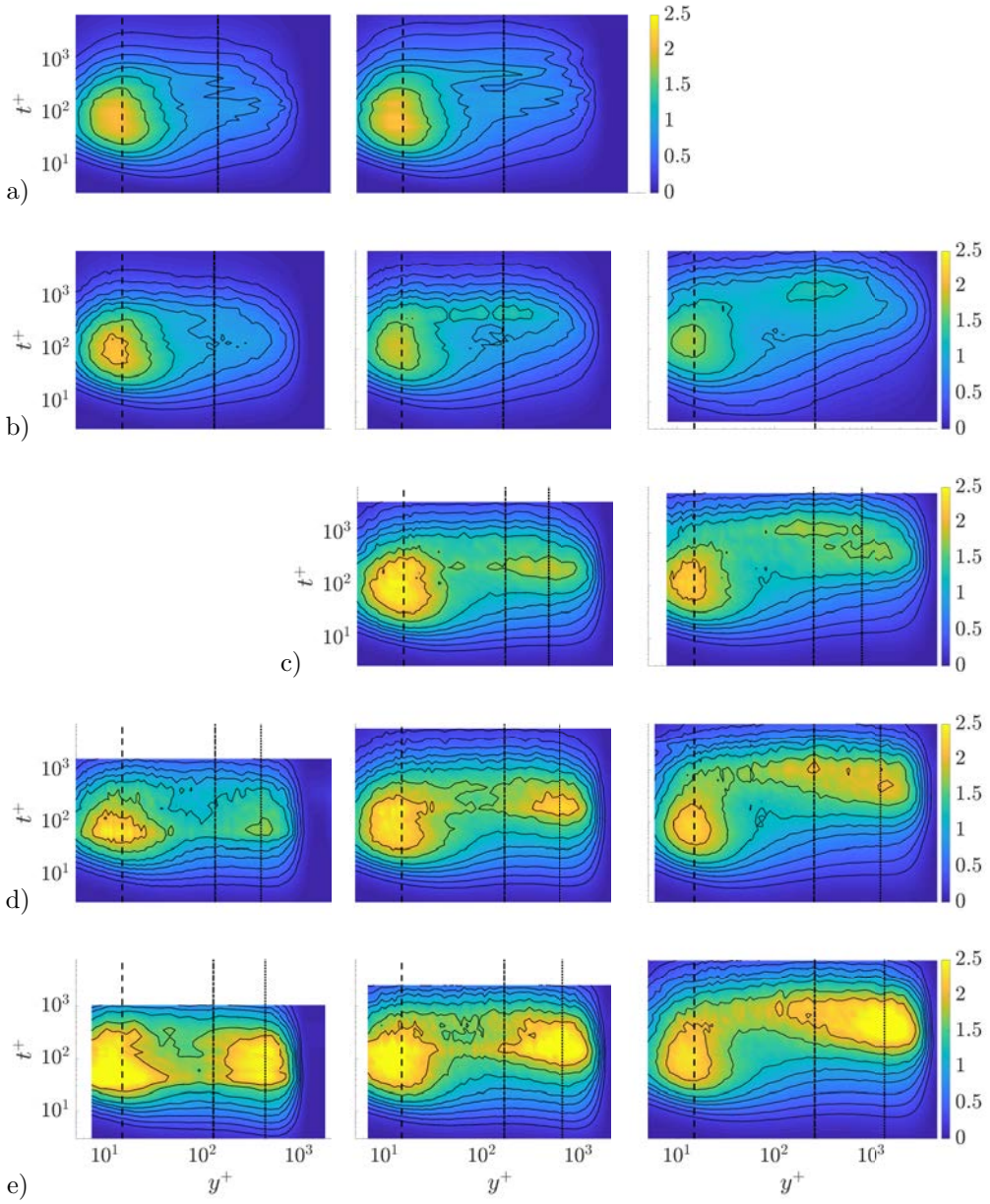

Figure 13: Inner-scaled premultiplied energy spectra of the streamwise velocity with contour levels at $f^+\Phi^+_{uu} = 0.25, 0.4, 0.575, 0.775, 0.95, 1.2, 1.6, 2.0$. Row a) $\beta \approx 0$ (LES data), b) $\beta \approx 0$ (Experimental data from Örlü (2009) and Örlü & Schlatter (2013)), c) $\beta \approx 0.75$, d) $\beta \approx 1.1$, e) $\beta \approx 2.2$. (Left panels) $Re_\tau \approx 1,200$, (middle panels) $Re_\tau \approx 1,900$, (right panels) $Re_\tau \approx 4,400$. Auxiliary vertical lines are located at (dashed) $y^+ = 15$ and (dash-dotted) $y^+ = 3.9Re_\tau^{0.5}$ for all the cases. Additionally vertical dotted lines at $y_{\max,\text{outer}}$ (identified as in §5.2) are located for all the APG cases.

These well-known features can be connected with the scale organisation of the flow through spectral analysis. Figure 13 shows the inner-scaled pre-multiplied power-spectral density of the streamwise velocity, $f^+\Phi^+_{uu}$, plotted in terms of the inner-scaled wall-normal position, y^+, and

the inner-scaled time, t^+. It should be remarked that the following results are presented in the time/frequency domain. This choice is motivated by the fact that converting temporal data into the spatial data requires a convection velocity and it is not clear which choice should be the most suitable (del Álamo & Jiménez 2009; Schlatter *et al.* 2010); in particular when comparing ZPG and APG TBLs, where a scale-independent convection velocity might lead to a biased interpretation of the results (Renard & Deck 2015). The overall shape of the near-wall region is relatively similar in all the configurations for both ZPG and APG. This energy distribution is connected with the inner peak which can be observed at $y^+ \approx 15$ in the streamwise variance profiles from Figure 12 and approximately corresponds to a streamwise wavelength of $\lambda_x^+ \approx 1,000$ (when the period t^+ is converted into a wavelength invoking Taylor's frozen turbulence hypothesis). This inner peak represents the footprint of the near-wall structure of elongated high- and low-speed regions (Kline *et al.* 1967). It should be recalled that the attenuated values in the near-wall peak at higher Re in the ZPG case, is an artifact of spatial resolution effects (Hutchins *et al.* 2009), which are not corrected for in the spectra as opposed to the variance profiles. The spectral maps from the LES are hence shown to highlight that the outer layer is unaffected by spatial resolution effects and that that the amplitude is attenuated merely for the inner-peak region. Note also again that the L^+ value for the ZPG data at the higher Re exceeds most of the inner-scaled wire lengths of the APG experiments (cf. §Appendix A). The main differences between the APG and ZPG configurations emerge when the power spectral density contours are compared for $y^+ > 100$; starting from that location the activity in all the APG configurations is more intense, especially for higher values of β. This behaviour is reflected in the onset of the outer spectral peak in the APG cases, which is in good agreement with the characteristic peak reported in previous studies (Harun *et al.* 2013; Bobke *et al.* 2017; Lee 2017). Apart from this outer peak, in the high-Re cases an additional region of high energy density emerges, for both ZPG and APG configurations. This second outer spectral peak is located at the middle of the logarithmic region, $y^+ \approx 3.9Re_\tau^{0.5}$, and is associated with the large-scale motions which were also observed in ZPG configurations at high Re_τ (Hutchins & Marusic 2007; Mathis *et al.* 2009; Marusic *et al.* 2015). This effect appears to be independent of the pressure gradient and is associated with phenomena which have longer t periods than those associated with the APG outer spectral peak (Harun *et al.* 2013).

Comparing the Re-evolution of the different APG configurations it can be observed that higher values of Re lead to more energetic large-scale motions with larger time periods t. Analysing the different configurations, it is observed that larger values of β are connected to larger power-spectral density, which confirms that larger values of β increase the population of large-scale motions as suggested by Harun *et al.* (2013). Configuration 3, in which β is the highest, shows the most energetic spectra. The contour lines reflect that the enhanced large-scale energy in the outer layer is spread over a range of wavelengths. This shows that, as mentioned in §3, the increase of the inner-scaled variance is related to the enhanced large-scale motions in the outer region. This is in good agreement with studies such as those by Harun *et al.* (2013) and Lee (2017) which discuss the wall footprint of large-scale structures on the inner region.

4.2. *Wavelength analysis and cut-off definition*

From the observation of Figure 13, it is apparent that a cut-off based on a fixed t^+ value would not completely separate the small and large scales in the spectra. For this reason, Taylor's frozen turbulence hypothesis is used in order to be able to define a proper scale-cut-off wavelength in the high-Re spectra. With this purpose, the convection velocity, U_c, has been taken as the local mean velocity, except for the region $U_c^+ < 10$ where it has been set to 10 u_τ (del Álamo & Jiménez 2009). This estimation of U_c is in agreement with previous studies in which the amplitude modulation in APG TBLs was studied (Dróżdż & Elsner 2017). Figure 14 shows the premultiplied energy spectra ($\kappa_x^+ \Phi_{uu}^+$) plotted against the inner-scaled wall-normal distance y^+ and the streamwise wavelength λ_x^+. Here it can be noted that the outer peak due to the high-Re effect is also present in the APG TBLs at a wavelength $\lambda_x \approx 6\delta_{99}$ as observed also for ZPG cases (Mathis *et al.* 2009). A second

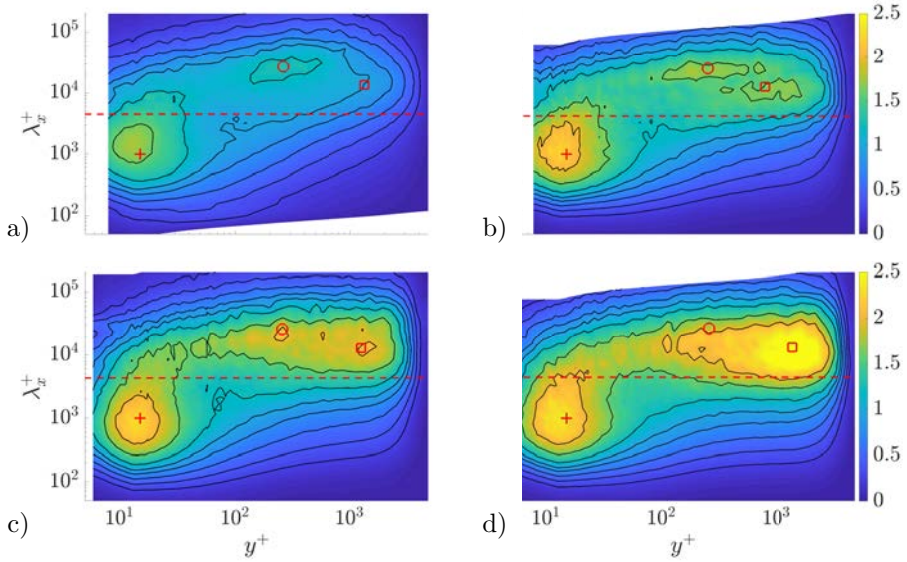

Figure 14: Inner-scaled premultiplied energy spectra of the streamwise velocity at $Re_\tau \approx 4,400$ with contour levels at $\kappa_x^+ \Phi_{uu}^+ = 0.25, 0.4, 0.575, 0.775, 0.95, 1.2, 1.6, 2.0$, for pressure-gradient strengths a) $\beta \approx 0$ (experimental data from Örlü (2009)), b) $\beta \approx 0.75$, c) $\beta \approx 1.1$, d) $\beta \approx 2.2$. Auxiliary red symbols are located at the following coordinates: (+) $(y^+ = 15, \lambda_x^+ = 1,000)$, (∘) $(y^+ = 3.9Re_\tau^{0.5}, \lambda_x/\delta_{99} = 6)$ for all the cases. Additionally red (□) symbols are located at $(y^+ = y^+_{\max,\text{outer}}, \lambda_x/\delta_{99} = 3)$ for all the APG cases and $(y/\delta_{99} = 0.3, \lambda_x/\delta_{99} = 3)$ for the ZPG case. An auxiliary horizontal dashed line is placed at $\lambda/\delta_{99} = 1$.

peak, ascribed to the APG effects, has a wavelength $\lambda_x \approx 3\delta_{99}$ in agreement with previous results such as the ones reported by Harun *et al.* (2013). The location of the APG-related spectral peak is identified according to the method proposed in §5.2.

In order to highlight the β effects on the scale organization along the boundary layer, in Figure 15 we show the premultiplied power-spectral density for various APG magnitudes and $Re_\tau \simeq 4,400$, at various wall-normal locations: a) $y^+ = 15$, b) $y^+ = 3.9Re_\tau^{0.5}$ and c) $y^+ = y^+_{\max,\text{outer}}$ for the APG cases and $y/\delta_{99} = 0.3$ for the ZPG case; note that insufficient spatial resolution effects are restricted to comparisons at $y^+ < 100$, *i.e.* subplot a), with the ZPG cases. Both inner and outer scaling are presented since some of the phenomena under study are related to outer-region dynamics. The Zagarola–Smits velocity $U_{ZS} = U_\infty \delta^*/\delta_{99}$ and the length scale δ_{99} are chosen as outer-scaling parameters as proposed by Maciel *et al.* (2018). In Figure 15a), the energy distribution in the near-wall region does not show differences in the pressure-gradient range under study. However, larger spectral densities are observed at higher β for the largest wavelengths ($\lambda_x/\delta_{99} > 1$, see Figure 15b)). This effect is in agreement with previous findings for ZPG TBLs at high Reynolds numbers (Hutchins & Marusic 2007). At $y^+ = 3.9Re_\tau^{0.5}$ it can be observed that the effect of the pressure-gradient strength becomes more evident since the case with stronger APGs shows larger energy levels. Comparing the APG cases with the ZPG profile it can be noticed, as discussed by Harun *et al.* (2013), that the large scales are dominant in the APG cases. For the configurations 1 and 2, the spectral peak at $\lambda_x/\delta_{99} \approx 6$ is evident as in the ZPG case. For larger values of β, instead, it appears that the spectral activity is spread over the range $\lambda_x/\delta_{99} \approx 3 - 6$ (see Figure 15d)), without a clear maximum. This result suggests that for higher values of β

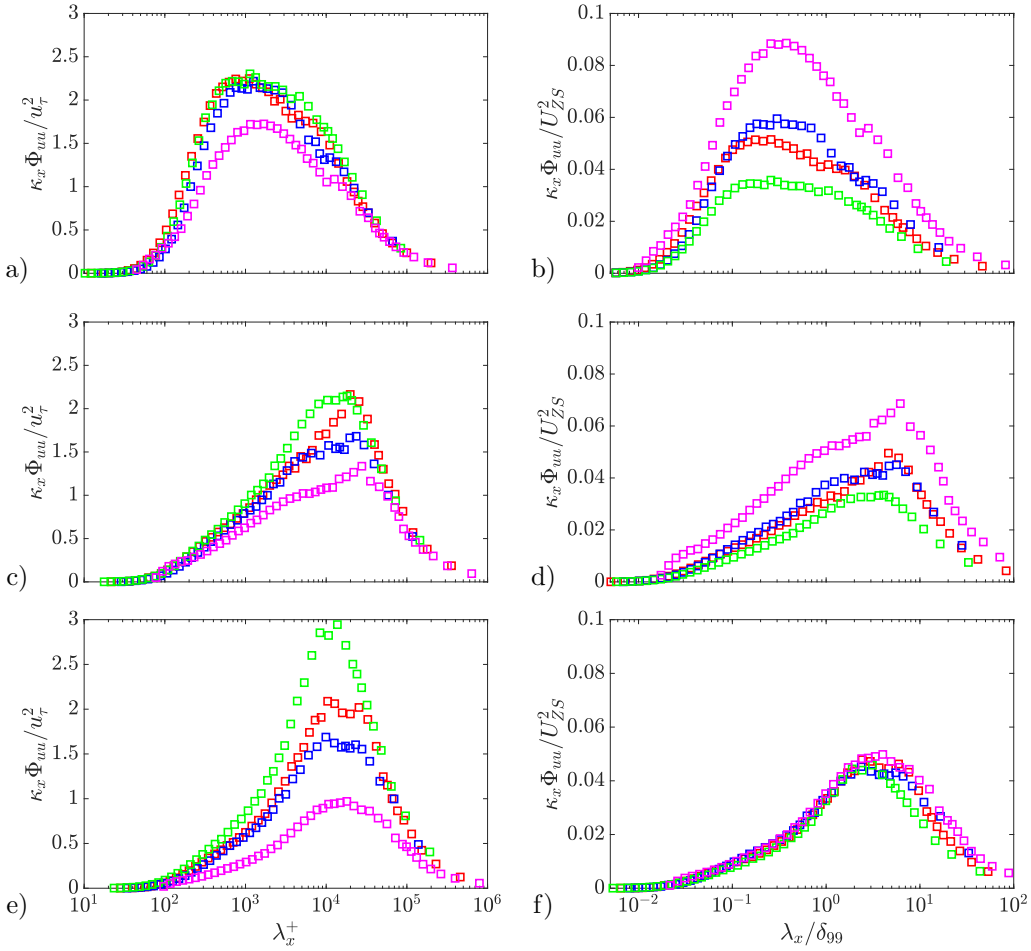

Figure 15: Premultiplied energy spectra non-dimensionalised in (a,c,e) inner units and (b,d,f) outer units at three different wall-normal locations: (a,b) $y^+ = 15$, (c,d) $y^+ = 3.9Re_\tau^{0.5}$ and (e,f) $y^+ = y^+_{\mathrm{max,outer}}$ for the APG cases and $y/\delta_{99} = 0.3$ for the ZPG case. Colours represent: (–) $\beta \approx 0$ (Experimental data from Örlü (2009)), (–) $\beta \approx 0.75$, (–) $\beta \approx 1.1$, and (–) $\beta \approx 2.2$. Reynolds number is $Re_\tau \approx 4,400$.

the dominant effect of the outer spectral activity in the logarithmic region is mainly due to pressure-gradient effects. In the present β range the spectral activity due to pressure-gradient effects is comparable to the high-Re activity only for sufficiently large values of β, *i.e.* for $\beta > 2$. In contrast with the observations made by Harun *et al.* (2013), who suggested that this peak is overshadowed by the presence of the structures with longer wavelengths, here we show that at high Reynolds numbers both effects are present, as evident from the plateau observed in Figure 15d). The last location under study corresponds to the outer peak due to pressure-gradient effects for the APG cases and $y/\delta_{99} = 0.3$ for the ZPG case. The wall-normal location for the ZPG case is chosen according to the $y_{\mathrm{max,outer}}/\delta_{99}$ location in the APG cases since, as will be shown later in §6.2, this particular value ($y/\delta_{99} = 0.3$) is closer to the APG outer peak location in this Re range. The energetic peak from the three APG configurations is associated with shorter wavelengths for progressively increasing values of β. The effects of the pressure gradient are more prominent than in the near-wall region when scaled in inner units. In contrast, the energy distribution appears to

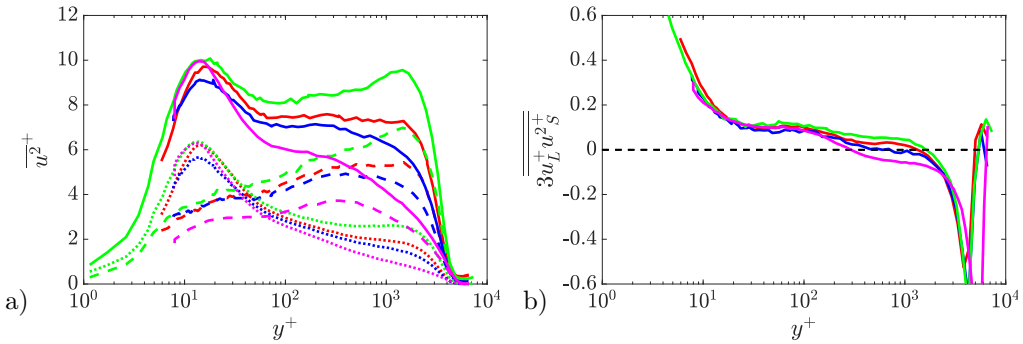

Figure 16: a) Decomposition of the velocity fluctuations (solid lines) into a small-scale (dotted lines) and a large-scale (dashed lines) component for $Re_\tau \approx 4,400$. b) Dominant scale-decomposed skewness term, $\overline{\overline{3u_L^+ u_S^{2+}}}$ for $Re_\tau \approx 4,400$ (right). Colour (–) represents $\beta \approx 0$, (–) $\beta \approx 0.75$, (–) $\beta \approx 1.1$, and (–) $\beta \approx 2.2$.

collapse when scaled using outer units (Figure 15f)). In the range of small scales ($\lambda_x/\delta_{99} < 1$) all the cases show the same distribution. For the large-scale range ($\lambda_x/\delta_{99} > 1$), it appears that the outer peak which is observed in all the APG cases at $\lambda_x/\delta_{99} \approx 3$ becomes dominant at high β values.

5. Inner/outer layer interactions

5.1. *Scale relationship*

The effect of the interaction between the different scales and their effect on the Reynolds stresses is quantified via a scale-decomposition analysis (Monty *et al.* 2011; Harun *et al.* 2013). Based on previous results from §4.2, the cut-off wavelength has been applied at $\lambda_x/\delta_{99} = 1$, which is a reasonable compromise to effectively separate the inner and outer peaks in the spectra, as apparent from the spatial spectral maps presented in Figure 14. Although the use of Taylor's hypothesis to define the cut-off filter in terms of streamwise wavelength depends on the choice of the convection velocity throughout the boundary layer, this is often the only possibility in single-point hot-wire measurements (Mathis *et al.* 2009; Harun *et al.* 2013).

Figure 16a) shows the small- and large-scale components of the streamwise velocity fluctuations. It is observed that with increasing pressure-gradient strength the penetration of the large-scale components toward the near-wall region increases. While the small-scale energy in ZPGs scales throughout the entire boundary-layer thickness (Marusic *et al.* 2010), it is clear that this does not extend to APG TBLs, where the small-scale energy contribution is also enhanced in the outer region, where spatial resolution effects are not to be expected (Hutchins *et al.* 2009). This has a clear impact on the correction schemes for spatial resolution effects that consider the viscous length-scale as the governing parameter (Smits *et al.* 2011), since these schemes should thus be employed with caution for APG TBLs. Moreover, this fact also implies that comparisons at (relatively large and) matched viscous-scaled hot-wire lengths (Harun *et al.* 2013) will not ensure the absence of measurement bias due to spatial resolution effects. In this respect, it should be noted, that the correction proposed by Smits *et al.* (2011) has only been employed on the ZPG TBLs profiles.

In order to understand the interaction between the small and large scales, the amplitude modulation, which is defined as the modulation of the envelope of the small scales by the large scales in the flow, is analysed in Figure 16b). In the present study, this is done using the correlation $\overline{\overline{3u_L^+ u_S^{2+}}}$ (where $\overline{\overline{X}} = \overline{X}/(\overline{u^{+2}})^{3/2}$ for any variable X), with u_S and u_L denoting the small- and

large-scale fluctuations of the streamwise velocity (Mathis *et al.* 2011). This quantity is described in studies such as those by Mathis *et al.* (2011) and Dogan *et al.* (2018) and is the only Reynolds-number-dependent component of the scale-decomposed skewness factor. The results show a highly modulated near-wall region with a clear influence of the Reynolds number. Outside the near-wall region, the modulation decreases until becoming negative at the middle of the log-region for the ZPG case and at a location closer to the outer peak position in the APGs. In general, modulation is higher in the APG cases as a result of the enhancement of the large-scale organisation in these flows.

The changes in the large-scale organisation and their impact on the small-scale organisation can be studied following the methodology described by Ganapathisubramani *et al.* (2012), in which the interaction between the large-scale and small-scale component of the streamwise velocity fluctuations is studied by conditionally averaging the small-scale intensity (u_S^2) for various values of the large-scale fluctuations (u_L). The procedure used to compute this conditional small-scale amplitude is as described in Ganapathisubramani *et al.* (2012) and is briefly explained in the following. The large-scale (u_L) and small-scale (u_S^2) fluctuations have been obtained by using a spectral filter with a cut-off wavelength of δ_{99}. Then, the signal for a wall-normal location is divided into individual segments of length δ_{99}/U_c, which are used as a representative signal segment. The value of the large-scale fluctuation in a segment is chosen as the value at the centre of that particular segment. The variance of the small-scale signal over the same segment is also computed and defined as the amplitude of the small scales conditioned on the strength of the representative large-scale signal, ${u_S^{2^+}}|_{u_L^+}$. Bins in the range $-6 < u_L^+ < 6$ with a spacing of 0.2 are created as in previous studies (Ganapathisubramani *et al.* 2012; Yoon *et al.* 2018). Using these bins, the number of occurrences of the representative fluctuation (u_L^+) within each bin is calculated across all wall-normal locations, $N[u_L^+(y)]$. Finally, the averaged small-scale variance for each bin of the large-scale fluctuation is calculated as:

$$\langle {u_S^+}^2({u_L^+}^2, y)\rangle = \frac{\sum u_S^{2^+}(y)|_{u_L^+(y)}}{N[u_L^+(y)]}. \tag{3}$$

Figure 17 shows the distribution of u_L^+ by means of the probability density function *p.d.f.* across the y direction for ZPG and APG cases at $Re_\tau \approx 4,400$, defined as:

$$p.d.f.[u_L^+(y)] = \frac{N[u_L^+(y)]}{\int N[u_L^+(y)]\mathrm{d}u_L^+}. \tag{4}$$

The results reported in this subsection have also been calculated for different cut-off values (spatial and temporal) as performed in the Appendix from Ganapathisubramani *et al.* (2012) in the range of $0.5 \leq \delta_{99}/U_c \leq 3$, and the general trends presented here are not affected. The figure shows a peak at $u_L^+ = 0$, therefore the small scales are more prominent in the near-wall region and at the boundary-layer edge, as indicated by Ganapathisubramani *et al.* (2012) and Yoon *et al.* (2018). Comparing both ZPG and APG cases, a wider distribution of large-scale fluctuations in the logarithmic region can be observed in the latter. The distribution of large-scale fluctuations is almost symmetric in the ZPG case, while the introduction of the pressure gradient breaks this symmetry. As β increases, the u_L^+ activity is displaced towards values of high momentum ($u_L^+ > 0$), while in the near-wall region is moved towards values of low momentum ($u_L^+ < 0$). The influence of these wider u_L^+ fluctuations on the small scales is observed in Figure 18 in which the small-scale variance $\langle {u_S^+}^2\rangle$ is represented against the u_L^+ and the wall-normal position. As shown by Ganapathisubramani *et al.* (2012), higher values of u_L^+ are associated with increasing values in the small-scale variance $\langle {u_S^+}^2\rangle$, this effect being more evident in the near-wall region. This modulation of the small scales by the large-scale fluctuations in the near-wall region is also observed in the APG case, but here the modulation of large-scale fluctuations is also present in the

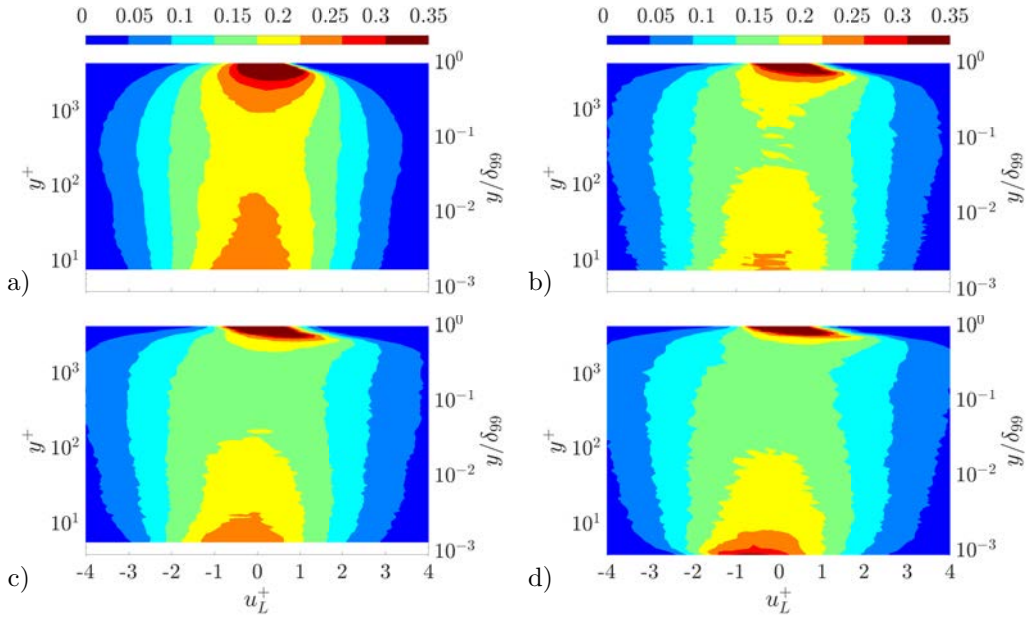

Figure 17: Probability density function of the large-scale fluctuation, as defined in equation (4), across wall-normal locations for $Re_\tau \approx 4,400$ and pressure-gradient strengths a) $\beta \approx 0$, b) $\beta \approx 0.7$, c) $\beta \approx 1.1$ and d) $\beta \approx 2.2$.

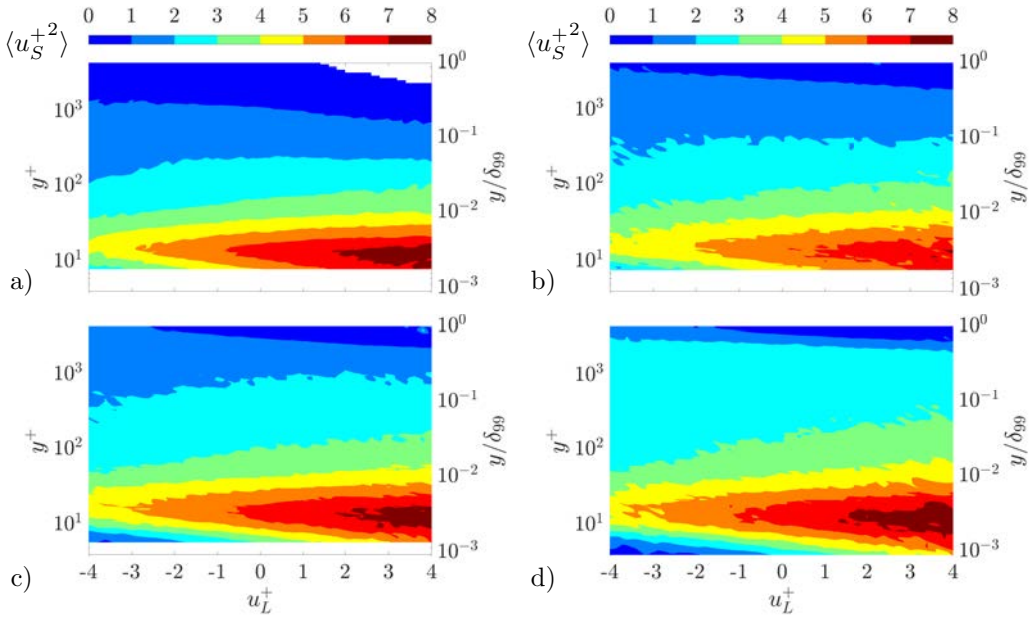

Figure 18: Small-scale variance as a function of large-scale fluctuation and wall-normal location $\langle u_S^{+2}(u_L^{+2}, y^+) \rangle$, computed with equation (3), for $Re_\tau \approx 4,400$ and pressure-gradient strengths a) $\beta \approx 0$, b) $\beta \approx 0.7$, c) $\beta \approx 1.1$ and d) $\beta \approx 2.2$.

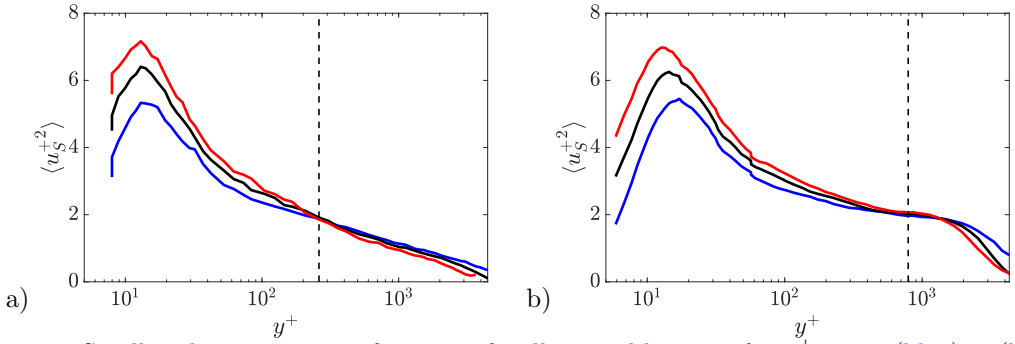

Figure 19: Small-scale variance as a function of wall-normal location for $u_L^+ = -2$ (blue), 0 (black) and 2 (red) for $Re_\tau \approx 4,400$ and pressure-gradient strength a) $\beta \approx 0$ and b) $\beta \approx 1.1$. The dashed vertical lines indicate approximate cross-over points between the $u_L^+ = 2$ and 0 curves, *i.e.*, a) $y^+ = 3.9Re^{0.5}$ and b) $y^+ = y^+_{\mathrm{max,outer}}$.

logarithmic region, where essentially no modulation is visible in the ZPG case. With increasing β, stronger amplification is observed in the near-wall region over a wider u_L^+ range than in the ZPG case. Note that the opposite is observed in the outer region, an observation connected with the intense interaction of the large scales in the near-wall region compared with the ZPG case. Figure 19 shows the wall-normal variation of small-scale variance for values of u_L^+ corresponding to -2, 0 and 2, *i.e.* negative, zero and positive large-scale streaks. Our results show that $\langle u_S^{+2} \rangle$ is higher for $u_L^+ = 2$ in the near-wall region in both the ZPG and a representative APG case. However, while for the ZPG case there is a cross-over point between the $u_L^+ = 2$ and $u_L^+ = 0$ curves at the middle of the logarithmic region, $y^+ \approx 3.9Re^{0.5}$ (Ganapathisubramani *et al.* 2012), in the APG case this cross-over point is located at a location closer to its corresponding outer peak. This result suggests that the small-scale fluctuations are strengthened in the presence of a large-scale high-speed event not only in the near-wall region but up to the outer peak location (Kitsios *et al.* 2017).

In the outer region, the behaviour of both APG and ZPG cases is similar, with high-speed large scales associated with diminishing small-scale turbulence activity and low-speed large scale events connected to intense small-scale variance. This is consistent with the results for ZPGs reported by Ganapathisubramani *et al.* (2012). The behaviour of the small-scale features can be analyzed using the small-scale variance for $u_L^+ = 0$, which represents the small-scale behaviour when the influence of the large scales is weak. In the near-wall region, this quantity presents similar near-wall peaks in both cases which means that the higher inner peak observed in the streamwise variance with increasing β is a consequence of the footprint of the large-scale features. When comparing the $u_L^+ = 0$ profile at higher y^+, the effect of the pressure gradient in the small-scales starts to become apparent with increasing $\langle u_S^{+2} \rangle$ values in the whole logarithmic region. This shows that small-scale activity is increased not only by the influence of the large scales. This observation could be associated with a displacement of the small-scale activity from the near-wall region towards the outer part of the boundary layer. This is in agreement with the results from Sanmiguel Vila *et al.* (2017*a*) which reports that the sweeps/ejections events of the TBL are moved farther from the wall with increasing strength of the pressure gradient, and with Vinuesa *et al.* (2018) who reported increased wall-normal convection in APG TBLs.

5.2. *Location of the spectral outer peak*

The identification of the outer peak location – as in the case of ZPG TBLs (Samie *et al.* 2018) – remains also challenging for APG flows as long as the β range is moderate, since the appearance of a clear outer peak in the streamwise variance profile (see Figure 12) is not apparent. Due to these

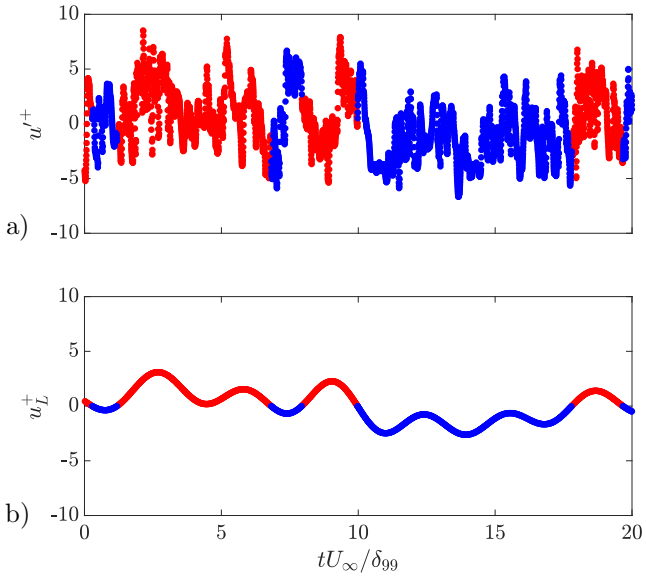

Figure 20: a) Instantaneous example of fluctuating signal (u'^+) and b) large-scale fluctuations component (u_L^+) computed based on a filter time scale of $tU_c/\delta_{99} = 1$ at $y^+ \approx 15$. Example case at $Re_\tau \approx 4,400$ and pressure-gradient strength $\beta \approx 1.1$. Red signal segments corresponds to $u_L^+ > 0$ and blue to $u_L^+ < 0$.

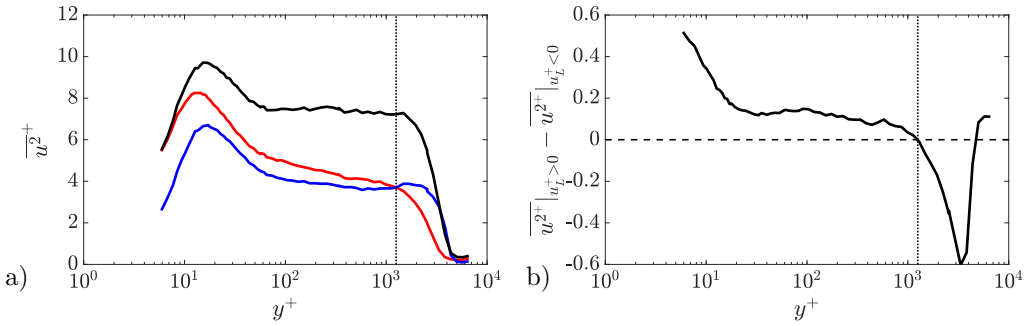

Figure 21: a) Streamwise variance calculated by signal segments with positive large-scale fluctuations $\overline{u^{2+}}|_{u_L^+>0}$ (red), negative large-scale fluctuations $\overline{u^{2+}}|_{u_L^+<0}$ (blue) and with the full signal length $\overline{u^{2+}}$ (black). b) Difference between the streamwise variance calculated by signal segments with positive and negative large-scale fluctuations $\overline{u^{2+}}|_{u_L^+>0} - \overline{u^{2+}}|_{u_L^+<0}$. Example case at $Re_\tau \approx 4,400$ and pressure-gradient strength $\beta \approx 1.1$. The dashed vertical lines indicate approximately the cross-over point between the $\overline{u^{2+}}|_{u_L^+>0}$ and $\overline{u^{2+}}|_{u_L^+<0}$ curves, *i.e.*, $\overline{u^{2+}}|_{u_L^+>0} - \overline{u^{2+}}|_{u_L^+<0} = 0$.

difficulties, Samie *et al.* (2018) analyzed an upper bound for the outer peak instead of the peak itself by means of a geometrical criterion. Here, a different method is proposed to locate the outer peak related to pressure-gradient effects. The method does not rely on geometrical constraints and, therefore, is valid even for APG TBLs flows with mild values of β. Based on the results reported in §5.1, it is evident that there exists a relation between the outer-peak location and the activity of the large- and small-scale fluctuations (see Figure 19). The first step of the method is to discriminate events related to high- and low-speed fluctuations. To this end, the large-scale component (u_L^+) is used as a filtering criterion to determine which raw-signal segments are related with events $u_L^+ > 0$ or $u_L^+ < 0$. This criterion is shown in Figure 20, where an instantaneous fluctuating velocity sample, u'^+, with its associated u_L^+, are presented. After identifying the corresponding segments of raw signal with events $u_L^+ > 0$, the streamwise variance $\overline{u^{2+}}|_{u_L^+>0}$ can be defined as the variance calculated by means of the signal segments corresponding to events $u_L^+ > 0$ as

$$\overline{u^{2+}}|_{u_L^+>0} = \frac{\sum u^{2^+}(u_L^+ > 0)|_{u_L^+(y)}}{N[u^+(u_L^+ > 0)]}. \tag{5}$$

Note that using the segments with events $u_L^+ < 0$, the $\overline{u^{2+}}|_{u_L^+<0}$ can also be obtained. Figure 21 shows the resulting variances and their difference. Our results indicate that the point of intersection of the $\overline{u^{2+}}|_{u_L^+>0}$ and $\overline{u^{2+}}|_{u_L^+<0}$ curves corresponds to the location of the outer peak due to the pressure-gradient effects in APG TBLs, $y_{\max,\text{outer}}$. This is observed in all the profiles from the present database and, as shown in the location of the spectral peaks presented in Figures 13 and 14. Additionally, this location is also represented in the high-order statistics from §3.2 and will be further studied in §6.2.

Further analysis of Figure 21a) shows that the variance due to low-speed events $u_L^+ < 0$ is practically constant in the region $y^+ > 100$. On the other hand, the variance due to high-speed events $u_L^+ > 0$ is decreasing throughout the whole logarithmic region. It is interesting to note that the maximum outer peak is reached when the contributions of low- and high-momentum events are equivalent. This may indicate that the observed outer spectral peak is a mixed effect of large-scale events with the small-scales ejected from the inner region (Sanmiguel Vila *et al.* 2017*a*; Vinuesa *et al.* 2018). Figure 21b) represents another form of modulation as also described in Figure 16b); nonetheless, it is important to remark that these two quantities are not identical, thus, the zero-crossing points of $3\overline{\overline{u_L^+}u_S^{2+}}$ and of $\overline{u^{2+}}|_{u_L^+>0} - \overline{u^{2+}}|_{u_L^+<0}$ are not the same. Applying the presented methodology to the experimental ZPG cases from Örlü (2009) the location obtained follows the relation $3.9Re_\tau^{0.5}$ as it was expected from the results of §5.1.

6. Assessment of scaling laws in the outer region

6.1. *Scaling of the streamwise mean velocity and fluctuation profiles*

The choice of proper velocity and length scales for APG TBL profiles is a topic of great interest. In recent studies (Kitsios *et al.* 2017; Maciel *et al.* 2018), different scaling parameters are proposed. In this section, the approximately constant-β region from configuration 1, over the streamwise region 2.7 m $\leq x \leq$ 4.4 m (*i.e.*, a streamwise distance of over $20\delta_{99}$) is used to test these recent scalings with our unique high-Re approximately constant-β database. The three different inflow velocities lead to the following Reynolds-number range in the approximately constant-β region: $3,610 < Re_\theta < 19,780$. It has to be noted that even in near-equilibrium APG cases, it is not expected to find self-similarity in the velocity profiles since, as stated by Townsend (1956) and Marusic *et al.* (2010), self-similarity can only be found for sink flows. In contrast, in boundary-layer flows, the mean velocity deficit $U_\infty - U$ in the outer part exhibits self-similarity only when Re is large enough. Figure 22 shows in the a) and c) panels the mean flow and streamwise variance normalised using the Zagarola–Smits velocity $U_{ZS} = U_\infty \delta^*/\delta_{99}$ and the length scale δ_{99} as proposed by Maciel *et al.* (2018). As reported in their study, the mean flow collapses in the

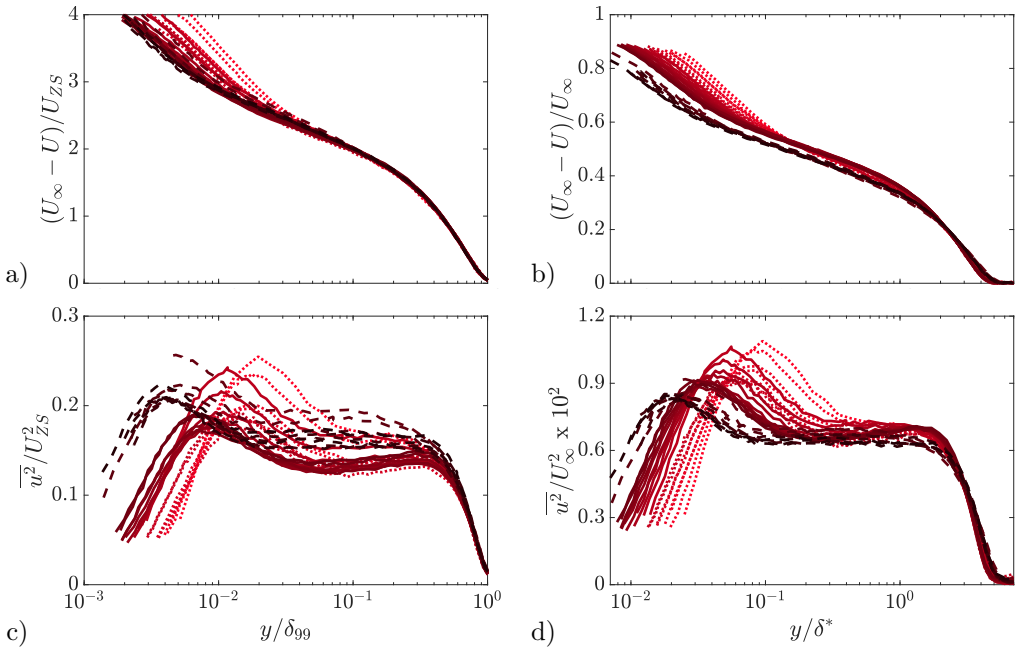

Figure 22: (a,b) Mean streamwise velocity profiles and (c,d) streamwise variance (in the approximately constant-β region 2.7 m $\leq x \leq$ 4.4 m) for $\beta \approx 1.1$ non-dimensionalised by: (a,c) U_{ZS}, and δ_{99}, (b,d) U_∞ and δ^*. Colours vary from light red to dark red with increasing Reynolds number. Line styles correspond to: dotted line $U_{ref} = 6$ m/s, solid line $U_{ref} = 12$ m/s and dashed line $U_{ref} = 30$ m/s.

outer region for $y/\delta_{99} \gtrapprox 0.1$, and the profiles exhibit a decreasing trend with Re outside this range. On the other hand, the streamwise variance profiles do not exhibit any region of collapse throughout the considered range; instead, there is a clear Re-trend. In Figure 22 b) and d) the scaling for near-equilibrium flows proposed by Kitsios *et al.* (2017) is employed, with δ^* and U_∞ considered as scaling parameters. Here, no scaling is observed in any region of the boundary layer, with a clear influence of Re in both outer and inner regions. The present results confirm the Re-trends exposed in the previous study of Bobke *et al.* (2017), and confirm that is not possible to obtain a single similarity variable in y in agreement with Townsend (1956). This fact may be related with the strong interaction between inner and outer regions in APG TBLs as reported in section §5, which suggests that TBLs require two different scales, in agreement with classical theory (Townsend 1956). Additionally, the scaling proposed by Maciel *et al.* (2018) is tested in Figure 26 for a set of cases at high-Re and different β values (not necessarily in near-equilibrium), including a ZPG case as a reference. It is interesting to observe that the β effect on the trends is analogous to the Re effect presented in Figure 22a) and c). Here, the mean velocity profiles from Figure 26a) show a good collapse for the cases with pressure-gradient effects for $y/\delta_{99} \gtrapprox 0.1$; while for the streamwise variance, no collapse is observed. On the other hand, the ZPG profile significantly deviates from the APG profiles in the whole range.

6.2. *Scaling of the inner and outer peak of the streamwise variance*

Based on the criterion described in §5.2, the outer peak location $y_{\max,\text{outer}}$ and its respective velocity fluctuation value $\overline{u^2}$ are analyzed. Here, it is important to remark that the maxima $\overline{u^2}^+$ from the inner and outer regions are analyzed independently. This is in contrast with the study of Maciel *et al.* (2018), who analysed the maximum $\overline{u^2}$ without making distinction between inner

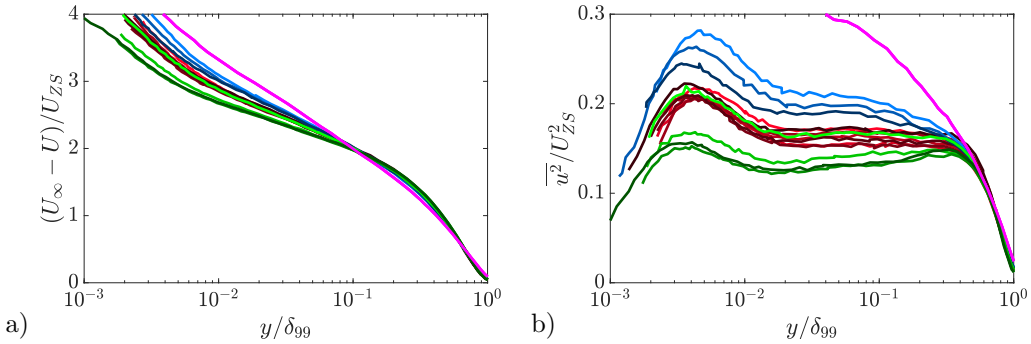

Figure 23: a) Mean streamwise velocity profiles and b) streamwise variance (in the region 3.1 m $\leq x \leq$ 4.4 m) for $U_{ref} = 30$ m/s non-dimensionalised by: U_{ZS}, and δ_{99}. Colours indicate the following APG cases: (red) configuration 1, (blue) configuration 2 and (green) configuration 3. Colours vary from light to dark with increasing Reynolds number. Additionally, a ZPG profile (magenta) at $Re_\tau \approx 4,400$ is included as a reference.

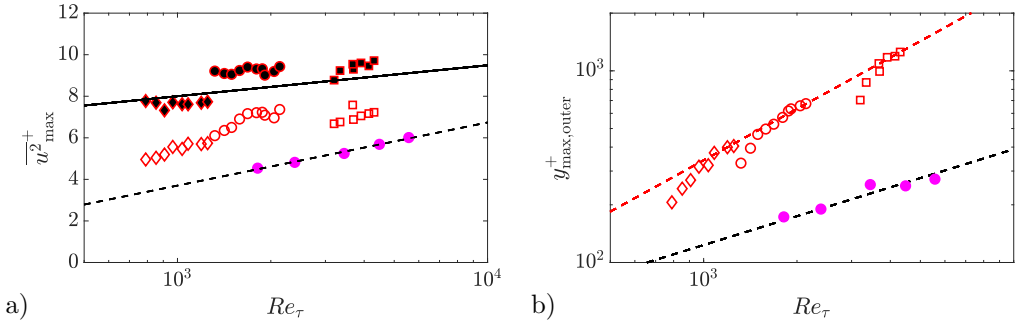

Figure 24: a) Maximum value of the inner-scaled streamwise variance against Re_τ. Black filled symbols represent the near-wall peak and open symbols the outer peak. Black line represents the relation $3.54 + 0.646\log(Re_\tau)$ for the ZPG inner peak taken from Samie *et al.* (2018). Magenta symbols indicate the outer peak values for the ZPG cases from Örlü (2009). Black dashed line represents the relation $-5.41 + 1.319\log(Re_\tau)$ for the ZPG outer peak fitted using the data shown. b) Inner-scaled wall-normal position of the outer peak location against Re_τ. The APG data shown corresponds to the approximately constant-β region 2.7 m $\leq x \leq$ 4.4 m for $\beta \approx 1.1$. Red dashed line represents the relation $0.73Re_\tau^{0.88}$. Magenta symbols indicate the outer peak location for the ZPG cases from Örlü (2009). Black dashed line represents the relation $3.9Re_\tau^{0.5}$. The symbols for the APG cases are reported in Table 2.

and outer regions. In the following, the ZPG outer peak location and its streamwise variance value have been calculated in the range $1,800 < Re_\tau < 5,500$ using the method outlined in §5.2 in order to be able to compare both outer peak results. Inner peak results for the ZPG cases are not shown due to the above-mentioned attenuation issues. Figures 24 and 25 show the inner/outer normalized evolution of the near-wall and outer peak values of the streamwise variance and the location of the outer peak for the approximately constant-β region from configuration 1, over 2.7 m $\leq x \leq$ 4.4 m, respectively. In Figure 24a) it can be observed that both the near-wall and the outer-peak values of $\overline{u^2}^+$ follow a Re_τ-trend that suggests that the functional form of the

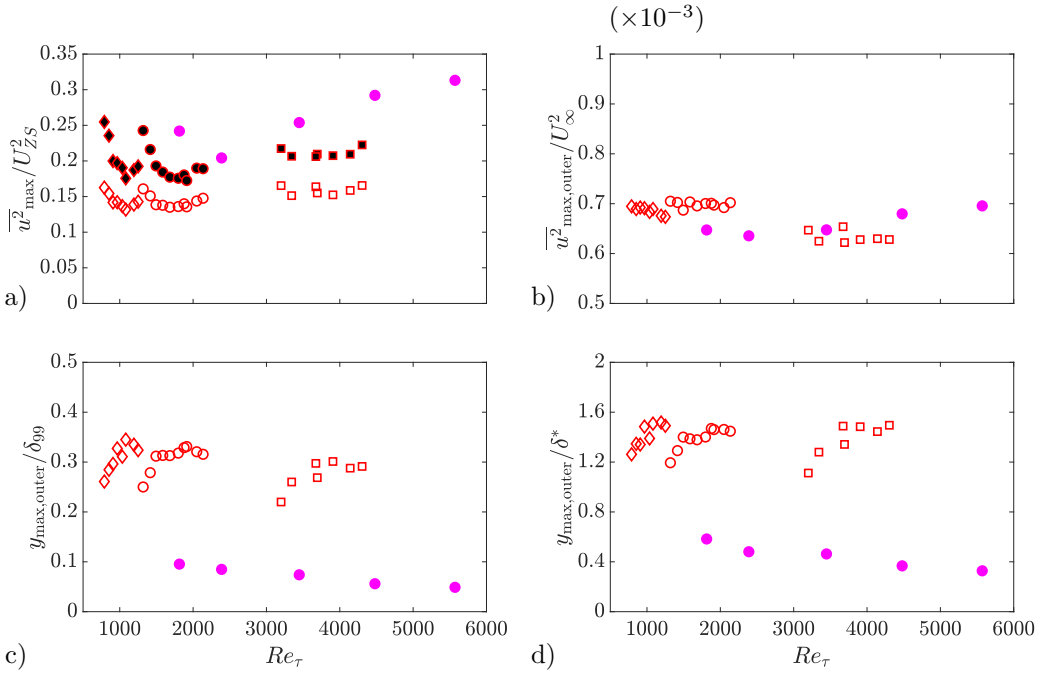

Figure 25: Maximum value of the streamwise variance normalized with a) U_{ZS} and b) U_∞ as a function of Re_τ. Black filled symbols represent the near-wall peak and open symbols the outer peak. Magenta symbols indicate the outer peak values for the ZPG cases from Örlü (2009). Wall-normal position of the outer-peak location normalized with c) δ_{99} and d) δ^* as a function of Re_τ. The data corresponds to the approximately constant-β region 2.7 m $\leq x \leq$ 4.4 m for $\beta \approx 1.1$. The symbols for the APG cases are reported in Table 2. Magenta symbols indicate the outer peak location for the ZPG cases from Örlü (2009).

Re-evolution for the inner/outer peaks for the APG case is similar to the proposed for ZPG cases. Again, the case with a $U_{ref} = 12$ m/s shows slighly higher values of $\overline{u^2}$ due to its slightly larger average β ($\beta_{avg} \approx 1.2$). The pressure-gradient effect increases the value of the near wall peak, without changing the functional form. However, more data at higher Re with a constant β would be required to confirm this observation. Figure 24b) show that a certain streamwise distance is required to reach a stable trend, which again has a functional form equivalent to those obtained in ZPG profiles. The distance required to converge is approximately $10\overline{\delta_{99}}$, where $\overline{\delta_{99}}$ denotes the average δ_{99} in the region between the beginning of the approximately constant-β region and the beginning of the constant-G region from Figure 10a). This observation is connected to the previous comments in §3.3 where it is reported that some streamwise development is needed to converge to "near-equilibrium" conditions for cases with non-constant-β history (Bobke *et al.* 2017). Figure 25a) presents the evolution of the near-wall and outer peaks $\overline{u^2}/U_{ZS}^2$; after a few points the values start following a slowly increasing trend with increasing Re_τ for both ZPG and APG cases. Comparing the near-wall peak values with the evolutions reported by Maciel *et al.* (2018) it is observed that the inner peak values are consistent with the proposed evolution against H_{12}. However, it appears that the values reported here for the outer peak are more consistent in order to describe the APG-peak effects. All the trends for y_{max} and $\overline{u^2}_{\max}$ reported by Maciel *et al.* (2018) have a discontinuity when plotted against β (around $\beta > 3$) or an abrupt drop when plotted against the shape factor H_{12}. This inflection point in their figures indicates the point where the outer peak becomes dominant, and therefore the $\overline{u^2}_{\max}$ is located on the APG outer

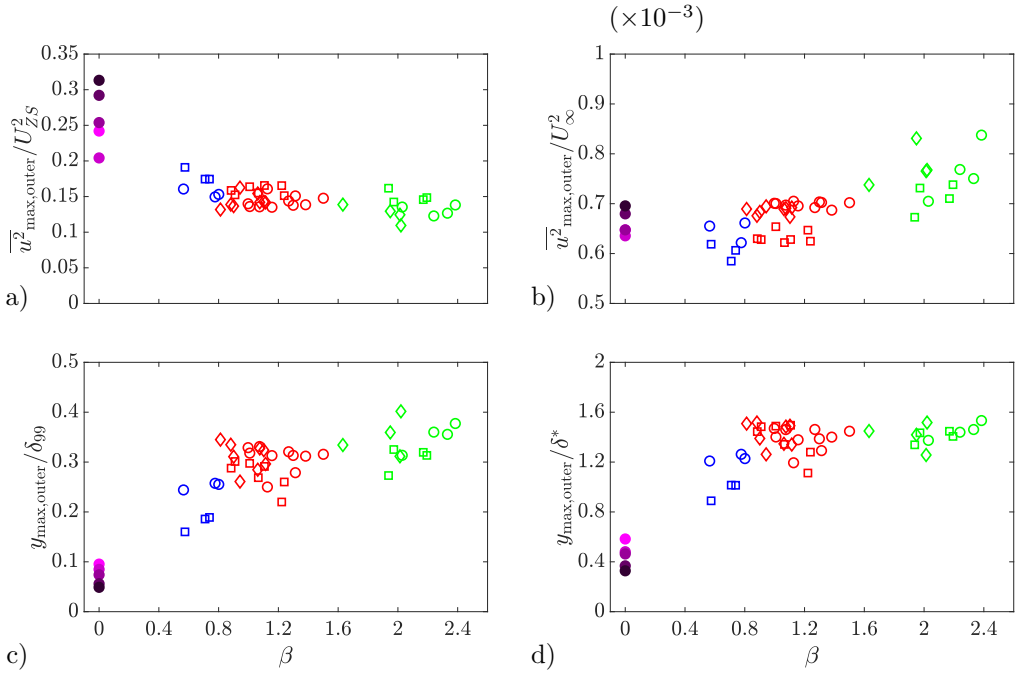

Figure 26: Maximum value of the streamwise variance at the outer peak location normalized with a) U_{ZS} and b) U_∞ against β. Wall-normal position of the outer peak location normalized with c) δ_{99} and d) δ^* against β. The data showed corresponds to the region 3.1 m $\leq x \leq$ 4.4 m. The colours and symbols for the APG cases are reported in Table 2. Magenta symbols indicate the ZPG outer peak location and value for the ZPG cases from Örlü (2009). Colour varies from light magenta to dark magenta with incresing Re.

peak. Here, instead, the outer-peak evolution is analysed separately, even when its value is not dominant. In contrast, Figure 25b) shows the outer peak normalized with U_∞ but do not show any clear common trend for APG and ZPG cases. This suggest that as pointed by Maciel *et al.* (2018) it may not be a adequate outer velocity scale. Figures 25c) and d) show $y_{\max,\text{outer}}$ scaled with δ_{99} and δ^*, respectively. Both trends tend to reach values of approximately 0.3 and 1.5, but for $y_{\max,\text{outer}}/\delta_{99}$ the trend appears to be slightly decreasing with increasing Re, and, in contrast, for $y_{\max,\text{outer}}/\delta^*$ the trend seems to be approximately constant for the APG case. In all the trends from Figure 25 it is also observed that a certain streamwise distance is required to reach a stabilised trend.

Figure 26 shows the evolution of the normalized outer peak $\overline{u^2}$ and of its location $y_{\max,\text{outer}}$ scaled with δ_{99} and δ^* against β, for all the cases in the range 3.1 m $\leq x \leq$ 4.4 m. Figure 26a) which presents $\overline{u^2}/U_{ZS}^2$ show that the values of the outer peak reported in Figure 26a) slightly decrease with increasing β. On the other hand, Figure 26b) which shows $\overline{u^2}/U_\infty^2$ has the opposite trend. The evolution of $y_{\max,\text{outer}}/\delta_{99}$ from Figure 26c) presents an increasing trend that complements the range of β missed in the study by Maciel *et al.* (2018). In the particular case of $\beta > 1$ and high-Re the location of the outer peak is approximately $0.3\delta_{99}$, which is in agreement with the observations of Harun *et al.* (2013) and justifies the decision of choosing this value as a comparison for the ZPG spectra in §4.2. For the case of $y_{\max,\text{outer}}/\delta^*$ shown in Figure 26d), the results confirm that for $\beta > 1$ the location of the outer peak scales with δ^* in our range of Re as predicted by Maciel *et al.* (2018). The observed small scatter is associated to the Re-effect as is

evidenced by the ZPG cases. For a more precise estimation a complete characterization of the $y_{\max,\text{outer}}$ in terms of β and Re it would be necessary to take into account both effects.

7. Conclusions

The present study analyzes a new high-quality database of APG TBL hot-wire measurements covering the Reynolds-number range $450 < Re_\theta < 23,450$ with pressure-gradient distributions resulting in values of β from zero up to ≈ 2.4. Hereby approximately constant and increasing pressure-gradient-parameter distributions were studied for different Reynolds numbers. As reported by Bobke *et al.* (2017), configurations which reach a constant-β distribution converge towards a canonical state after a sufficiently long downstream length as it can be inferred from the defect shape factor G. These cases present skin-friction coefficient and shape factor distributions which appear to follow the empirical laws proposed by Vinuesa *et al.* (2017) for constant-β TBLs, which are similar to those previously proposed for ZPG TBLs (Nagib *et al.* 2007). Additionally, the curves developed by Mellor & Gibson (1966) were also tested and some discrepancies are reported. For all the APG and ZPG configurations under study, the inner-scaled wall-normal locations of the outer peak of the variance, of the zero-crossing of the skewness and of the minimum of the flatness are the same. The effect of the pressure gradient on the large-scale organisation was studied by means of the pre-multiplied power-spectral density $f^+\Phi^+_{uu}$, which shows large energetic structures in the outer region with increasing pressure gradient. At higher Reynolds numbers, the large structures due to β effects are more energetic, and also structures resembling the ones observed in high-Reynolds-number ZPG TBLs appear. The large structures due to the APG effects exhibit a spectral peak at wall-normal location $y/\delta^* \approx 1.5$ in contrast to the structures associated with the ZPG, which show high levels of energy at $y^+ \approx 3.9Re_\tau^{0.5}$, *i.e.* in the middle of the logarithmic region. In addition to that, the the pre-multiplied streamwise power-spectral density (computed based on Taylor's frozen turbulence hypothesis) $\kappa_x^+\Phi^+_{uu}$ is analysed for the high-Re cases at different wall-normal locations. The results highlight that the higher pressure-gradient strength excites a wider range of wavelengths compared to the ZPG cases ($\lambda_x/\delta_{99} \approx 1-6$). The near-wall region is more energetic as β increases, as a consequence of the interaction with the large scales but the location of the inner spectral peak in the power-spectral density does not appear to change with respect to ZPG TBLs. Scale-decomposition analysis shows that the small-scale component does not scale as in ZPG cases and therefore additional work must be carried out in order to understand the implications of using the inner-scaled hot-wire length L^+ to compare different databases or correct near-wall data. Modulation of the large scales increases with β as the distribution of the fluctuations for large-scale components u_L^+ becomes broader, and stronger as the cross-over point of zero modulation is located farther from the wall in APG TBLs compared to ZPG TBLs. Additionally, the methodology proposed by Ganapathisubramani *et al.* (2012) is employed to study the modulation of the large scales over the small scales. Our results show that broad large-scale fluctuations contribute to increase the small-scale variance over the whole boundary layer but also suggest that the small scales are locally enhanced by the pressure-gradient strength when there are no large-scale fluctuations. Based on the reported interactions between high- and low-speed events, a method to locate the outer peak due to pressure gradient is presented and its location is connected with the interaction of these events. Finally, the present database is used to test the scalings proposed by Kitsios *et al.* (2017) and Maciel *et al.* (2018). Our results show that while our conclusions seem to be in good agreement with those discussed in Maciel *et al.* (2018), no complete self-similarity can be observed in the profiles within our approximately constant-β region, as opposed to the findings by Kitsios *et al.* (2017). This confirms the previous results from Townsend (1956), who showed that the sink flow is the only turbulent boundary layer exhibiting self-similarity. Additionally, the outer-peak location and its streamwise variance value is analysed in the present database supplementing the evolutions for high values of β presented by Maciel *et al.* (2018). Although the pressure-gradient range is limited for the near-equilibrium case, we expect the present database with higher Reynolds numbers to contribute towards the

characterisation of near-equilibrium APG TBLs. These cases should be further investigated in order to fully understand complex pressure-gradient effects in wall-bounded turbulent flows.

The mean and higher-order statistics of the new APG TBL database are available under the following URL: www.flow.kth.se.

Acknowledgements

CSV acknowledges the financial support from Universidad Carlos III de Madrid within the program "Ayudas para la Movilidad del Programa Propio de Investigación". RÖ, RV and PS acknowledge the financial support from the Swedish Research Council (VR) and the Knut and Alice Wallenberg (KAW) Foundation as part of the Wallenberg Academy Fellow programme. CSV, SD and AI were partially supported by the Grant DPI2016-79401-R funded by the Spanish State Research Agency (SRA) and European Regional Development Fund (ERDF).

Appendix A. Experimental parameters for all the profiles in the present study

Configuration	x [mm]	β	G	U_∞ [m/s]	Re_θ	Re_{δ^*}	Re_τ	u_τ [m/s]	δ_{99} [mm]	H_{12}	ν/u_τ [μm]	L^+	Δt^+	TU_∞/δ_{99}
1	240	-0.04	6.73	12.2	900	1,320	370	0.58	9.4	1.47	25.6	20	0.38	38,870
1	600	-0.01	6.88	12.1	1,510	2,150	550	0.53	15.4	1.43	28.0	19	0.31	31,420
1	1,100	0.02	7.16	12.1	2,290	3,240	760	0.50	22.6	1.41	29.9	18	0.28	24,120
1	1,800	0.29	7.96	11.7	3,420	4,900	1,000	0.44	33.6	1.43	33.5	16	0.22	20,950
1	2,100	0.51	8.16	11.5	4,000	5,750	1,130	0.43	39.3	1.44	34.6	15	0.21	24,940
1	2,500	0.75	8.35	5.7	2,630	3,890	750	0.22	50.3	1.48	67.4	8	0.16	6,770
1	2,500	0.89	9.08	11.1	4,910	7,210	1,290	0.39	49.0	1.47	38.1	14	0.17	22,650
1	2,700	0.94	8.90	5.6	2,910	4,360	790	0.21	56.0	1.50	70.9	7	0.15	9,980
1	2,700	1.13	9.63	10.9	5,470	8,130	1,320	0.37	53.4	1.49	40.5	13	0.15	20,320
1	2,900	1.06	9.09	5.5	3,240	4,870	850	0.20	62.2	1.51	73.0	7	0.14	5,290
1	2,900	1.31	10.13	10.6	6,090	9,190	1,420	0.35	59.8	1.51	42.3	12	0.14	17,710
1	3,150	1.11	9.42	5.3	3,610	5,500	910	0.20	68.9	1.52	75.9	7	0.13	7,760
1	3,150	1.38	10.50	10.4	6,740	10,240	1,490	0.34	66.1	1.52	44.2	12	0.13	18,850
1	3,400	1.08	9.81	5.3	3,950	6,040	970	0.19	76.9	1.53	79.7	7	0.12	17,180
1	3,400	1.30	10.81	10.1	7,360	11,230	1,590	0.32	72.9	1.53	46.0	11	0.12	16,690
1	3,650	0.90	9.77	5.2	4,290	6,550	1,040	0.18	84.1	1.53	81.3	6	0.11	14,730
1	3,650	1.16	11.12	10.0	8,010	12,260	1,680	0.31	80.4	1.53	47.8	11	0.11	17,470
1	3,900	0.81	9.94	5.1	4,660	7,120	1,080	0.18	90.8	1.53	83.9	6	0.11	3,360
1	3,900	1.01	11.07	9.8	8,570	13,090	1,800	0.31	87.5	1.53	48.7	11	0.10	22,480
1	4,050	1.00	11.01	9.8	8,870	13,500	1,880	0.31	91.5	1.52	48.7	11	0.10	21,510
1	4,200	0.88	10.05	5.0	5,000	7,640	1,190	0.17	102.0	1.53	85.5	6	0.10	9,890
1	4,200	1.07	10.99	9.5	9,060	13,830	1,910	0.30	95.3	1.53	49.8	11	0.10	19,020
1	4,400	1.10	9.98	5.0	5,220	7,930	1,250	0.17	109.1	1.52	87.3	6	0.10	2,730
1	4,400	1.27	10.73	9.5	9,430	14,260	2,050	0.30	102.5	1.51	50.0	10	0.10	14,760
1	4,525	1.50	10.99	9.6	9,960	15,080	2,140	0.30	106.8	1.51	50.0	11	0.10	18,070

Table 6: Experimental parameters for configuration 1 at $U_{ref} = 6$ and 12 m/s.

Configuration	x [mm]	β	G	U_∞ [m/s]	Re_θ	Re_{δ^*}	Re_τ	u_τ [m/s]	δ_{99} [mm]	H_{12}	ν/u_τ [μm]	L^+	Δt^+	TU_∞/δ_{99}
1	240	-0.03	6.74	30.9	1,890	2,660	700	1.33	8.0	1.41	11.3	46	1.96	116,670
1	600	0.00	7.56	30.6	3,080	4,400	1,030	1.21	12.8	1.43	12.4	42	1.63	95,460
1	1,100	0.04	7.76	30.7	4,770	6,680	1,430	1.13	19.1	1.40	13.4	39	1.40	96,270
1	1,800	0.24	8.05	29.6	6,990	9,790	1,960	1.05	28.0	1.40	14.3	19	1.22	63,380
1	2,100	0.39	8.19	29.1	7,900	11,030	2,150	1.01	31.9	1.40	14.8	19	1.13	27,410
1	2,300	0.55	8.40	28.7	8,950	12,570	2,400	0.98	36.9	1.40	15.4	34	1.07	31,130
1	2,500	0.71	8.61	28.5	10,260	14,450	2,670	0.96	41.4	1.41	15.5	34	1.03	27,590
1	2,700	0.91	9.13	26.6	10,870	15,490	2,680	0.87	45.9	1.42	17.1	31	0.84	31,860
1	2,900	1.10	9.49	26.7	12,440	17,810	2,920	0.85	51.2	1.43	17.5	30	0.81	28,720
1	3,150	1.22	9.82	26.5	14,110	20,330	3,200	0.82	57.8	1.44	18.1	29	0.76	25,190
1	3,400	1.24	10.26	25.8	15,380	22,360	3,340	0.78	64.6	1.45	19.3	14	0.68	29,950
1	3,650	1.07	10.29	25.6	16,990	24,600	3,690	0.77	71.5	1.45	19.4	27	0.66	21,440
1	3,775	1.01	10.49	25.2	17,290	24,990	3,670	0.74	74.9	1.45	20.4	26	0.61	30,300
1	3,900	0.91	10.48	25.3	18,270	26,580	3,910	0.75	78.5	1.45	20.1	14	0.63	28,970
1	4,100	0.88	10.38	25.0	19,270	27,840	4,140	0.74	84.6	1.44	20.4	13	0.61	26,610
1	4,300	1.11	10.33	24.4	19,780	28,440	4,300	0.72	90.7	1.44	21.1	13	0.57	24,170

Table 7: Experimental parameters for configuration 1 at $U_{ref} = 30$ m/s.

Configuration	x [mm]	β	G	U_∞ [m/s]	Re_θ	Re_{δ^*}	Re_τ	u_τ [m/s]	δ_{99} [mm]	H_{12}	ν/u_τ [μm]	L^+	Δt^+	TU_∞/δ_{99}
2	240	-0.02	6.74	12.0	770	1,140	320	0.58	8.4	1.48	26.4	20	0.36	43,100
2	240	-0.02	7.09	30.7	1,700	2,420	610	1.29	7.0	1.43	11.4	46	1.89	87,650
2	600	0.00	7.30	12.0	1,370	2,010	480	0.52	14.1	1.46	29.3	18	0.29	25,440
2	600	0.00	7.27	30.4	3,010	4,220	980	1.19	12.1	1.40	12.3	43	1.61	50,100
2	1,100	0.03	7.44	12.0	2,060	2,950	680	0.49	21.1	1.43	31.2	17	0.26	17,110
2	1,100	0.04	7.65	30.1	4,550	6,340	1,380	1.11	18.3	1.39	13.3	40	1.39	32,920
2	1,800	0.16	7.91	11.8	3,050	4,370	920	0.45	31.1	1.43	33.8	16	0.22	11,370
2	1,800	0.13	7.96	29.5	6,780	9,400	1,910	1.03	27.2	1.39	14.3	37	1.20	21,630
2	2,100	0.25	8.18	11.7	3,590	5,150	1,030	0.43	35.8	1.44	34.9	15	0.21	9,820
2	2,100	0.17	8.00	29.7	7,490	10,360	2,100	1.03	30.6	1.38	14.6	36	1.17	29,040
2	2,500	0.35	8.35	11.5	4,240	6,100	1,180	0.42	42.6	1.44	36.1	15	0.19	8,100
2	2,500	0.26	8.13	30.3	9,100	12,540	2,470	1.02	36.4	1.38	14.7	36	1.16	24,960
2	2,900	0.45	8.77	11.2	4,960	7,190	1,310	0.40	50.1	1.45	38.2	14	0.17	6,700
2	2,900	0.41	8.56	29.6	10,820	15,010	2,770	0.96	43.3	1.39	15.6	34	1.03	20,480
2	3,400	0.57	9.18	10.9	6,030	8,800	1,490	0.37	60.7	1.46	40.7	13	0.15	5,370
2	3,400	0.57	8.73	28.6	13,200	18,390	3,300	0.93	53.7	1.39	16.2	32	0.95	16,010
2	3,900	0.78	9.64	10.6	7,030	10,310	1,650	0.35	71.0	1.47	43.1	12	0.14	13,460
2	3,900	0.78	9.68	10.6	6,950	10,200	1,650	0.35	71.6	1.47	43.5	12	0.13	4,420
2	3,900	0.71	9.05	27.8	15,640	21,880	3,760	0.88	64.7	1.40	17.2	31	0.85	12,900
2	4,400	0.80	9.89	10.3	7,900	11,640	1,820	0.33	82.4	1.47	45.3	12	0.12	11,220
2	4,400	0.74	9.54	27.0	18,120	25,570	4,190	0.82	76.5	1.41	18.3	29	0.75	10,580

Table 8: Experimental parameters for configuration 2.

Configuration	x [mm]	β	G	U_∞ [m/s]	Re_θ	Re_{δ^*}	Re_τ	u_τ [m/s]	δ_{99} [mm]	H_{12}	ν/u_τ [μm]	L^+	Δt^+	TU_∞/δ_{99}
3	240	-0.02	6.83	6.3	450	690	210	0.33	9.5	1.55	46.2	11	0.36	33,210
3	240	-0.04	6.80	12.3	890	1,320	360	0.58	9.4	1.47	26.0	20	0.37	39,360
3	600	-0.01	7.11	6.3	810	1,220	310	0.30	15.9	1.50	51.4	10	0.29	19,860
3	600	0.00	6.83	12.2	1,490	2,130	560	0.54	15.6	1.43	28.1	19	0.32	23,520
3	1,100	0.05	6.96	6.3	1,250	1,820	450	0.28	24.2	1.46	53.6	10	0.26	13,000
3	1,100	0.06	7.11	12.2	2,270	3,220	760	0.51	22.6	1.42	29.9	18	0.28	16,230
3	1,800	0.27	7.73	6.1	1,930	2,820	600	0.25	36.8	1.46	61.1	9	0.20	9,550
3	1,800	0.26	7.96	12.2	3,490	4,980	1,030	0.46	33.8	1.43	32.9	16	0.23	10,780
3	2,100	0.44	8.00	5.9	2,240	3,290	670	0.24	42.8	1.47	64.0	8	0.19	9,160
3	2,100	0.42	8.13	11.7	3,970	5,690	1,130	0.43	39.6	1.43	34.9	15	0.21	11,760
3	2,500	0.78	8.77	5.7	2,720	4,070	750	0.22	52.7	1.49	70.0	7	0.15	8,180
3	2,500	0.75	8.72	11.2	4,750	6,900	1,250	0.40	47.3	1.45	37.7	14	0.18	15,460
3	2,900	1.19	9.38	5.5	3,300	5,010	840	0.20	63.4	1.52	75.9	7	0.13	8,680
3	2,900	1.32	9.84	10.7	5,900	8,800	1,400	0.36	58.7	1.49	42.1	12	0.14	12,720
3	3,400	1.63	10.22	5.2	3,960	6,170	940	0.18	78.4	1.56	83.7	6	0.11	8,960
3	3,400	2.03	11.06	10.1	7,430	11,390	1,570	0.32	74.1	1.53	47.3	11	0.11	12,280
3	3,900	2.01	11.58	4.9	4,930	7,890	1,030	0.16	97.8	1.60	94.9	6	0.08	7,590
3	3,900	2.33	12.29	9.5	8,920	14,060	1,720	0.28	91.3	1.57	53.3	10	0.09	9,370
3	4,200	1.95	12.36	4.8	5,340	8,650	1,060	0.15	108.4	1.62	102.6	5	0.07	7,080
3	4,200	2.38	13.29	9.4	9,980	16,020	1,840	0.27	104.1	1.60	56.4	9	0.08	11,730
3	4,400	2.02	13.36	4.8	5,960	9,850	1,100	0.14	120.4	1.65	109.4	5	0.06	7,920
3	4,400	2.24	12.88	9.2	10,310	16,410	1,890	0.27	107.4	1.59	56.7	9	0.08	11,120

Table 9: Experimental parameters for configuration 3 at $U_{ref} = 6$ and 12 m/s.

Configuration	$x(mm)$	β	G	U_∞	Re_θ	Re_{δ^*}	Re_τ	u_τ (m/s)	δ_{99} (mm)	H_{12}	ν/u_τ (μm)	L^+	Δt^+	TU_∞/δ_{99}
3	2,100	0.38	8.43	29.2	8,520	11,880	2,260	0.98	34.9	1.39	15.5	34	1.06	25,120
3	2,500	0.69	8.79	28.5	10,180	14,260	2,570	0.93	42.0	1.40	16.3	32	0.95	23,730
3	2,900	1.23	9.56	27.2	12,530	17,910	2,940	0.85	52.0	1.43	17.7	30	0.80	19,840
3	3,400	1.94	10.43	25.5	16,030	23,370	3,450	0.77	66.9	1.46	19.4	27	0.66	15,230
3	3,900	2.17	11.76	24.1	19,870	29,820	3,830	0.68	83.3	1.50	21.7	24	0.52	13,020
3	4,250	1.97	12.23	23.4	22,240	33,780	4,160	0.65	95.6	1.52	23.0	23	0.47	14,690
3	4,400	2.19	12.12	23.2	23,450	35,370	4,410	0.64	101.6	1.51	23.0	23	0.47	13,680

Table 10: Experimental parameters for configuration 3 at $U_{ref} = 30$ m/s.

References

del Álamo, J. C. & Jiménez, J. 2009 Estimation of turbulent convection velocities and corrections to Taylor's approximation. *J. Fluid Mech.* **640**, 5–26.

Alfredsson, P. H., Segalini, A. & Örlü, R. 2011 A new scaling for the streamwise turbulence intensity in wall-bounded turbulent flows and what it tells us about the "outer" peak. *Phys. Fluids* **23**, 041702.

Alving, Amy E. & Fernholz, H. H. 1995 Mean-velocity scaling in and around a mild, turbulent separation bubble. *Phys. Fluids* **7**, 1956–1969.

Bobke, A., Vinuesa, R., Örlü, R. & Schlatter, P. 2017 History effects and near equilibrium in adverse-pressure-gradient turbulent boundary layers. *J. Fluid Mech.* **820**, 667–692.

Chauhan, K. A., Monkewitz, P. A. & Nagib, H. M. 2009 Criteria for assessing experiments in zero pressure gradient boundary layers. *Fluid Dyn. Res.* **41**, 021404.

Clauser, F. H. 1954 Turbulent boundary layers in adverse pressure gradients. *J. Aero. Sci.* **21**, 91–108.

Clauser, F. H. 1956 The turbulent boundary layer. *Adv. Appl. Mech.* **4**, 1–51.

Cohen, E. & Gloerfelt, X. 2018 Influence of pressure gradients on wall pressure beneath a turbulent boundary layer. *J. Fluid Mech.* **838**, 715–758.

Cutler, A. D. & Johnston, J. P. 1989 The relaxation of a turbulent boundary layer in an adverse pressure gradient. *J. Fluid Mech.* **200**, 367–387.

Cuvier, C., Srinath, S., Stanislas, M., Foucaut, J. M., Laval, J. P., Kähler, C. J., Hain, R., Scharnowski, S., Schröder, A., Geisler, R., Agocs, J., Röse, A., Willert, C., Klinner, J., Amili, O., Atkinson, C. & Soria, J. 2017 Extensive characterisation of a high reynolds number decelerating boundary layer using advanced optical metrology. *J. Turbul.* **18**, 929–972.

Dengel, P. & Fernholz, H.H. 1990 An experimental investigation of an incompressible turbulent boundary layer in the vicinity of separation. *J. Fluid Mech.* **212**, 615–636.

Dogan, E., Örlü, R., Gatti, D., Vinuesa, R. & Schlatter, P. 2018 Quantification of amplitude modulation in wall-bounded turbulence. *Fluid Dyn. Res.* **51**, 011408.

Dróżdż, A & Elsner, W 2017 Amplitude modulation and its relation to streamwise convection velocity. *Int. J. Heat Fluid Flow* **63**, 67–74.

East, L. F. & Sawyer, W.G. 1980 An investigation of the structure of equilibrium turbulent boundary layers. In *Turbulent Boundary Layers: Experiment, Theory and Modelling, CP-271, AGARD*, p. 6.1–6.19.

Eitel-Amor, G., Örlü, R. & Schlatter, P. 2014 Simulation and validation of a spatially evolving turbulent boundary layer up to $Re_\theta = 8300$. *Int. J. Heat Fluid Flow* **47**, 57–69.

Felsch, K. O., Geropp, D. & Walz, A. 1968 Method for turbulent boundary layer prediction. *In: Proceedings of the Stanford Conference on the Computation of Turbulent Boundary Layers* pp. 170–176.

Ganapathisubramani, B., Hutchins, N., Monty, J. P., Chung, D. & Marusic, I. 2012 Amplitude and frequency modulation in wall turbulence. *J. Fluid Mech.* **712**, 61–91.

Gungor, A.G., Maciel, Y., Simens, M.P. & Soria, J. 2016 Scaling and statistics of large-defect adverse pressure gradient turbulent boundary layers. *Int. J. Heat Fluid Flow* **59**, 109–124.

Harun, Z., Monty, J. P., Mathis, R. & Marusic, I. 2013 Pressure gradient effects on the large-scale structure of turbulent boundary layers. *J. Fluid Mech.* **715**, 477–498.

Hultmark, M, Bailey, S. C. C. & Smits, A. J. 2010 Scaling of near-wall turbulence in pipe flow. *J. Fluid Mech.* **649**, 103–113.

Hutchins, N. & Marusic, I. 2007 Large-scale influences in near-wall turbulence. *Phil. Trans. R. Soc. A.* **365**, 647–664.

Hutchins, N., Nickels, T. B., Marusic, I. & Chong, M. S. 2009 Hot-wire spatial resolution issues in wall-bounded turbulence. *J. Fluid Mech.* **635**, 103–136.

Jiménez, J. 2018 Coherent structures in wall-bounded turbulence. *J. Fluid Mech.* **842**, P1.

Kitsios, V., Atkinson, C., Sillero, J.A., Borrell, G., Gungor, A.G., Jiménez, J. & Soria, J. 2016 Direct numerical simulation of a self-similar adverse pressure gradient turbulent boundary layer. *Int. J. Heat Fluid Flow* **61**, 129–136.

Kitsios, V., Sekimoto, A., Atkinson, C., Sillero, J. A., Borrell, G., Gungor, A. G., Jiménez, J. & Soria, J. 2017 Direct numerical simulation of a self-similar adverse pressure gradient turbulent boundary layer at the verge of separation. *J. Fluid Mech.* **829**, 392–419.

Kline, S., Reynolds, W. C., Schraub, F. & Runstadler, P. 1967 The structure of turbulent boundary layers. *J. Fluid Mech.* **30**, 741–773.

Lee, J. H. 2017 Large-scale motions in turbulent boundary layers subjected to adverse pressure gradients. *J. Fluid Mech.* **810**, 323–361.

Lee, J. H. & Sung, H. J. 2008 Effects of an adverse pressure gradient on a turbulent boundary layer. *Int. J. Heat Fluid Flow* **29**, 568–578.

Lindgren, B. & Johansson, A. V. 2002 Evaluation of the flow quality in the MTL wind-tunnel. *Tech. Rep., Royal Institute of Technology (KTH), Stockholm, Sweden.*

Lindgren, B., Johansson, A. V. & Tsuji, Y. 2004 Universality of probability density distributions in the overlap region in high Reynolds number turbulent boundary layers. *Phys. Fluids* **16**, 2587–2591.

Maciel, Y., Rossignol, K.S. & Lemay, J. 2006 A study of a turbulent boundary layer in stalled-airfoil-type flow conditions. *Exp. Fluids* **41** (4), 573–590.

Maciel, Y., Wei, T., Gungor, A. G. & Simens, M. P. 2018 Outer scales and parameters of adverse-pressure-gradient turbulent boundary layers. *J. Fluid Mech.* **844**, 5–35.

Marusic, I., Chauhan, K. A., Kulandaivelu, V. & Hutchins, N. 2015 Evolution of zero-pressure-gradient boundary layers from different tripping conditions. *J. Fluid Mech.* **783**, 379–411.

Marusic, I., McKeon, B. J., Monkewitz, P. A., Nagib, H. M., Smits, A. J. & Sreenivasan, K. R. 2010 Wall-bounded turbulent flows at high Reynolds numbers: Recent advances and key issues. *Phys. Fluids* **22**, 065103.

Marušić, I. & Perry, A. E. 1995 A wall-wake model for the turbulence structure of boundary layers. Part 2. Further experimental support. *J. Fluid Mech.* **298**, 389–407.

Mathis, R., Hutchins, N. & Marusic, I. 2009 Large-scale amplitude modulation of the small-scale structures in turbulent boundary layers. *J. Fluid Mech.* **628**, 311–337.

Mathis, R., Marusic, I., Hutchins, N. & Sreenivasan, K. 2011 The relationship between the velocity skewness and the amplitude modulation of the small scale by the large scale in turbulent boundary layers. *Phys. Fluids* **23**, 121702.

Mellor, G.L. & Gibson, D.M. 1966 Equilibrium turbulent boundary layers. *J. Fluid Mech.* **24**, 225–253.

Menter, F. R. 1994 Two-equation eddy-viscosity turbulence models for engineering applications. *AIAA J.* **32**, 1598–1605.

Miller, M. A., Estejab, B. & Bailey, S. C. C. 2014 Evaluation of hot-wire spatial filtering corrections for wall turbulence and correction for end-conduction effects. *Exp. Fluids* **55** (5), 1735.

Monty, J. P., Harun, Z. & Marusic, I. 2011 A parametric study of adverse pressure gradient turbulent boundary layers. *Int. J. Heat Fluid Flow* **32**, 575–585.

Nagano, Y. & Houra, T. 2002 Higher-order moments and spectra of velocity fluctuations in adverse-pressure-gradient turbulent boundary layer. *Exp. Fluids* **33** (1), 22–30.

Nagano, Y., Tagawa, M. & Tsuji, T. 1993 Effects of adverse pressure gradients on mean flows and turbulence statistics in a boundary layer. In *Turbulent Shear Flows 8*, pp. 7–21. Springer.

Nagano, Y., Tsuji, T. & Houra, T. 1998 Structure of turbulent boundary layer subjected to adverse pressure gradient. *Int. J. Heat Fluid Flow* **19**, 563–572.

Nagib, H. M., Chauhan, K. A. & Monkewitz, P. A. 2007 Approach to an asymptotic state for zero pressure gradient turbulent boundary layers. *Phil. Trans. R. Soc. A.* **365**, 755–770.

Nagib, H. M., Christophorou, Chris & Monkewitz, P. A. 2004 High Reynolds number turbulent boundary layers subjected to various pressure-gradient conditions. *IUTAM Symposium on one hundred years of boundary layer research, G. E. A. Meier and K. R. Sreenivasan (Eds.), Göttingen, Germany* pp. 383–394.

Örlü, R. 2009 Experimental studies in jet flows and zero pressure-gradient turbulent boundary layers. *Ph. D. thesis, Royal Institute of Technology, Stockholm, Sweden.*

Örlü, R., Fransson, J. H. M. & Alfredsson, P. H. 2010 On near wall measurements of wall bounded flows – the necessity of an accurate determination of the wall position. *Prog. Aero. Sci.* **46**, 353–387.

Örlü, R. & Schlatter, P. 2013 Comparison of experiments and simulations for zero pressure gradient turbulent boundary layers at moderate Reynolds numbers. *Exp. Fluids* **54**, 1547.

Örlü, R., Segalini, A., Klewicki, J. & Alfredsson, P. H. 2016 High-order generalisation of the diagnostic scaling for turbulent boundary layers. *J. Turbul.* **17**, 664–677.

Österlund, J. M. 1999 Experimental studies of zero pressure-gradient turbulent boundary layer flow. *Ph. D. thesis, Royal Institute of Technology, Stockholm, Sweden.*

Perry, A.E. 1966 Turbulent boundary layers in decreasing adverse pressure gradients. *J. Fluid Mech.* **26** (3), 481–506.

Renard, N. & Deck, S. 2015 On the scale-dependent turbulent convection velocity in a spatially developing flat plate turbulent boundary layer at Reynolds number. *J. Fluid Mech.* **775**, 105–148.

Rodríguez-López, E., Bruce, P. J. K. & Buxton, O. R. H. 2015 A robust post-processing method to determine skin friction in turbulent boundary layers from the velocity profile. *Exp. Fluids* **56**, 68.

Rotta, J.C. 1962 Turbulent boundary layers in incompressible flow. *Prog. Aero. Sci.* **2**.

Samie, M., Marusic, I., Hutchins, N., Fu, M. K., Fan, Y., Hultmark, M. & Smits, A. J. 2018 Fully resolved measurements of turbulent boundary layer flows up to $Re_\tau = 20\,000$. *J. Fluid Mech.* **851**, 391–415.

Samuel, A.E. & Joubert, P.N. 1974 A boundary layer developing in an increasingly adverse pressure gradient. *J. Fluid Mech.* **66** (3), 481–505.

Sanmiguel Vila, C., Örlü, R., Vinuesa, R., Schlatter, P., Ianiro, A. & Discetti, S. 2017*a* Adverse-pressure-gradient effects on turbulent boundary layers: Statistics and flow-field organization. *Flow Turbul. Combust.* **99**, 589–612.

Sanmiguel Vila, C., Vinuesa, R., Discetti, S., Ianiro, A., Schlatter, P. & Örlü, R. 2017*b* On the identification of well-behaved turbulent boundary layers. *J. Fluid Mech.* **822**, 109–138.

Schlatter, P., Li, Q, Brethouwer, G, Johansson, A. V. & Henningson, D. S. 2010 Simulations of spatially evolving turbulent boundary layers up to Re_θ=4300. *Int. J. Heat Fluid Flow* **31**, 251–261.

Schlatter, P. & Örlü, R. 2010 Quantifying the interaction between large and small scales in wall-bounded turbulent flows: A note of caution. *Phys. Fluids* **22**, 051704.

Schlatter, P. & Örlü, R. 2012 Turbulent boundary layers at moderate Reynolds numbers: inflow length and tripping effects. *J. Fluid Mech.* **710**, 5–34.

Segalini, A, Cimarelli, A, Rüedi, J.-D., Angelis, E De & Talamelli, A 2011 Effect of the spatial filtering and alignment error of hot-wire probes in a wall-bounded turbulent flow. *Meas. Sci. Tech.* **22**, 105408.

Skåre, P. E. & Krogstad, P. 1994 A turbulent equilibrium boundary layer near separation. *J. Fluid Mech.* **272**, 319–348.

Skote, M., Henningson, D.S. & Henkes, R.A.W.M. 1998 Direct numerical simulation of self-similar turbulent boundary layers in adverse pressure gradients. *Flow Turbul. Combust.* **60**, 47–85.

Smits, A. J., Monty, J. P., Hultmark, M, Bailey, S. C. C., Hutchins, N. & Marusic, I. 2011 Spatial resolution correction for wall-bounded turbulence measurements. *J. Fluid Mech.* **676**, 41–53.

Spalart, P. R. & Watmuff, J. H. 1993 Experimental and numerical study of a turbulent boundary layer with pressure gradients. *J. Fluid Mech.* **249**, 337–371.

Stratford, B. S. 1959 An experimental flow with zero skin friction throughout its region of pressure rise. *J. Fluid Mech.* **5**, 17–35.

Townsend, AA 1956 The properties of equilibrium boundary layers. *J. Fluid Mech.* **1**, 561–573.

Vinuesa, R., Bobke, A, Örlü, R. & Schlatter, P. 2016 On determining characteristic length scales in pressure-gradient turbulent boundary layers. *Phys. Fluids* **28**, 055101.

Vinuesa, R., Negi, P. S., Atzori, M., Hanifi, A., Henningson, D. S. & Schlatter, P. 2018 Turbulent boundary layers around wing sections up to $Re_c = 1,000,000$. *Int. J. Heat Fluid Flow* **72**, 86–99.

Vinuesa, R. & Örlü, R. 2017 Measurement of wall-shear stress. In *Experimental Aerodynamics* (ed. S. Discetti & A. Ianiro). CRC Press Taylor & Francis Group, Boca Raton, FL.

Vinuesa, R., Örlü, R., Sanmiguel Vila, C., Ianiro, A., Discetti, S. & Schlatter, P. 2017 Revisiting history effects in adverse-pressure-gradient turbulent boundary layers. *Flow Turbul. Combust.* **99**, 565–587.

Vinuesa, R., Rozier, P. H., Schlatter, P. & Nagib, H. M. 2014 Experiments and computations of localized pressure gradients with different history effects. *AIAA J.* **52** (2), 368–384.

Wei, T. & Maciel, Y. 2018 Derivation of Zagarola-Smits scaling in zero-pressure-gradient turbulent boundary layers. *Phys. Rev. Fluids* **3**, 012601.

Yoon, M., Hwang, J. & Sung, H. J. 2018 Contribution of large-scale motions to the skin friction in a moderate adverse pressure gradient turbulent boundary layer. *J. Fluid Mech.* **848**, 288–311.